AN ABSTRACT OF THE DISSERTATION OF

Melissa J. Taylor for the degree of Doctor of Philosophy in Materials Science presented on May 23, 2011.

Title: Transient Electric Birefringence for the Characterization of Cellulose Nanocrystals and Tobacco Mosaic Virus

Abstract approved: _____

John Simonsen

The development of a transient electric birefringence (TEB) apparatus for macroparticle characterization is herein discussed. The experimental difficulties encountered were related largely to poor data resolution. Misalignment and strain birefringence in optical components further complicated results. Improved data digitization methods were developed, and precise mathematical models were derived in order to characterize stray birefringence. These were discussed in context of published linear estimations for TEB.

A size exclusion technique specific to cellulose nanocrystals was developed using liquid crystal phase separation. The size distribution differences for distinct liquid crystal phases were determined from diffusion coefficients measured with the TEB apparatus. Size distributions were compared to standard microscopy sizing techniques, specifically AFM and TEM.

Methods for absolute size distribution determination from measured diffusion coefficients were considered and attempted using a simplified method of linear inverse theory. We conclude that absolute size distribution solutions for inverse theory will require a significant reduction in experimental noise, as well as the development of more accurate mathematical models.

Transient Electric Birefringence for the Characterization of Cellulose Nanocrystals and Tobacco Mosaic Virus

by

Melissa J. Taylor

A DISSERTATION

submitted to

Oregon State University

in partial fulfillment of
the requirements for the
degree of

Doctor of Philosophy

Presented May 23, 2011
Commencement June 2012

Doctor of Philosophy dissertation of Melissa J. Taylor presented on May 23, 2011.

APPROVED:

Major Professor, representing Materials Science

Director of the Materials Science Program

Dean of the Graduate School

I understand that my dissertation will become part of the permanent collection of Oregon State University libraries. My signature below authorizes release of my dissertation to any reader upon request.

Melissa J. Taylor, Author

ACKNOWLEDGEMENTS

I would like to thank my advisor Dr. John Simonsen for his guidance and patience with me throughout the development of this research method. I would also like to acknowledge Dr. Wei Kong for allowing us the use of her lab space and equipment through the initial stages of our work, and Chad Teters for his guidance throughout the initial learning curve. Gratitude must also be expressed to Dr. Bill Hetherington for the donation of valuable lab space, as well as for his invaluable advice along the way. I would also like to thank my husband and life long collaborator, Dr. Bradley Matson, without whose technical and financial support this research would not have advanced as far.

TABLE OF CONTENTS

Page

TABLE OF CONTENTS (Continued)

TABLE OF CONTENTS (Continued)

LIST OF FIGURES

LIST OF FIGURES (Continued)

LIST OF FIGURES (Continued)

LIST OF FIGURES (Continued)

LIST OF TABLES

DEDICATION

I would like to dedicate this work to my aunt Rose, who inspired my childhood dream of having the “ultimate initials” after my name, and in loving memory to my uncle John, who gave me my first graphic calculator upon learning there was at last a science major in the family.

Chapter 1 – Introduction

1.1 The Motivation: From Cellulose to TEB

This research began as an investigation to improve production and characterization of rigid, rod shaped cellulose nanocrystals (CNCs) for applications such as polymer composites, medical materials, and electro-optical devices. As is often the case with biological nanoparticles, the large polydispersity of the resulting suspensions caused significant difficulties in the control and design of subsequent CNC based materials. Since standard separation techniques such as gel permeation chromatography often fail to differentiate between rigid particles varying only in length (i.e. having roughly uniform diameter), preliminary work went into developing novel size exclusion techniques. Apparent success was obtained using liquid crystal (LC) phase separation of CNC suspensions above critical concentrations.

Challenges then arose as to how to fully characterize the success of LC phase separation sizing. Microscopy methods such as AFM, TEM and SEM do not sufficiently sample the bulk suspension to provide statistically sound data, and agglomeration upon sample drying adds additional uncertainty to the estimated sizes of imaged particles. Light scattering techniques probe the bulk of the suspension and provide statistically significant sampling. The mathematical theory behind these techniques are based on spherical particles, however. As such, dynamic light scattering (DLS) yielded average hydrodynamic volumes based on radius of gyration, but not detailed size distributions regarding particle length. Static light scattering (SLS) was also attempted. However, SLS models rely on extrapolation to infinite dilution (i.e. Zimm and Berry plots). This required a higher

degree of experimental accuracy for low sample concentrations than we were able to reproducibly achieve.

Partway into this research on unsatisfying particle sizing techniques, we were introduced to Transient Electric Birefringence (TEB), in which anisotropic particles are aligned in an electric field. The rotational diffusion coefficient is measured directly from time-dependent optical signals resulting from bulk alignment of particles in suspension. Since rotational coefficients can be related directly to particle length given appropriate a priori information, this seemed the most sensitive means to get length information from our samples.

The research turned to the development a TEB apparatus to characterize cellulose nanocrystals. In the course of this development, numerous electronic and optical challenges were encountered which forced a review and revision of the traditional data capturing techniques and optical assumptions used by previous TEB experimentalists. For this reason, the chapters in this dissertation will be divided into seemingly disparate sections: those related to the production and preparation of cellulose nanocrystal suspensions, and those relating to the development and improvement of the TEB characterization technique. The outcome of this work is twofold. Firstly, a novel method for size exclusion of cellulose nanocrystals has been developed, as demonstrated using the TEB technique. Secondly, a TEB apparatus has been developed with improved data resolution for use in subsequent experiments. Since no commercial TEB apparatus is yet available, we hope that outlining the challenges we encountered will ease the way for the future researchers seeking to utilize this technique.

1.2 Cellulose Nanocrystals

1.2.1 Introduction

Cellulose is considered to be the most abundant biopolymer on earth. Its low cost and physical and chemical properties make it an easily exploitable source of biomass for many commercial uses. It is synthesized in plant cell walls in hierarchical structures of crystalline microfibrils embedded in lignins and hemicelluloses. When cellulose from wood pulp or cotton is beaten in water, long strands are produced, called *fibrils*, which are composed of microcrystalline sections interconnected by amorphous regions. The cellulose itself is composed of repeating β-(1,4)-linked glucopyranosyl subunits (Figure 1.2.1.1 a) forming long chains arranged in parallel. These subunits are linked in equatorial-equatorial orientation such that the ring oxygen of one glycosyl unit can form hydrogen bonds with the C3 hydrogen of the previous ring, thus preventing free rotation around the glycosil linkage and stiffening the cellulose chain (Figure 1.2.1.1 (b)) [1, 2], giving the ribbon-like character of the cellulose macromolecules.

The crystallinity of the cellulose elementary fibril arises from parallel, ribbon-like cellulose macromolecules fitting closely together. There are multiple ways in which the chains can be packed together, giving rise to several polymorphs of crystalline cellulose. The native cellulose synthesized by plants and certain bacteria and fungi is Cellulose I. Cellulose I is not the most thermodynamically stable polymorph. It is readily converted to the more stable Cellulose II polymorph upon merceration (swelling in concentrated sodium hydroxide) or regeneration (solubilization in solvent followed by precipitation in water.) Cellulose III can be reversibly produced from cellulose I and II by treatment of liquid ammonia, with Cellulose I and II giving rise to polymorph III_1 and III_{11} respectively. Heating polymorphs III_1 and III_{11} to 206°C in glycerol gives rise to polymorphs

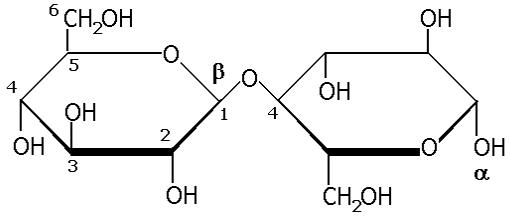

(a) Cellobiose Repeat Unit

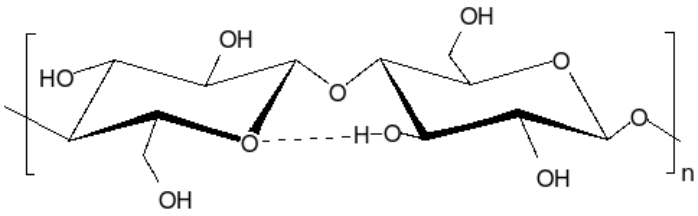

(b) Intrachain Hydrogen Bonding

Figure 1.2.1.1: The cellobiose repeat unit. The β-D-glucopyanosyl-(1$\rightarrow$4)-α-D-glucopyanosyl unit (a) is the repeating unit in cellulose. The cellobiose repeat unit is stabilized by intra-chain hydrogen bonding (b), giving the ribbon-like structure of the cellulose macromolecule.

IV_1 and IV_{11} respectively. The precise crystal structure of cellulose and all its polymorphs is under continuous study. A detailed discussion is beyond the scope of this paper; please refer to [3] and references therein for further reading.

The amorphous regions along the elementary microfibril arise from imperfect cellulose chain packing, likely due to stress during biosynthesis. It has been deduced that elementary cellulose microfibrils are synthesized by rosettes of terminal complexes (TCs) in plant plasma membranes. Groups of these TCs are responsible for elongating all cellulose macromolecular chains in the microfibril simultaneously. Since the cellulose macromolecules form two-fold screw symmetry along their length [4], torsional stress release during synthesis causes repeated regions of lesser order along the fibril. Severe acid hydrolysis preferentially degrades these regions of lesser order, resulting in crystalline cellulose fragments, or whiskers. Initially, acid attack is very rapid, breaking only

the molecular hinges between crystalline regions to leave disconnected crystallites, after which a levelling off of the reaction rate occurs. The level off degree of polymerization (LODP) from this process varies depending on the cellulose source. Typical LODP values for purified cotton are 200-250 [5], where degree of polymerization (DP) is as defined by the total molecular weight of the polymer crystallite divided by the molecular weight of the monomer unit.

Stable colloidal suspensions of crystalline whiskers can be prepared by adding surface charges. This was first described by Rånby in 1951 [6], with the use of sulfuric acid as the hydrolysing acid in place of hydrochloric acid. The introduction of sulfate ester groups onto the crystallite surface leads to electrostatic stabilization of suspensions [4]. An alternative method for adding surface charge involves oxidation of primary or secondary hydroxyls to carboxylic acids. In both cases, electrostatic repulsion from surface charge prevents agglomeration of individual cellulose crystallites, resulting in more stable suspensions.

1.2.2 Microcrystalline and Nanocrystalline Cellulose

1.2.2.1 Defintions and Terminology in Scale

There is some discontinuity in the literature over the past decades between the use of the terms colloids, micelles, microcrystals and nanocrystals. Examples of references claiming to produce colloids or micellular solutions have been referenced decades later as having produced nanocrystals, such as the 2005 reference [7] to Rånby's 1949 report "Aqueous Colloidal Solutions of Cellulose Micelles" [8]. Likewise, [7] redefines Revol, Godbout, and Gray's "microcrystallites" [9] as nanocrystal suspensions. The change in terminology was likely concurrent with both the evolving definitions of nanomaterials and the

increased understanding of cellulose structure. Although there is currently no internationally accepted definition for a nanomaterial, a terminology standard will be laid down here for clarity.

The American Chemistry Council in March of 2007 proposed that an *Engineered Nanomaterial* be defined as "any intentionally produced material that has a size in 1, 2, or 3-dimensions of typically between 1-100 nanometers." [10] Although a parallel definition is not in place for bio-nanomaterials, the same nomenclature is generally adopted. As such, Rånby's 60 Å by 600 Å micelles [8], as well as Revol et. al.'s 100-200 nm by 5-10 nm particles [9] qualify as nanomaterials. For all other incongruencies, the above definition will be applied in this work. Following this, microcrystalline materials will be defined as those in which a size of the smallest dimension is between 1μm and 100 μm.

1.2.2.2 Production of Micro and Nanocrystalline Cellulose

The mechanism of acid hydrolysis of amorphous cellulose starts with the rapid protonation of the glycosidic bond, followed by fission of this bond to form a carbonium ion (Figure 1.2.2.1, steps 1 and 2.) The carbonium is attacked by water in the rate determining step (Figure 1.2.2.1, step 3) to form the free sugar residue and re-form the hydronium. If the acid used is hydrochloric, the resulting crystallites will have uncharged surfaces. If sulfuric acid is used, and additional esterification of the surface hydroxyls by sulfate ions will occur, resulting in charged surface groups (Figure 1.2.2.2).

Acid hydrolysis produces nanocrystalline cellulose in aqueous suspension. Although freeze drying can be used to obtain nanocrystalline cellulose in the dry state, the process generally results in significant agglomeration. Characterizing dielectric and hydrodynamic properties for CNCs in liquid suspension is therefore the preferred method for our research. The remainder of this section will specifically describe cellulose nanocrystals,

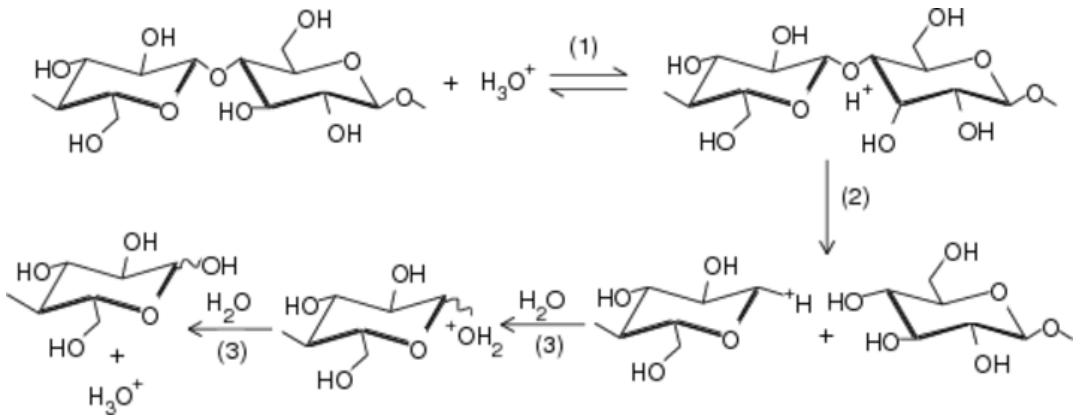

Figure 1.2.2.1: Mechanism of acid hydrolysis of cellulose. Rapid protonation of the glycosidic bond by hydronium ion (step 1) is followed by fission of this bond to form a carbonium (step 2). The carbonium is attacked by water in the rate determining step (3) to form the free sugar residue and re-form the hydronium. (Schematic recreated from reference [11].)

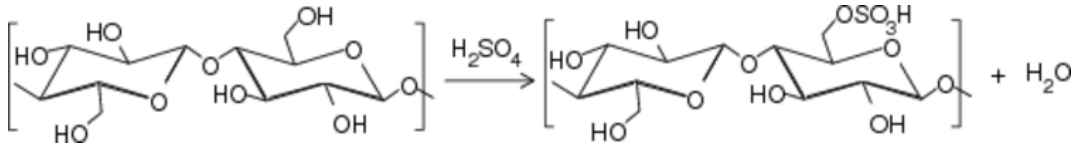

Figure 1.2.2.2: Esterification of cellulose surface hydroxyls by sulfuric acid.

beginning with a discussion of the cellulose suspension stability as it pertains to surface charge and dielectric properties of cellulose nanocrystals. The last section of this chapter will pertain to electric birefringence as a method for measuring hydrodynamic properties.

1.2.3 Stability of Cellulose Nanocrystals Suspensions

A colloidal system results when one of the three states of matter, liquid, solid or gas, is finely dispersed in another state. The classification system defines an aerosol as a dispersion of liquid in a gas phase, a sol as a solid in liquid phase, and an emulsion as two non-miscible liquids. If the colloids are self-attracting, they are called lyophylic (hydrophilic if solution is water), or lyophobic (hydrophobic in aqueous system) if they are self-repelling [12]. The stability of these suspensions is balanced by competing forces [13]. Firstly, an attractive force between particles exists due to long range hydrodynamic interactions. Additional long range coulombic interactions between particles arise from the sign and magnitude of the charge on the particle, as well as their counterion distribution and the supporting polyelectrolytes in the surrounding medium. When two macroions approach each other, short-range attractive forces can occur from van der Waals interactions. Fourthly, a strong hydration repulsive force dominates over all the others when macroions are brought closer together.

The balance of these forces determines the behavior of a colloidal suspension. If individual colloids begin to adhere to one another, the initial floc can accumulate other particles to form larger agglomerates in a process called flocculation. If agglomerates are a different density than the surrounding solution, phase separation can occur by gravity sedimentation for denser agglomerates, or by "creaming" for less dense agglomerates. The stability and phase behavior of suspensions was described by a classic theory developed by Derjaguin, Verwey, Landau, and Overbeek (DVLO theory) in the 1940's. The

theory attempts to predict the potential energy of a particle in solution, V_T, as a function of competing energy functions, $V_T = V_A + V_R + V_S$, where A and R subscripts represent the potential energy contributions from attractive and repulsive forces, and S is due to that of the solvent. In order to understand DLVO theory better, some basic concepts of electric double layer and solution ionic strength must first be addressed.

1.2.3.1 Electric Double Layer and Zeta Potential

Models for the Electric Double Layer: Most colloidal particles in aqueous suspensions carry some surface charge due to various reasons. The first could be a surface functional group ionization event, such as a -COOH $\longrightarrow$ -COO^- H^+. Secondly, ions dissolved in solution could bind to an otherwise charge-neutral surface due to molecular dipoles. A third possibility is an exchange of higher valence ion replacing lower valence ions on the surface. This effect lowers the overall solution ionic strength (IS). IS is defined by both the valency and concentrations of all ion species in solution as $\Sigma_i {z_i}^2 c_i$, where z_i and c_i are the valency and concentrations of ion species i. The charge density on the particle surface, σ^0 (in $\mu C/cm^2$) interacts with the solution IS to form the Electric Double Layer (EDL). In simplest functional model, the solution side of the surface/particle boundary is considered to be composed of several layers. Due to steric hindrance, ions in solution are unable to penetrate the particle surface. They instead interact with σ^0 to form a layer of ions along the particle surface. Figure 1.2.3.1, (a) and (b) shows two simple models for the organization of these ions as a function of distance from the particle surface. Figure 1.2.3.1 (c) shows the Stern Model as a hybrid of these two, where the electric double layer is composed of a rigid Helmholtz layer nearest the surface, followed by a diffuse layer (also called the Gouy-Chapman Layer) extending into the bulk of the solvent. Surface potentials are shown as a function of distance from surface for all three models (Figure

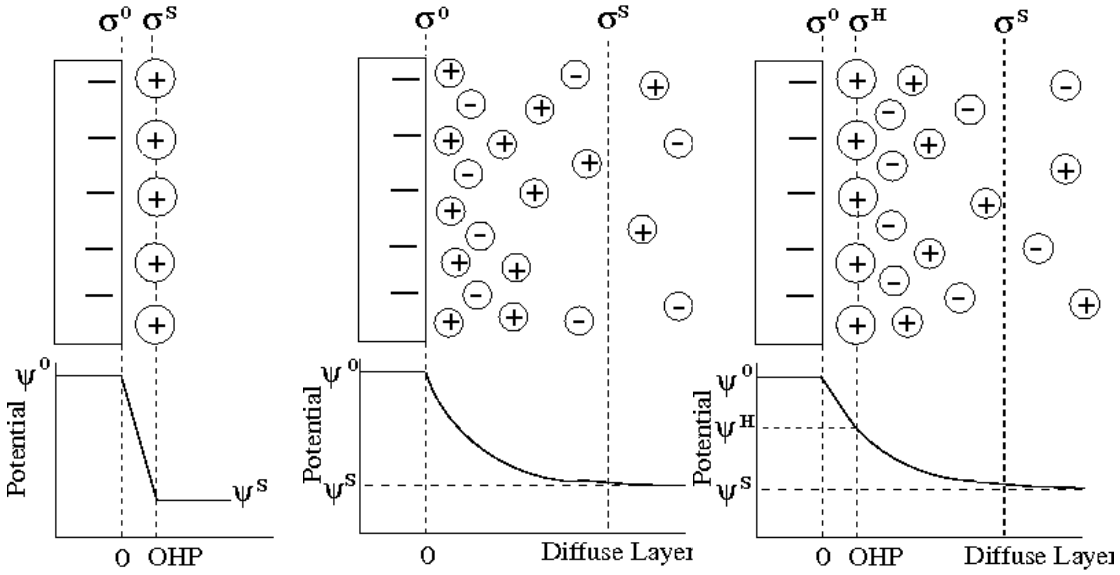

Figure 1.2.3.1: Development of the Stern Model for the electric double layer (c) as a combination of two simpler models, (a) and (b). The Helmholtz model (a) depicts a rigidly absorbed layer of counterions to a charged surface. The Gouy-Chapman model (b) depicts an exponentially decaying concentration of counterion concentration from the particle surface ($distance = 0$) to the solution bulk. Electric potentials as a function of distance from particle surface are depicted below, where Ψ is the electric potential and σ the charge density at the surface (0), the bulk solution (S), and the Helmholtz Plane (H) respectively

1.2.3.1 [12]).

For most purposes, a more complex model is necessary to interpret experimental data. When certain ion types absorb specifically to the surface (i. e. through chemical affinity rather than purely coulombic forces), whereas others only interact through electrostatic interactions, the Grahame Model can be used [14]. In this case, the Stern Layer is sub-divided into two layers (Figure (1.2.3.2). The inner layer is called the Inner Helmholtz Plane (IHP), and makes up a total charge density σ^i at a distance β from the surface. The outer Helmholtz Plane is composed of nearest solvated ions which can only approach the IHP at a distance d. These ions interact with long range electrostatic forces which

are independent of ionic chemical properties, so this layer is said to be non-specifically adsorbed. The potential at the OHP (Ψ^d) is the diffuse-layer potential, also known as the Stern potential in this model, after which point an exponentially decaying potential arises as the ion concentration decreases to that of the solvent bulk. This layer is composed of thermally diffused, non-specifically adsorbed ions which are either attracted to the particle surface charge or to the Stern layer. At a distance d^{ek} from the surface, a shear potential is defined, which is called the electrokinetic potential, or zeta- potential (ζ).

Zeta-potential: A charged particle in an externally applied electric field will move at a fixed velocity in a process called electrophoresis (where the particle moves with respect to the liquid). The counterpart is electro-osmosis, where the liquid moves with respect to the particle. In either case, a tangential flow of solvent across the particle surface occurs, generally with a very thin layer of fluid adhering to the surface [14]. At this boundary, defined in the Grahame Model as the "slip plane" [16] or "shear" plane" [12], the hydrodynamically stagnant layer extending from the surface gives way to the region in which tangential flow of both solvent and ions will occur. The electrochemical potential extending from a charged particle surface to the solvent bulk is illustrated in Figure (1.2.3.2), where ζ is defined at the shear plane.

The velocity at which the particle moves in the applied field depends on solution viscosity and dielectric constant, as well as the zeta-potential. The definition of a shear plane is abstract, however, since transitions between the layers are generally not sharp. It is possible that the immobilization of fluid extends beyond the beginning of the diffuse part of the EDL, and the difference between the diffuse layer potential Ψ^d and the actual zeta potential is dependent on ionic strength (IS) of the solution. If the IS is high, the decay of the electric potential is steeper than at low IS, so $|\zeta| \leq |\Psi^d|$ [14].

There is no direct method to measure ζ experimentally. Instead, the velocity $\mathbf{V}_S$ of the

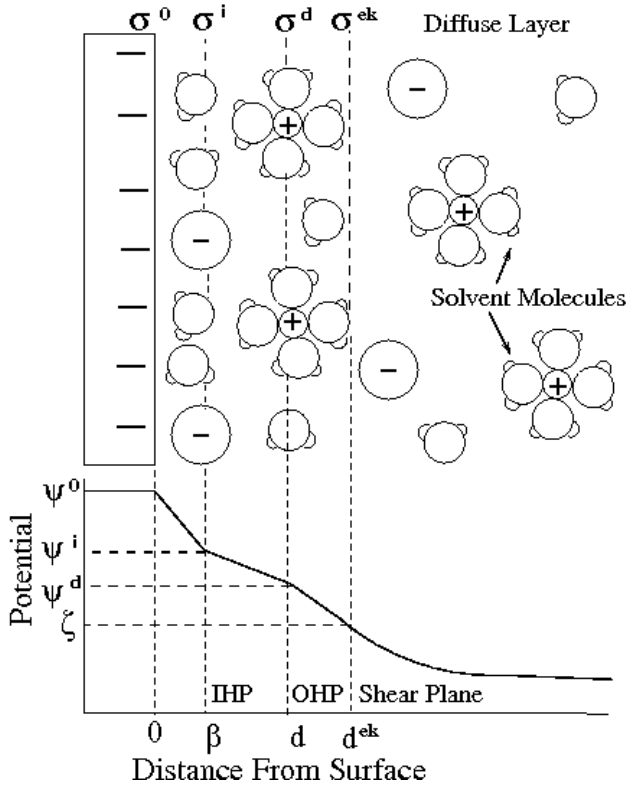

Figure 1.2.3.2: The Grahame Model of the electric double layer. The zeta-potential, ζ, occurs at the shear plane. Ions specifically adsorbed (defined as those with chemical affinity to the surface other than coulombic interactions) occur at a distance β, also known as the Inner Helmholtz Plane (IHP). Solvated ions interact non-specifically at a distance d to make up the Outer Helmholtz Plane (OHP). Charge densities are represented by σ and surface potentials by Ψ. The electrochemical potential drops off linearly through the IHP and OHP, then exponentially through the diffuse layer. The potential at the OHP (distance d) is the diffuse-layer potential Ψ^d, also known as the Stern potential in this model. The potential at the shear plane (beyond OHP at the boundary of the diffuse layer) is the electrokinetic, or zeta-potential (ζ). At this point, the hydrodynamically stagnant layer extending from the surface gives way to a region in which tangential flow of ions will occur in an external electric field. The fixed surface charge density, σ^0, the charge density at the IHP (σ^i), and the charge density in the diffuse layer (σ^d) satisfy the condition of electroneutrality, that is $\sigma^0 + \sigma^i + \sigma^d = 0$. (Schematic distilled and recreated from [12, 14, 15].)

particle moving in the electric field $\mathbf{E}$ is measured and used to calculate ζ via a parameter called electrophoretic mobility μ_e, where $\mathbf{V}_S = \mu_e \mathbf{E}$. The relationship between μ_e and ζ depends on the model chosen. The location of ζ in the EDL depends on the particle surface charge density, the EDL properties, and the solution IS and permittivity. Two models exist for calculating ζ from μ_e, both using a parameter κa, where $1/\kappa$ represents the EDL thickness and a is the radius of the entire electro-kinetic unit (particle plus double layer up to the shear plane.) In the thick atmosphere approximation ($\kappa a \ll 1$), the Hückel model applies, $\mu_e = (2e\zeta)/3\eta$, where η is the viscosity of the suspending medium and e is the elementary charge [17]. This is appropriate for small molecules in low IS solutions. In the thin atmosphere regime ($\kappa a \gg 1$), the Smoluchowski limit is used, where $\mu_e = (e\zeta)/\eta$. For typical colloids (between 100 and 1000 nm in diameter) dispersed in 1 mM aqueous KCl solutions, κa can vary between 10 to 100, whereupon neither model is completely satisfied. Although more complicated models have been proposed to address such discrepancies, one should keep in mind is that ζ is a function of solution IS as well as certain mathematical approximations. It is therefore problematic to determine an accurate ζ without accurate knowledge of particle and EDL dimensions. Comparative values can be measured under "identical" conditions as a means to rapidly compare modifications of electrical state between two colloidal systems [14]. If accurate ζ values are required for a given particle, a priori information about the particle's size and EDL thickness must be applied.

For these reasons, there are no absolute calibration standards available for zeta-potential measurements. There are, however, a few well-characterized colloids against which experimental zeta-potentials can be compared for reference. One such colloid is the BI-ZR3 reference material provided by Brookhaven Instruments Corporation [18]. Following the preparation procedure outlined in [17], a zeta-potential of -53 mV $+/-$ 4 mV is expected. As a rule of thumb, a colloid is considered to have "good stability" if the ζ is between

$\pm$ 40 mV and $\pm$ 60 mV, where the sign is representative of positive or negative surface charge. The significance of the zeta-potential to colloid stability is will be demonstrated in the following section.

1.2.3.2 Suspension Stability and DLVO Theory

Colloidal suspensions are inherently unstable due to the constant presence of attractive forces, specifically van der Waals forces. The second law of thermodynamics likewise predicts a coalescence of smaller particles to reduce surface energy. For simple molecules, these attractive forces vary as r^{-6}, where r is the intermolecular distance. For colloids, attractive forces are the sum of individual pair-wise molecular forces, and thus the attractive forces vary between D^{-1} and D^{-2} depending on shape and size, where D is the shortest distance between particles [17]. Therefore, colloids will attract each other over much longer ranges than simple molecules and, without a stabilizing repulsive force, will readily flocculate.

Considering the electric double layer discussed above, we can imagine that the repulsive forces for colloids in suspension will not arise from bare Coulomb forces alone. (Recall that the coulomb force is $F = k_e \frac{q_1 q_2}{r^2}$, where q_1 and q_2 are two point charges, r is the distance between them, and k_e is Coulombs constant). In the presence of the double layer, coulombic charges in particles are shielded from one another, and the electrostatic repulsion arises from interference between double layers. Like charges on adjacent particle double layers would result in electrostatic repulsion and discourage agglomeration. This is described by

$$V_{repulsion} = \frac{A a^2 \zeta^2}{R} e^{-s/r_D}, \tag{1.2.1}$$

where A is a constant, a is the radius of (spherical) particles, ζ is the zeta-potential, R

is the distance between particle centers, s is the distance between particle surfaces (i. e. $s = R - 2a$), and r_D is the double layer thickness. This equation is valid for particles that are small with respect to r_D ($a \ll r_D$). When $a \gg r_D$, eqn. 1.2.1 is replaced by

$$V_{repulsion} = \frac{1}{2} A a^2 \zeta^2 ln(1 + e^{-s/r_D}). \tag{1.2.2}$$

The Debey-Hückel theory allows us to estimate the thickness of the double layer as

$$r_D = \frac{\varepsilon RT}{2\rho F^2 I b^{\ominus}}^{1/2}, \tag{1.2.3}$$

where I is the ionic strength of the solution, ρ is the mass density, and $b^{\ominus} = 1\ mol\ kg^{-1}$. In the absence or reduction of the surface charge, attractive van der Waals forces will cause particles to flocculate. This attractive force is given by

$$V_{attraction} = \frac{B}{s}, \tag{1.2.4}$$

where B is a constant [12].

The van der Waals forces are cumulative and long ranged between multiple particles, whereas electrostatic forces only come into play when particles are close enough for charge layers to interfere. The net interaction energy can be seen as a subtraction of the van der Waals attractive forces from the electrostatic repulsion curve as seen in Figure 1.2.3.3. The point of maximum repulsive energy in the net interaction energy curve is known as the energy barrier, and represents the kinetic energy two colliding particles must have in order to agglomerate. The energy trap region represents the area after which the energy barrier is cleared and all net forces are attractive. Thus particles are “trapped” in agglomerates, also called coagulated. At high ionic strength, a second minimum in the net interaction energy curve can occur which can result in flocculation. Agitation can

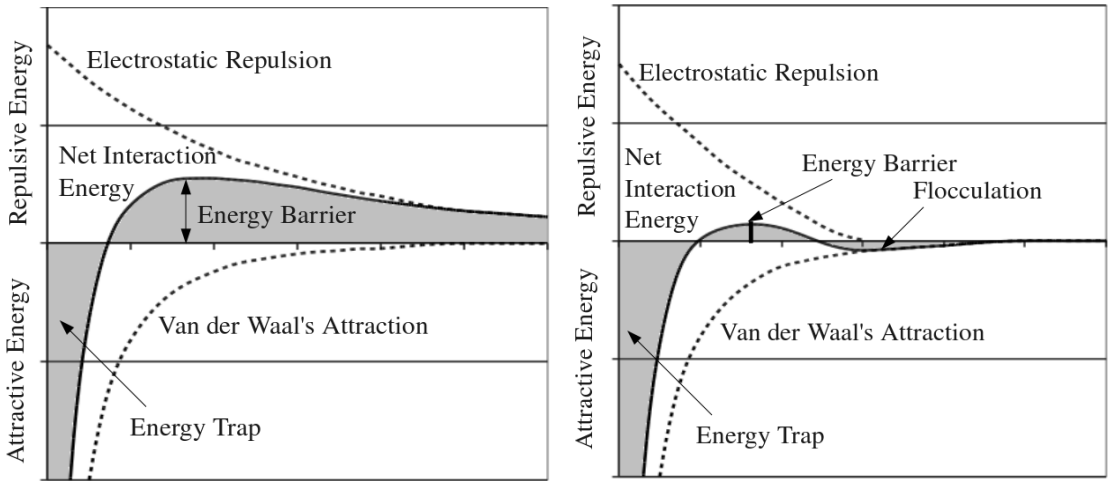

(a) No Flocculation (b) Flocculation

Figure 1.2.3.3: The electrostatic repulsion curve derived from the combination of the van der Waals attractive forces and the electrical repulsion curve as a function of inter-particle distance. The maximum in the net interaction energy corresponds to an energy barrier that must be overcome on order for particles to agglomerate. The energy trap region represents the energy region in which particles are irreversibly agglomerated. At high ionic strengths, a second energy minimum can result in a reversible flocculation region [12].

often disrupt flocculated material, whereas coagulates are irreversibly agglomerated. The overall stability of a colloidal suspension increases as the height of the energy barrier increases, which is largely due to changes in the electrostatic repulsion curve arising from EDL interactions. Thus stability is more influenced by surface properties and solution IS than the bulk properties of the colloid.

1.2.4 Cellulose Nanocrystals as Liquid Crystals

1.2.4.1 Overview of Liquid Crystals

The electric double layer (EDL) potentials discussed above influence how particles with anisotropic geometries align with one another when concentrations exceed the dilute (i.e.

non-interacting) regime. For long rigid rods, liquid crystal (LC) behavior is often observed, where both the geometric anisotropy and EDL properties determine the macroscopic nature of the LC alignment. The term "liquid crystal" is used to describe a hybrid state of matter with properties between that of a liquid and a solid crystal. Particles display long range order while retaining fluidity. In the case of thermotropic LCs, the order evolves with some phase transition upon a temperature change. Lyotropic LC order is dependent on both temperature and concentration of the LC particles in some solvent. Lyotrophic LCs are therefore more influenced by the EDL properties extending into the solvent, as particles will interact primarily with one another via their electric double layers.

A detailed overview of liquid crystal phases and subclassifications is beyond the scope of this work. Specific to our studies are the concepts of nematic liquid crystals, in which rigid rod-shaped particles align with one another along their long axes as shown in Figure 1.2.4.1 (a). A subclassification of nematic order is chiral nematic, where planes of nematically aligned molecules stack of helically as shown in Figure 1.2.4.1 (b). For particles which themselves have anisotropic optical properties, nematic order can impart a macroscopic birefringence in the system.

1.2.4.2 Cellulose Nanocrystals as Liquid Crystals

The high aspect ratio for cellulose nanocrystals arises from acid hydrolysis of amorphous regions between long crystalline segments of the cellulose elementary fibril, where crystalline segments are long with respect to the fiber diameter. Depending on the cellulose source, average crystallite dimensions can range between 100-1000 nm in length, and vary between 3-20 nm in width [7]. The first stable colloidal suspensions of such crystallites were produced by Rånby and Ribi [8, 19], followed by the first electron microscopy

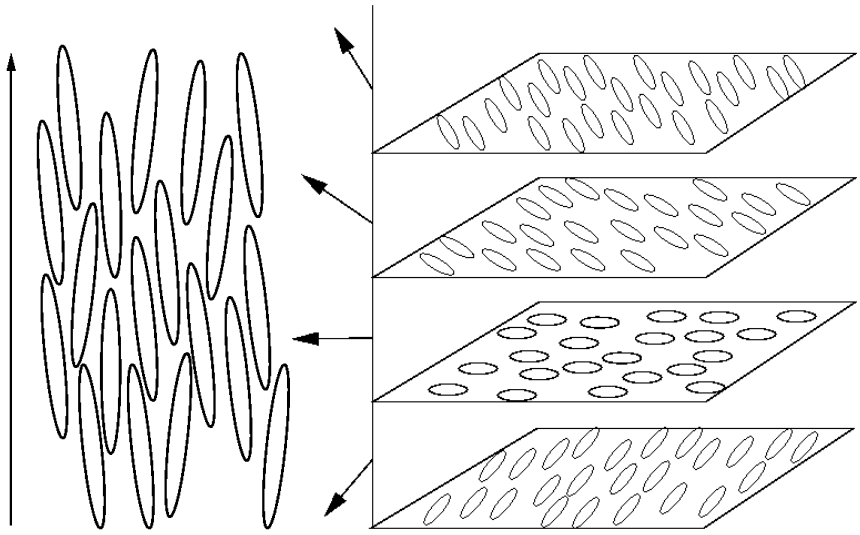

(a) Nematic LC Phase (b) Chiral Nematic LC Phase

Figure 1.2.4.1: Nematic (a) and chiral nematic (b) liquid crystal phases.

verification that acid hydrolyzed native cellulose was indeed colloidal suspensions of individual crystallites [20, 21]. It was soon thereafter observed that these colloidal suspensions formed birefringent regions when dried from dilute solutions [22], and displayed liquid crystal behaviour under gel flow shear stress. Due to the strong birefringence of native cellulose, the resulting macroscopic birefringence could be observed directly through crossed polarizers; the liquid crystal regions were determined by electron-micrograph to arise from parallel alignment of crystallites along their long axes.

In more recent studies, Revol, et. al. observed the formation of stable chiral nematic liquid crystalline phases for sulfuric acid treated kraft pulp [23]. This chiral nematic is a helical stacking of nematic phases around a cholesteric axis. At dilute concentrations, Brownian motion causes particles to be randomly oriented. As concentration increased by the evaporation of solvent (water), birefringent droplets, or tachtoids, were observed to form then coalesce into a continuous anisotropic fluid phase [9, 23]. It was proposed by Revol and co-workers that, in the absence of an assymmetric “twisting agent” in these

solutions, the cholesterolic stacking must arise from either a twist in the microfibril crystal structure [24] or a twist in the distribution of surface charge groups [23]. Support for this theory comes from [25], where the addition of trace electrolyte disrupted a spontaneous phase separation, possibly due to shielding of this twisted morphology.

Another series of publications investigated the effect of surface charge, ionic strength and counterion species on isotropic-chiral nematic phase transition behaviour [26–29]. These rely on a modification to Onsager's original model for liquid crystal phase separation of rigid rods [30] propsed by Stoobants, Lekkerkkerker, and Odjik (SLO) [31]. Onsager's original model for uncharged, perfect rigid rods of diameter D and length L predicted a critical concentration for phase separation that depended only on the aspect ratio, L/D. For polyelectrolytes, the surface charge plays an important role in the free energy of the system due to electrostatic interactions. Modifications to Onsager's theory involve methods to estimate the effective diameter produced by the surface charge, as well as the twisting factor arising from electrostatic repulsion. Since both of these interactions depend on surface charge density, counterion size and density, and solution ionic strength (that is the shielding effects), the system becomes increasingly intractable. Experimental evidence suggests that the equilibrium is governed by a balance between hydrophobic attraction and electrostatic repulsion [27]. Size fractionation is also a key factor, with longer particles forming more ordered phases [28].

1.2.4.3 Liquid Crystal Phase Separation

Onsager's original theory used the excluded volume effect to predict the critical concentration for ordered phase formation using the aspect ratio for rigid rods. It has been observed that the critical concentration for cellulose was generally lower than predicted by Onsager because of an increase in effective diameter due to a surface charge cloud [32].

Refinements of Onsager's theory sought to include electrostatic effects, as well as hydration forces, hydrophobic interactions and hydrogen bonding. For polydisperse suspensions of cellulose whiskers, variation of solution properties had profound effects [2]. The observed outcome was phase separation, where isotropic and anisotropic LC phases co-exist in equilibrium for a range of critical concentrations. Extensive studies have been done to correlate the phase separation behavior to surface charge [28], counterion strength [33], solution ionic strength [26], and nano-whisker concentration [32]. The interfacial tension between the phases was also addressed [34]. The ordering properties have been studied using ultra-small-angle X-ray scattering [35], parabolic focal conics [36], and small angle neutron scattering [29]. The size exclusion properties of the phases has generally been overshadowed by the electrostatic consideration. Our work seeks to elucidate the relative size distributions in the isotropic and anisotropic phases of cellulose nanowhiskers. Section 4.1.3 will discuss the experimental procedures employed for the size fractionation of CNCs.

1.2.4.4 Refractive Index and Birefringence

From the above discussion of the surface electric properties of macroparticles in solvent suspension, it becomes intuitive that such properties would react under the influence of an externally applied electric field. This gives rise to a variety of techniques in which to probe dielectric properties of particles. One such technique uses external fields to align particles in an applied field, and thus provides hydrodynamic properties via diffusion coefficients. If the alignment in solution gives rise to a macroscopic optical anisotropy, the effect is called electric birefringence. A brief overview of the technique will be provided in the following section. A more comprehensive literature review of the technique will follow in subsequent chapters.

1.3 Transient Electric Birefringence

The application of macroparticles as inclusions in homogeneous matrices for conductive polymers, artificial dielectrics, and porous composites is a rapidly developing field. When considering bulk dielectric properties of inhomogeneous materials, the Effective Medium Theory (EMT) provides a powerful tool for estimating radiative properties [37, 38] and effective transport properties, such as dielectric constants [39]. One of the most widely used of the EMT is the Maxwell-Garnett (MG) approximation [40], also known as the Claussius-Mossotti relation [41], which considers an exact calculation of the electrostatic distortion caused by a spherical or ellipsoidal inclusion in a homogeneous matrix. This requires the dielectric constants of both the medium and the inclusion, as well as the dimensions of inclusion and its volume fraction in the material. Although the MG model breaks down for inclusions with a higher degree of anisotropy or a larger size distribution, more sophisticated approaches to the model still require well characterized parameters for dielectric constants. Electro-optic (EO) techniques provide a means to measure dielectric parameters for anisotropic inclusions, as well as providing diffusion coefficients from hydrodynamic theory. Diffusion coefficients can also be used to estimate size and dimensions of inclusions. Therefore, EO techniques are promising characterization tools for macroparticles required for composites with customizable mechanical and dielectric bulk properties.

The EO phenomena, which include light scattering, birefringence, and dichroism in an electric field, rely on three domains of physics to obtain information on macromolecules. These are hydrodynamics, electrostatics, and optics [38]. Chapter 2 will expound upon the electrostatics and relate these to refractive index of a material and the electronic surface properties of colloidal particles. The hydrodynamic aspects will be discussed in chapter 3, including a method for measuring rotary diffusion coefficients to determine particle size

distributions. A mathematical approach to the optics specific to electric birefringence will be covered in Section 4.2.

1.3.1 The Apparatus

Figure 1.3.1.1 shows a typical electro-optic experimental setup. A sample is placed between plane parallel electrodes attached to an external voltage source. Plane polarized monochromatic light emerges from a polarizer oriented at 45 degrees with respect to the electrodes. The light passes through the sample between the plane parallel electrodes. A second linear polarizer (referred to as the analyzer) is placed after the cell at crossed position to the first. When the applied electric field is off, the sample is isotropic and light emerges from the cell in the same polarization state as it entered: linearly polarized orthogonal to the analyzer. The light is thus extinguished by the analyzer. Upon the application of an external electric field, the sample becomes increasingly anisotropic as the particles align with the field. This causes the sample to macroscopically behave as a uniaxial crystal, in which the two orthogonal components of the incident linearly polarized light (parallel and perpendicular to the applied field) now travel through the media at different velocities. The two components become shifted from one another by phase angle δ, and the light emerging from the cell is now elliptically polarized (Figure 1.3.1.2). Some component of the elliptically polarized light exiting the cell will be parallel to the transmission axis of the analyzer and will pass through to the detector beyond. The ellipticity increases exponentially in time as the field persists and the sample becomes increasingly anisotropic. This provides an optical means to measure orientation as a function of field strength and duration. The equation given by Benoit [42] to describe the time-dependent

rise response is

$$\Delta n = \Delta n_0 \left[1 + \frac{\gamma - 2}{2(\gamma + 1)} exp(-D_R t) - \frac{3\gamma}{2\gamma + 1} exp(-2D_R t)\right], \tag{1.3.1}$$

where Δn_0 is the steady state birefringence, D_R is the rotational diffusion coefficient, and γ is a function of both induced and permanent dipole moments given by $\gamma = \mu'^2/(\alpha_\parallel - \alpha_\perp$. Here μ' is the screened permanent dipole and $\alpha_\parallel$ and $\alpha_\perp$ are the electric polarizabilities along the symmetry and transverse axes of the anisotropic particle, respectively. The removal of the field results in an exponential decay of the signal as the sample returns to the isotropic state. The decay curve provides a means to observe field-free diffusion properties of the material unbiased by the electronic properties, and is given by

$$\Delta n = \Delta n_0 \, exp(-6D_R t). \tag{1.3.2}$$

Figure 1.3.1.3 illustrates a typical electro-optic signal for a transiently applied electric field.

1.3.2 Indices of Refraction and Birefringence

The refractive index of a material (n) is defined by the ratio of electromagnetic radiation's velocity in a vacuum ($c \approx 3 \times 10^8$ m/s) to the phase speed of a specific frequency of radiation in a material υ such that $n = \frac{c}{\upsilon}$. If a material has two different refractive indices depending on crystallographic direction, it is referred to as birefringent. For the case in which there is only one anisotropic axis (called the optical axis), the material is uniaxial. The birefringence is defined as $\Delta n = n_e - n_o$, where n_e and n_o are the indices for polarizations parallel and perpendicular to the optical axis respectively. If alignment occurs along the direction of an externally applied field (along the x-axis in figure 1.3.1.1),

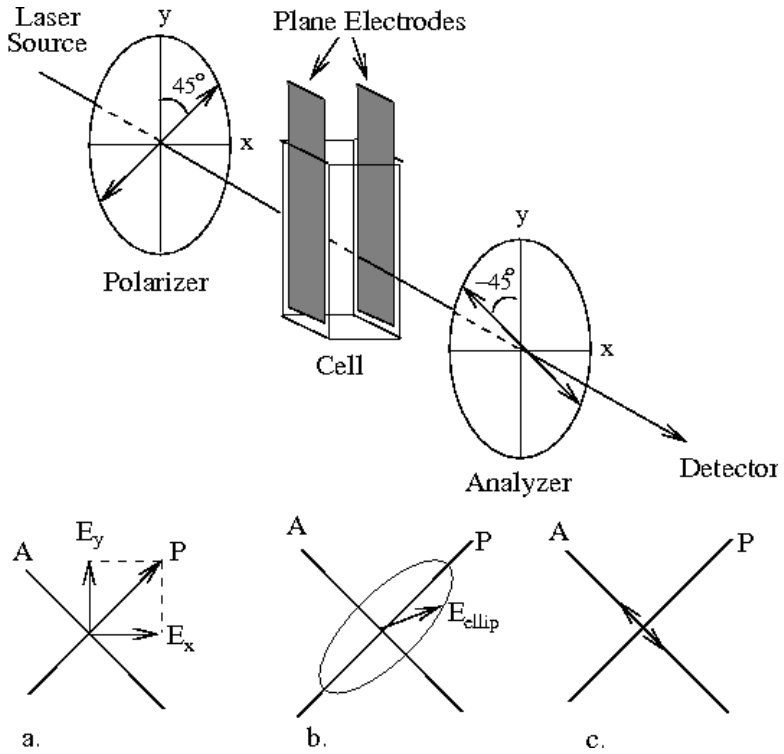

Figure 1.3.1.1: Electric birefringence apparatus. A coherent, monochromatic light source first passes through a linear polarizer at 45° with respect to the horizontal axis (x). The light emerges from this polarizer plane polarized at 45 degrees with respect to the lab x-axis, where the orthogonal components can be projected onto the x and y directions as depicted in a.) When an electric field is applied across the cell (along the x-axis), the E_x and E_y components of the incident beam emerge phase shifted from one another, giving rise to elliptically polarized light. The polarization ellipse is depicted in b.) Only the component of the elliptically polarized beam parallel to the analyzer transmission axis at -45° emerges, as depicted in c.)

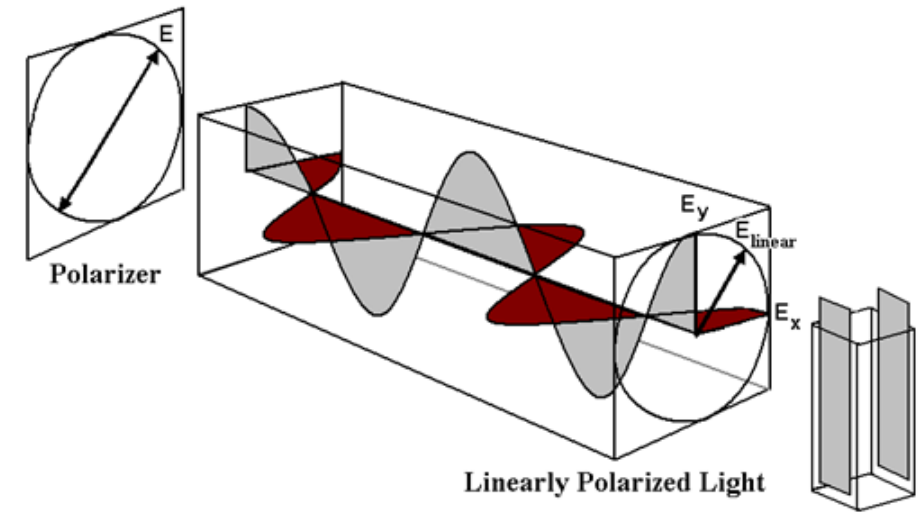

(a) Linearly polarized light (in phase components) entering cell

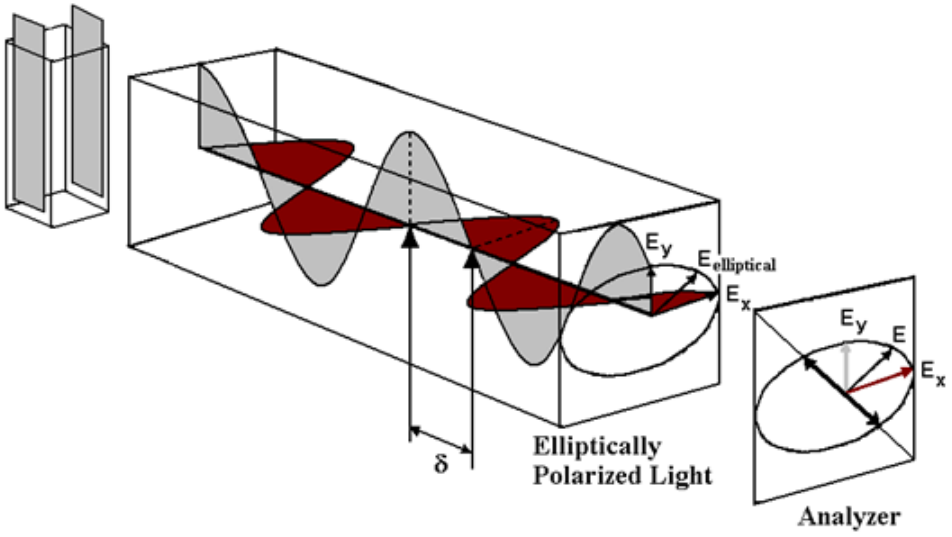

(b) Elliptically polarized light (phase shifted components) emerging from birefringent sample

Figure 1.3.1.2: Phase shift resulting from sample birefringence. Linear polarized light resulting from in-phase orthogonal components passes through a Kerr cell. The emerging light becomes phase-shifted by δ and the resulting vector of the orthogonal components is elliptically polarized.

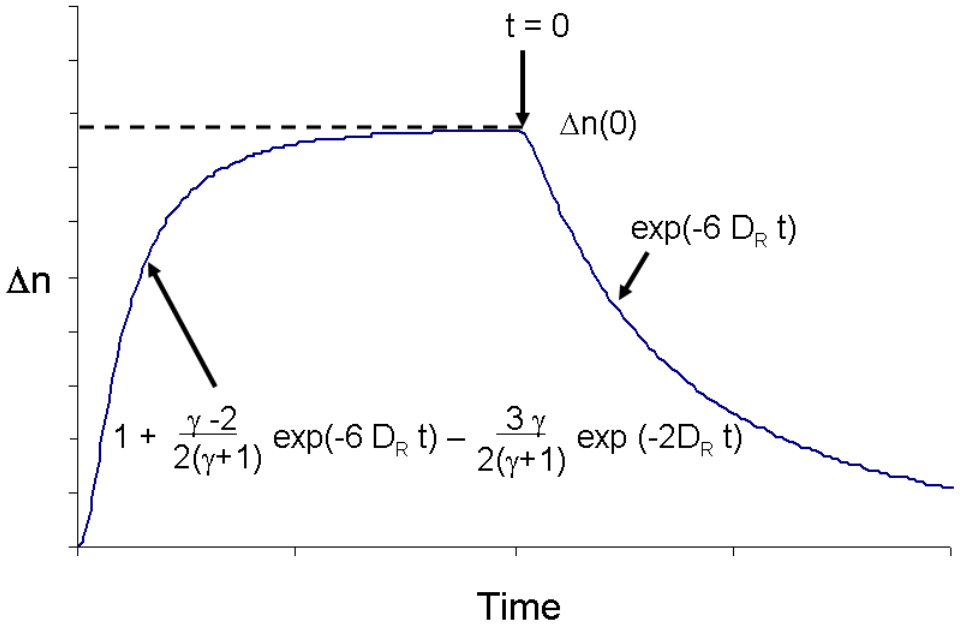

Figure 1.3.1.3: Rise and fall for a transient electric birefringent curve. The rise is dependent on both rotational diffusional coefficients D_R and dipole moment γ of the material, whereas the field-free decay is a function of the diffusion only.

then the anisotropic axis of the material is parallel to the external field, and we define the birefringence induced in our sample as

$$\Delta n = n_x - n_y = n_{\parallel} - n_{\perp}. \tag{1.3.3}$$

The refractive index for both the x and y components is related to the optical path length of the cell by

$$N_{\parallel} = \frac{L\, n_{\parallel}}{\lambda_0} \tag{1.3.4a}$$

$$N_{\perp} = \frac{L\, n_{\perp}}{\lambda_0}, \tag{1.3.4b}$$

where N is the number of wavelengths of light of each component in a cell of length L, with λ_0 being the wavelength of light in a vacuum. The phase shift between the two components is thus

$$\delta = 2\,\pi(N_{\parallel} - N_{\perp}) = \frac{2\,\pi\, L\, \Delta n}{\lambda_0}, \tag{1.3.5}$$

where $\Delta n = n_{\parallel} - n_{\perp}$ in the birefringence in the material.

1.3.2.1 Kerr Constants

The magnitude of the induced birefringence, Δn, can be related to the intensity of the applied electric field E using the Kerr law

$$B = \frac{\Delta n}{\lambda E^2} = \frac{\delta}{2\pi l E^2}, \tag{1.3.6}$$

where λ wavelength of monochromatic light used, E is the external field intensity, δ and l are the phase shift and path length through the cell, and B is the Kerr constant specific

to the sample [43]. Historically, the Kerr constant was an observed value for a given system [43–47] obtained by plotting the observed birefringence against the square of the field strength. The plot is linear in the low field regime, that is where the potential energy of a macromolecule U aligned in an external field is less than the Boltzmann energy, $U \ll k_B T$. An alternate Kerr constant was proposed by Debye [48] as

$$K = \frac{\Delta n}{nE^2} = \frac{B\lambda}{n}, \tag{1.3.7}$$

where n is the refractive index of the system in the absence of an applied electric field. The refractive index of a material can be related by Maxwell's equations to the propagation of a field in that material and the dielectric permittivity, giving rise to a method for relating the measured Kerr constant to the electric properties of the material. In 1939, Peterlin and Stuart [49] derived a model to relate the specific Kerr constant to the optical anisotropy and polarizability of axially symmetric molecules in insulating systems under an alternating applied field. This was re-derived by O'Konski [50] as

$$K_{sp} = \frac{2\pi(g_1 - g_2)}{15n^2}(b^2 + 2c), \tag{1.3.8}$$

where g_1 and g_2 are the optical anisotropies along the symmetry and transverse axes respectively, and b and c are related to the dipole moments and polarizabilities. Specifically, $b = \mu B_1/k_B T$ and $c = (\alpha_1 - \alpha_2)/2k_B T$. Here μ is the permanent dipole moment, α_1 and α_2 are the excess polarizabilities of the particle along the symmetry and transverse axes, and B_1 is the internal field function relating the externally applied field to the resulting internal field experienced at the dipole. (For detailed description, see [50]). Benoit [42] later derived the relation for particles aligned under a rectangular electric pulse (static

field) for conducting systems of rigid macromolecules as

$$\Delta n(t \to \infty) = \frac{2\pi}{15}(g_1 - g_2)VE^2(p_1 - p_2 + q) = K\lambda E^2, \tag{1.3.9}$$

where λ is the wavelength of light used, V is the volume fraction of the ellipsoids modelled, q is the induced dipole term and p_1 and p_2 are related to the permanent dipole moments along the symmetry and transverse axes respectively (as restated in [51]).

In each case, the electric free energy equations were derived from Laplace's equation for electrically insulating systems. The local internal field acting on the macromolecule thus depends on the dielectric permittivity of the medium and on the static electric properties of the macromolecule [52]. Clearly this is inadequate for ionizable polyelectrolytes in conducting media, where ion transport mechanisms become significant. For example, it has been observed that the electrolyte concentration in aqueous suspensions of TMV significantly affects the orientation of the molecule in an electric field, [50, 53], implicating ion atmosphere polarizaility effects [54, 55]. Maxwell-Wagner polarization could also result in charge accumulation at interfaces between volume elements with different electrical properties [53, 56, 57]. While the literature continues to develop and refine the models for polyelectrolytes in conducting media, a basic understanding of dielectric permittivity and polarizability is required before expounding upon these models. The subsequent chapter will develop basic theories for the alignment mechanisms of polarizable elements in conducive media.

Chapter 2 – Literature Review Part 1: TEB for Dielectric Properties

2.1 Electro-Optic Effect: A Historical Overview

The Kerr effect was first observed in 1875 by the Reverend John Kerr using plate glass electrified with a Ruhmkorff induction apparatus between crossed Nicol prisms. When the electric field was oriented at 45 degrees with respect to the incident beam's electric field vector, light began to emerge from the glass, continuously growing brighter, then gradually returning to zero when the field was removed. Kerr's interpretation of this phenomena was that "the particles of the dielectric throughout the field are electrically polarized, and tend to arrange themselves end to end $\cdots$ and $\cdots$ that the effect of the electric force is to superinduce a uniaxial structure upon the primitive structure." [1]

In 1897, Larmor made the first clear proposal that the Kerr effect was due to molecular orientation [2]. Langevin later proposed equations for the energy of electrically anisotropic molecules as a function of orientation in 1910 [3, 4]. Using the Boltzmann equation, he derived an orientation distribution function to calculate probability of alignment as a function of angle. He obtained an equation for the Kerr constant, but the equation was limited to axial symmetry and did not account for permanent dipole. A more general case was addressed by Enderle [5] and Voigt [6, 7], which still did not include permanent dipole or optical activity. In 1921, Gans was the first to recognize the relationship between the Kerr constant and the optical anisotropy of the molecule giving rise to the extent of depolarization of scattered light [8]. Debye [9, 10] and Sack [11] further developed theoretical relationships between molecular optical properties and light scattering.

A pivotal work to establish the theory of double refraction of a colloidal system under sinusoidal electric fields was done by Peterlin and Stuart in 1939 [12]. The action of a pulsed rectangular field on rigid macromolecules was investigated independently by Benoit [13] and O'Konski and Zimm [14] in the early 1950's. The development of such short orienting pulses was critical for the study of polyelectolytes and biological macromolecules in aqueous media, where energy dissipation, joule heating and electrophoresis become dominating effects. Tinoco broadened the birefringence theory to the most general case in 1963, applying it to fibrogen [15]. Since then, advances in instrument sensitivity and theory has allowed electric birefringence to be applied to semiflexible polymer systems and small biopolymers with longest dimensions less than 10 nm [15]. Since our work is with rigid rod-like nanocrystals, the bulk of this dissertation will focus on theories pertaining to that regime.

2.2 Electro-Optic Effect: The Principles

2.2.1 Maxwell's Equations and Refractive Index

The refractive index of a material can be related by Maxwell's equations to the propagation of a field in that material and the dielectric permittivitiy. Therefore, to understand the relationship between the electrostatics and the optics, one must first be reminded of Maxwell's equations governing electromagnetic phenomena. If we consider the macroscopic average of a field or charge source (where volume is large with respect to atomic

volumes), these can be given as [16]:

$$\boldsymbol{\nabla} \times \mathbf{H} - \frac{1}{c}\frac{\partial \mathbf{D}}{\partial t} = \frac{\mathbf{J}}{c} \tag{2.2.1a}$$

$$\boldsymbol{\nabla} \times \ \mathbf{E} + \frac{1}{c}\frac{\partial \mathbf{B}}{\partial t} = 0 \tag{2.2.1b}$$

$$\boldsymbol{\nabla} \cdot \mathbf{D} = \rho \tag{2.2.1c}$$

$$\boldsymbol{\nabla} \cdot \mathbf{B} = 0, \tag{2.2.1d}$$

where **E** and **B** are the volume-averaged electric field and magnetic induction, **J** is the current density, ρ is charge density, and c is the speed of light. **D** and **H** are field quantities called electric displacement and magnetic field, and have values given by

$$D_\alpha = E_\alpha + (P_\alpha - \sum_\beta \frac{\partial Q'_{\alpha\beta}}{\partial x_\beta}) \tag{2.2.2a}$$

$$H_\alpha = B_\alpha - (M_\alpha + ...) \tag{2.2.2b}$$

where the quantities **P**, **M**, and $Q'_{\alpha\beta}$ represent the macroscopically averaged electric dipole, magnetic dipole, electric quadrupole, and other moment densities of the media in or due to the presence of an external field.

Alternatively, in MKS units [17] using the conversion factor for the speed of electromagnetic fields in vacuum ($c = (\mu_0\epsilon_0)^{-1/2}$), Maxwell's macroscopic equations are

$$\boldsymbol{\nabla} \times \mathbf{H} = \epsilon_0 \frac{\partial \mathbf{E}}{\partial t} \tag{2.2.3a}$$

$$\boldsymbol{\nabla} \times \ \mathbf{E} = -\mu_0 \frac{\partial \mathbf{H}}{\partial t} \tag{2.2.3b}$$

$$\boldsymbol{\nabla} \cdot \mathbf{E} = 0 \tag{2.2.3c}$$

$$\boldsymbol{\nabla} \cdot \mathbf{B} = 0, \tag{2.2.3d}$$

where the ϵ_0 and μ_0 are the vacuum permittivity and permeability respectively. For isotropic, nonconducting media, ϵ_0 and μ_0 are replaced by ϵ and μ, and the speed of propagation for electromagnetic fields is now $\upsilon = (\epsilon\mu)^{-1/2}$, analogous to c in vacuum. If we define two proportionality constants, called the relative permittivity $\epsilon_r = \dfrac{\epsilon}{\epsilon_0}$ and relative permeability $\mu_r = \dfrac{\mu}{\mu_0}$, we get $\upsilon = (\epsilon\mu)^{-1/2} = (\mu_r\mu_0\epsilon_r\epsilon_0)^{-1/2} = c(\epsilon_r\mu_r)^{-1/2}$. The definition of index of refraction for a material is the ratio of the speed of light in vacuum to the speed of light in the material, that is

$$\frac{c}{\upsilon} \equiv n = (\epsilon_r\mu_r)^{1/2}. \tag{2.2.4}$$

For nonmagnetic media, $\mu_r = 1$, such that n equals the square root of the relative permittivity, $n = \sqrt{\epsilon_r}$. This gives the relation between electromagnetic fields propagating in a media to the permittivity and permeability of that media and the index of refraction of the media. With this broad picture in mind, the following sections expand on the specifics for electro-optic Kerr effect in inhomogeneous media.

2.2.2 Kerr Effect: The Molecular Origin

2.2.2.1 Maxwell's Equations in Anisotropic Media

We turn now to the study of light through matter using four macroscopically averaged quantities defined as:

(1) the volume density of electric charge ρ,

(2) the volume density of electric dipoles (*polarization*) **P**,

(3) the volume density of magnetic dipoles (*magnetization*) **M**, and the

(3) electric current per unit area (*current density*) **J**.

These values are related to the macroscopically averaged fields **E** and **H** by

$$\boldsymbol{\nabla} \times \mathbf{H} = \epsilon_0 \frac{\partial \mathbf{E}}{\partial t} + \frac{\partial \mathbf{P}}{\partial t} + \mathbf{J} \tag{2.2.5a}$$

$$\boldsymbol{\nabla} \times \ \mathbf{E} = -\mu_0 \frac{\partial \mathbf{H}}{\partial t} - -\mu_0 \frac{\partial \mathbf{M}}{\partial t} \tag{2.2.5b}$$

$$\boldsymbol{\nabla} \cdot \mathbf{H} = -\boldsymbol{\nabla} \cdot \mathbf{M} \tag{2.2.5c}$$

$$\boldsymbol{\nabla} \cdot \mathbf{E} = -\frac{1}{\epsilon_0} \boldsymbol{\nabla} \cdot \mathbf{P} + \frac{\rho}{\epsilon_0}, \tag{2.2.5d}$$

Using the abbreviations $\mathbf{D} = \epsilon_0 \mathbf{E} + \mathbf{P}$ and $\mathbf{B} = \mu_0(\mathbf{H} + \mathbf{M})$, often referred to as the *electric displacement* and the *magnetic induction*, respectively, we can obtain the compact forms of Maxwell's equations

$$\boldsymbol{\nabla} \times \mathbf{H} = \frac{\partial \mathbf{D}}{\partial t} + \mathbf{J} \tag{2.2.6a}$$

$$\boldsymbol{\nabla} \times \ \mathbf{E} = -\frac{\partial \mathbf{B}}{\partial t} \tag{2.2.6b}$$

$$\boldsymbol{\nabla} \cdot \mathbf{B} = 0 \tag{2.2.6c}$$

$$\boldsymbol{\nabla} \cdot \mathbf{D} = \rho, \tag{2.2.6d}$$

We can now use Ohm's law to relate conductivity σ to the electric field response of conduction electrons by $\mathbf{J} = \sigma \mathbf{E}$, where $\mathbf{D} = \epsilon \mathbf{E}$ is the constitutive relation describing the aggregate response of bound charges ([16], page 287). The electric susceptibility, χ, arises from an alternative form of the bound charge response,

$$\mathbf{P} = (\epsilon - \epsilon_0)\mathbf{E} = \chi \epsilon_0 \mathbf{E}, \tag{2.2.7a}$$

whereupon

$$\chi = \frac{\epsilon}{\epsilon_0} - 1. \tag{2.2.7b}$$

The electric susceptibility, generally expressed an a tensor, turns out to be an important parameter for the study of anisotropic optical media. The tensoral nature of χ accounts for different magnitudes of polarizations arising in different directions with respect to the applied electric field [17]. From the derivation of equation 2.2.4, the index of refraction is $n = (\epsilon_r \mu_r)^{1/2}$ where $\mu_r = 1$ for vacuum and non-magnetic media. As $\epsilon = \epsilon_0(1 + \chi)$, we now have a link between susceptibility tensor and refractive index of an anisotropic system, as addressed in Section 2.2.2.2.

The above argument applies to both an external electric field E_{ext} applied across the medium as well as the electric field from a light source probing the media E_L. In this case, the susceptibility is a function of both electric fields, $\chi = \chi(E_{ext}, E_L)$. However, the applied electric field for electro-optic experiments are typically orders of magnitude greater than the field of the light used to probe the birefringence, an thus E_L is negligible. Therefore the study of non-magnetic media using low intensity lasers will concern only the dielectric permittivity and susceptibility related to the applied field and neglect the effects of the laser source.

2.2.2.2 Susceptibility Tensors for Anisotropic Media

Under the influence of an external electric field, a polarizable molecule experiences a charge perturbation and an induced dipole moment P_i given by

$$P_i = \mu_0 + \sum_j \alpha_{ij} E_j + \sum_{jk} \beta_{ijk} E_j E_k + \sum_{jkl} \gamma_{ijkl} E_j E_k E_l + \ldots, \tag{2.2.8}$$

where μ_i is the permanent dipole moment, α_{ij} is the linear polarizability tensor, and β_{ijk} and γ_{ijkl} are the first and second molecular hyperpolarizabilities respectively [18]. The applied field components, denoted E_i, E_j, and E_k, act on the molecule in terms of the Cartesian coordinates i, j and k. The molecular polarization is related to the macroscopic sample polarization P_I by

$$P_I = P_0 + \sum_J \chi^{(1)}_{IJ} E_J + \sum_{JK} \chi^{(2)}_{IJK} E_J E_K + \sum_{JKL} \chi^{(3)}_{IJKL} E_J E_K E_L + \ldots, \tag{2.2.9}$$

where P_0 is the permanent polarization and $\chi^{(1)}$, $\chi^{(2)}$, $\chi^{(3)}$ are the linear, second, and third-order susceptibility tensors, respectively. Here, capital indices represent tensor elements in χ. For weak external fields, the higher order terms can be neglected, and in the absence of permanent polarizability, the above reduces to

$$P_X = \chi_{11} E_X + \chi_{12} E_Y + \chi_{13} E_Z \tag{2.2.10a}$$

$$P_Y = \chi_{21} E_X + \chi_{22} E_Y + \chi_{23} E_Z \tag{2.2.10b}$$

$$P_Z = \chi_{31} E_X + \chi_{32} E_Y + \chi_{33} E_Z \tag{2.2.10c}$$

or more succinctly

$$P_I = \sum_J \chi^{(1)}_{IJ} E_J. \tag{2.2.10d}$$

The macroscopic lab frame is represented by coordinates X, Y, and Z, and the molecular coordinates represented by x, y, and z. The susceptibility tensor of the anisotropic medium

is thus

$$\chi^{(1)} = \begin{pmatrix} \chi_{11} & \chi_{12} & \chi_{13} \\ \chi_{21} & \chi_{22} & \chi_{23} \\ \chi_{31} & \chi_{32} & \chi_{33} \end{pmatrix}. \tag{2.2.11}$$

From the previous sections, we know that $n = (\epsilon_r)^{1/2}$ for nonmagnetic media, with $\epsilon = \epsilon_0(1 + \chi)$. It follows that $n = (\chi + 1)^{1/2}$ for linear, isotropic systems. For anisotropic media, n is also a tensor. To bridge the susceptibility tensor to the refractive index tensor, the parameters of polarizability and dielectric permittivity should be addressed.

2.2.2.3 Dielectric Permittivity and Polarizability.

The *electric displacement* field $\mathbf{D}$ given in equation 2.2.6 ($\mathbf{D} = \epsilon_0\mathbf{E} + \mathbf{P}$) relates the externally applied field $\mathbf{E}$ to that in the medium via the polarization, $\mathbf{P}$. The polarization is related to susceptibility by $\mathbf{P} = \boldsymbol{\chi}\epsilon_0 \times \mathbf{E}$, or

$$\begin{pmatrix} P_x \\ P_y \\ P_z \end{pmatrix} = \epsilon_0 \begin{pmatrix} \chi_{xx} & \chi_{xy} & \chi_{xz} \\ \chi_{yx} & \chi_{yy} & \chi_{yz} \\ \chi_{zx} & \chi_{zy} & \chi_{zz} \end{pmatrix} \begin{pmatrix} E_x \\ E_y \\ E_z \end{pmatrix}. \tag{2.2.12}$$

Combining $\mathbf{D}$ with $\mathbf{P}$ gives

$$\mathbf{D} = \epsilon_0\mathbf{E} + \mathbf{P} \tag{2.2.13a}$$

$$= \epsilon_0\mathbf{E} + \boldsymbol{\chi}\epsilon_0 \times \mathbf{E} \tag{2.2.13b}$$

$$= \epsilon_0(1 + \boldsymbol{\chi}) \times \mathbf{E} \tag{2.2.13c}$$

$$= \epsilon_0\boldsymbol{\epsilon} \times \mathbf{E}, \tag{2.2.13d}$$

where $\boldsymbol{\epsilon}$ is now the dielectric tensor. The index of refraction is therefore related to the susceptibility tensor via the polarization and the electric field directions. If the electric field of the light is polarized parallel to the x axis, for example, the refractive index in the x direction will be $n_{xx} = (1 + \chi_{xx})^{1/2}$. An anisotropic material with different refractive indices in different directions results in the state of birefringence. By placing the polarized probe beam at 45 degrees with respect to the orienting field **E** in the Kerr cell apparatus, the tensor geometry simplifies by symmetry operations, and we get the equations described in section 1.3.2.

A more descriptive origin of **P** comes from the definition of ϵ_r in section 2.2.1 as the ratio of an electric field strength in vacuum, E_0, to that in a material, E. This quantity can be measured by placing the material of interest between two plates of area A separated by a distance d. A potential ϕ is placed across the plates. The resulting electric field between them in the absence of the material would be $E_0 = 4\pi\sigma$, where $\sigma = q/A$ and +q and -q are the charges on the plates in a vacuum. If the charge on the plates remains the same and the space between is filled with the dielectric material, then $E = \dfrac{4\pi\sigma}{\epsilon}$ is the decreased electric field strength. This decrease in field strength is found to be $E_0 - E = 4\pi\sigma(\epsilon - 1)/\epsilon$, meaning the surface electric density is reduced by $P = \sigma(\epsilon - 1)/\epsilon$ [19].

The polarization of the dielectric, or the charge density on the dielectric surface, can be explained by the lining up of individual dipoles of the dielectric media with the field. There are several factors which can effect the polarizability of the media. The first comes from a media composed of molecules with permanent dipole moments, which would orient in a direction that opposes the field. The second would be a media with polarizable molecules, ones which have a tendency to shift nuclear or electronic charge densities in response to a field. The third effect could arise from networks of hydrogen bonds in liquids, such as water, which can shift to reduce to decrease the field strength [20]. Regardless of the mechanism, the alignment of the dielectric media with the field gives

rise to a change in charge density on the surface of the dielectric from σ to σ/ϵ so that the entire dielectric can be considered a dipole with total charge $+PA$ on one side and $-PA$ on the other. The moment μ of this dipole is PAd, and thus the polarization of the dielectric can be considered an an average dipole moment per unit volume. That is $\mathbf{P} = pA\mathbf{d}/Ad$ [19].

2.2.2.4 The Internal Field of Ideal Gases: The Debye equation

The above discussion shows that the externally applied field is not always the same as the field felt internally by a group of polarizable molecules. If the dielectric under polarization is a dilute gas, the Debye equation can be used to determine the orientation distribution for N particles per unit volume with dipole moment $\boldsymbol{\mu}$ using the Boltzmann distribution for the temperature of the dielectric. The Debye equation is

$$\frac{\epsilon - 1}{\epsilon + 2} = \frac{4\rho}{3M}\pi N_A(\alpha_0 + \alpha_d), \tag{2.2.14}$$

where ρ and M are the density and molecular weight of the gas, $\alpha_0 = \mu_p^2/3k_BT$, μ_P is the permanent dipole moment, and α_d is the polarizability of the molecule. (For full derivation of equation 2.2.14, see [19], Chapter 2.) We can consider α_d to arise from a sum of electronic α_e and atomic α_a polarizabilities, with α_d increasing with atomic number, size, and low ionization potential. Setting $\mu_p = 0$ and assuming ϵ at a wavelength λ is related by $\epsilon(\lambda) = n^2(\lambda)$, the static electric field can be extrapolated as $\lambda \to 0$ to get the Clausius-Mosotti expression:

$$\frac{n^2 - 1}{n^2 + 2} = \frac{4\pi\rho N_A}{3M}\alpha_e. \tag{2.2.15}$$

This expression can be combined with equation 2.2.14 to provide an alternate representation of Debye's equation:

$$\frac{\epsilon - 1}{\epsilon + 2} - \frac{n^2 - 1}{n^2 + 2} = \frac{4\pi\rho N_A \, \mu_p^2}{3k_B MT}. \tag{2.2.16}$$

The Debye equation holds for a wide variety of gases at ordinary pressure, and has been extended to dilute solutions of polar molecules in nonpolar solvents. It falls short, however, in calculating dipole moments or dielectric constants of pure liquids and more complex anisotropic systems [19].

2.2.2.5 Dielectrics of Pure Liquids

The failure of the Debye equation to predict dipole moments of pure liquids from their static dielectric constants led to a series of models during the first half of the previous century. Onsager examined the effect of spherical polar molecules, assuming a dipole in the center of a spherical cavity polarizes the surrounding media of permittivity ϵ. This resulted in a reaction field $\mathbf{R}$ at the dipole proportional to the dipole moment. Therefore, polar molecules in an external field $\mathbf{E}$ experience an internal field $\mathbf{E}_i$ composed of the reaction field and a cavity field $\mathbf{E}_c$, which can be derived from the homogeneous field using the Laplace equation. The Onsager equation arises

$$\mu^2 = \frac{9k_B TM}{4\pi\rho N_A} \frac{(\epsilon - \epsilon_\infty)(2\epsilon + \epsilon_\infty)}{(\epsilon + 2)^2}, \tag{2.2.17}$$

where ϵ_∞ is again obtained from $n^2(\lambda) = \epsilon(\lambda)$ as $\lambda \to 0$ (i. e. for a static electric field), ρ and M are the density and molecular weights of the dielectric, and N_A is Avogadro's constant. When $\epsilon \to \epsilon_\infty$, as with atmospheric pressure gases, this becomes Debye's equation [19].

Other modifications of Debye's equation have been made to account for irregularities and inconsistencies, such as Kirwood (references 12 and 38 from [19]) and Frölich (reference 39 from [19]) taking into account molecular interactions. These theoretical model modifications are useful in determining internal fields and dipole moments of pure liquids. For a solution in which polar molecules are sufficiently separated from one another by non-polar solvent, Debye's equation can be approximated as for the case of non-interacting gases.

These attempts to correlate dipole moment to macroscopic permittivity are useful for limited cases. Colloids suspended in conducting media, specifically aqueous systems where the solvent is both polar and hydrogen bonding, bring added complexity. The solvent contains ionized electrolytes, which can associate with the macroion by shielding the surface charge, or remain in the bulk solution and contribute to the macroscopic dielectric constant. It quickly becomes an intractable problem to completely solve for the general case. From the basic principles of simple electrolytes, more specific models for distinct experimental systems abound in the literature.

2.2.2.6 Simple Electrolytes Staring with the Debye-Hückel Equation

In order to understand how an externally applied field influences polyionic macroparticles suspended in an inhomogeneous system, start with a electrolyte in solution. Point charges arise from such electrolytes dissociating in polar liquids. In the simplest model, the solvent is considered to be a uniform dielectric medium surrounding the electrolyte ions. Here, point charges attract counterions to form electric double layers. These counterion layers effectively shield the electrostatic potential of that particle. Describing the ion surface as a plane with an electrostatic potential $\Psi(x)$, the concentration of mobile positive ions per unit volume a given distance x from the particle surface P is given by the

Boltzmann equation, $n_+(x) = n_\infty exp(-ze\Psi(x)/k_BT)$. Here n_∞ is the concentration of positive ions in the bulk far from the surface, e is the unit charge of a proton, and z is the valency of the ion. Charge neutrality in the bulk defines an identical expression for the negative ions, $n_-(x) = n_\infty exp(+ze\Psi(x)/k_BT)$. These mobile ions will also contribute to the electrostatic field of P. First calculate the charge density $\rho(x)$ as a function of number of ions at position x:

$$\rho(x) = \sum_i z_i e n_i = ze[n_+(x) - n_-(x)]. \tag{2.2.18}$$

The Poisson equation relating charge density ρ to electrostatic potential Ψ yielding $\nabla^2\Psi = -\frac{\rho}{D\epsilon_0}$, where D is the dielectric constant of the solution. Substituting $n_+(x)$ and $n_-(x)$ from Boltzmann equations into eqn 2.2.19, the famous Poisson-Boltmann (P-B) equation is obtained:

$$\nabla^2\Psi = \frac{zen_\infty}{D\epsilon_0}(e^{ze\Psi/k_BT} - e^{-ze\Psi/k_BT}), \tag{2.2.19a}$$

or in hyperbolic sine form, where $sinh = (e^x - e^{-x})/2$,

$$\nabla^2\Psi = \frac{2zen_\infty}{D\epsilon_0} sinh(ze\Psi/k_BT). \tag{2.2.19b}$$

This form of the P-B equation is a nonlinear second order differential equation. It can be linearized when the electrostatic potential is small, that is $ze\Psi/k_BT \ll 1$, where the assumption $sinh(x) \approx [(1+x) - (1-x)]/2 = x$ holds. The result is the linearized P-B equation, also known as the Debye-Hückel equation

$$\nabla^2\Psi = \frac{2zen_\infty}{D\epsilon_0}(ze\Psi/k_BT) = \kappa^2\Psi \tag{2.2.20}$$

where

$$\kappa^2 = \frac{2z^2e^2n_\infty}{D\epsilon_0 k_B T} \tag{2.2.21}$$

defines a quantity known as the Debye screening length. This can be thought of as a reciprocal rate at which ionic distribution decreases with distance around a central ion [21]. At $1/\kappa$, the charge from P is shielded from surrounding charges in the solution [20].

2.2.2.7 Surface Charge of Macromolecules Suspended in Electrolyte Media

The discussion in Section 2.2.2.6 applies for simple electrolytes with spherical symmetry around a test ion. For simple ionic/electrolyte solutions, the Debye-Hückel limiting law provides a means to calculate activity coefficients of ions in dilute solutions of known ionic strength. In their original approach, Debye and Falkenhagen treated simple electrolytes as point charges in a dielectric continuum [22]. For finite concentrations of simple electrolytes, deviations from the limiting law can be used to determine effects not taken into account by the limiting law, such as short-range interionic forces and solvent molecular effects [23]). This approach is inadequate for polyelectrolytes, however, where particle dimension and shape are important constants in the system [24]. A high charge density occurs near the polyion due to the cumulation of many counterions attracted to the surface charge, which leads to the situation where the the limiting law will not apply even at low equivalent concentrations [23]. A rigid polyelectrolyte has a fixed configuration of charges, thus a high degree of charge asymmetry between the polyion and the surrounding small ions. If a strict Boltzmann distribution is applied for a moderate surface potential, surface concentrations of counterions in excess of 100 molar would result [21]; this is an unrealistic situation. Instead, the finite size and mutual interactions leads to an upper limit of condensed counterions, resulting in statistical separations of a saturated

Stern layer, followed by a Gouy-Chapman layer which follows the predicted Boltzmann distribution [25]. [For a a refresher on electric double layers, see Section 1.2.3.]

Theories to explain the dielectric constant and conductivity of polyelectrolyte systems must also take into account charge transport processes from charges in the solvent, as well as the ion atmosphere around the polyion and inside the suspended particles [24]. This results in different assumptions for polyelectrolyte systems. For example, the dielectric constant that governs the interaction for point charges at large separations is that of the pure solvent, whereas this bulk dielectric constant may have little effect in colloidal systems. The valency of the counterions and charge density around a polyion are relevant for polyionic species, whereas ion size and shape is irrelevant in simple electrolytes [23].

The crux of this issue is that, while simple electrolyte systems can be modelled tractably, the extension of these models to macroion solutions is complex and diversified amongst practitioners of the field. The interpretation of data cannot be undertaken without some thought as to the appropriate chemical aspects of the system under study. Despite these difficulties, it remains useful to understand simple electrolytes as a basic foundation for more complex models of polyionic particles.

2.2.2.8 Transient Techniques for Electric Birefringence

From the discussion of Maxwell's equation relating to refractive index of a material via dielectric properties, we segue to optical methods of probing dielectric properties. If we imagine a suspension of anisotropic macromolecules with dimensions on the order of the wavelength of light, the intensity of light scattered by the suspension will be proportional to the statistical array of such particles [26]. When an external electric field interacts with induced and permanent dipoles to align macroparticles, the change in scattered light can be used as a measure of the distribution function. This method is particularly sensi-

tive when the plane of observation is perpendicular to the electric field and the resulting alignment manifests as a macroscopic birefringence [27]. However, the application of a continuous DC field creates difficulties for electric birefringence in conductive media. These difficulties include Joule heating, electrophoresis, and time-dependent electrode polarization effects. Such problems can be minimized by using short pulsed square wave fields and observing the transient behavior of the particles, a technique referred to as Transient Electric Birefringence (TEB).

While in theory both induced and permanent dipole effects can be extrapolated from a pulsed DC field rise and decay curve, the uncertainty involved limits the usefulness of this method. Alternatively, applying a continuous AC field and recording the response as a function of frequency allows one to discern between permanent and induced dipole effects. The dispersion frequency for the permanent dipole response, ω_c will be much lower than that of the induced dipole, so frequencies above ω_c are related to induced dipole alone. Frequencies below ω_c are related to both permanent and induced dipoles [28]. The dielectric dispersion (or Debye frequency) occurs when the polarizability of the ion cloud can no longer respond the the field, typically at frequencies of 10^{10} Hz and greater. At lower frequencies, the dielectric relaxation response τ is described as a function of field angular frequency similar to the Debye relaxation for simple molecules. In the case of rigid macromolecules and particles, this electric polarization is a function of boundary layer potential [29] as well as surface conductivity [30], both of which are influenced by the electrolyte properties.

Continuous AC fields can also result in difficulties with heating, as well as creating electrode polarization effects [31, 32]. An alternative method for measuring frequency dependency uses pulsed AC fields and allows the alignment to reach steady state, as with the pulsed DC field. For an induced dipole moment, the optical response will have an alternating component at twice the frequency of the applied field which decreases in

amplitude with increasing frequency. This response is superimposed with an additional time-averaged DC component [26, 31, 33]. A full characterization of both components as a function of frequency provides information regarding permanent and induced dipole moments, as well as rotary diffusion coefficients, which in turn provide size and shape information for rigid particles. A basic summary of the theory ensues.

2.3 Transient Electric Birefringence in Suspensions of Rigid Macromolecules

The alignment of rigid rod-like colloidal particles in an electric field was observed as early as 1912 for V_2O_5 sols (see references 7-9 in [34]). It was recognized that alignment occurred due to an anisotropic deformation of the electric double layer around the particle, with the largest polarization occurring along the long axis. Studies of Tobacco Mosaic Virus (TMV) later showed the effect of the induced dipole moment on this alignment was a function of electrolyte concentration and solvent conductivity [14,32,35]. The effect of a permanent dipole for polyethylene sulfonate was demonstrated to be significant, even in the presence of large ionic polarizability [36]. Understanding the behavior of these nanoparticles in an electric field thus requires knowledge of both their average electric charge and their permanent dipole moments. In addition, one should consider two-dimensional surface conductivity from large mobilities of charge carriers along the surface and polarization effects between volume elements in the suspension (Maxwell-Wagner polarization.) Since this research is primarily concerned with aqueous suspensions of rod-like cellulose nanocrystals, the discussion will be narrowed to nonconducting colloids with ionizable surface charge dispersed in electrically conducting media.

2.3.1 Dipole Moments of Macromolecules

The description of dipole moments for nanoparticles and macromolecules is considerably more complicated than for simple molecules. The difficulty arises in the particle medium interface. The induced interfacial dipole moments (IDM) can be broken into two broad categories, that of surface charge dependent IDMs (CDIDM) and that due to the bulk dielectric properties of the particle and the medium, known as Maxwell-Wagner IDM (MWIDM). Each dominate in different frequency regimes, as well as different magnitudes of contribution to the overall IDM. A basic understanding of each allows us to discern the mechanisms of alignment for a nanoparticle in an electric field.

Maxwell-Wagner-Sillars The Maxwell-Wagner-Sillars (MWS) interfacial polarizability (MWIDM) depends on the difference between the dielectric constants and specific conductivities of the bulk particle and the medium. Upon the application of an electric field, accumulation of field at one side of the particle causes charges near the interface to migrate, thus depleting the opposite side of the particle, as shown in Figure 2.3.1.1 (a). For conductive particles, this charge migration occurs within the particle, whereas for nonconductive particles, it occurs on the surface. The characteristic relaxation time is therefore dependent on the particle size and dimension, and the thickness of the induced electric double layer, $1/\chi_E$ (Figure 2.3.1.1 (b).) For typical dispersions of nanoparticles, this mechanism relaxes at higher frequencies than the CDIDMs, around and above 1 MHz. Three mechanisms exists for this migration: distortion of the electron cloud around atoms, atomic polarization within molecules, and orientational polarization of molecules in the particle.

Charge Dependent Induced Dipole Moments The CDIDM arise from distortion of the electric double layer (EDL) around a colloidal particle. They are influenced by the pH and ionic strength of the medium, as well as the size and polydispersity of the particles. There is likewise a strong dependence on the surface charge of the particle, both from permanent charges fixed to the surface and the counter charges adsorbed to the surface. The diversity of theoretical models in the literature to describe the family of CDIDM reflect the diversity of particles studied. Likewise, the strong dependence on surface properties has led to variable results in the literature for similar samples under different ionic conditions. In general, however, CDIDMs are characterized by large, sub MHz dispersion frequencies, and they predominate over MWIDM in systems of highly charged particles in low conducting medium.

Most published models for CDIDMs can be summarized in terms of the size of the largest particle axis, the total surface charge in the EDL, the MWS component of the electric polarizability, and either the zeta potential, EDL thickness, EDL potential, or the surface conductivity. The inter-relations of the latter four properties are described in Chaper 1. The MWS component is coupled to the CDIDM through the sharing of ions between mechanisms. Figure 2.3.1.1 illustrates the spatial distribution of surface charges resulting from the combined mechanisms and the electrostatic potential associated with it.

2.3.2 AC Pulse Dynamics

Peterlin and Stuart [12] developed the general equation for the birefringence induced in a solution of axially symmetric macromolecules under the influence of an electric pulse as

$$\frac{\Delta n}{n} = \frac{2\pi C_v}{n^2}(g_1 - g_2)\int f(\theta)\frac{3cos^2\theta - 1}{2}2\pi sin\theta d\theta \qquad (2.3.1)$$

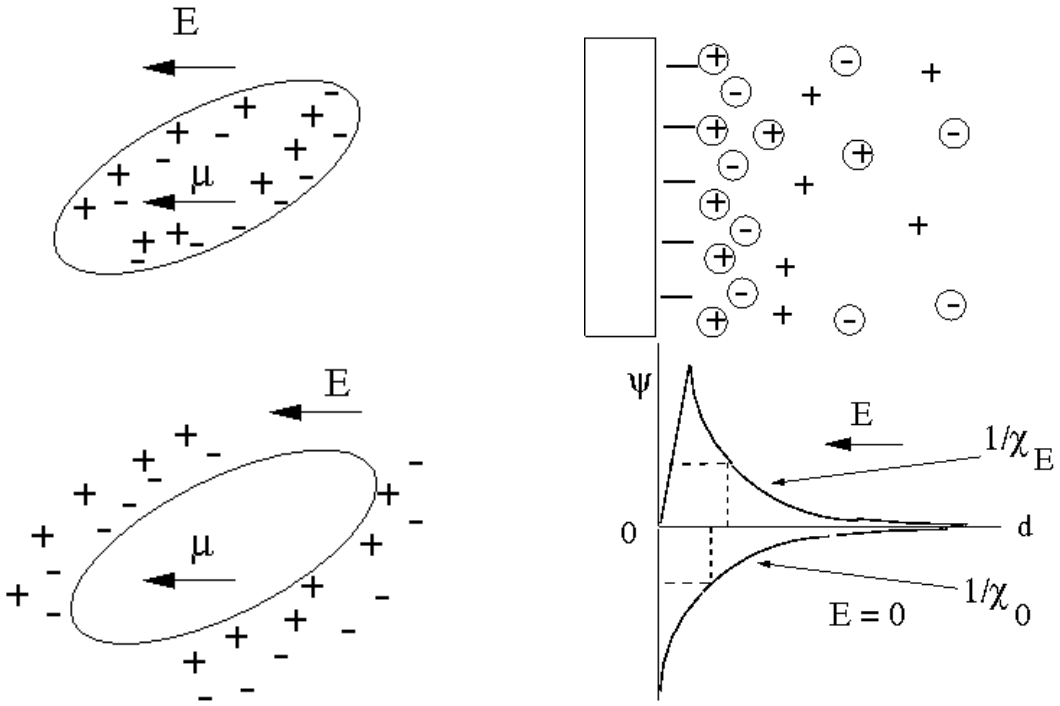

(a) Maxwell-Wagner induced dipole moment (μ).

(b) Spatial distribution of free electric charge.

Figure 2.3.1.1: Maxwell-Wagner (MW) induced dipole moment. The MW induced dipole moment (μ) is shown for conductive (top) and nonconductive (bottom) particles in non-conductive and conductive medium, respectively. (b) Spatial distribution of a charge surface between a conductive and non-conductive medium. Circled charges are ions collected via the Maxwell-Wagner-Sillars mechanism. The diagram below illustrates the surface potential ψ as a function of distance d in the presence and absence of an electric field, E. The diffuse layer thicknesses are described in the presence and absence of an electric field by $1/\chi_E$ and $1/\chi_0$ respectively. (Figure recreated from [37].)

where C_v is the volume fraction of particles,$\Delta n = n_{\parallel} - n_{\perp}$, n is refractive index of solvent, $g_1 - g_2$ is the optical anisotropy between axial symmetry and transverse axes (1 and 2 respectively), θ is the angle between the particle's axial symmetry axis and macroscopic alignment axis, and $f(\theta)$ is the angular distribution function. $f(\theta)$ can be interpreted as the probability of finding a particle at an angle θ with respect to field direction per unit solid angle for steady state birefringence, and is (following the Boltzmann distribution) mathematically expressed as

$$f(\theta) = \frac{e^{\frac{-U}{kT}}}{\int e^{\frac{-U}{kT}} 2\pi sin\theta d\theta}. \tag{2.3.2}$$

The constants k and T are the Boltzmann constant and the temperature, and U is the total dipole interaction energy $U = U_1 + U_2$, where U_1 and U_2 reflect the permanent and induced contributions respectively. (For detailed derivation, see [36].)

For an alternating field, this distribution function becomes time and frequency dependent. For rod-like particles, Plummer and Jennings [26] described an additional factor in the light-scattering equations at twice the frequency of the applied field in addition to the change obtained in DC fields. The connection of this component to the distribution function is discussed by Stoylov [33] and summarized as follows.

For an applied field $E_0 sin\ \omega t$, where E_0 is the maximum amplitude and ω is the angular frequency, the calculated birefringence Δn can be separated in to a component due solely to induced dipole (Δn_i), and one due only to the permanent dipole (Δn_p). The induced component is dependent on the angular frequency by

$$\Delta n_i = \Delta n_{i,ave} \left[1 \pm \frac{cos(2\omega t - \phi_i)}{(1 + 4\omega^2 \tau^2)^{1/2}} \right], \tag{2.3.3}$$

where $\Delta n_{i,ave}$ is the average birefringence observed and ϕ_i is the phase angle between

the birefringence and the applied field according to $tan\phi_i = 2\omega\tau$. A plot of $tan\,\phi_i$ versus ω therefore provides the characteristic birefringence relaxation time τ. $\Delta n_{i,ave}$ is the same birefringence as would be observed upon application of a steady field $E_0/\sqrt{2}$ (or E_{rms}) and is the only birefringence observed at high frequency. The doubled frequency component arises due to the fact that the induced dipole fluctuates between zero and max, where max occurs at $\pm E_0$. It therefore occurs twice for each cycle of the applied field. The phase angle exists because at low frequencies the molecular orientation follows the field, but the rotational diffusion takes a finite time and a lag is observed.

The permanent dipole contribution is given by

$$\Delta n_p = \Delta n_{p,0}\left[\frac{1}{1+9\,\omega^2\tau^2} + \frac{cos(2\omega t - \phi_p)}{(1+9\,\omega^2\tau^2)^{1/2}(1+4\,\omega^2\tau^2)^{1/2}}\right], \tag{2.3.4}$$

and the permanent dipole phase angle by

$$\tan\,\phi_p = \frac{5\,\omega\tau}{1-6\,\omega^2\tau^2}. \tag{2.3.5}$$

It likewise is composed of an alternating frequency at twice the applied field frequency and a time independent component, both of which reduce to zero at high frequency.

The overall response is a summation of induced and permanent dipole effects, given by [31] as

$$\Delta n = \Delta n_{st} + \Delta n_{alt}\,cos(2\,\omega t - \phi_{alt}), \tag{2.3.6}$$

where Δn_{st} is the steady state component and Δn_{alt} is the magnitude of the alternate component with phase angle ϕ_{alt}. For a permanent dipole along the symmetry axis of the molecule, Δn_{st} is given by

$$\Delta n_{st} = \frac{\Delta n_0}{P+1}\left[P + \frac{1}{1+9\,\omega^2\tau^2}\right], \tag{2.3.7}$$

where Δn_0 is the low frequency limiting value of Δn_{st}, and P represents the relative magnitudes of permanent and induced dipole effects as

$$P = k_B T \frac{\alpha_{\parallel} - \alpha_{\perp}}{\mu^2}. \tag{2.3.8}$$

Extracting information regarding each mechanism requires a frequency sweep experiment to isolate the regimes where only induced dipole effects dominate. Figure 2.3.2.1 shows Δn_{st} and Δn_{alt} as a function of frequency for different values of P.

In addition to the magnitude of the birefringence, the phase shift between the excitation frequency and the alternating response frequency, ϕ_{alt}, can provide characteristic relaxation times of the electric polarizabilities from $tan\phi_{alt} = 2\omega\tau$. Thurston and Bowling describe the low and high frequency limits of ϕ_{alt} as 0 to 90 degrees, 90 to 180 degrees, or 180 to 270 degrees depending on the value of P, as seen in Figure 2.3.2.2.

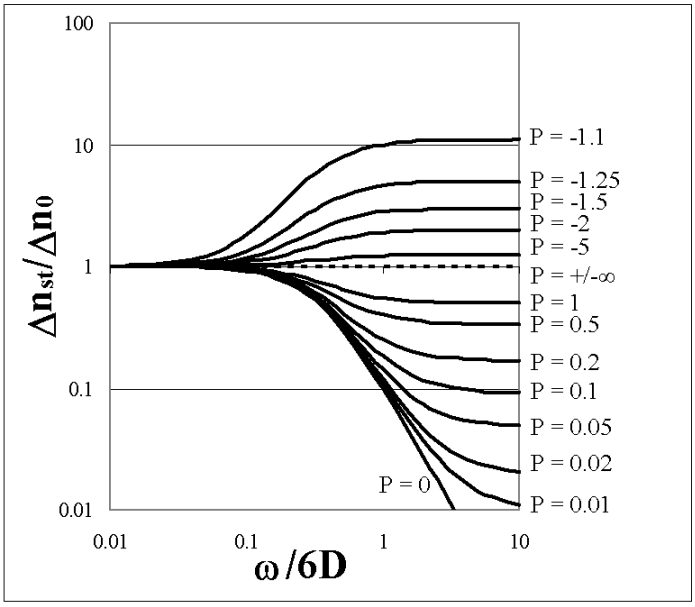

(a) Steady state component

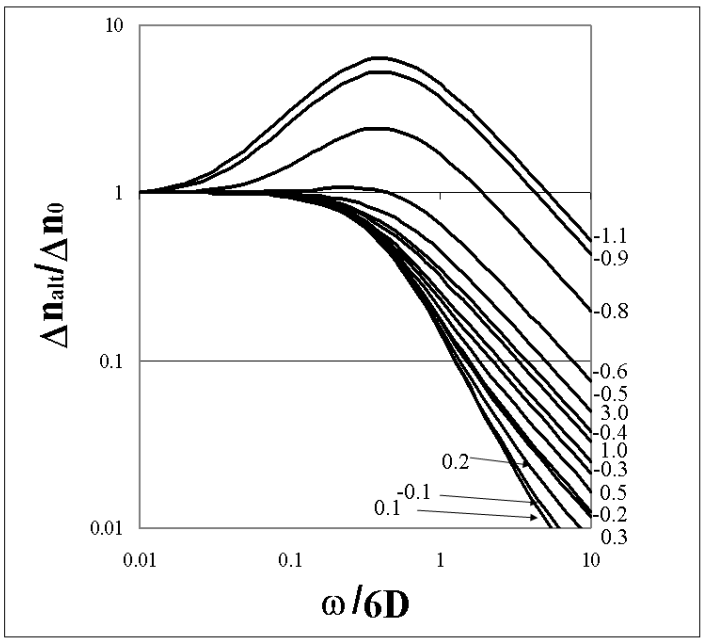

(b) Alternating component

Figure 2.3.2.1: Steady and alternating components with frequency. Normalized birefringence values for each component are shown as a function of diffusion coefficient D and radial frequency ω for values of P ranging from 0 (purely permanent dipole) to $\pm\infty$(purely induced dipole) in Equation 2.3.8 (recreated from [31]).

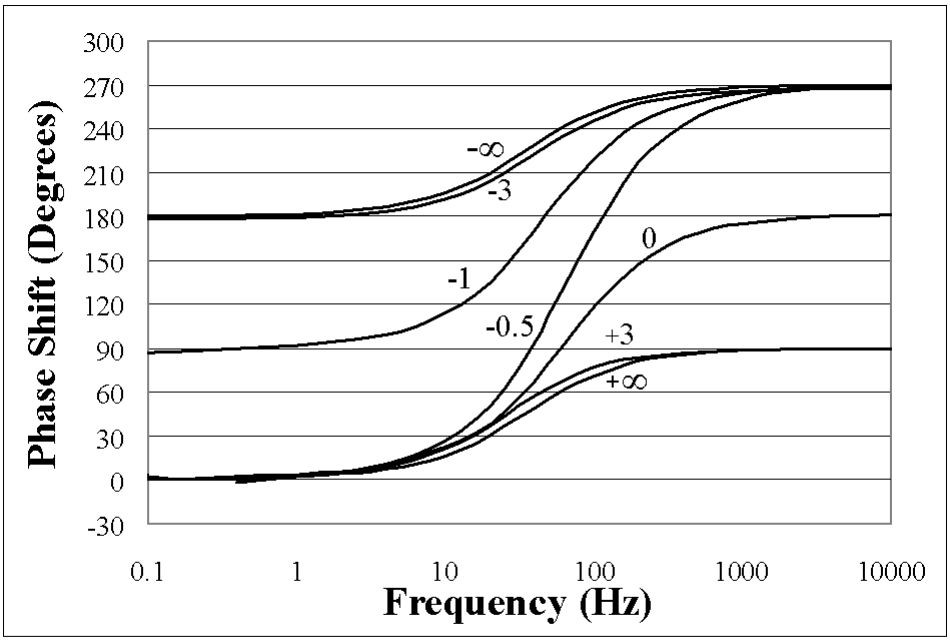

Figure 2.3.2.2: High and low frequency dependence of phase angle. The frequency dependence of phase angle between excitation and alternating response frequency is shown for different values of P in Equation 2.3.8. (Recreated from Figure 4 in [31] using a diffusion coefficient of 100 s^{-1}.)

Chapter 3 – Literature Review Part 2: TEB for Hydrodynamic Properties

3.1 Hydrodynamic Theory

3.1.1 Overview

Historically, hydrodynamics was synonymous with fluid dynamics, and referred to the study of liquids in motion. With the study of macromolecular phenomena as early as 1821, when Robert Brown observed the random motion of plant particles in water, the field has turned to the study of frictional coefficients of particles in solution. Stokes demonstrated the translational coefficient dependence on particle dimension in 1856, developing a reference model of equivalent sphere of Stokes radius to describe the particle. He later related the rotational friction coefficient to particle volume in 1880. The Perrin equations developed in the 1930's [1, 2] extended Stokes equation to ellipsoids of revolution, and provided three translational coefficients as functions of dimension of this ellipsoid. The observation of flow birefringence by James Maxwell in 1856 allowed for the study of optical properties of macromolecules without fixed structure. John Kerr observed in 1896 that certain solutions became birefringent under the influence of an electric field. This provided a means to measure dipole-dipole interactions of macromolecules, as well as relate flexibility and induced dipole moments. This was facilitated by Peterlin and Stuart in 1939 [3], who developed an equation to relate the induced birefringence of a suspension of axially symmetric particles in a sinusoidal electric field to the orientation distribution function. Benoit [4] and O'Konski [5] simultaneously developed a model for the alignment under rectangular electric pulse. In the decades since, many models have

been developed to extrapolate hydrodynamic constants from optical measurements of colloidal suspensions, including high and low field regimes, conducting and non-conducting media, isotropic and orientational light scattering, etc. We will limit our discussion to the models appropriate to the cellulose nanocrystal suspension in aqueous media, but we will need the background of hydrodynamic theory to get us started.

3.1.2 Hydrodynamics: The Particulars

Hydrodynamics deals with the behavior of bodies in fluids and the effects of fluid viscosity on a particle being acted upon by an external force. The dynamics of charged particles is first interpreted in context of its dependence on the hydrodynamic friction factor, which is a function of the particle's shape and upon interparticle interactions. Any deviation from predicted behaviour must then arise from electrical properties of the system. It is therefore important to understand hydrodynamic principles in order to differentiate the electrical interactions described in the previous chapter. The basics of hydrodynamic properties in terms of solution viscosities and particle friction factors will first be discussed. The subsequent sections will discuss how diffusional coefficients from hydrodynamic measurements can be used to obtain information regarding a particles shape and size.

3.1.2.1 Units of Viscosity

The force required to accelerate a 1 g mass by 1 cm per second per second is defined (historically in CGI units) as a dyne, where

$$1\ dyne = 1\ g\ cm\ s^{-2}. \tag{3.1.1}$$

The inertial friction of a moving particle in solution is defined, in viscosity terms, as the tangential force per unit area ($dyne\ cm^{-2}$) required to maintain a unit difference in velocity ($1\ cm\ s^{-1}$) between two parallel planes separated by 1 cm of fluid. This is the poise in CGI units, that is:

$$1\ poise = 1\ dyne\ s\ cm^{-1} = 1\ g\ cm^{-1}\ s^{-1} \tag{3.1.2}$$

The viscosity to density ratio is the kinematic viscosity, or the Stoke:

$$1\ Stoke = 1\ Poise\ cm^3\ g^{-1} = 1\ cm^2\ s^{-1} \tag{3.1.3}$$

If a particle moves slowly enough, the inertial effects are negligible. The Reynolds number (R) determines the relative importance of inertial and viscous effects, where

$$R = \frac{(fluid\ density\ \times\ speed\ \times\ particle\ size)}{viscosity} = \frac{\rho\, u\, l}{\mu} \tag{3.1.4}$$

Low Reynolds numbers occur when viscosity dominates, and high numbers when inertial forces dominate. For example, in water ($\mu = 10^{-2}\, g\, cm^{-1}\, s^{-1}, \rho = 1\, g\, cm^{-3}$), polystyrene nanoparticles of 90 nm in diameter moving at $10^{-3}\ cm\ s^{-1}$ will have a small Reynolds number (9×10^{-7}), indicating it will stop moving when the force accelerating it is removed (with the exception of Brownian motion.)

3.1.2.2 Boundary Conditions

Hydrodynamic dissipation is dependent on a particle's velocity with respect to the solvent, where surface interactions between solvent and particle define certain boundary conditions. Two extreme cases are called the 'slip' and 'stick' boundary condition. In

the ‘slip’ condition, there is no interaction, and the solvent slips along the surface of the particle. In the ‘stick’ condition, the first solvent layer adjacent to the particle sticks to it and moves with it at the same velocity as the particle [6]. In the case of isolated spherical particles under ‘stick’ condition, the velocity field dissipates with a long and short range component described by the power laws r^{-3} and r^{-1} respectively. The wake of this hydrodynamic velocity is reflected by other particles in the system, so the cumulative hydrodynamic interaction is r^{-m}, with certain restrictions on allowed values [7].

From the discussion of electric double layers and zeta potential in chapter 1, we can imagine that these boundary conditions are highly simplified for the case of colloidal particles and macromolecules. For complex double layers, a clear slip plane is often absent as shown by the Grahame model (Figure 1.2.3.2). However, for simplicity we will use the ‘slip’ and ‘stick’ conditions in our derivation of diffusion coefficients to come.

3.1.2.3 Translational Friction Coefficient

The accelerating force acting on a particle in solution is equal to the mass of the particle (m) times the acceleration, that is $F = m\,\dfrac{d\mathbf{u}}{dt}$, where $\mathbf{u}$ is the particle velocity. Solvent drag in viscous solutions creates an opposing force F_{frict} which is proportional to the particle’s velocity by a proportionality coefficient f, known as the translational friction coefficient. That is $F_{frict} = -f\mathbf{u}$, where the negative sign indicated the force is in the opposite direction as velocity. When the $\mathbf{F}$ and F_{frict} are equal in magnitude, acceleration goes to zero, and a constant velocity $\mathbf{u} = \mathbf{F}/f$ is achieved for $\mathbf{F} = -\mathbf{F}_{frict}$. Thus we obtain a means to calculate translational coefficients from measurements of equilibrium velocity. For a spherical particle, Stokes derived f for the ‘stick’ solvent boundary condition as $f = 6\pi\eta_0 R_0$, where η_0 is the solvent viscosity and R_0 is the particle radius. For the ‘slip’ condition, $f = 4\pi\eta_0 R_0$. For asymmetrically shaped particles, hydrodynamic

properties can be taken into account by modelling an ellipsoid of revolution, either oblate or elongate. Frictional forces will vary depending on the orientation of the molecule with respect to the flow direction. In the general case, $f = 6\pi\eta_0 R_0 F(p)$, where $F(p)$ is the Perrin function for oblate or elongate ellipsoids, and p is the axial ratio of the ellipsoid. Specifically for a circular cylinder of length L and radius r, the axial ratio is $p = L/r$, and $f = 6\pi\eta_0 L/(2\,ln\ p\ + \gamma)$, where γ depends on end effects.

3.1.2.4 Rotational friction coefficient

A constant torque F_{rot} applied to a particle in solution will result in an angular velocity ω. If F_{rot} is balanced by an opposing solvent frictional force F_{frict}, ω will be constant after some transient period. The rotational friction coefficient ζ is defined in terms of the opposing frictional force $\mathbf{F}_{frict} = \mathbf{F}_{rot} = \mathbf{F}$ as $\boldsymbol{\omega} = \mathbf{f}/\zeta$. For a sphere, Stokes derived $\zeta = 8\pi\eta_0 V$ for the 'stick' boundary condition and $\zeta = 0$ for the 'slip' condition.

For asymmetric particles, if we assume rotation occurs around a single axis through the center of mass, a single angle θ to a reference axis (for example a line passing through the long axis of a cylinder) can be related to angular velocity by $\omega = d\theta/dt$. A variable $p(\theta)$ is defined such that the number of particles per unit volume with an orientation between θ and $d\theta$ is $p(\theta)d\theta$. At equilibrium, $p(\theta)$ is a constant, since all values of θ are equally likely. In the presence of an orienting torque, some values of θ become more likely, and $p(\theta)$ becomes dependent on θ. This rotational diffusion can be modelled analogously to translational diffusion using Fick's first law, where $J(\theta)$ is now defined as the net number of molecules that transverse the angle θ in the positive direction over a time dt. The 'rotational flux' is thus

$$J(\theta) = -D[dp(\theta)/d\theta]t, \tag{3.1.5}$$

where D is the rotational diffusion coefficient. Fick's second law, again analogously written to translation diffusion is

$$dp(\theta)dt = -D[d^2p(\theta)/d\theta^2]. \tag{3.1.6}$$

The relationship between the rotation frictional and diffusion coefficient is

$$D = k_bT/\zeta, \tag{3.1.7}$$

where k_BT is the thermal energy in the system.

3.1.2.5 Rotational diffusion of cylindrical rods

Analogously to the translational friction coefficient, Stokes approximation for a cylindrical rod is

$$\zeta = \frac{\pi\eta_0 L^3}{3\,ln(p) + \gamma} \tag{3.1.8}$$

and thus

$$D = \frac{3k_bT}{\pi\eta_0 L^3}[3\,ln(L/d) - \gamma]. \tag{3.1.9}$$

Since the rod diameter d only appears in the logarithm, a large change in diameter contributes negligibly to D. Thus D can be used to estimate the rod length, L. Again γ is a frictional factor which depends on the model. Perrin [1,2] derived more general equations for the diffusion coefficients for rigid regular spheroids using the equation

$$D = \frac{A\,F(r)}{x^3}\ , \tag{3.1.10}$$

where $A = 3k_BT/\pi\eta$, x and d are the major and minor dimensions of the particle, r is the aspect ratio x/d, and $F(r)$ is a function of the particle geometry. For elongated particles, the $F(r)$ equation for prolate spheroids applies, where

$$F(r) = \frac{r^4}{2(r^4-1)}\left(\frac{2(r^2-1)}{r(r^2-1)^{1/2}} ln[r + (r^2-1)^{1/2}] - 1\right). \tag{3.1.11}$$

In the limiting case for cylindrical rods with aspect ratio $r > 10$, this reduces to $F(r) = ln(2r) - \gamma$, where γ is a function that accounts for end effects, and is generally dependent on r. Perrin calculated this originally as 0.5, independent of r. Burgers later calculated this to be 0.8 [8] and thus derived the torque constant for a cylinder to be

$$T/\omega = \frac{8\pi\eta a^3}{3(log_e 2a/b - 0.80)} \tag{3.1.12}$$

for a particle of length $2a$ and half width b [9, 10]. This was readdressed by Riseman [11], Broersma [10, 12] and Tirado [13, 14] for end effects, with slight difference in the torque constant with each consideration. All three models can be written in the general form

$$D = \frac{3k_BTln((L/d) - \gamma)}{\pi\eta L^3}, \tag{3.1.13}$$

where γ is the numeric correction factor which differs between models. Broersma gave this as [10]

$$\gamma = 0.887 - 7\left[\frac{1}{ln(L/d)} - 0.28\right]^2, \tag{3.1.14}$$

and in a later writing gave this as

$$\gamma = 1.57 - 7\left[\frac{1}{ln(L/d)} - 0.28\right]^2, \tag{3.1.15}$$

which eased certain discrepancies between experimental data for TMV [15] and the Burgers model. He later modified this model slightly to account for the velocity of the cylinder wall near the ends, as well as the flat ends of the cylinder [12]. This modified Broersma value (reported privately to Newman [8] and later reported by Tirado [14]) was

$$\gamma = -0.76 + 7.5\left[\frac{1}{ln(2L/d)} - 0.27\right]^2. \tag{3.1.16}$$

valid for $0.15 < 1/ln\ 2(L/d) < 0.35$ [8, 14]. Broerma published a more general model as [12, 14]

$$\gamma = -0.446 - 0.2/ln\ 2(L/d) - 16/(ln\ 2(L/d))^2 + 63/(ln\ 2(L/d))^3 - 62/(ln\ 2(L/d))^4. \tag{3.1.17}$$

Contrary to this, Tirado obtained the value of

$$\gamma = -0.662 + 0.917/p - 0.050/p^2, \tag{3.1.18}$$

and found this to fit experimental data better than that of Broersma's refined model [14].

The above discussions is meant to illustrate the uncertainty in modelling rotational coefficients for rigid cylindrical molecules. No widely accepted model is currently available in the field. The diversity in published models for rigid particles of symmetrical geometry alone should alert us to the difficulties and uncertainties still associated with estimating particle lengths from measured diffusion coefficients. With this in mind, the following section will summarize a few attempts in the literature to determine size distributions from TEB measurements of diffusion coefficients.

3.2 Transient Electric Birefringence for Measuring Particle Sizes.

Chapter 2 dealt mostly with the rise curve behavior of Transient Electric Birefringence, where the characteristic rise time is a function of the diffusion coefficient and dipole moment of the particle, and of the electric field strength. In the absence of the field, the dipole effects are irrelevant and the decay to the isotropic state is solely a function of rotary diffusion coefficient. The decay behavior therefore provides a method of measuring hydrodynamic properties for anisotropic particles in suspension. These measurements however come in the form of indirect observations. The first challenge comes from choosing the correct model for the data, as discussed in Section 3.1.2.5 A second challenge then arises as to how to relate the measured data to specific hydrodynamic properties using the appropriate model. A common method for doing this is with Linear Inverse Theory (LIT) as summarized below.

3.2.1 The Inverse Problem

According to William Menke [16],"Inverse theory is an organized set of mathematical techniques for reducing data to obtain useful information about the physical world on the basis of inferences drawn from observations." A wide variety of applications occur in which desired model parameters must be obtained indirectly from noisy observable data. A parameter estimation, or linear inverse problem arises in the form

$$y_k = \int_a^b F_k(\lambda) s(\lambda) d\lambda + \sum_{i=0}^{N_L} L_{ki} \beta_i + \epsilon_k, \tag{3.2.1}$$

where $F_k(\lambda)$ is a known function operating on a function or vector to be estimated, $s(\lambda)$. The data produced is the observable y_k, and ϵ_k are the unknown noise components [17].

The extra optional sum over L_i knowns allows for N_L unknown β_i parameters to be included. We can, for example, account for a constant background by setting $N_l = 1$ and all $L_{ki} = 1$.

Data arising from imperfect detection of a system under study, indirect measurements, or from multicomponent systems can result in an *ill-posed problem*, that is one in which a unique solution may not exist. An exact solution to equation 3.2.1 using a Fourier transform solution requires very accurate data over an essentially infinite range in t, and thus cannot be practically applied to real data [17]. Approaches to solving this difficulty usually rely on reducing the degrees of freedom and fitting parameters to a coarse histogram, that is to create a "discrete spectra" [17–19] such that

$$y_k = \sum_{m=1}^{N_g} c_m F_k(\lambda_m) s(\lambda_m) + \sum_{i=1}^{N_L} L_{ki}\beta_i + \epsilon_k \ , \tag{3.2.2}$$

where C_m are the weights of the quadrature formula. The solution $s(\lambda)$ is determined at N_g gridpoints λ_m.

Damped linear least squares (references 1-3 in [18]) are widely used solutions to discrete spectra. The weakness of these methods lies in the necessity of knowing the number of parameters, N_λ, beforehand if grossly incorrect solutions are to be avoided. Serious errors occur if the applied number of degrees is too small (inadequate modelling) or too large, where the solution becomes unstable due to noise. Preferable to presetting the number of parameters, N_λ should be decided upon during the analysis using constraints and requlatizers. Strategies to accomplish this may incorporate prior knowledge, such as using statistically expected means and covariances of the solution, or by forcing all positive $s(\lambda)$ values into the analysis. In addition, the principle of parsimony states that, of the set of all possible solutions Ω, the simplest one should be selected which still reveals novel information. Doing so ensures that the details included in the solution are necessary to

the fit and therefore less likely to be artefacts [17].

A method for accomplishing the above was proposed by Provencher as a constrained regularization method for inverting data represented by linear integral equations [17], and a Fortran IV package for solving equation 3.2.1 via equation 3.2.2 was subsequently released as CONTIN [20]. This package has found widescale use in dynamic light scattering for autocorrelation functions (see for example Brookhaven Instrument's software packages). The improvement of this package over other methods of inverting noisy data centers around its ability to incorporate statistical prior knowledge into its reguarizer in order to prevent unbounded errors in *ill-posed* problems. The regularization arises from the switch from continuous to discrete histograms (i. e. from Equation 3.2.1 to Equation 3.2.2), whereupon we go from an *ill-posed* problem to merely an *ill-conditioned* one. Still, however, a large number of solutions Ω' may satisfy eqn. 3.2.2 up to the experimental error ϵ_L. We could take an ordinary constrained least-squares solution to Equation 3.2.2 using both parsimony and assuming all positive $s(\lambda)$ such that

$$V(\alpha) = \| \boldsymbol{M}_{\epsilon}^{-1/2}(\boldsymbol{y} - \boldsymbol{A}\,\boldsymbol{x}) \|^2 + \alpha^2 \| \boldsymbol{r} - \boldsymbol{R}\,\boldsymbol{x} \|^2 = minimum \tag{3.2.3}$$

where $\| \bullet \|$ is the Euclidean norm, $\boldsymbol{M}_{\epsilon}$ is the covariance matrix of ϵ_k, $\boldsymbol{y}$ is a $N_y \times 1$ vector with elements y_k, and $\boldsymbol{A}$ is a combined matrix containing $c_m F_k(\lambda_M)$ and L_{ki} from Equation 3.2.2. The second term, called the regularizer, is defined by the user via a $N_{reg} \times 1$ array $\boldsymbol{r}$, a $N_{reg} \times N_x$ array $\boldsymbol{R}$, and the *regularization parameter* α. Although other methods are available for inverse theory, the CONTIN method of Provencher has passed the test of time for over two decades, and is familiar to us through our use of a Brookhaven Instruments DLS.

Without going into mathematical detail regarding the CONTIN subroutines, we should simply take from this overview that real experimental data has noise which will signif-

icantly bias convergence of solutions for linear inverse problems. Care must be taken to penalize solutions that violate statistical prior knowledge. The regularizor defined in CONTIN can help accomplish this, but not without careful thought on the experimenters part as to what appropriate constraints should be used for the system. The importance of such a regularizor, as well as the constraints which define it, will be evident in an alternate inverse solution for TEB analysis discussed in section 3.2.3.

In the case of TEB decay data, the extrapolated data of interest comes from the model proposed by equation 3.1.9 for the rotational diffusion coefficient

$$D = \frac{3k_bT}{\pi\eta_0 L^3}[3\,ln(L/d) - \gamma], \tag{3.2.4}$$

where L and d are the length and diameter of the anisometric particle, η_0 is the solution viscosity, and γ is a friction factor dependent on the model. If the rotational diffusion coefficient can be measured from the exponential decay of the electro-optic transient decay curves, the length of the particle can be calculated as long as the aspect ratio and friction factor can be estimated to some decree of accuracy. For a polydisperse system, the exponential decay is multi-order, representing the combined diffusion coefficients for all contributing species. Extracting all coefficients requires complex mathematics and often results in multiple solutions for systems containing more than 3 components. If a series of representative diffusion coefficients could be extracted however, a particle size distribution could be determined using inverse methods. Since linear inverse problems require both adequate models and accurate and relatively noise free data, we will spend some time discussing methods for extracting the diffusion coefficients from multi-exponential (and typically noisy) TEB decay data.

3.2.2 Using TEB Decay curve to Determine Diffusional Coefficients

Upon termination of the pulse (i. e. removal of the electric field), the decay to isotropic suspension (random particle orientation) is a diffusion controlled process. For a monodisperse colloid suspension, the rotational coefficient, initially described by Benoit [4], can be obtained from the single exponential decay as a function of time t

$$\Delta n(t) = \Delta n(0) exp(-6Dt) \tag{3.2.5}$$

where D is the rotary diffusion coefficient, $\Delta n(0)$ is the equilibrium value of n when $t = 0$ (defined at the end of the pulse as the start of the field free decay as shown in Figure 1.3.1.3). In order to extract D, a plot of $ln[\Delta n(t)/\Delta n(0)]$ versus t results in a straight line with slope $-6D$. For a polydisperse system, equation 3.2.5 becomes a multi-exponential decay, with each species contributing to the decay curve. Thus

$$\Delta n(t) = \sum_i \Delta n(0)_i exp(-6D_i t). \tag{3.2.6}$$

The plot of $ln[\Delta n(t)/\Delta n(0)]$ versus t results in a curved line, where the degree of curvature represents the polydispersity of the system. Solutions to the multi-exponential decay become impractical for more than two components, since there are an infinite number of solutions. Experimental noise also makes many of these solutions unstable, so it becomes necessary to apply mathematical restraints in order to find physically meaningful solutions [21].

One such method, referred to as the 'peeling method', involves taking the limiting slope of the curved log plot (D_1) for long decay times The method assumes that at least two diffusion constants can be obtained, and that $D_2 \gg D_1$ [22–24]. After determining

the limiting slope, the data is compensated by subtracting D_1, then replotted to get D_2. If the redrawn plot is not linear, the process is repeated to get a series of diffusion coefficients. This method is limited by the greater uncertainty at longer decay times, where $\Delta n(t)/\Delta n(0)$ is very close to zero and baseline errors become more significant.

A more theoretically satisfactory method involves taking the logarithms of both sides of equation 3.2.7 and differentiating with respect to t. The slope of this log plot, $S(t)$ is

$$S(t) = \frac{d}{dt} ln[n(t)] = \frac{-6 \sum_i D_i n_i(0) e^{-6D_i t}}{\sum_i n_i(0) e^{-6D_i t}}. \tag{3.2.7}$$

It is theoretically possible to fit a Laplace transform to this provided parameters n and D are known [25], as shown by [26]. However, since the Laplace transform is essentially a summation through infinitely small intervals [25], the superposition of a family of exponentials from a continuous spectrum of exponents results. This is a situation where one cannot extract more than two average exponents unless the data is certain to within 1 percent, as shown mathematically by Lanczos [27].

A third method, shown to be more reproducible and reliable, involves the initial slope of the normalized semi-log plot at $t = 0$ [15, 28–31]. This initial slope was found to be dependent on particle shape and size distribution, the electric field strength (by effecting the extent of orientation), and the electrical dipole moments [25, 32, 33]. An average coefficient $< D >$ is thereby determined under specific experimental conditions. The uncertainty of this method lies in the interpretation in 'initial' slope as used by various authors. While this method has been widely used [15, 25, 34, 35], authors do not specify the statistical criteria which is used to cease the curve fitting. In our work, we have found this approach to yield consistently decreasing diffusional coefficients as fitting criteria are relaxed, as will be shown in the experimental section. As such, while convenient and less prone to signal to error problems, this approach lacks a solid theoretical rational for its

use.

In more recent work, authors have used CONTIN [36, 37] to extract the diffusion coefficients from the continuous distributions of TEB exponential decays. As discussed above, this method can be reliable if appropriate statistical constraints are imposed. These authors used the same parameters for dynamic light scattering and TEB data, using CONTIN to extract translational and diffusion coefficients respectively. They reported consistent length and diameter values for cellulose nanocrystals from both methods [37].

3.2.3 The Evolution of a Truncated Pulse Particle Sizing Technique

It has been argued that the axial dipole moment increases with particle size. It will therefore be larger particles that have a higher degree of alignment at steady state under the influence of a low-intensity applied field [38]. Smaller particles with smaller dipole moments would require a higher amplitude field to produce the same degree of alignment [39], assuming the pulse was of sufficient duration to allow all particles to achieve their steady state orientation distribution. Using this principle, Jennings developed a two parameter function to describe particle distributions, using two different field strengths. They used alternating pulses of sufficient duration to allow all particles to align (such that the distribution function given in equation 2.3.2 approaches unity). They also chose alternating fields of high enough frequency to avoid the effects of permanent dipole moment, thereby simplifying the alignment mechanism. They made the assumption that at low field amplitude, only large particles would align, and small particles would align fully only at high field amplitudes [39].

Prior to this work, Stoylov and Sokerov recognized that the distribution function was dependent on the duration of the electric fields as well as the amplitude, where low amplitude fields favoured alignment of the more easily oriented larger particles. Since different

constituent sizes of particles under the same amplitude field require different lengths of time to achieve the same degree of statistical alignment, they were able to estimate a distribution of sizes for Tobacco Mosaic Virus by varying both parameters [31].

An alternate method applied by Yoshioka and Watanabe [30] involved integrating the area under the decay curve to get an average diffusion constant. A combined method was proposed by Watson and Jennings in order to obtain a distribution function from a single transient response [21]. In this method, the value of $1/ < D >$ was calculated from the integrated area under the time dependent decay curve, and the value $< D >$ obtained from the initial decay slope. Under low and high field strength conditions, the ratio of the weighted averages of each provided a method to calculate a size distribution breadth σ from $< 1/D >_L < D >_L = < 1/D >_H < D >_H = exp(9\ \sigma^2)$. Therefore, a single transient measured under either high or low field conditions lead to σ directly, eliminating the uncertainty of multiple pulses. The probability distribution function $f(l)$ was determined using a log normal function

$$f(l) = \frac{1}{l\ \sigma(2\pi)^{1/2}} exp\left[\frac{-[ln(l/m)]^2}{2\sigma^2}\right] \tag{3.2.8}$$

where $\int_0^\infty f(l)dl = 1$, m is the median, and σ is the breadth parameter. If the number density for a species i is N_i, then

$$\int_0^\infty l^n f(l) = \sum_i N_i l_i^n, \tag{3.2.9}$$

and the n^{th} moment of the distribution depicted by

$$I(n) = \int_0^\infty l^n f(l) dl \tag{3.2.10}$$

becomes

$$I(n) = m^n e^{(n^2\sigma^2)}. \tag{3.2.11}$$

A refined version of the two parameter method involved compiling a histogram of sized distributions using truncated pulses [34]. In theory, for fields of sufficiently high alternating frequency to prevent permanent dipole contributions, increasing the duration of the field pulse would increase the degree of overall alignment, with larger particles adding continuously with longer pulse duration. A series of deliberately truncated pulses of equal amplitude provided average diffusion coefficients from the initial slope of the decay as a function of truncation time. From Benoit's equation for the rise time (equation 1.3.2), we can imagine that for purely induced dipole moment, $\mu = 0$ and equation 1.3.2 reduces to

$$\Delta n = \Delta n_0 \left[1 - exp(-6Dt)\right]. \tag{3.2.12}$$

This is symmetric to the decay equation. As such, the maximum birefringence of any particle species is $\Delta n_0 \left[1 - exp(-Dt)\right]$. We can model the decay for non-equilibrium conditions as

$$\Delta n = \Delta n_0 \left[1 - exp(-6D\theta)\right] exp(-6Dt), \tag{3.2.13}$$

where θ is the restricted pulse duration. For a polydisperse system, this is a summation over all species i such that

$$\Delta n = \sum_{i=1}^{r} (\Delta n_0)_i \left[1 - exp(-6D_i\theta)\right] exp(-6Dt). \tag{3.2.14}$$

The weighted factor $\Delta n_0 \left[1 - exp(-Dt)\right]$ allows us to write the initial slope coefficient

for truncated pulses as

$$< D_\theta >= \frac{\sum_{i=1}^{r} c_i \Phi_i' D_i \left[1 - exp(-6D\theta)\right]}{\sum_{i=1}^{r} c_i \Phi_i' \left[1 - exp(-6D\theta)\right]}, \tag{3.2.15}$$

where c_i is the volume fraction and $\Phi_i' = \Delta\alpha E^2/15k_BT$ is the orientation function for induced dipole mechanisms only, where electric polarizability $\Delta\alpha = \alpha_1 - \alpha_2$. The average value $< D >$ is interpreted in terms of particle geometry and polarization mechanism, and realistic experimental expressions are given in Table 1 of [34].

To proceed from there, one should recall the interpretation of D for regular spheroids from the Perrin equations [1] as $D = A\,F(r)/x^3$, where $A = 3k_BT/\pi\eta$ (η is the solvent viscosity and k_B and T have their usual meanings), x is the length of the particle major axis, r is the particle aspect ratio, $r = x/d > 1$, and $F(r)$ is a function of the axis ratio. Solving for a distribution function then relies on a solution of m measured values of $< D_\theta >$ using a set of linear equations based on a model for the appropriate geometry. The expression for D_θ for rods from Table 3 of [34] provides

$$< D_\theta >= A\,F(r) \frac{\sum_{i=1}^{r} N_i \left[1 - exp(-6D\theta)\right]}{\sum_{i=1}^{r} N_i l_i^3 \left[1 - exp(-6D\theta)\right]} \ . \tag{3.2.16}$$

Rearranging gives

$$\sum N_i \left[< D_\theta > l^3 - A\,F(r)\right] \left[1 - exp(-6D_i\theta)\right] = 0 \ , \tag{3.2.17}$$

Choosing an appropriate model for $F(r)$ takes us full circle back to the discussion in section 3.1.2.5 regarding conflicting models for cylindrical particles. While inverse theory can be used to apply experimental data to different models to optimize fits, the technique becomes increasingly intractable if data is noisy. It likewise fails if inaccurate models are used. Our results were applied to several different models, with slight differences in size

distributions resulting from each. Section 6.3.1.2 shows size distributions from models assuming constant diameter, constant aspect ratio, or gradiated aspect ratio, with disparate solutions arising in each case. In a polydisperse system, it is likely that multiple models may be appropriate, and the inverse problem becomes considerably more complex.

Chapter 4 – Materials and Methods

This chapter details the experimental protocols used throughout this research, and is divided into three major sections. Section 4.1 summarizes the production, purification, and liquid crystal phase separation of cellulose nanocrystals. Section 4.2 details the mathematical principles which allow experimentally-measured light intensity to be correlated with the polarization state of that light. Although this may seem abstract for a methods chapter, it is included here as a simplified tool for the researcher not trained in optics. The optical setup specifically relevant for TEB is outlined and demonstrated through model and experimental data. The pitfalls of linear estimations used by past TEB analysts is elucidated. Section 4.3 concludes by detailing the TEB apparatus and related electronics.

4.1 Cellulose Nanocrystals

4.1.1 Carboxylated Cellulose Nanocrystal (C.CNC) Production

4.1.1.1 Dust Free Deionized Water (DF-diH_2O)

All water used for reactions and washing steps was first deionized, then filtered for dust using an APEC Countertop Reverse Osmosis (RO-Ctop) water treatment system with a CT-1SED first stage sediment filter (part # K2525), a CT-24CAB second stage Carbon filter (part # K2553) and a Stage 3, 100 Dalton MWCO (Dow Filmtec TW30-1812-75) reverse osmosis filter. The final carbon filter unit was bypassed to prevent carbon particulates from being re-introduced. Dust-free water was analyzed using dynamic light

scattering (DLS) and compared to deionized water to ensure that unit was functioning as desired.

4.1.1.2 Hydrochloric Acid Hydrolysis

Avicel PH-101 microcrystalline cellulose (80 g, Fluka, from cotton linters) starting material was suspended in 1 liter of 2.4 N HCl (aq). This was brought up to 100°C with stirring under nitrogen reflux (Figure 4.1.1.1) over a 15 to 20 minute heating period, then stirred for an additional hour. Stirring was then stopped and the suspension was allowed to cool and settle (still under nitrogen reflux) for up to an hour until mixture reached room temperature. Clear supernatant was siphoned off the settled solids (Figure 4.1.1.2). The solid pellet was washed with dust free deionized water (DF-diH_2O) until the conductivity of supernatant was less than 100 μS. Washing was performed by sequential dilutions of settled solids with DF-diH_2O, overnight settling of solids and siphoning off of clear supernatant. With large enough containers, in this case a 6 L Erlenmeyer flask, the $\sim$300 mL pellet of microcrystaline cellulose could be diluted up to 1:20 upon each washing, requiring fewer wash steps.

Alternatively, washing was a carried out using centrifugation at 3400 RPM for 45 minutes with a table top centrifuge (Heraeus Instruments, Labofuge 400). Supernatants after each centrifugation were decanted and pellets resuspended in DF-diH_2O until final conductivity of discarded supernatant was less than 100 μS. It was observed, however, that the turbidity of centrifugation supernatants was significantly higher than those from overnight gravity sedimentation (Figure 4.1.1.2), indicating a greater loss in smaller particles. As such, the more time-consuming gravity method was generally preferred.

When the discarded supernatant dropped to the desired conductivity (using either washing method), the remaining pellet was re-suspended in dust-free diH2O to $\sim$500

mL total volume and transferred to a 3 L three-neck round bottom flask in preparation for the carboxylation reaction.

4.1.1.3 Carboxylation Reaction

After HCl hydrolysis, the pH of the slurry was adjusted to 9.7 with aqueous NaOH (4 M). To this, 60 mg of 2,2,6,6-Tetramethylpiperidine-1-oxyl (TEMPO) free radical (Aldrich) per g cellulose and 1 g NaBr (EM Scientific) per 10 g cellulose was added and stirred for around 30 minutes to dissolve the TEMPO. The reaction was initiated by adding 6% sodium hypochlorite (NaOCl) until the oxidation/reduction potential (ORP) reached 500 mV. Oxidation reaction was continued with suspension maintained at pH >9.7 and the ORP above 400 mV for 24 hours.

Controlled feed rates of NaOH and NaOCl were used to prevent undesired side reactions from occurring due to excess NaOCl. Feedback regulators were designed using a pH probe (VWR, SympHony Glass Semi-Micro pH Electrode cat # 14002-760) with an Omega PHCN-70 (Omega Technologies) controller, and an ORP probe (VWR SympHony Glass Combination Redox Electrode, cat # 14002-858) with a Jenco 3675 pH/ORP (Jenco Electronics, Ltd.) controller. Controllers were wired to OEM style peristaltic pumps (Omega, FPU100 series). The pumps were used to add 4 M NaOH and % NaOCl from reservoir burets dropwise to the reaction whenever lower pH and ORP set limits were encountered over the entire 24 hour reaction. After 24 hours, reaction was quenched by the addition of 100 mL methanol, then subsequently allowed to settle overnight undisturbed.

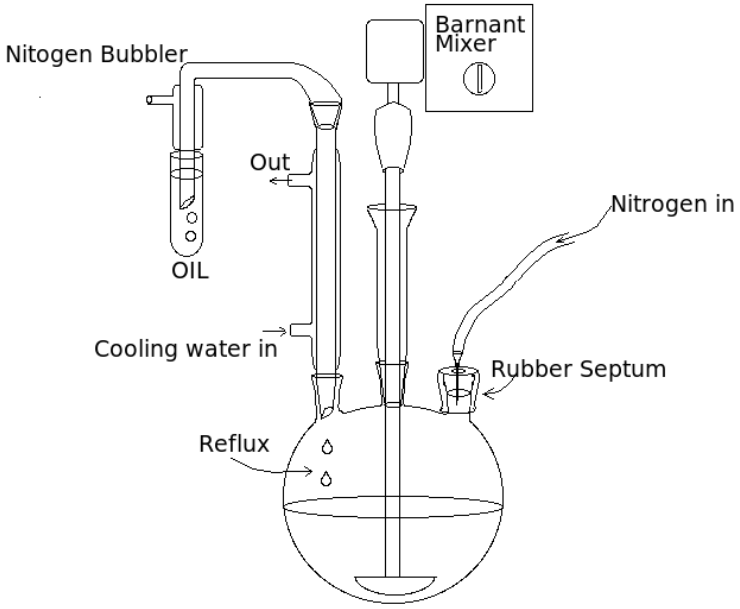

(a) HCl hydrolysis schematic

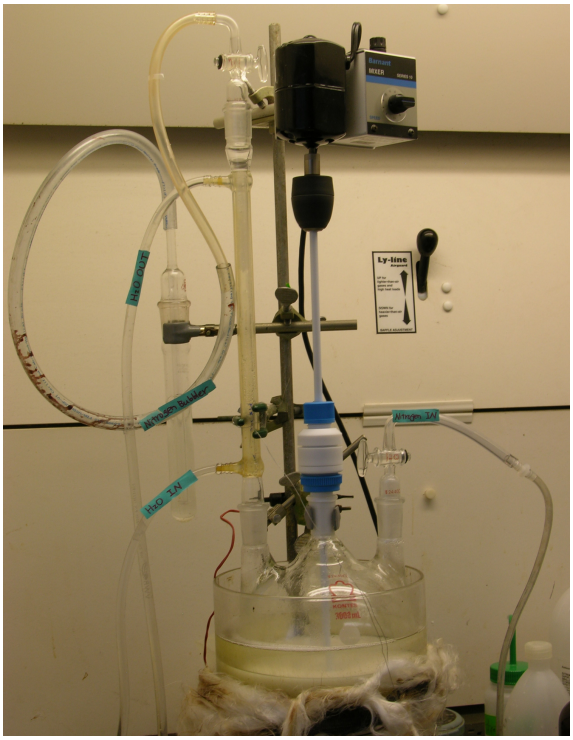

(b) Lab View of HCl hydrolysis

Figure 4.1.1.1: Hydrochloric acid hydrolysis of Avicel PH-101. Reaction is performed at 100°C under nitrogen reflux to minimizes oxidation side products.

Figure 4.1.1.2: Photograph of HCl hydrolysis after sedimentation. Avicel PH-101 microcrystallin cellulose was allowed to settle and cool for 1 hour after hydrolysis, resulting in a clear supernatant.

4.1.1.4 Nanocrystal Purification

After overnight settling, a clear supernatant could be observed above a white pellet (similar to Figure 4.1.1.2, with supernatant being clear yellow). After siphoning off the supernatant, the pellet was further separated from reaction solution by centrifugation at 3400 RPM for 45 minutes (Heraeus Instruments, Labofuge 400). Centrifugation pellets were then dialyzed against diH2O until no further decrease in conductivity was observed. The pellets were then diluted with DF-diH2O to approximately 1% solids (wt/wt), then ultrasonicated at a duty cycle of 45%, power output of 4.5 (Branson Sonifier, model 250) to expedite dispersion of microcrystalline aggregates into the desired nanocrystal whiskers. Sonication time was kept to a minimum to avoid nanocrystal degradation (generally less than 1 hour), and stopped when solution was observed to turn from translucent, non-dispersive scattering (white, milky appearance representative of >1 μm particles) to a clearer, Rayleigh scattering suspension. Specifically, suspension was observed to show blue and red shifts with transmitted and reflected white light, respectively, due to the

nanoscale size dispersion of crystallites (Figure 4.1.1.3). Figure 4.1.1.4 shows the same C.CNC suspension before and after sonication as imaged through an optical microscope between crossed polarizers. The absence of visible crystals in the sonicated suspension indicates only the presence of nanosized particles. Suspension was then filtered down to 0.7 μm with glass microfiber filters (Whatman GF/7) to remove remaining cellulose aggregates and microcrystalline cellulose.

4.1.2 C.CNC Characterization Techniques

4.1.2.1 Carboxylic Acid Titration

Conductometric titration of surface carboxyl groups was done according to the protocols of [1, 2] using 0.01 N NaOH titration standard solution (VWR). An excess of HCl was added initially to titration sample to acidify all surface carboxyls. NaOH was then added dropwise using a digital syringe pump (KDScientific, model 100 series). Conductivity was measured using a VWR SympHony Conductivity probe (K=1.0, cat # 11388-372) and volume was plotted against conductivity. Three distinct slopes could be seen with increasing volume of NaOH (Figure 4.1.2.1). These correspond to the titration of excess HCl (rapid decrease in conductivity), the titration of C.CNC surface carboxyls (slow conductivity decrease), and the addition of excess NaOH (increasing conductivity). Due to solubility limits for acidified C.CNC's, a sharp transition between the HCl titration slope and carboxylic acid titration slope could not be obtained. As such, linear regions of each slope were fit and the intercepts of the fitted lines were used to obtain the titration volume specific to the carboxylic acid surface groups. Typical values for the levelling-off degree of acidification of CNC (occurring at TEMPO reaction times 24 hours) ranged from 1.1 mmol to 1.3 mmol of carboxylic acid per gram cellulose.

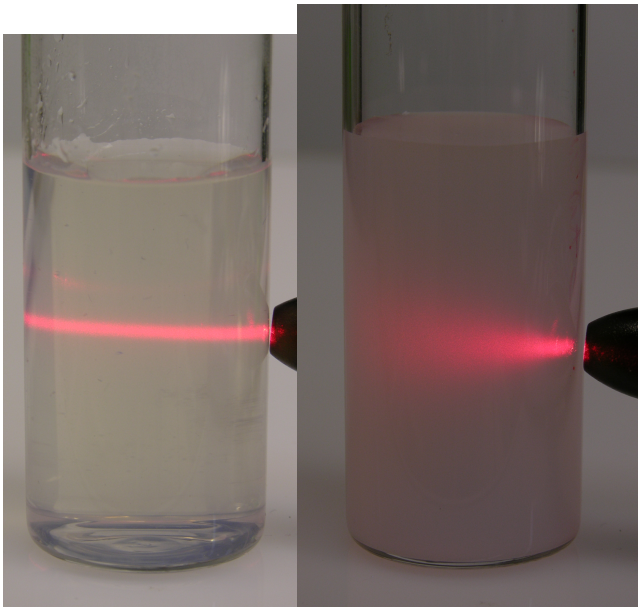

(a) Sonicated (b) Unsonicated

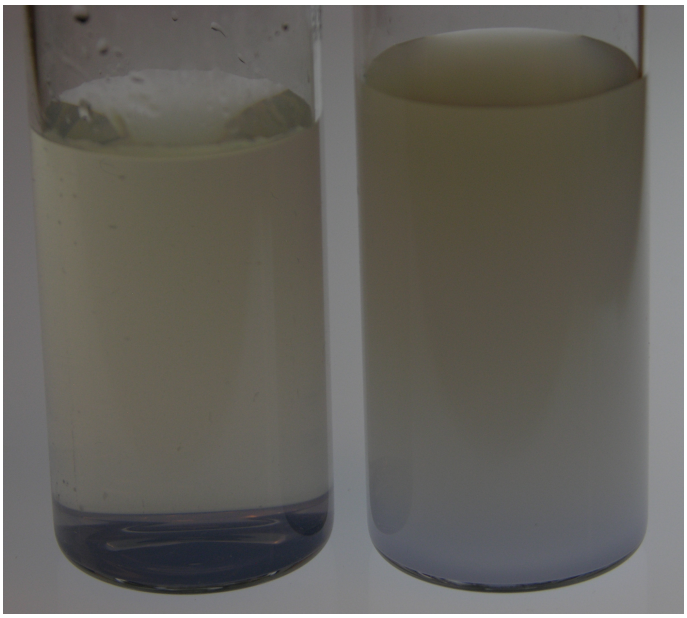

(c) Red Shift to blue shift

Figure 4.1.1.3: Photograph of C.CNC suspensions before and after sonication. Suspensions were at 2.5 wt% solids both before (b) and after (a) sonication. The same suspensions show red shift or blue shift depending on angle of observation (c), indicating the presence of nanocrystals.

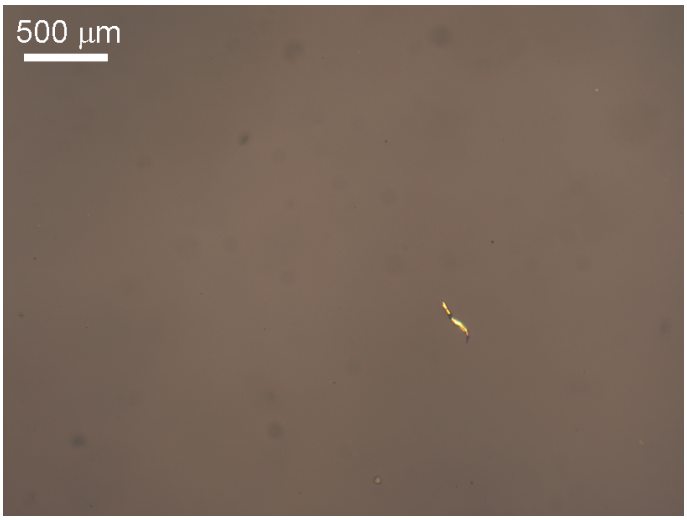

(a) Sonicated

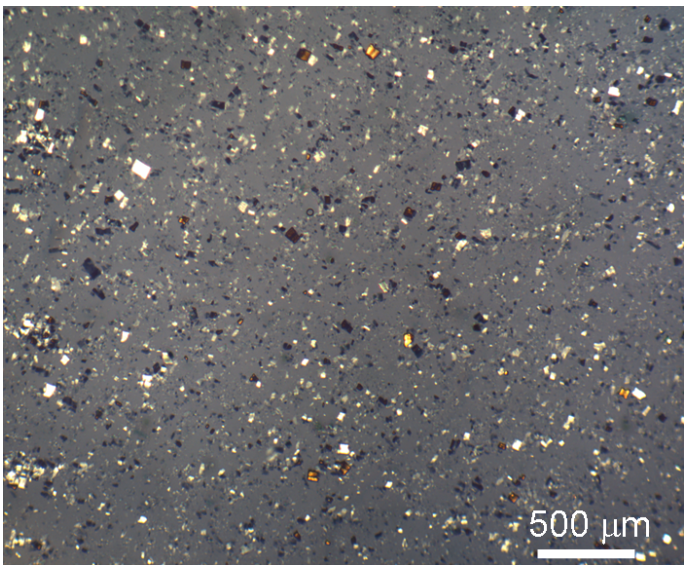

(b) Unsonicated

Figure 4.1.1.4: Optical microscopy of C.CNC before and after sonication. C.CNC (2.5 wt% solids before (b) and after (a) sonication) is magnified under an optical microscope (Nikon Eclipse E400 at 100X magnification) between crossed polarizers and photographed with a QImaging Micropublisher 5.0 RTV digital camera. The absence of optically visible crystals in (a) indicates only nano-sized crystals present.

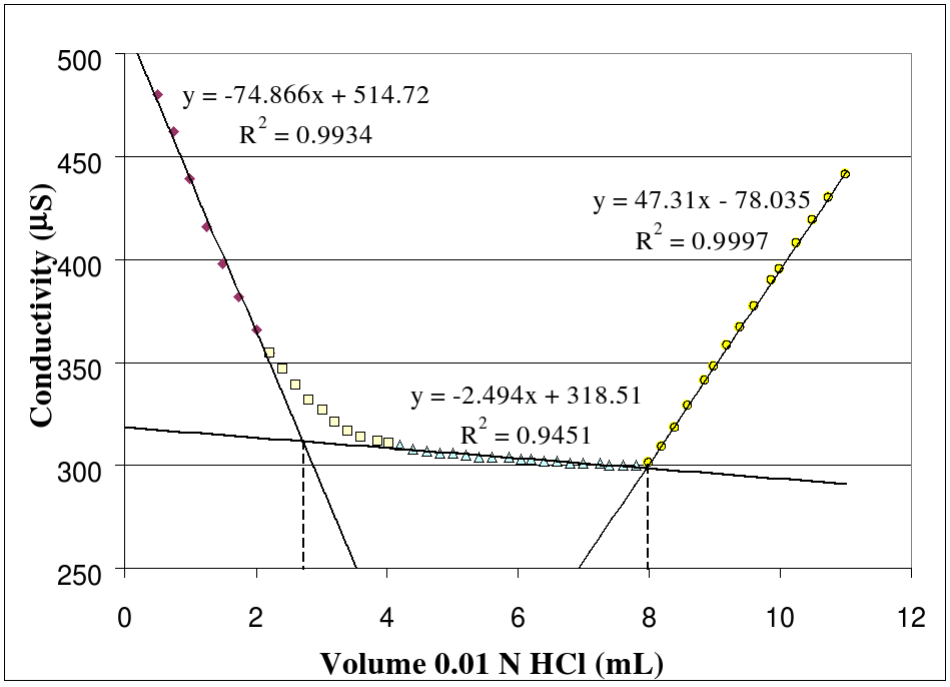

Figure 4.1.2.1: Typical titration data for C.CNC. Initial linear fits to the excess HCl neutralization curve (0 to 2 mL) and excess NaOH curve (8 to 12 mL) are extrapolated to their intersection with the carboxylate titration curve (4 to 8 mL) to obtain more accurate titration volumes.

4.1.2.2 Atomic Force Microscopy (AFM) Imaging

AFM was performed using a Dimension 3100 series Scanning Probe Microscope (Veeco Metrology Inc., Santa Barbara, CA) in contact mode. Tips used were silica nitride of varied origin (Veeco, Ted Pella, Budget Sensors) with typical radii of 10 nm.

4.1.2.3 Dynamic Light Scattering (DLS)

Dynamic Light Scattering (DLS) was done on a Brookhaven Instruments Corporation (BIC) BI-200SM Multiangle Research Goniometer with a BI-9000 AT Autocorrelator. Data was analyzed with BIC Bi-SLSW Static Light Scattering software and BI-DLSW Dynamic Light Scattering Software.

4.1.2.4 Zeta Potential

Zeta potential was measured with a Brookhaven Instruments Corporation (BIC) Zeta-Plus/ZetaPALS Zeta Potential Analyzer, calibrated and standardized with their BI-ZR3 reference material dispersed in 1 mmol aqueous KCl. Typical zeta potentials for C.CNCs ranged from -59 to -66 mV, indicating good stability.

4.1.2.5 Fourier Transform Infra-Red Spectroscopy (FTIR)

IR spectra were generally obtained on free cellulose films using a Thermo Nicolet, NEXUS 470 series FTIR, and processed with the Thermo-Nicolet custom software OMNIC (version 6).

4.1.3 Liquid Crystal Phase separation

4.1.3.1 Phase Separation: Protocol Development

Aliquots of a C.CNC suspension (batch MJTII-11, conductivity of 520 μS per cm at 1.63% solids, pH 6.8, 520 μS) were simultaneously concentrated and dialyzed using a tangential flow, hollow fiber filtration module (Spectrum Labs MicroKros, 500 kDa pore size, 0.5 mm fiber ID). High ionic strength phase separations were dialyzed once while concentrating 10 to 1. Total permeate was measured to be 113 μS and retentate was calculated from relative volumes to be 395 μS at the initial concentration of 1.63%. Final retentate after concentration (measured to be 6.4%) was diluted to 6%, 5%, 4% and 3% solids in aliquots of 2 mL volumes, then placed in NMR tubes and allowed to phase separate up to three months with frequent photographic documentation. Low ionic strength samples were dialyzed seven times followed by a 1:10 dilution each time with dust free de-ionized water. Permeate was monitored until the conductivity ceased to decrease, starting at 115 μS and ending at 12 μS with the final dialysis. Retentate (5.7% solids, measured after dilution to be 188 μS at 1.63%) was diluted to 4%, 3%, 3.5%, and 2% in 0.5 mL aliquots and allowed to phase separate in NMR tubes for several months alongside the high IS suspensions. Figures 4.1.3.1 and 4.1.3.2 demonstrate the dependence of phase separation on concentration and time, where the low ionic strength samples separated at lower percent solids and with shorter time periods.

Figure 4.1.3.3 shows the entire volume for both the low and high IS LC phase separations at 41 days. It is postulated that the surface charge interactions between particles accelerate the phase separation behavior, since surface charge interactions would be reduced at high IS due to shielding effects. In addition, lower IS suspensions resulted in higher volume fractions of ordered phases for lower concentrations. To help elucidate

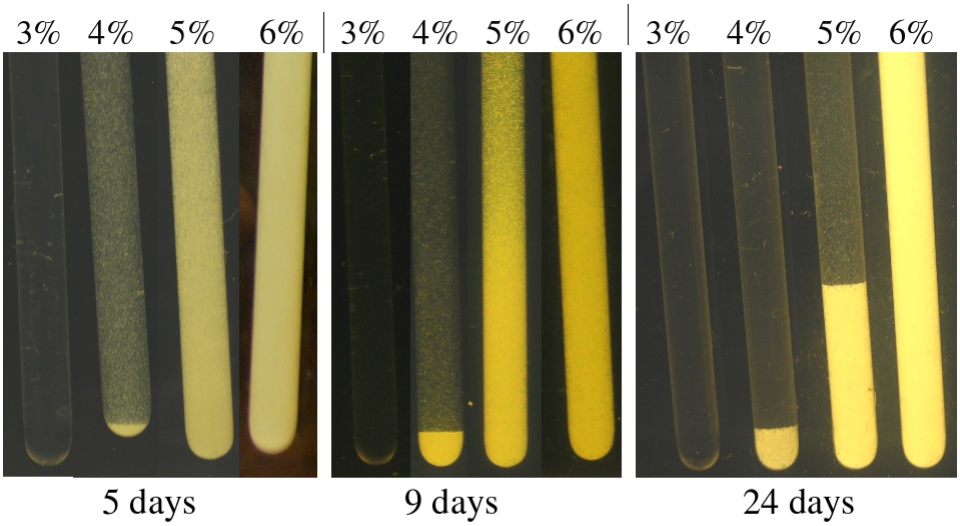

Figure 4.1.3.1: High Ionic strength C.CNC samples phase separated 24 days. C.CNC samples had a conductivity of 395 μS at 1.63% solids, and were photographed regularly for up to 24 days to monitor rate of phase separation. Suspensions were placed between two crossed linear polarizer sheets for birefringence visualization.

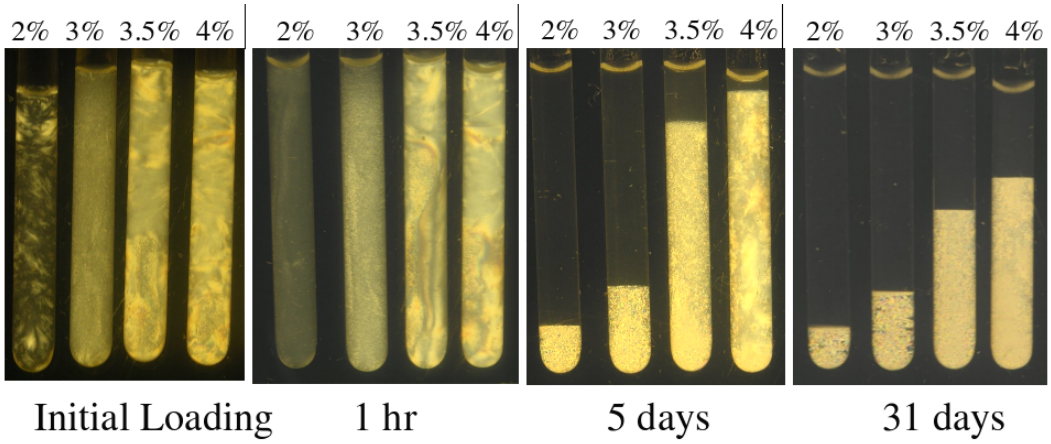

Figure 4.1.3.2: Low IS C.CNC samples phase separated for two months. C.CNC samples had a conductivity of 188 μS at 1.63% solids. These were phase separated for up to two months and photographed regularly between crossed polarizer sheets to monitor rate of separation. The emergence of birefringent droplets, or tachtoids, coalescing over time into a continuous anisotropic fluid phase is in agreement with other published works [3, 4].

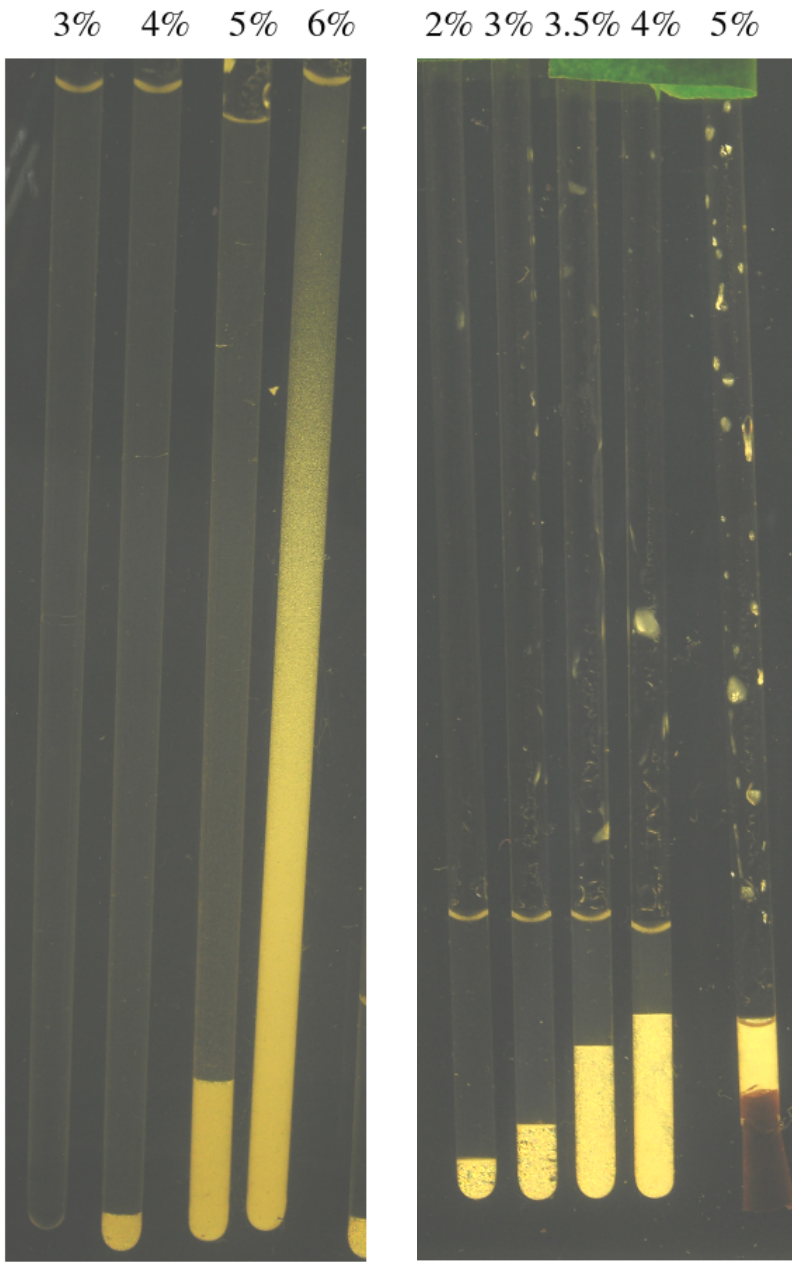

(a) High IS (b) Low IS

Figure 4.1.3.3: Comparison of high and low IS C.CNC after 41 days of separation. Tachtoid coalescence progressed slower for the high IS C.CNCs, occurring at a lower volume fraction for equivalent concentrations. (See Table 4.1.3.1.) Since the glass tube for the 5% concentration in the low IS regime was broken at day one, and remaining suspension corked and saved, it is guessed that no phase separation occurred above 5% at low IS.)

Table 4.1: Volume fraction of anisotropic phases for low and high IS separations. The volume fraction of the anisotropic phases was determined for low and high ionic strength liquid crystal phase separations after 41 day from Figure 4.1.3.3. ([1]: Value in question. See figure 4.1.3.3 for explanation.)

	Vol. % Anisotropic Phase	
Percent Solids	High IS	Low IS
2	-	19.0%
3	0%	29.0%
3.5	-	56.2%
4	4.5%	70.5%
5	15.1%	100%[1]
6	Undetermined	-

whether this effect was due to surface charges alone or to interactions with free ions in solution, the surface charge dependence on phase separation was investigated. A sample of C.CNC (batch MJTII-11) was ion exchanged with Amberlite MB-150 H^+/OH^- ion exchange resin to remove the Na^+ countercharge and acidify the surface carboxylates. Resin was added until conductivity ceased to decrease and final pH was 3.3. IR spectra were taken after exchange, indicating the shift from -COO^-Na^+ to -COOH with the addition of a peak at 1723 cm^{-1} (Figure 4.1.3.5) and the shift from 1605 to 1613 cm^{-1} [5,6]. Ion exchanged C.CNCs were then concentrated to 2%, 3%, 4%, and 4.5 % solids with the MicroKros module and allowed to phase separate. No change was observed from initial loading, even after 4 months, indicating the necessity of a surface charge to form LC phase separations (Figure 4.1.3.4).

4.1.3.2 Phase Separation: Preparative Scale-up

In order to accelerate the phase separation process for the scale up and size analysis, the low IS regime was adopted. Multiple 10 mL aliquots of C.CNC (batch MJTII-11) were dialyzed and concentrated with a 0.1 μm pore size hollow fiber filtration module (Spec-

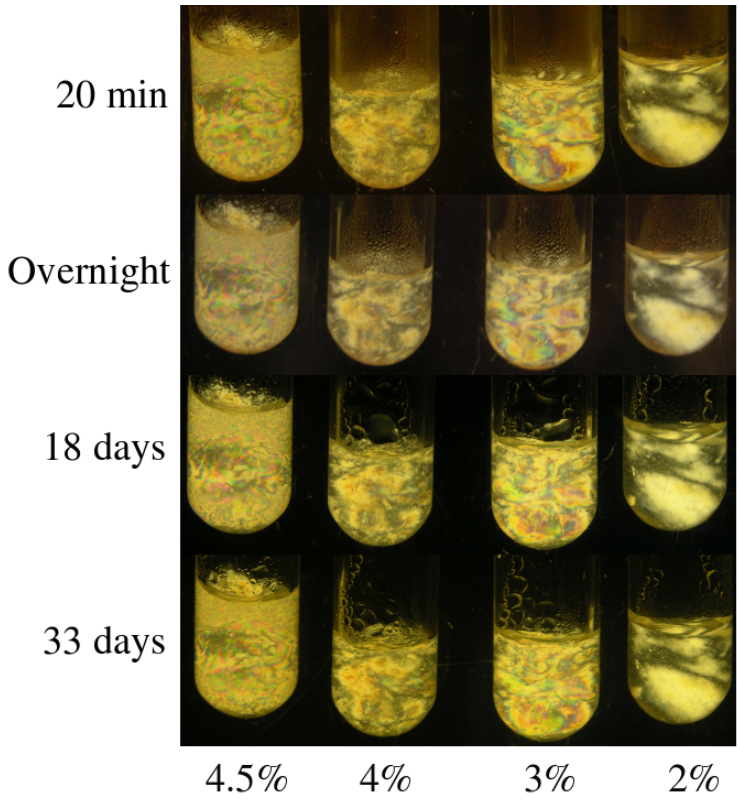

Figure 4.1.3.4: C.CNC LC separations in the absence of surface charge. H^+/OH^- ionic exchanged C.CNCs are photographed between crossed polarizer sheets, showing no liquid crystal phase separation in the absence of surface charge.

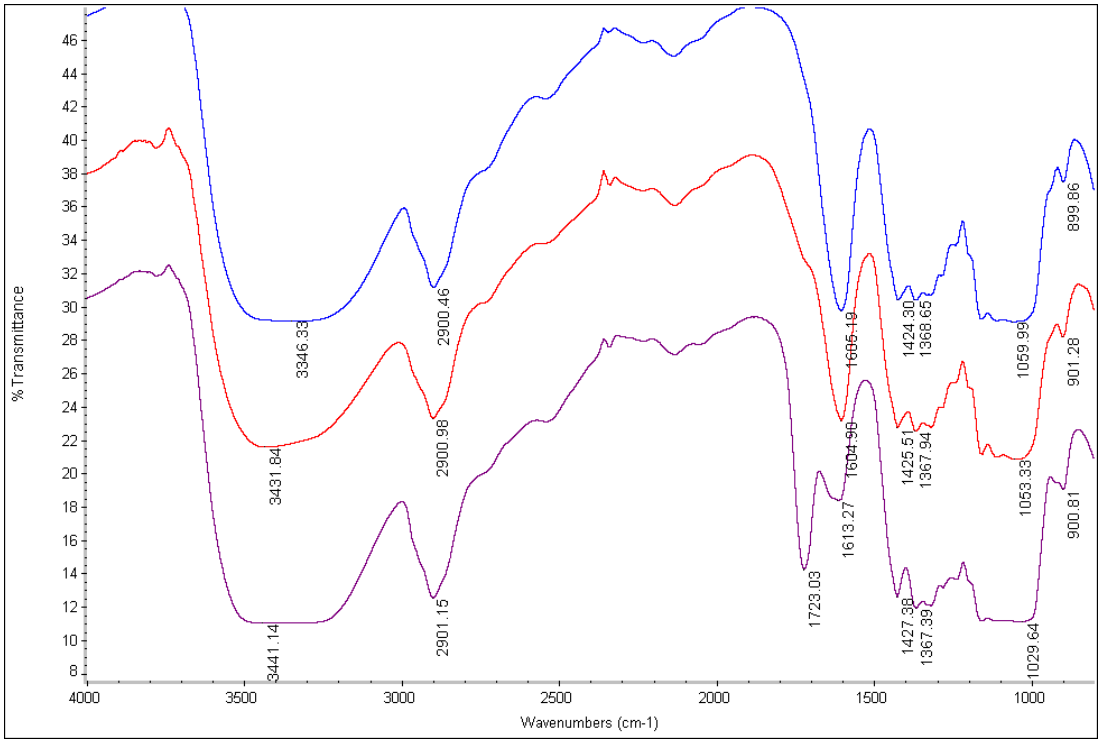

Figure 4.1.3.5: IR spectra of C.CNCs with and without surface charge. IR spectra were taken on unmodified C.CNCs (top spectrum), and on C.CNCs microcrossed using hollow fiber filtration modules (middle spectrum) indicating slight shifts in protonation upon removal of excess Na^+ counterion. The bottom spectrum shows C.CNCs that were ion exchanged with H^+/OH^- mixed bed ion exchange resin (Amberlite MB-150, Sigma). The shift from -COO^-Na^+ to -COOH upon ion exchange can be seen with the addition of a C = O stretching peak at 1723 cm^{-1} [5, 6] and the shift of the 1605 cm^{-1} peak to 1613 cm^{-1}.

trum Labs MicroKros, 0.5 mm fiber ID) seven times with a 1:10 dilution each time with dust-free diH_2O. The larger pore size from the initial LC phase separation experiment was selected in hopes of removing the small particulates thought to arise from the harsh processing conditions. The final suspension was diluted to 3.1% solids (giving a total mass of 17 g) aiming for the roughly 50/50 volume fraction separation between 3% and 3.5% in figure 4.1.3.2. After 20 days, no further separation between the lower anisotropic (birefringent) phase and the upper isotropic phase could be observed. The separation was stopped at 22 days and the top phase was carefully removed from the lower by siphoning through a narrow capillary tube. To avoid mixing effects between phases, removal of the top phase was stopped several millimeters before the phase boundary. Subsequent aliquots were collected into separate vials for several millimeters into the bottom phase (see Figure 4.1.3.6 for volume approximations). The uppermost and lower most fractions only were used for analysis, and the three inner aliquots were observed for further phase separation to determine the degree of cross contamination due to mixing upon phase removal (Figure 4.1.3.7.)

4.1.3.3 Characterization of Separate Phases

After separating the top and bottom phases for the scaled up LC phase separation (Figure 4.1.3.6), percent solids were re-measured. The top phase remained the same as the initial, unseparated suspension (3.1%), whereas the bottom-most phase was measured to be 3.5%. The mass redistribution could not be explicitly accounted for, as the total volume before and after phase separation could not be accurately measured. It was supposed that the increase in concentration in the bottom phase without depletion in the top phase could have arisen from evaporation of liquid water through the parafilm seal. Figure 4.1.3.8 shows characteristic AFM images taken for each phase, possibly indicating an overall

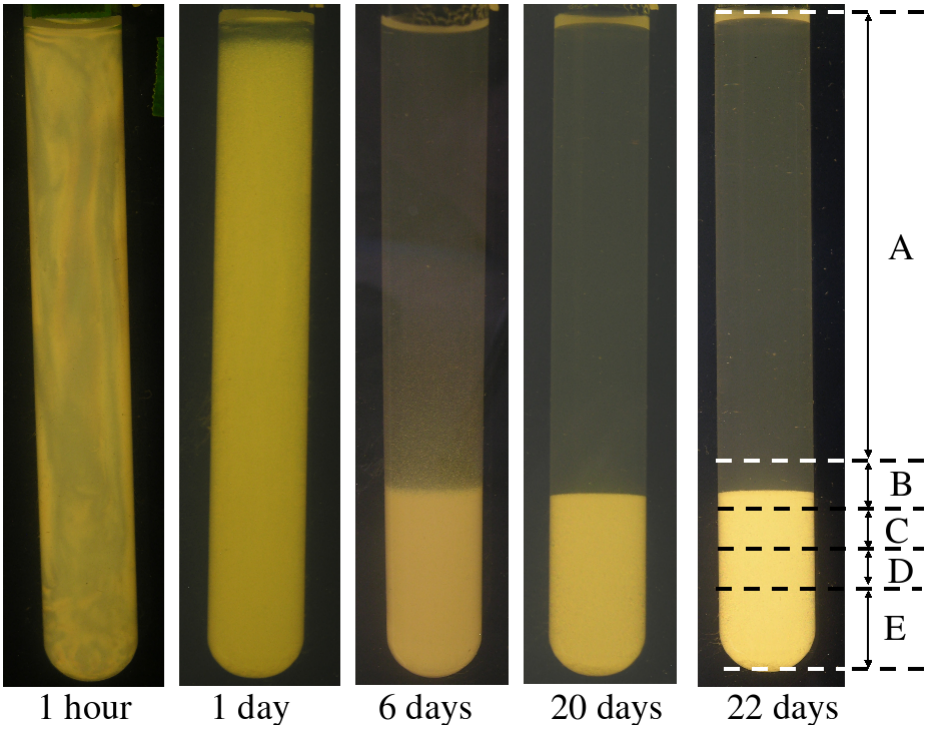

Figure 4.1.3.6: Preparative C.CNC phase separation. A scaled-up C.CNC phase separation (17 g suspension at 3.1% solids) was left for 22 days and photographed regularly between crossed polarizers. At 22 days, top phase was siphoned off to point B, then sequential portions were taken as shown by the dashed lines. Aliquots B through D were placed in separate vials for further observation. Phase A (top) and phase E (bottom) were used for further experiments.

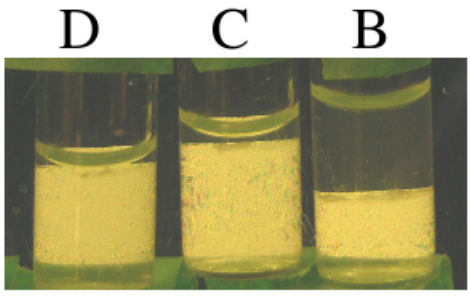

Figure 4.1.3.7: Aliquots B through D from Figure 4.1.3.6. Aliquots were left undisturbed for 8 months after siphoning to estimate the degree of mixing upon separation of anisotropic and isotopic phases.

difference in size distribution for the two phases. The ordered, anisotropic phase appears in AFM to contain a larger fraction of longer nanocrystals than the isotropic top phase. It was not attempted to get comprehensive size distributions from AFM images, as it is our belief that such sizing techniques are limited by inadequate sampling and experimental selection bias (i. e. hand picking), as well as by tip broadening artefacts.

4.2 Polarized Light: The Bare Essentials for TEB

4.2.1 Overview

The beginning researcher using optical methods for measuring birefringence must have a basic working understanding of polarized light and the techniques used to measure and characterize it. Many introductory descriptions for TEB provide equations for light intensity as a function of optical alignment for various optical components, but neglect a full derivation of these equations. In addition, experimenters often report equations which have been simplified by assumptions of negligible phase shift or small misalignment of optical components. Since such negligible phase shifts are not necessarily universal for all experimental settings, this assumption can result in significant errors when applied across laboratory environments without in-house optimization. Understanding full derivations of optical models allows the experimenter to identify optical errors specific to their system. It therefore seems intuitive that these principles should be addressed. The section is not meant to be a comprehensive description of polarized light, but rather to introduce some basic tools for electric birefringence. (For further reading, please refer to [7–11], from which this section was compiled.)

Section 4.2.2 will begin by reviewing published methods for approximating different TEB regimes. The assumptions made by previous authors will be outlined, and the con-

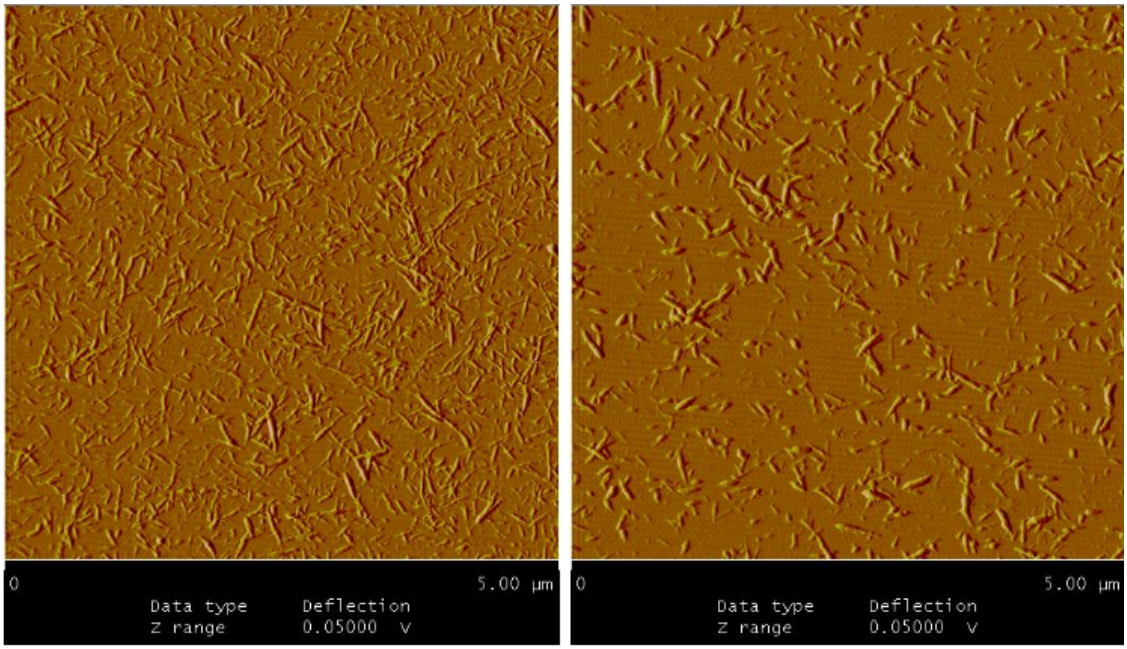

(a) Top phase (A) in Figure 4.1.3.6

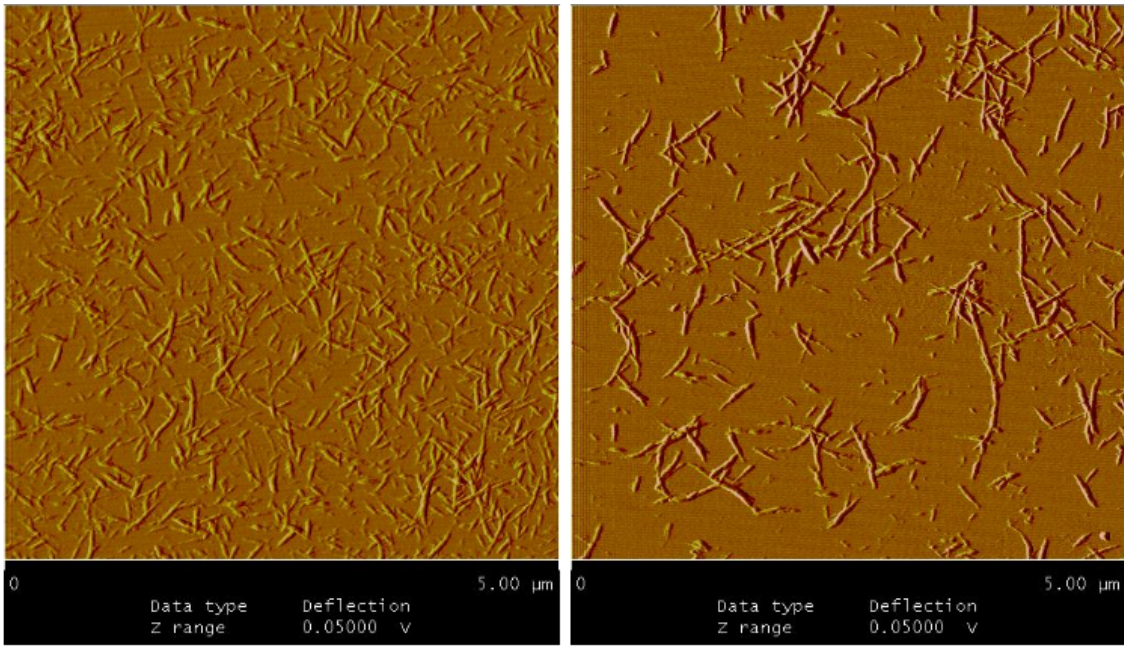

(b) Bottom phase (E) in Figure 4.1.3.6

Figure 4.1.3.8: AFM images of scaled-up LC separation. The images from left and right were taken at different locations on the same sample, illustrating the difficulty with imaging techniques. Inhomogeneous deposition upon sample evaporation, as well as arbitrary selection of imaging region, can lead to statistically non-representative sampling.

tribution of these assumptions to measurement error will be addressed. Sections 4.2.3 through 4.2.5 will provide a more rigorous and mathematically correct method, first by describing the wave equation of light and a method for describing the polarization state known as the polarization ellipse. The Stokes parameters will then be introduced, which are real measurable intensities used to fully characterize the polarization state. After describing a Mueller matrix method to determine how Stokes parameters are changed by an ideal optical component, the two common experimental setups for transient electric birefringence will be described. Section 4.2.6 will then illustrate how slight errors in optical alignment or stray birefringences can introduce significant errors in measured intensities. Mathematical models and experimental examples will be provided as illustration of these caveats. Hopefully by the end of this discussion the reader will appreciate the importance of proper optical alignment and mathematical models, and will have the tools to achieve this experimentally.

4.2.2 Malus's Law and the Myth of a Linear TEB Regime

The classic means to describe light intensity passing through two ideal linear polarizers in an optical path comes from Malus's Law, which states

$$I = I_0 \, cos^2\Theta_i, \tag{4.2.1}$$

where I is the intensity of light emerging from the second polarizer, I_0 is the initial intensity of light entering the first polarizer, and Θ_i is the angle between the linear polarization axes of the two. In the TEB regime, the polarizers are generally at crossed positions,

where $\Theta_x = \Theta_i + \frac{\pi}{2}$ and thus $cos^2(\Theta_i + \frac{\pi}{2}) = sin^2\Theta_x$. Malus's law is therefore rewritten

$$I = I_0 \, sin^2\Theta_x. \tag{4.2.2}$$

If a Kerr cell is inserted between two stationary crossed polarizers, the effect of the phase shift induced by the birefringent sample is to effectively change the angle Θ_x. Equation 4.2.2 can be rewritten in terms of the ellipticity ω of the light emerging from the sample as

$$I = I_0 sin^2\omega. \tag{4.2.3}$$

If a quarter wave plate is inserted between the cell and the analyzer, with it's fast axis perfectly aligned with the polarizer, this equation becomes

$$I = I_0 sin^2(\omega - \alpha), \tag{4.2.4}$$

where α is the offset angle of the analyzer from crossed position. Equations 4.2.2 and 4.2.4 will be derived explicitly in the following sections. For now, it will simply be stated that Equation 4.2.4 is the mathematically correct form of the model with a quarter wave plate precisely aligned with the polarizer and an analyser offset by some angle α. It is likewise described by the first term of Equation (3) in reference [12]. Clearly there is not a linear relation between ellipticity and light intensity in the most literal application of the model. Many attempts to linearize this equation have been made [12–14] using assumptions for negligibly small phase shifts and offset angles. Trusting these linearizations without an understanding of the uncertainty introduced by stray light and slight misalignment of optical components is a common mistake amongst TEB analysts. It therefore seems prudent to discuss linearization methods commonly used so that experimentalists can apply the appropriate equations to their own apparatus.

4.2.2.1 Linearizations for TEB optics

According to the method of Jennings [12], the total optical phase difference is defined as $P = \delta + p_s$, where δ is the phase shift due to the sample birefringence, and p_s is the total stray phase contribution arising from misalignment or strain birefringence of optical components. Equation 4.2.4 is written $I = I_0 sin^2(P/2)$, where ellipticity is equal to one-half the phase shift, $\omega = P/2$. If we let $I = I_{signal} + I_a$, where I_a is a constant background contribution, $I_a = a\ I_0$, then $I = I_0 sin^2(P/2) + a\ I_0$. If we express the $sin(P/2)$ term as a series expansion, then $sin(\frac{P}{2}) = \frac{P}{2} - \frac{(P/2)^3}{3!} + \frac{(P/2)^5}{5!} - \frac{(P/2)^7}{7!} + \cdots$. If P is small, we can neglect higher order terms and $I \approx I_0(P/2)^2 + a\ I_0$, which gives rise to the right hand side of Equation (3) in reference [12]. For perfect alignment and no stray birefringence p_s present, $P = \delta$ and $I \approx I_0(\frac{\delta}{2})^2 + a\ I_0$. Rearranging and defining $I_\delta = I - a\ I_a$ gives $I_\delta = I_0(\frac{\delta^2}{4})$, and solving for δ gives $\delta = 2(\frac{I_\delta}{I_0})^{1/2}$, which is Equation (4) in [12] describing the quadratic approximation of the detected response.

Now, if we consider stray birefringence p_s, once again $P = \delta + p_s$. Expanding the sine and again neglecting higher order terms gives $I \approx I_0(\frac{\delta}{2} + \frac{p_s}{2})^2 + a\ I_0$. Thus $\frac{I - a}{I_0} \approx \frac{1}{4}(\delta^2 + p_s^2 + 2\delta p_s) + const.$ In the absence of an electric field, the induced birefringence $\delta = 0$, and $I_{E=0} = \frac{I_0}{4} p_s^2 + const$, which represents a baseline intensity for a given optical arrangement. Since the p_s component is cumulative, arising from either deliberate or unintentional misalignment and/or strain birefringence in optical components, the condition typically results where $p_s \gg \delta^2$. Therefore measuring the change in light intensity from the baseline gives $\frac{\Delta I}{I_0} = \frac{1}{4}(\delta^2 + 2\delta p_s)$. If we assume negligible background intensity, dividing ΔI by the baseline gives

$$\frac{\Delta I}{I_{E=0}} = \left[(\delta^2 + 2\delta p_s)/p_s^2\right] \approx 2\frac{\delta}{p_s}, \tag{4.2.5}$$

which is the so called linear response. Since ΔI is now a function of δ rather than δ^2, the sign of the birefringence can be obtained using a quarter wave plate and a non-zero analyzer offset. Choosing the offset angle for the expected phase shift must be carefully considered if significant errors are to be avoided, however.

The mathematically complete expression follows from Equation 4.2.52, redefining total intensity S_0''' as $I(\alpha + \delta/2) = I_0 sin^2(\alpha - \delta/2)$. The baseline intensity for the same optical alignment in the absence of field induced birefringence is $I_{E=0} \equiv I(\alpha) = I_0 sin^2\alpha$. If we consider only the change in birefringence do to the phase shift, $\Delta I_\delta = I(\alpha - \delta/2) - I(\alpha)$, normalized by the baseline intensity $I(\alpha)$, we get

$$\frac{\Delta I_\delta}{I_\alpha} = \frac{sin^2(\alpha + \delta/2) - sin^2\alpha}{sin^2\alpha} = \frac{sin^2(\alpha + \delta/2)}{sin^2\alpha} - 1 \tag{4.2.6}$$

as reported in [12] and [15]. Jennings plots the error between the linearized model (Equation 4.2.5) and the mathematically complete description (Equation 4.2.6) as a function of analyser offset angle α for two different phase differences in Figure 3 of [12]. Since the phase difference changes over time in a given TEB pulse, this is not necessarily an experimentally helpful way to think about the issue. An alternate way to visualize this problem is shown in Figure 4.2.2.1, where the changing phase shift is plotted (horizontal axis) against the offset angle of the analyzer (vertical axis) for different error percents between the two models. By selecting an acceptable experimental error and a set offset angle, the range of experimental phase shifts which will give errors less than that desired can be extrapolated. However, for α near zero, a very small range of phase shifts will give significant errors, upwards of 50%. As such, the linearized model should not be used for small phase shifts and small offset angles if one is to obtain accurate diffusion coefficients. To avoid errors entirely, Equation 4.2.6 should be applied, and the diffusion coefficients deconvoluted from experimental data using the mathematically complete model.

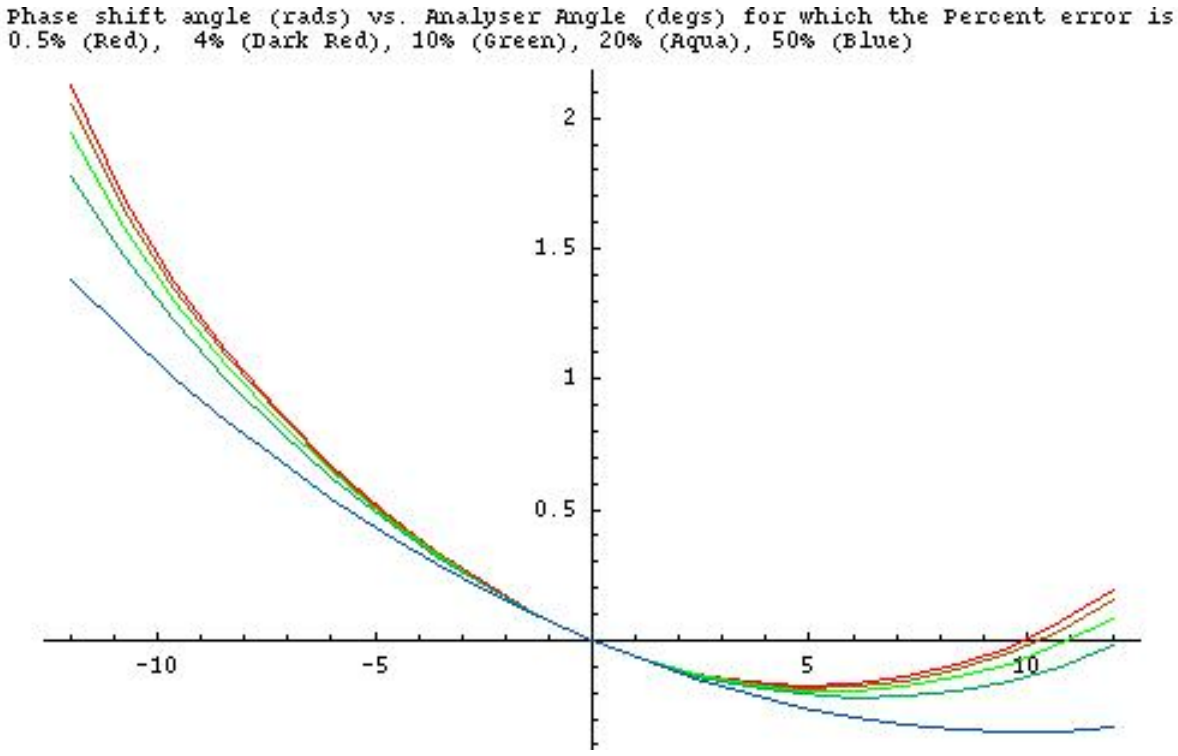

Figure 4.2.2.1: Error between Equation 4.2.5 and Equation 4.2.6. The linearized quarter wave model (Equation 4.2.5) and the mathematically complete model (Equation 4.2.6) diverge significantly for small phase shifts at small offset angles. The phase shift (δ) in radians is plotted on the vertical axis against the analyzer offset angle α in degrees (horizontal axis) for different errors between 0.5% (uppermost curve) to 50 % (lowest curve). At α near zero, a very small range of δ will give significant errors, indicating the danger of applying the linear model for a quarter wave plate at small α and small experimental phase shifts.

This section has avoided the full derivation of the mathematically complete model in order to illustrate the difficulties associated with the simplification often used in the TEB literature. The subsequent sections will derive the complete model from fundamental optical theory, starting with a description of light in the form of the wave equations.

4.2.3 Wave Equations

The wave equation, developed by Young in the early 19th century, combines the Newtonian mechanical wave equation with mechanical energy associated with wave amplitude. For a wave propagating in one dimension as a function of time t, it is given as

$$\frac{\delta^2 u(x,t)}{\delta x^2} = \frac{1}{\nu^2}\frac{\delta^2 u(x,t)}{\delta t^2} \,, \tag{4.2.7}$$

where the velocity of propagation ν is proportional to the ratio of tension to density in a mechanically equivalent string undergoing wave motion, and the oscillation or optical disturbance $u(x,t)$ is related to displacement from a straight line connecting the ends of the string. If we take the Fourier transform of the one dimensional formula, defined in the time domain, we can rewrite (4.2.7) in terms of angular frequency ω as

$$\frac{\delta^2 \mathbf{u}(x,t)}{\delta x^2} = \frac{-\omega^2 \mathbf{u}(x,t)}{\nu^2} \,. \tag{4.2.8}$$

This is the equation of a harmonic oscillator, the solution to which is

$$\mathbf{u}(x,\omega) = A\omega e^{ikx} + B\omega^{-ikx} \,. \tag{4.2.9}$$

The sinusoidal solution, using the trigonometric identity $e^{\pm ix} = cox(x) \pm i\ sin(x)$, is

$$\mathbf{u}(x,\omega) = A\ sin(\omega t + kx) + B\ sin(\omega t - kx) \,, \tag{4.2.10}$$

where $k = \omega/\nu$. Incorporating Maxwell's theory for the electromagnetic nature of light, we can divide the electric field vector into two orthogonal components in the $x-y$ plane. Assuming the direction of propagation, z is normal to the $x-y$ plane, the two orthogonal

components are

$$E_x(z,t) = E_{0x}cos(\omega t + kz + \delta_x) \tag{4.2.11a}$$

and

$$E_y(z,t) = E_{0y}cos(\omega t + kz + \delta_y)\ , \tag{4.2.11b}$$

where E_{0x} and E_{0y} are the maximum amplitudes and δ_x and δ_y are the absolute phases of each component.

4.2.4 The Polarization Ellipse

The amplitudes of each component in Equation (4.2.11) and the phase shift between them give rise to the state of polarization. The polarization is said to be instantaneous in that, at optical frequencies, the time for a wave to undergo one cycle is around 10^{-15} seconds. The polarization ellipse can be derived by revisiting Equation (4.2.11)

$$E_x(z,t) = E_{0x}cos(\tau + \delta_x) \tag{4.2.12a}$$

$$E_y(z,t) = E_{0y}cos(\tau + \delta_y), \tag{4.2.12b}$$

where $\tau = \omega t + kz$ is referred to as the propagator. These can be rewritten

$$\frac{E_x}{E_{0x}} = cos\ \tau\ cos\ \delta_x - sin\ \tau\ sin\ \delta_x \tag{4.2.13a}$$

$$\frac{E_y}{E_{0y}} = cos\ \tau\ cos\ \delta_y - sin\ \tau\ sin\ \delta_y\ . \tag{4.2.13b}$$

Therefore

$$\frac{E_x}{E_{0x}} sin\ \delta_y - \frac{E_y}{E_{0y}} sin\ \delta_x = cos\ \tau\ sin(\delta_y - \delta_{xy}) \tag{4.2.14a}$$

$$\frac{E_x}{E_{0x}} cos\ \delta_y - \frac{E_y}{E_{0y}} cos\ \delta_x = sin\ \tau\ sin(\delta_y - \delta_x)\ . \tag{4.2.14b}$$

Squaring and adding Equations (4.2.14) eliminates the propagator and gives the resultant vector as $E_x(z,t)$ and $E_y(z,t)$ propagate

$$\frac{E_x^2}{E_{0x}^2} + \frac{E_y^2}{E_{0y}} - 2\frac{E_x}{E_{0x}}\frac{E_y}{E_{0y}} cos\ \delta = sin^2\delta\ , \tag{4.2.15}$$

where $\delta = (\delta_y - \delta_x)$. Recognizing this as the general equation of an ellipse, a convenient means to describe the polarization state arises, as shown in Figure 4.2.4.1. In general, the axes of the polarization ellipse will not be parallel to the x and y orthogonal wave components. As such, a rectangle parallel to the x and y axes is constructed such that the sides are tangent to the polarization ellipse. The length of each sided of this rectangle provides the magnitude of E_{0x} and E_{0y}. This rectangle is used to define an auxiliary angle α such that

$$tan\ \alpha = \frac{E_{0x}}{E_{0y}}, \tag{4.2.16}$$

for α for $0 \leq \alpha \leq \frac{\pi}{2}$. The polarization orientation is given by the angle θ between the horizontal or x-axis and the major axis of the ellipse. The sides of a second rectangle in which the ellipse is circumscribed allows us to define the polarization angle as

$$tan\ 2\theta = \frac{2E_{0x}E_{0y}}{E_{0x}^2 - E_{0y}^2}\ . \tag{4.2.17}$$

The ellipticity (also called the eccentricity) describes the "fatness" of the ellipse, and is defined by an angle ω (with $-\frac{\pi}{4} \leq \omega \leq \frac{\pi}{4}$) such that $tan\ \omega = \pm\frac{B}{A}$, where $2A$ and

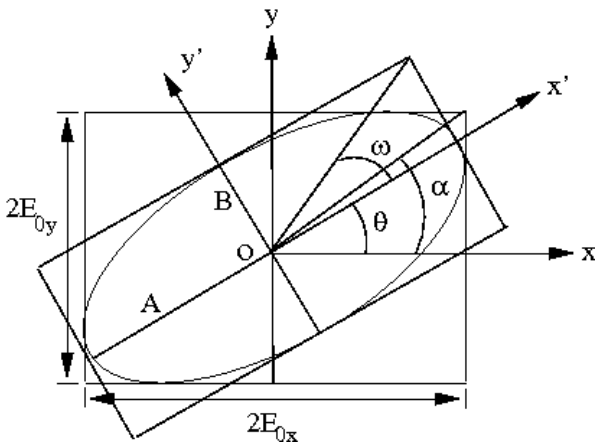

Figure 4.2.4.1: The polarization ellipse. Major and minor axes $2A$ and $2B$ are rotated an angle θ with respect to the $x - y$ coordinate system.

$2B$ are the major and minor axes of the ellipse, respectively. The extrema are therefore described by $B = 0$, and thus $\omega = 0$ for linear polarization, and $B = A$, $\omega = \pm\frac{\pi}{4}$ for circularly polarized light. From the definition of the auxiliary angle in Equation (4.2.16) we can obtain the useful relation

$$sin\ 2\omega = (sin\ 2\alpha)\ sin\ \delta \tag{4.2.18}$$

to relate ellipticity to amplitudes and phase shifts of the components. While this is the most general description of elliptical polarization, it can be simplified by setting up experimental parameters such that $\alpha = \theta = 45$, in which case a direct comparison between ellipticity and phase shift can be made such that

$$sin\ 2\omega = sin\ \delta. \tag{4.2.19}$$

4.2.5 Experimental Measurements

4.2.5.1 Stokes Parameters

One can imagine the polarization ellipse being traced out by the electric field vector of light in a plane transverse to the direction of propagation. However, as the time scale of a single trace is on the order of 10^{-15} seconds, it would be impossible to experimentally measure the polarization ellipse. Additionally, the polarization ellipse can only describe light that is completely polarized. Since real light consists of many simple waves in rapid succession, it is often partially or unpolarized. It is impossible to measure the absolute phase or amplitude of a simple wave, so we instead refer to superpositions of simple waves of independent phases in terms of four Stokes parameters. These parameters arise from mathematical manipulation of the two orthogonal wave Equations 4.2.15, to give

$$(E_{0x}^2 + E_{0y}^2)^2 - (E_{0x}^2 - E_{0y}^2)^2 - (2E_{0x}E_{0y}cos\ \delta)^2 = (2E_{0x}E_{0y}sin\ \delta)^2\ . \tag{4.2.20}$$

We equate the quantities inside the parentheses to the four Stokes parameters for a plane wave and define the four Stokes parameters as

$$S_0 \equiv I_0 + I_{90} = E_{0x}^2 + E_{0y}^2 \tag{4.2.21a}$$

$$S_1 \equiv I_0 - I_{90} = E_{0x}^2 - E_{0y}^2 \tag{4.2.21b}$$

$$S_2 \equiv I_{+45} - I_{-45} = 2E_{0x}E_{0y}\ cos\ \delta \tag{4.2.21c}$$

$$S_3 \equiv I_{rcp} - I_{lcp} = 2E_{0x}E_{0y}\ sin\ \delta\ . \tag{4.2.21d}$$

These can be interpreted where S_0 is the total intensity, S_1 describes the difference in intensities between linear horizontal and linear vertical polarizations, S_2 the difference

between linear $+45^\circ$ and -45° polarizations, and S_3 the difference between right and left circular polarized light. The significance of Stokes parameters is that they are real, measurable intensities, which are derived from the time averaged square of the unobservable parameters E_{0x}, E_{0y} and the phase shift δ.

The four Stokes parameters hold the relation

$$S_0^2 \geq S_1^2 + S_2^2 + S_3^2 \tag{4.2.22}$$

Since S_0 is the total intensity of light, the equality holds only if light is fully polarized. In the case $S_1 = S_2 = S_3 = 0$, the light is natural, or unpolarized. The degree of polarization P for any polarization state is defined as

$$P = \frac{I_{pol}}{I_{tot}} = \frac{(S_1^2 + S_2^2 + S_3^2)^{1/2}}{S_0^2} \tag{4.2.23}$$

for $0 \leq P \leq 1$, with 1 corresponding to fully polarized, and 0 to natural or unpolarized light.

The Stokes intensities for an optical beam are measured from the time averaged polarization ellipse, but the time averaging can be formally bypassed by representing the real optical amplitudes in Equation (4.2.11) in terms of complex amplitudes

$$E_x(t) = E_{0x} exp[i(\omega t + \delta_x)] = E_x exp[i\omega t] \tag{4.2.24a}$$

$$E_y(t) = E_{0y} exp[i(\omega t + \delta_y)] = E_y exp[i\omega t]\,, \tag{4.2.24b}$$

where

$$E_x = E_{0x}\, exp(i\delta_y) \tag{4.2.24c}$$

and

$$E_y = E_{0y}\, exp(i\delta_y)\ . \tag{4.2.24d}$$

The stokes parameters now become

$$S_0 = E_x E_x^* + E_y E_y^* \tag{4.2.25a}$$

$$S_1 = E_x E_x^* - E_y E_y^* \tag{4.2.25b}$$

$$S_2 = E_x E_y^* + E_x E_y^* \tag{4.2.25c}$$

$$S_4 = i(E_x E_y^* - E_x E_y^*) \tag{4.2.25d}$$

where * indicate the complex conjugate of Equations (4.2.24c) and (4.2.24d). Substituting Equations (4.2.24c) and (4.2.24d) into Equations (4.2.25) results in the forms show in Equation (4.2.21).

4.2.5.2 Stokes Vector

The mathematical means to represent the Stokes parameters for an incident beam is a column vector, called the Stokes vector

$$\mathbf{S} = \begin{pmatrix} S_0 \\ S_1 \\ S_2 \\ S_3 \end{pmatrix} \tag{4.2.26}$$

or, by incorporating Equation 4.2.21

$$\mathbf{S} = \begin{pmatrix} E_{0x}^2 + E_{0y}^2 \\ E_{0x}^2 - E_{0y}^2 \\ 2E_{0x}E_{0y}\, cos\, \delta \\ 2E_{0x}E_{0y}\, sin\, \delta \end{pmatrix} . \tag{4.2.27}$$

Thus, for example, the Stokes vector for linear horizontally polarized light, with$E_{0x} = 1$ and $E_{0y} = 0$, would be

$$\mathbf{S} = I_{Tot} \begin{pmatrix} 1 \\ 1 \\ 0 \\ 0 \end{pmatrix} , \tag{4.2.28}$$

where $I_{Tot} = E_{0x}^2$ is the total intensity.

Considering the more general case of linear polarization at some angle θ from the x axis, start by demonstrating that for any linear polarization, the phase difference in Equation (4.2.27) is equal to zero. Hence, for all forms of linear polarization at any

orientation, it can immediately be written $S_3 = 0$. The relative intensities of the x and y components for the beam, as well as the -45 and +45 degree components are found by projecting the light vector onto these axes such that $E_{0x} = cos\alpha$, $E_{0y} = sin\alpha$, $E_{0,+45} = cos(45-\alpha)$, and $E_{0,-45} = sin(45-\alpha)$ as shown in Figure 4.2.5.1. The normalized Stokes vector for linearly polarized light at any angle θ from the x-axis (using the identities $cos^2x - sin^2x = cos\ 2x$ and $2\ sin\ x\ cos\ x = sin\ 2x$) is thus

$$\mathbf{S} = I_{Tot} \begin{pmatrix} 1 \\ cos\ 2\alpha \\ sin\ 2\alpha \\ 0 \end{pmatrix} . \tag{4.2.29}$$

In this case, $I_{Tot} = E_0^2$, which is defined in terms of the auxiliary angle α (Figure 4.2.5.1) from the x-axis such that

$$E_{0x} = E_0\ sin\ \alpha \tag{4.2.30a}$$

$$E_{0y} = E_0\ cos\ \alpha \tag{4.2.30b}$$

for $0 < \alpha < \frac{\pi}{2}$. Again, when $\alpha = \theta = \frac{\pi}{4}$, a simplification and direct comparison between ellipticity and phase shift δ can be made.

In the most general case of elliptical polarization, with ellipticity ω and orientation θ, the Stokes vector is

$$\mathbf{S} = I_{Tot} \begin{pmatrix} 1 \\ cos(2\omega)\ cos(2\theta) \\ cos(2\omega)\ sin(2\theta) \\ sin(2\omega) \end{pmatrix} , \tag{4.2.31}$$

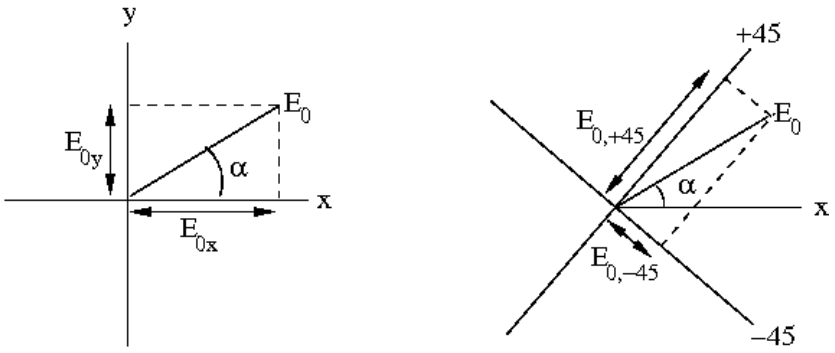

Figure 4.2.5.1: The Stokes intensities of linear polarized light. The polarization angle θ from the x-axis is determined by projecting the light vector onto x, y, +45 and -45 axes such that $E_{0x} = cos\alpha$, $E_{0y} = sin\alpha$, $E_{0,+45} = cos(45 - \alpha)$, and $E_{0,-45} = sin(45 - \alpha)$.

where $I_{Tot} = E_{0x}^2 + E_{0y}^2$. This can also be written

$$\mathbf{S} = I_0 \begin{pmatrix} 1 \\ cos(2\alpha) \\ sin(2\alpha)\, cos(\delta) \\ sin(2\alpha)\, sin(\delta) \end{pmatrix}, \tag{4.2.32}$$

where $I_0 = E_0^2 = E_{0x}^2 + E_{0y}^2$. In the simplifying case where $\alpha = \theta = 45$, and from $sin\ 2\omega = sin\ \delta$ (Equation (4.2.19)), these equations become

$$\mathbf{S} = I_0 \begin{pmatrix} 1 \\ 0 \\ cos(\delta) \\ sin(\delta) \end{pmatrix} = I_0 \begin{pmatrix} 1 \\ 0 \\ cos(2\omega) \\ sin(2\omega) \end{pmatrix}. \tag{4.2.33}$$

In an experimental setting, the principle of optical equivalence states that it is impossible by any measurement technique or instrument to distinguish between incoherent sums of simple waves which together may form a beam with the same Stokes parameters.

Experimental conditions are therefore set up in which only the desired parameters can be measured. By using linear polarizers, all polarizations of light except for that parallel to the axis of the polarizer can be excluded. In conjunction with an intensity detector, only the component of light polarized in a specific direction is then measured. The use of compensators allows the experimenter to induce a specific phase shift between the two components of light, and in conjunction with linear polarizers, determine the orientation of the polarization and the relative phases. In order to interpret how the Stokes vector of incident light is affected by an optical element, Mueller matrices will now be introduced.

4.2.5.3 Mueller Matrices

A mathematical means to interpret the Stokes parameters for an incident beam of light passing through an optical component, such as a polarizer, is the Mueller matrix method. To understand how optical elements interact with polarized light in order to change its state, assume that the light incident on the element has Stokes parameters S_i, where $i = 0, 1, 2, 3$. The beam emerges with new states $S_i^{'}$, (again $i = 0, 1, 2, 3$) which can be expressed in terms of four linear combinations

$$S_0^{'} = m_{00}S_0 + m_{01}S_1 + m_{02}S_2 + m_{03}S_3 \tag{4.2.34a}$$

$$S_1^{'} = m_{10}S_0 + m_{11}S_1 + m_{12}S_2 + m_{13}S_3 \tag{4.2.34b}$$

$$S_2^{'} = m_{20}S_0 + m_{21}S_1 + m_{22}S_2 + m_{23}S_3 \tag{4.2.34c}$$

$$S_3^{'} = m_{30}S_0 + m_{31}S_1 + m_{32}S_2 + m_{33}S_3\ . \tag{4.2.34d}$$

This is shown in matix form

$$\begin{pmatrix} S_0' \\ S_1' \\ S_2' \\ S_3' \end{pmatrix} = \begin{pmatrix} m_{00} & m_{01} & m_{02} & m_{03} \\ m_{10} & m_{11} & m_{12} & m_{13} \\ m_{20} & m_{21} & m_{22} & m_{23} \\ m_{30} & m_{31} & m_{32} & m_{33} \end{pmatrix} \begin{pmatrix} S_0 \\ S_1 \\ S_2 \\ S_3 \end{pmatrix} , \tag{4.2.35}$$

which is more concisely stated

$$\mathbf{S}' = \mathbf{B} \cdot \mathbf{S} . \tag{4.2.36}$$

The matrix, **B**, describing the operation performed by the compensator is known as the Mueller matrix. If the transverse elements of the plane wave depicted in Equation (4.2.11) interact with matter, the polarization state is almost inevitably altered by the changing of amplitudes E_{0x} and E_{0y}, phase δ_x or δ_y, direction of orthogonal field components $E_x(z,t)$ or $E_y(z,t)$, or by transferring energy from polarized to unpolarized field components. If successive optical elements are encountered along an optical path, the total transformation of the stokes vector for the incident light can be calculated using a single Mueller matrix train encompassing all encountered components according to

$$\mathbf{M}_T = \prod_{i=1}^{n} \mathbf{M}_i . \tag{4.2.37}$$

The train is calculated by starting with the first element encountered, then left-multiplying successively until all transforming elements have been accounted for.

It is beyond the scope of this paper to derive the components of the Mueller matrix. Full derivations for various optical components can be found in texts on polarized light. For the sake of brevity, the Mueller matrices for linear polarizers and quarter wave retarders are necessary for understanding the transient electric birefringence experiment.

The general Mueller Matrix for an ideal linear polarizer at an angle χ with respect to

the horizontal (x) axis is

$$\frac{1}{2}\begin{pmatrix} 1 & cos(2\chi) & sin(2\chi) & 0 \\ cos(2\chi) & cos^2(2\chi) & cos(2\chi)sin(2\chi) & 0 \\ sin(2\chi) & cos(2\chi)sin(2\chi) & sin^2(2\chi) & 0 \\ 0 & 0 & 0 & 0 \end{pmatrix}. \tag{4.2.38}$$

The general Mueller Matrix for a compensator at an azimuthal angle ψ with respect to the x-axis with a phase retardance ϕ is

$$\begin{pmatrix} 1 & 0 & 0 & 0 \\ 0 & cos^2(2\psi) + sin^2(2\psi)cos\phi & sin(2\psi)cos(2\psi)(1 - cos\phi) & -sin(2\psi)sin\phi \\ 0 & sin(2\psi)cos(2\psi)(1 - cos\phi) & sin^2(2\psi) + cos^2(2\psi)cos\phi & cos(2\psi)sin\phi \\ 0 & sin(2\psi)sin\phi & -cos(2\psi)sin\phi & cos\phi \end{pmatrix}. \tag{4.2.39}$$

4.2.5.4 TEB Setup Without a Quarter Wave Plate

A coherent monochromatic light source is used as the source, in this case a linearly polarized HeNe laser. The source is aligned with and first passed through a linear Glan-Thompson polarizer, hitherto called the polarizer, aligned with its transmission axis at 45 degrees with respect to the laboratory horizontal axis. An electro-optic cell follows, which is comprised of two planer parallel electrodes oriented along the laboratory vertical axis. The beam passes between these electrodes and though a second linear polarizer, called the analyzer, with its transmission axis at -45 degrees to the lab vertical axis. When the electric field is turned on, the birefringence induced in the cell causes the linearly polarized light entering the cell to exit as elliptically polarized due to a phase lag δ between

the orthogonal components of the electric field of the incident light. The Stokes vector for the light emerging from the cell, using Equation (4.2.31) for $\theta = 45$ is

$$\mathbf{S} = I_0 \begin{pmatrix} 1 \\ 0 \\ cos(2\omega) \\ sin(2\omega) \end{pmatrix}, \tag{4.2.40}$$

where ω is the ellipticity of the polarization ellipse defined via the major and minor axes A and B by $tan\ \omega = \frac{B}{A}$. The assumption that $\theta = 45$ arises from the fact that only in the case of a dichroic media is the polarization ellipse rotated from the incident beam orientation. Since the orthogonal absorption coefficients for optical light are generally the same for aqueous suspensions, this is not the case.

The beam now passes though the linearly polarizing analyzer, which from Equation (4.2.38) has the Mueller matrix at $\chi = -45$ degrees

$$\frac{1}{2} \begin{pmatrix} 1 & 0 & -1 & 0 \\ 0 & 0 & 0 & 0 \\ -1 & 0 & 1 & 0 \\ 0 & 0 & 0 & 0 \end{pmatrix}. \tag{4.2.41}$$

The light emerging from the analyzer is therefore described by the Stokes vector

$$\mathbf{S}' = \frac{I_0}{2} \begin{pmatrix} 1 & 0 & -1 & 0 \\ 0 & 0 & 0 & 0 \\ -1 & 0 & 1 & 0 \\ 0 & 0 & 0 & 0 \end{pmatrix} \begin{pmatrix} 1 \\ 0 \\ cos(2\omega) \\ sin(2\omega) \end{pmatrix} = \frac{I_0}{2} \begin{pmatrix} 1 - cos(2\omega) \\ 0 \\ -1 + cos(2\omega) \\ 0 \end{pmatrix} \tag{4.2.42}$$

Since the experiment measures the total intensity of light passing through the analyzer, which is given by the first Stokes parameter in Equation (4.2.42), the only term of interest is

$$S_0^{'} = \frac{I_0}{2}\left(1 - cos(2\omega)\right). \tag{4.2.43}$$

From the trigonometric identity $2\,sin^2 A = 1 - cos(2A)$, the classic Malus' Law relationship is obtained, where

$$S_0^{'} = I_0\, sin^2\omega = I_0\, sin^2\left(\frac{\delta}{2}\right). \tag{4.2.44}$$

Here the ellipticity ω replaces Θ_x in Equation 4.2.2 and $\omega = \frac{\delta}{2}$ for $\alpha = \theta = \frac{\pi}{4}$ from equation 4.2.19.

For $0 \leq \omega \leq \frac{\pi}{2}$, an increasing intensity of light results as ellipticity increases. For the case of $\omega = \frac{\pi}{2}$, the light is linearly polarized at an orientation angle $\theta = -\frac{\pi}{4}$, and thus a maximum transmittance through the analyzer occurs. For $\frac{\pi}{2} \leq \omega \leq \pi$, the intensity decreases again, demonstrating an optical over-rotation case.

If the analyzer is not perfectly crossed with the polarizer (that is $\chi \neq -\frac{\pi}{4}$), the general form for a linear polarizer in Equation 4.2.38 is used, and the resulting intensity is

$$S_0^{'} = \frac{I_0}{2}\left(1 - cos(2\omega)\, sin(2\chi)\right). \tag{4.2.45}$$

The result for misalignment from crossed position by ± 10 and ± 20 degrees is demonstrated in Figure 4.2.5.2. The overall intensity decreases in magnitude, but has the same phase as for the aligned case. Since the intensity does not follow the phase shift linearly in all cases, care must be taken to apply a cosine squared function to the model in order to extract the experimental phase shift. The experimental results under an aligning AC pulse for a suspension of cellulose nanocrystals is shown in Figure 4.2.5.3. Note that the

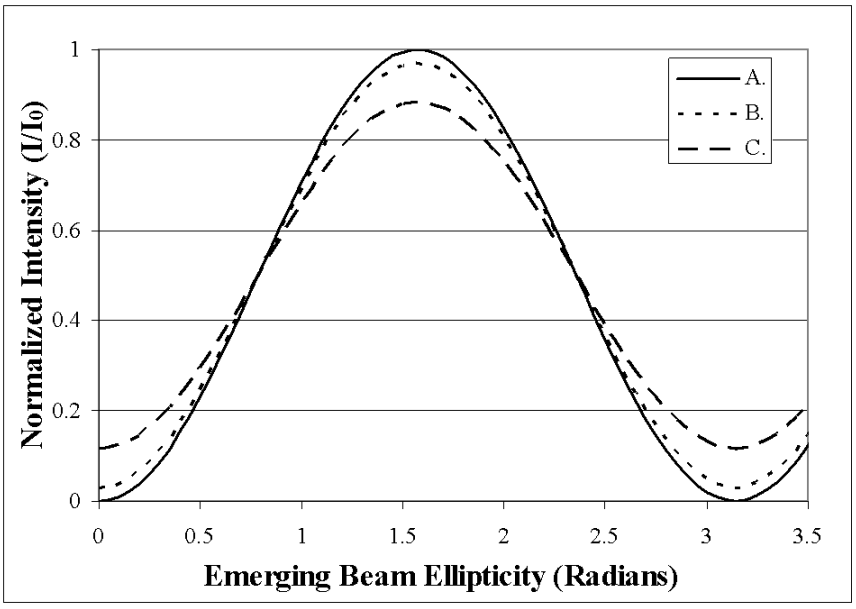

Figure 4.2.5.2: Model of Equation (4.2.42). Intensity of transmitted light for polarizer and no quarter wave plate, with analyzer offset from crossed position by A.) 0 degrees; B.) ± 10 degrees, and C.) ± 20 degrees as a function of increasing ellipticity.

peak-to-peak intensity begins to decrease at an offset angle $>\mid \pm 2 \mid$ degrees. This could indicate the start of an over-rotation regime, or could be due to optical misalignment of the beam as the physical component of the analyzer is rotated. To determine this, the plots would need to be normalized using a careful characterization of a full 0 to 90 degree rotation of the analyzer. This requires accurate neutral density filters, which were not available at the time of this experiment.

4.2.5.5 TEB Setup With a Quarter Wave Plate

In a second experimental setup, a quarter wave retarder may be inserted between the cell and analyzer with its fast axis aligned parallel to the polarizer transmission axis. In this setup, the elliptical light emerging from the cell is transformed by the Mueller matrix for

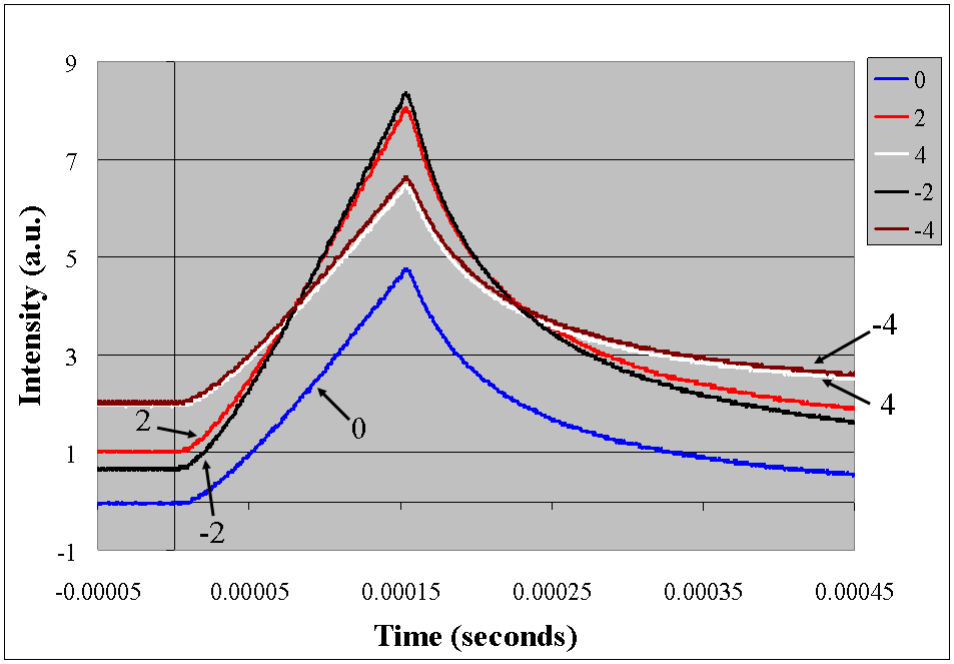

Figure 4.2.5.3: Experimental data in the absence of a quarter wave plate. The sample is cellulose nanocrystals under a 100 kHz AC pulse. The intensity of transmitted light is shown with an analyzer offset from crossed position by $-4 < \alpha < +4$ as a function of time.

a compensator with $\phi = \frac{\pi}{2}$ and $\psi = 45$. From Equation (4.2.39), this is calculated as

$$\begin{pmatrix} 1 & 0 & 0 & 0 \\ 0 & 0 & 0 & -1 \\ 0 & 0 & 1 & 0 \\ 0 & 1 & 0 & 0 \end{pmatrix}. \tag{4.2.46}$$

The Stokes vector for the beam emerging from the quarter wave plate is thus

$$\mathbf{S}' = I_0 \begin{pmatrix} 1 & 0 & 0 & 0 \\ 0 & 0 & 0 & -1 \\ 0 & 0 & 1 & 0 \\ 0 & 1 & 0 & 0 \end{pmatrix} \begin{pmatrix} 1 \\ 0 \\ cos(2\omega) \\ sin(2\omega) \end{pmatrix} = I_0 \begin{pmatrix} 1 \\ -sin(2\omega) \\ cos(2\omega) \\ 0 \end{pmatrix}. \tag{4.2.47}$$

From the parameter $S_3 = 0$, it is immediately determined that this is linearly polarized light. Passing this light through the analyzer at $\chi = -45$ degrees then gives

$$\mathbf{S}'' = \frac{I_0}{2} \begin{pmatrix} 1 & 0 & -1 & 0 \\ 0 & 0 & 0 & 0 \\ -1 & 0 & 1 & 0 \\ 0 & 0 & 0 & 0 \end{pmatrix} \begin{pmatrix} 1 \\ -sin(2\omega) \\ cos(2\omega) \\ 0 \end{pmatrix} = \frac{I_0}{2} \begin{pmatrix} 1 - cos(2\omega) \\ 0 \\ -1 + cos(2\omega) \\ 0 \end{pmatrix}, \tag{4.2.48}$$

which is the same seen in Equation (4.2.42). If we rotate the analyzer slightly from crossed position with the polarizer, say by an angle α, the applied Mueller matrix becomes

$$\frac{1}{2}\begin{pmatrix} 1 & cos2(\chi \pm \alpha) & sin2(\chi \pm \alpha) & 0 \\ cos2(\chi \pm \alpha) & cos^2 2(\chi \pm \alpha) & cos2(\chi \pm \alpha) sin2(\theta \pm \alpha) & 0 \\ sin2(\chi \pm \alpha) & cos2(\chi \pm \alpha) sin2(\chi \pm \alpha) & sin^2 2(\chi \pm \alpha) & 0 \\ 0 & 0 & 0 & 0 \end{pmatrix}. \tag{4.2.49}$$

The result is that the total intensity from S_0 is

$$S_0''' = \frac{I_0}{2}\left[1 - sin\ 2\omega\ cos\ 2(\chi \pm \alpha) + sin\ 2(\chi \pm \alpha)\ cos\ 2\omega\right]. \tag{4.2.50}$$

Using the trigonometric identity $sin(A - B) = sin\ A\ cos\ B - cos\ A\ sin\ B$ and defining $\chi = -\frac{\pi}{4}$ (recall the analyser is at crossed position with polarizer, plus some small offset α), this becomes

$$\begin{aligned} S_0''' &= \frac{I_0}{2}\left[1 - sin(2\alpha - \frac{\pi}{2} - 2\omega)\right] \\ &= \frac{I_0}{2}\left[1 - cos(2\alpha - 2\omega)\right] \\ &= \frac{I_0}{2}\left[1 - cos\ 2(\alpha - \omega)\right]. \end{aligned} \tag{4.2.51}$$

From the trigonometric identity $cos\ 2A = 1 - 2sin^2 A$ comes the form

$$S_0''' = I_0 sin^2(\alpha - \omega), \tag{4.2.52}$$

which was given at the beginning of this section as Equation 4.2.4. Thus when the quarter wave plate fast axis is perfectly aligned with the polarizer transmission axis, the result of a positive or negative analyzer offset is to shift the function as seen in Figure 4.2.5.4.

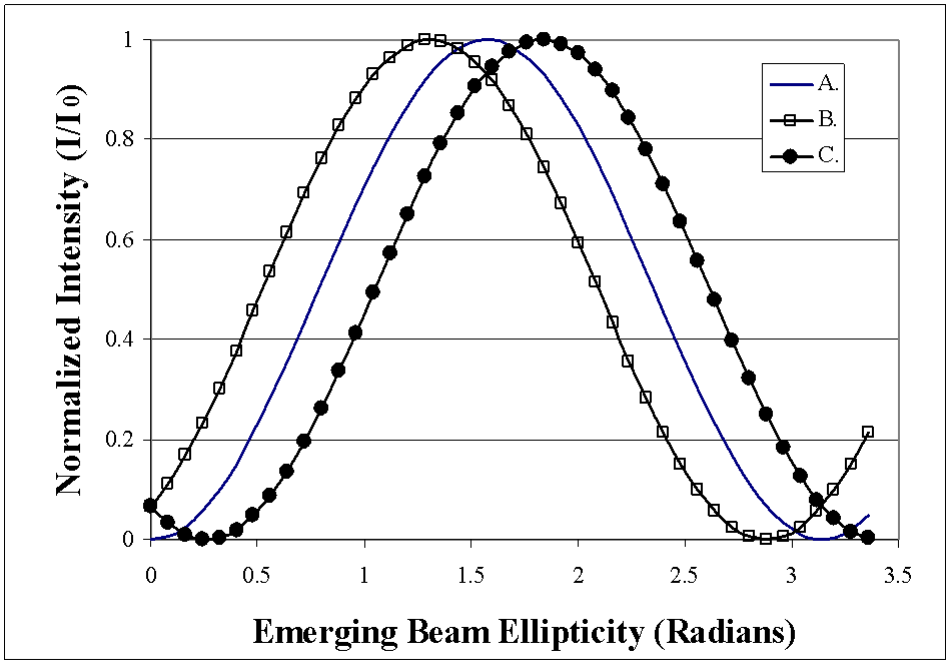

Figure 4.2.5.4: Model of Equation (4.2.50). Intensity of transmitted light for aligned polarizer and quarter wave plate, and analyzer offset from crossed position by A.) 0 degrees; B.) -15 degrees, and C.) +15 degrees as a function of increasing ellipticity.

This method is useful for increasing the sensitivity, considering that a positive offset will shift the curve backwards. This results in a greater intensity difference with increasing alignment at the beginning of the pulse. However, it is not strictly linear in a mathematical sense. A cosine squared function should still be used for deconvolution of data if an error free analysis of optical response is desired.

The models that follow an idealized Malus' Law do not necessarily represent the experimental reality of an exponentially increasing ellipticity with time as particles align. Figure 4.2.5.5 shows the same setup for experimental data as an analyzer is rotated from $-1 < \alpha < +4$. We can see that the asymmetry around the aligned position gives rise to the sign of the birefringence. The sensitivity increases at positive values of α, but as the total baseline intensity of light also increases, the signal to noise level at higher α values

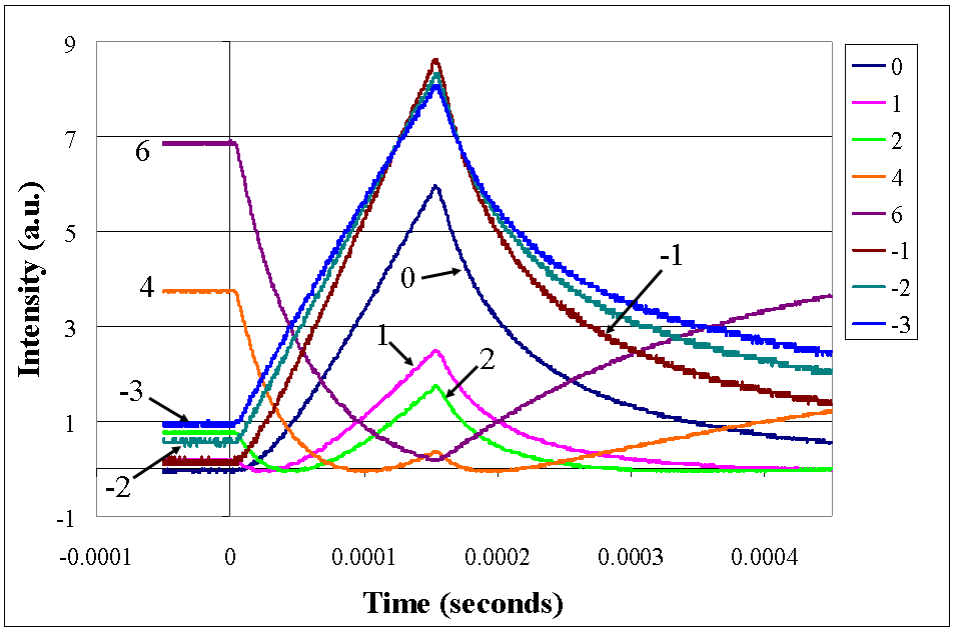

Figure 4.2.5.5: Experimental data for an aligned quarter wave plate. The intensity of transmitted light through cellulose nanocrystals under a 100 kHz AC pulse is shown for an analyzer offset from crossed position by $-3 < \alpha < +6$.

soon supersedes the benefits of this sensitivity. Generally, the optimal value of α must be determined experimentally for each setup.

For prefect alignment of the quarter wave plate and accurate offset angles of the analyser, there should be symmetry between negative and positive offset angles in Figure 4.2.5.5. This would result in the baseline signals overlapping. Careful examination of the 2 and -2 degree offset curves in Figure 4.2.5.5 shows this is not the case, which brings up the important issue of alignment errors under typical experimental conditions. The next section will describe some typical alignment errors encountered in TEB experiments.

4.2.6 Experimental Caveats

4.2.6.1 Misaligned Quarter Wave Plate

The model in Figure 4.2.5.4 shows the case for perfect alignment of the quarter wave fast axis with the polarizer. As seen from the experimental data in Figure 4.2.5.3, perfect offset angles are difficult to achieve. Symmetry of the signal at ± 2 and ± 4 degree offsets is expected, whereas deviations from this are observed arising from inaccurate settings. The experimental difficulty of comes from the minimum gradation unit marked on a rotary mount holding the anaylzer, which is typically 2 degrees. While the crossed position can be determined optically by finding the minimum intensity, the offset angle is set from this minimum using the marked gradations on the mount. As such, precise α settings are difficult to achieve in the lab setting without a full characterization of the intensity curve from minimum intensity to maximum intensity, in which case the polarizers are fully aligned. Few detectors can measure this range without reaching a saturation limit, so well characterized neutral density filters must be inserted into the optical path. This introduces errors due to internal reflection, light scattering, and optical inconsistencies in the filters.

Likewise, precise alignment of the quarter wave plate is difficult to achieve. The most accurate method for aligning it is to replace the stationary analyzer with a motorized rotating analyzer. As the analyzer revolves in time, the signal passed to the detector is sinusoidal, the peak-to-peak values of which can be monitored by an oscilloscope. (Rotation frequencies above 1 Hz will typically be fast enough for most oscilloscopes to trigger on.) The quarter wave plate can then be adjusted under these conditions to achieve a maximum peak-to-peak value, which corresponds to the closest alignment of the quarter wave plate fast axis with the linear polarization axis of the first polarizer. Again, neutral

density filters are required to measure the maximum intensity, and the accuracy of this technique is limited by the alignment of the ND filters as well. In addition, due to the thickness variations of the wave plate being on the order of a wavelength of the laser, slight tilts from perfect vertical position with respect to the laser can result in non-integer values of light wavelengths propagating through the plate. Therefore, precise alignment requires control of six degrees of freedom in the lab frame, as well as much practice and skill. As such, slight errors in quarter wave alignment will inevitably be present. In order to understand this, the most general description of S_0 for a quarter wave plate and analyzer at arbitrary angles ψ and χ respectively will be considered. From Equations (4.2.38) and (4.2.39) for elliptical polarized light at an orientation angle of $\theta = 45$, S_0 becomes

$$\begin{aligned} S_0 = 1 + cos\ 2\omega\ sin\ 2\psi\ cos\ 2\psi\ cos\chi\ + sin\ 2\omega\ sin\ 2\omega\ cos\ 2\chi \\ +cos\ 2\omega\ sin^2 2\psi\ sin\ 2\chi - sin\ 2\omega\ cos 2\psi\ sin\ 2\chi \end{aligned} \tag{4.2.53}$$

From this equation, Figure 4.2.6.1 shows the effect of a quarter wave compensator misaligned by up to 45 degrees with the analyzer at -45. In addition to a shift of the function, the peak-to-peak value decreases with increasing misalignment leading to errors in the measured birefringence. From the model, the significance of these errors may seem negligible in the case of realistic misalignment values ($< \pm 5$ degrees). However, the experimental results in Figure 4.2.6.2 show the effects of a ± 2 degree offset of the quarter wave plate with the analyzer cross-aligned with the polarizer. Small misalignments can become significant in the scale of experimental intensities.

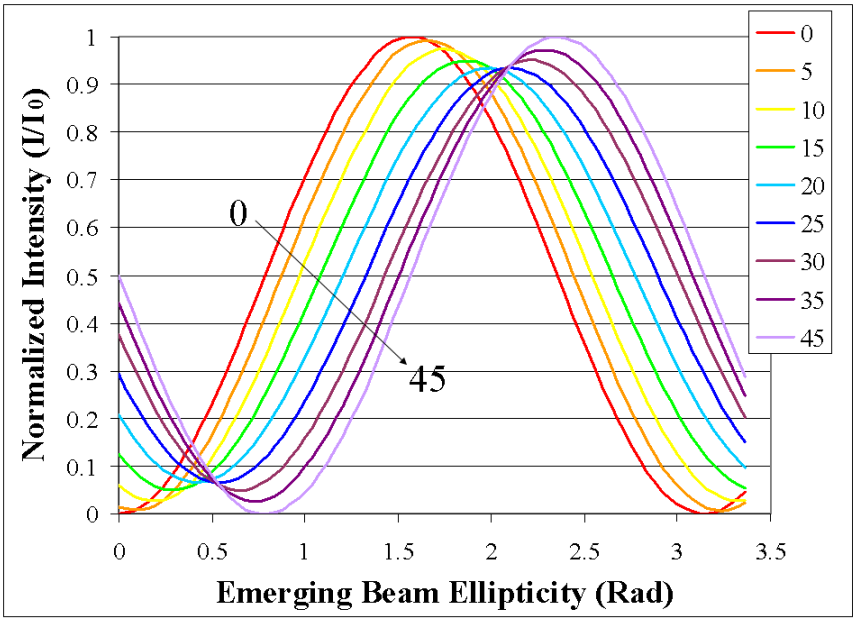

Figure 4.2.6.1: Model of quarter wave plate misaligned with polarizer. Misalignment of wave plate increases from 0 degrees (perfect alignment) to 45 degrees from left to right following the arrow. Analyzer is set at -45 degrees with respect to the lab horizontal axis for all cases (crossed with polarizer).

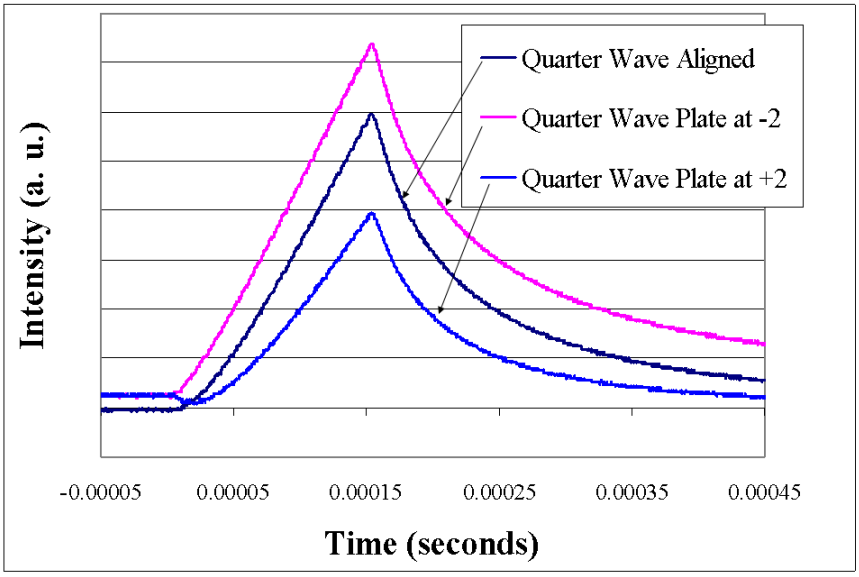

Figure 4.2.6.2: Experimental data for aligned analyzer and misaligned wave plate. Sample is cellulose nanocrystals under a 100 kHz AC pulse with analyzer set to -45 degrees (crossed with polarizer) and quarter wave plate misaligned by 0, $+2$ and -2 degrees.

4.2.6.2 Misaligned Quarter Wave with Offset Anaylzer

The most realistic experimental case arises when both the analyzer and quarter waveplate are offset by some unintentional, or in the case of the analyzer, intentional angle. Figure 4.2.6.3 shows modeled data for various cases of the quarter wave plate and analyzer offset by ± 10 degrees.

Figure 4.2.6.5 shows experimental data in the case of a quarter wave plate offset by to ± 1 degrees and an analyzer offset for variable angles. Experimentally, the model fits fairly well, with lower misalignment angles resulting in significant systematic errors. Slight discrepancies arise, such as the curves for quarter wave plate (Q) at 46 degrees and analyzer (A) at -44 degrees, and for Q at 44 and A at -46 degrees , which the model predicts to be identical (Figure 4.2.6.4). However, the case for symmetric and antisymmetric offset values for quarter wave plate and analyzer result in similar baselines and difference

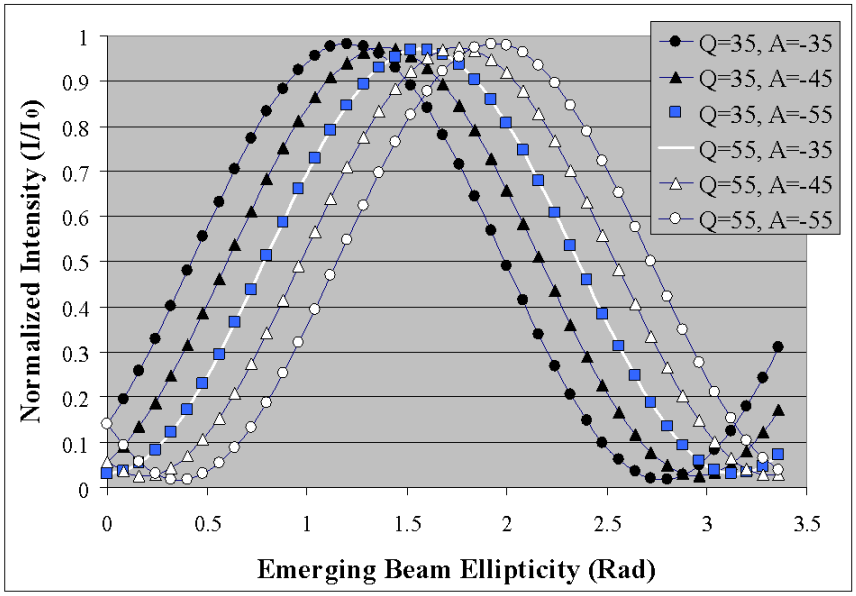

Figure 4.2.6.3: Model for both misaligned analyzer and quarter wave plate. Analyzer (A) and a quarter wave plate (Q) are misaligned by up to ± 10 degrees as a function of time.

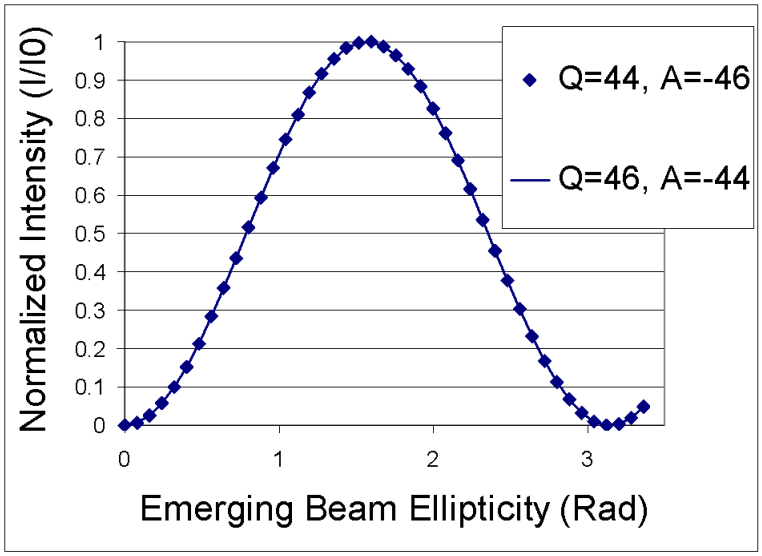

Figure 4.2.6.4: Model for symmetrically misaligned analyzer and wave plate. Analyzer (A) and quarter wave plate (Q) are aligned at Q=44, A=-46 and Q=46, A=-44 for the diamonds and solid line, respectively.

in initial sign of the birefringence, just as predicted by the model. The discrepancies in expected peak-to-peak intensities re-enforces the argument that accurate alignment of optics is both important, and difficult to achieve without appropriate alignment protocols. In this case, a rotating anaylzer was not available, and quarter wave plate alignment was estimated by adjusting both analyzer and quarter wave plate until a minimum intensity was observed. Here also, the sensitivity of the detector and the digitization resolution of the oscilloscope can become the limiters to accurate alignment.

4.2.6.3 Stray Birefringences in Optical Components

In addition to misalignment in the intended optical components, unintended sources of birefringence can be added to the setup in the form of mechanical or optical strain in glass plates. Rarely are fused silica or glass plates completely amorphous; birefringence can arise from glass flow alignment during cell fabrication. In addition, mechanical strain on plates can induce birefringence. Figure 4.2.6.6 shows the effects of increasing the strain on the face of a glass cuvette by increasing the tightness of a set screw holding the cell in place during a TEB experiment.

The maximum strain setting in Figure 4.2.6.6 (that is the highest mechanical strain that could be applied without risk of breaking the cell) is shown in Figure 4.2.6.7 for an analyzer offset from $-6 < \alpha < +6$ degrees. The induced strain appears to behave as a compensator with an arbitrary phase lag and orientation, which is why the initial decrease in birefringence does not disappear with negative or positive analyzer offset as it does with the aligned quarter wave plate in Figure 4.2.5.5.

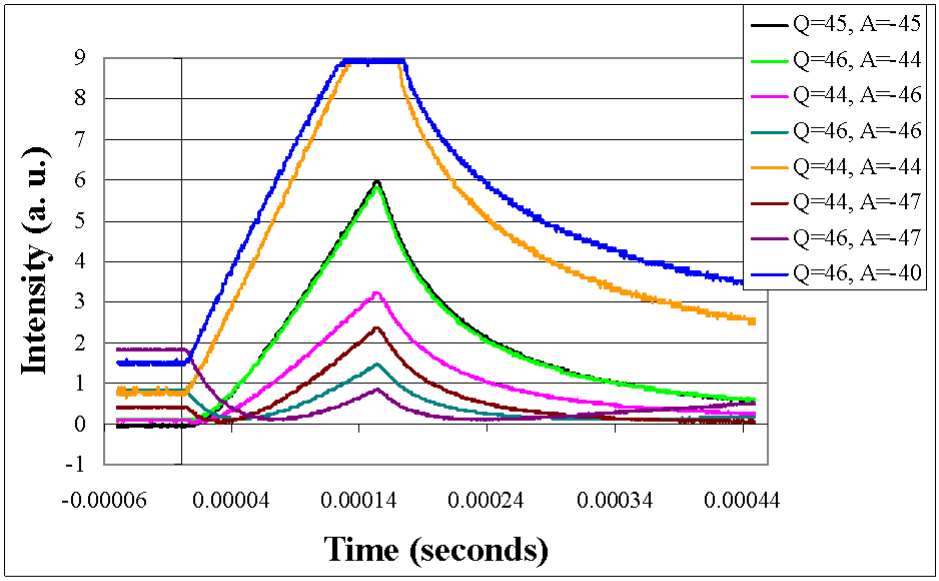

(a) Analyzer and Quarter Wave Plate Offset, Full Curves

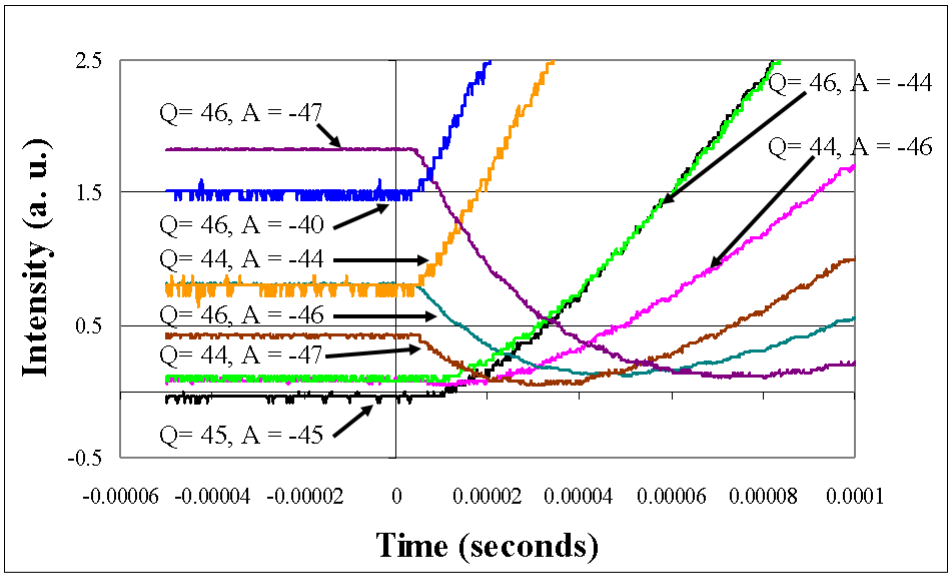

(b) Analyzer and Quarter Wave Plate Offset, Baseline Expanded

Figure 4.2.6.5: Experimental data for misaligned quarter wave plate and analyzer. Cellulose nanocrystals are aligned under a 100 kHz AC pulse. A quarter wave plate (Q) is misaligned from 45 degrees by ± 1 degree, and the analyzer (A) is misaligned from -45 degrees by -2 to $+5$ degrees. The right plot shows the baseline expanded to validate the symmetric (44/-44 and 46/-46) and antisymmetric (44/-46 and 46/-44) coincident baselines predicted by the model in Figures 4.2.6.3 and 4.2.6.4.

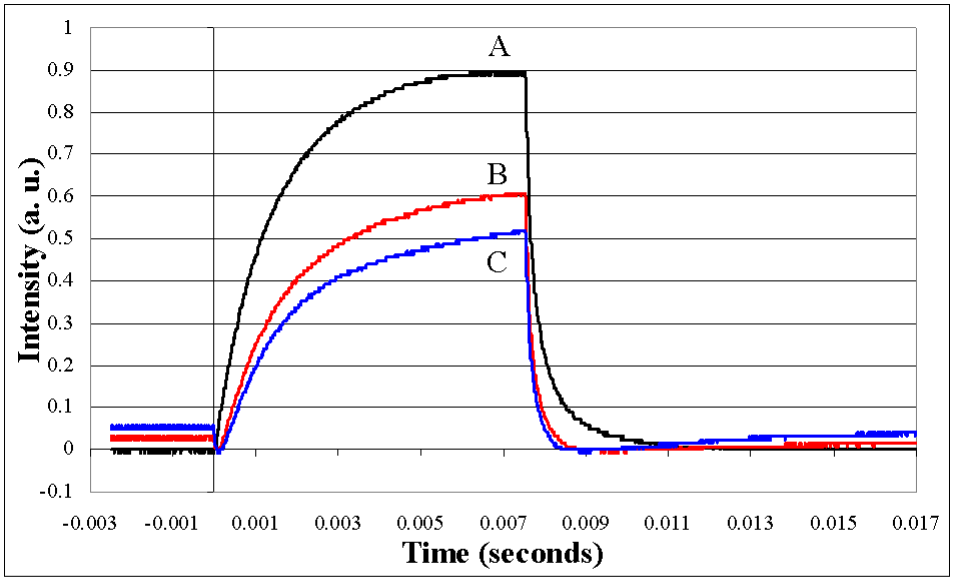

(a) TEB with cell strain birefringence

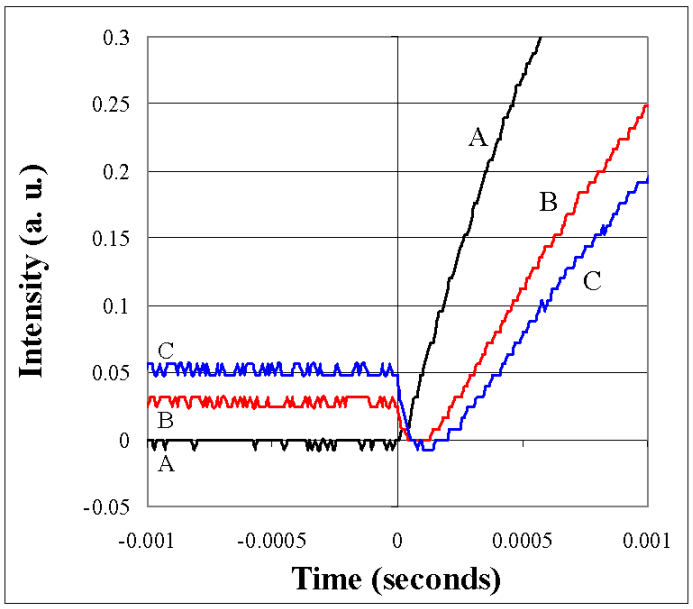

(b) Strain birefringence expanded around baseline

Figure 4.2.6.6: Experimental TEB with mechanically strained glass cuvette. Cellulose nanocrystals are aligned under a 100 kHz AC pulse without a quarter wave plate. Stray birefringence arises from mechanical strain on the cuvette, with strain increasing from minimal (curve A, top) to an experimental maximum (curve C, bottom). The initial dip upon application of electric field is shown expanded in the right plot.

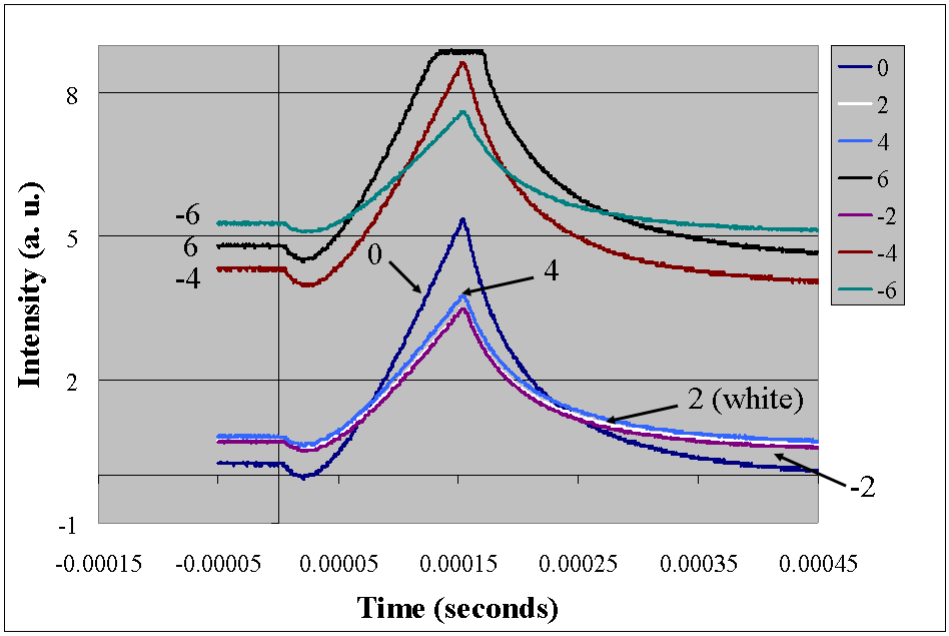

Figure 4.2.6.7: TEB with strain birefringence and offset analyzer. Data is from cellulose nanocrystals aligned under a 100 kHz AC pulse under a mechanically strained glass cuvette and no quarter wave plate. The intensity of transmitted light is shown for an analyzer offset from crossed position with the polarizer by $-6 < \alpha < +6$ degree.

4.3 Equipment and Electronic Devices

4.3.1 Optical Setup

The light source is a linearly polarized (minimum polarization ratio of 500:1) UniPhase HeNe laser, model 1107P (2 mW, $\lambda = 632.5$ nm) with a Gaussian ($1/e^2$) beam diameter of 0.48 mm. To optimize the intensity of the beam entering the cell, the laser is nominally aligned with and passed through a Glan Thompson polarizer, extinction coefficient 10^5, set with its polarization axis at 45 degrees with respect to the laboratory horizontal plane. A Kerr cell follows. The beam leaving the cell is passed through a second Glan polarizer set at crossed positions to the first polarizer (Figure 4.3.1.1). The beam intensity is measured by a 500 MHz bandwidth, sensitivity 0.57A/W photodiode, Hamamatsu - S5972, Newark part number 62M0263, and a low noise, high bandwidth amplifier circuit based on OPA127 op amps (see Figure 4.3.2.2 for circuit schematic). The detector was calculated to have a bandwidth of 1.0 MHz and was measured using a picosecond pulsed laser (built into the 2500 Optical Fiber Analysis System from Photon Kinetics) and a Tektronix DSA8200, 50 GHz digital oscilloscope to ensure the circuit was behaving as predicted. The circuit is powered at $\pm$10 V by an HP 6255A Dual DC power supply with a 200 μV rms, 1 mv peak-to-peak ripple/noise criteria.

4.3.2 TEB Kerr Cell Design

Kerr cells were built from quartz cuvettes with a path lengths of either 1 cm or 2 cm. Two stainless steel planar electrodes are set 1 mm apart by Teflon spacers, with the polarization of the incident beam at 45 degrees with respect to the applied field (parallel to the laboratory horizontal plane), propagating parallel to the electrodes (Figure 4.3.2.1).

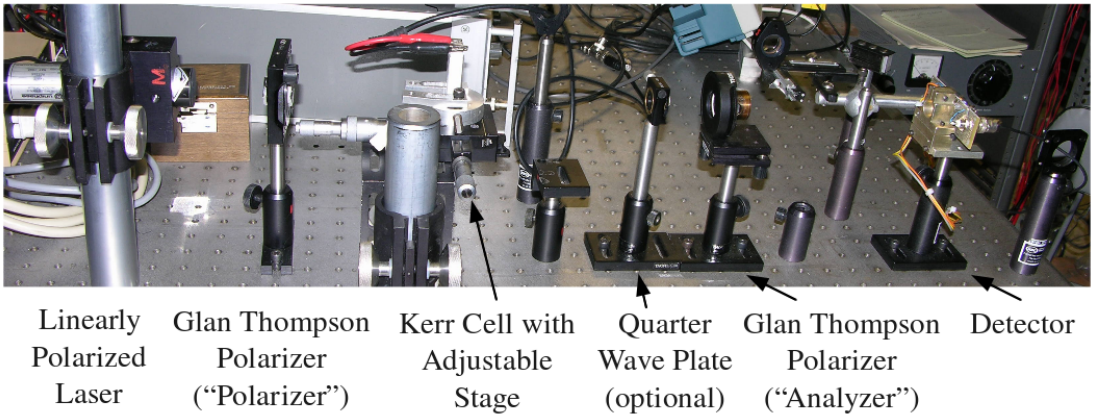

(a) TEB optical path

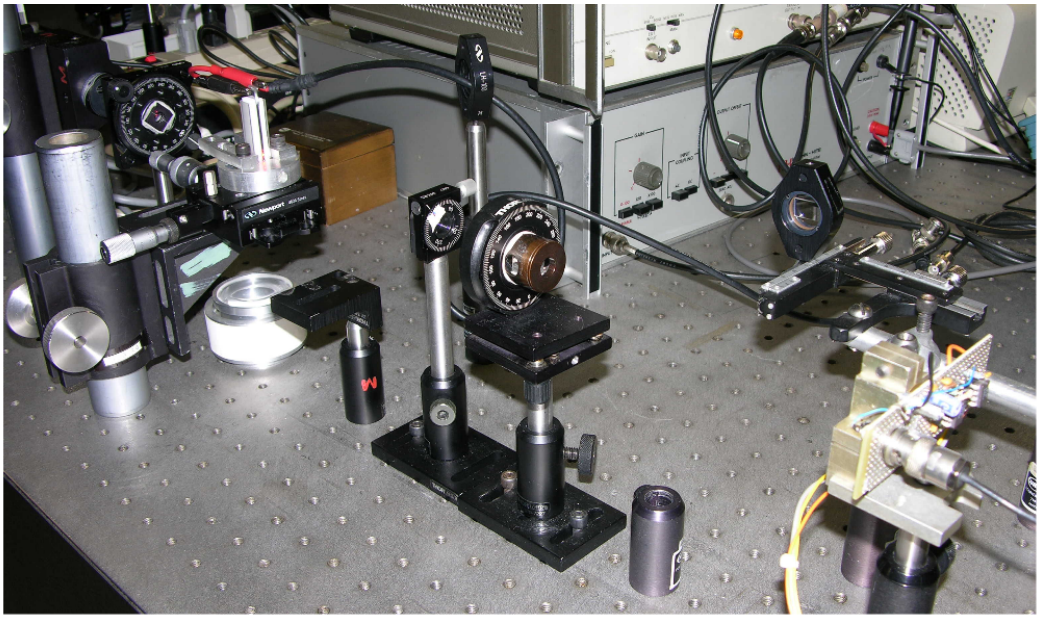

(b) Optical path viewed from the detector

Figure 4.3.1.1: Photograph of the TEB optical path.

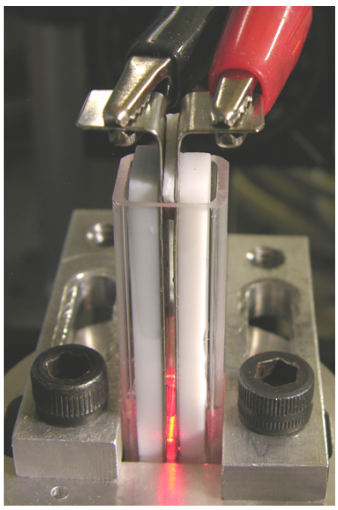

(a) Photograph of Kerr cell in use.

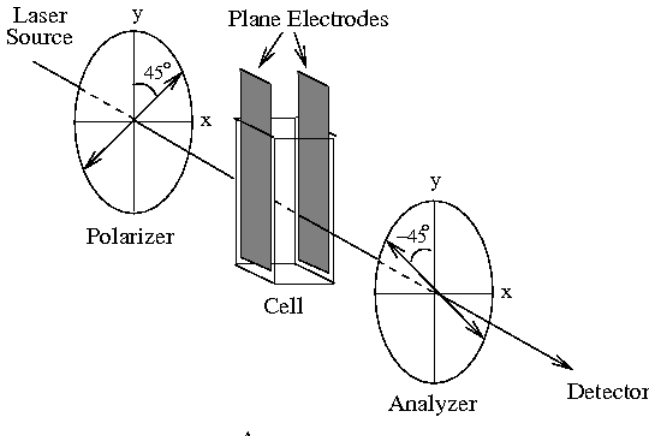

(b) Schemetic of Kerr cell in optical path.

Figure 4.3.2.1: Kerr cell design. Two stainless steel planar electrodes are set 1 mm apart and held in place by two 4 mm Teflon spacers on either side. An additional 1 mm Teflon spacer between electrodes at top acts as as a seal for the cell (a). The polarized laser beam is passed between electrodes through solution as shown in (b).

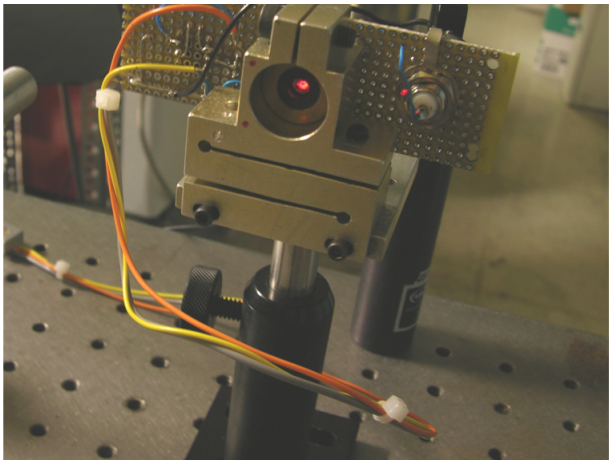

(a) Photodiode detector and amplification circuit.

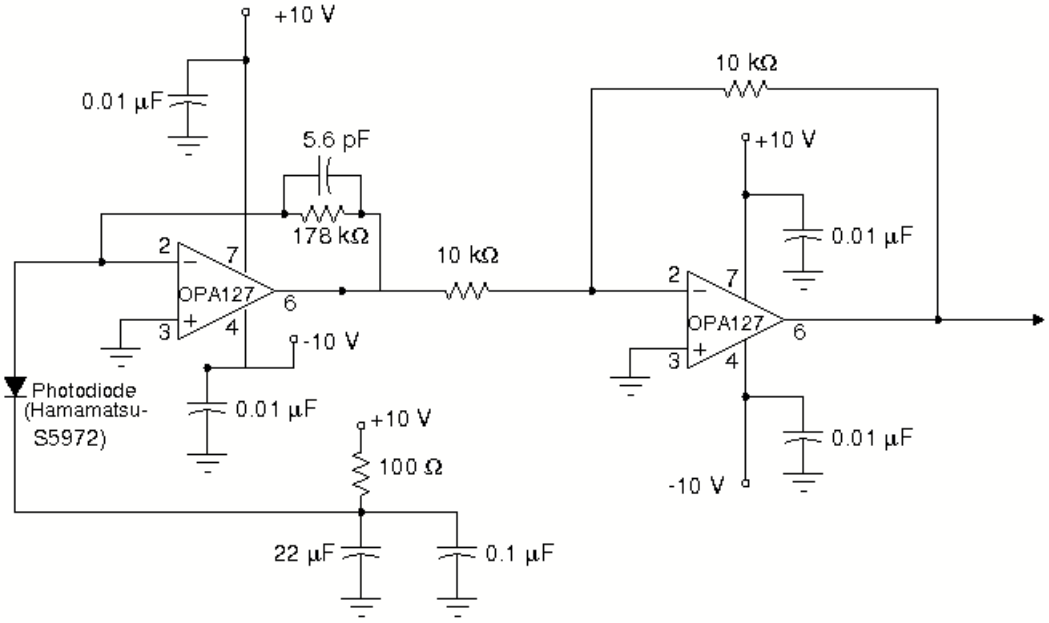

(b) Circuit schematic for the detector amplification circuit.

Figure 4.3.2.2: TEB photodiode detector and preamp circuit mounted in an adjustable stage (a) and the schematic for the amplification circuit (b).

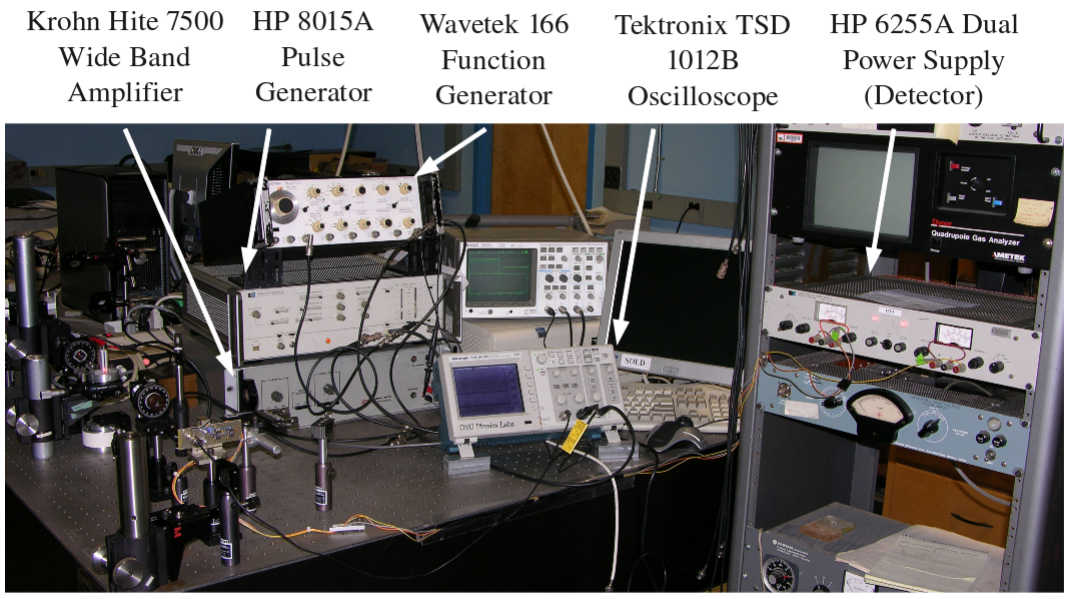

Figure 4.3.3.1: Photograph of the TEB electronics.

4.3.3 TEB Electric Pulse Generation

The electric pulse was either generated by a Wavetek 166 function generator gated through a HP 8015A pulse generator, or by a Tektronix AFG3021B arbitrary digital function generator, then amplified by a Krohn-Hite model 7500 wideband amplifier. Radio frequency (50-100 kHz) sinusoidal pulses were applied across the electrodes at 100-300 V/mm field strengths.

4.3.4 Optical Signal Digitization and Measurement of Excitation Pulse

The output voltage generated by the detector circuit and the voltage across the cell was digitized by a Tektronix TDS1012B, 100 MHz bandwidth, 8-bit vertical resolution digital storage oscilloscope (DSO). This DSO has a 2 mV to 5 V per division vertical sensitivity (80 μV to 0.2 V resolution) and a 5 ns to 50 sec per division time base range (1 GSa/s to

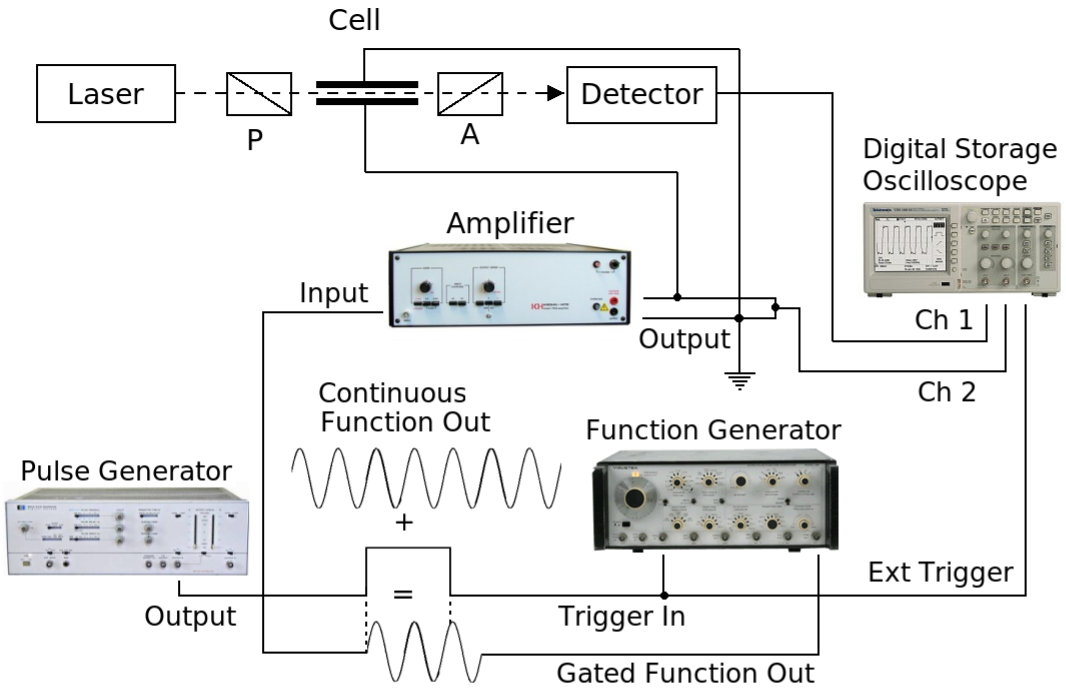

Figure 4.3.3.2: Schematic diagram for the TEB apparatus. A HeNe laser (Uniphase, model 1107P) is passed through a polarizer (P), a Kerr cell, and an analyzer (A). The wave completion function of the Wavetek 166 function generator is illustrated with the modulation of a continuous alternating waveform gated with the pulse generator (HP8015A). Output is amplified by a Krohn-Hite 7500 wide band amplifier before being applied across the cell. Output from the detector and amplifier are digitized by a Tektronix TDS1012B digital storage oscilloscope.

5 Sa/s sampling frequency) The memory depth is 2500 samples at all time base ranges. Figure 4.3.4.1 shows the vertical voltage scales for each available gain, and the resolution limits at each vertical scale.

In order to understand the limitations of using a digital storage oscilloscope as a digitization tool, one must understand the basics of anolog-to-digital (ADC) conversion as well as the basic theory behind the DSO operation. A brief discussion of ADC and DSO operation can be found in the discussion chapter (Section 6.2), followed by experimental examples of the limitations of tool.

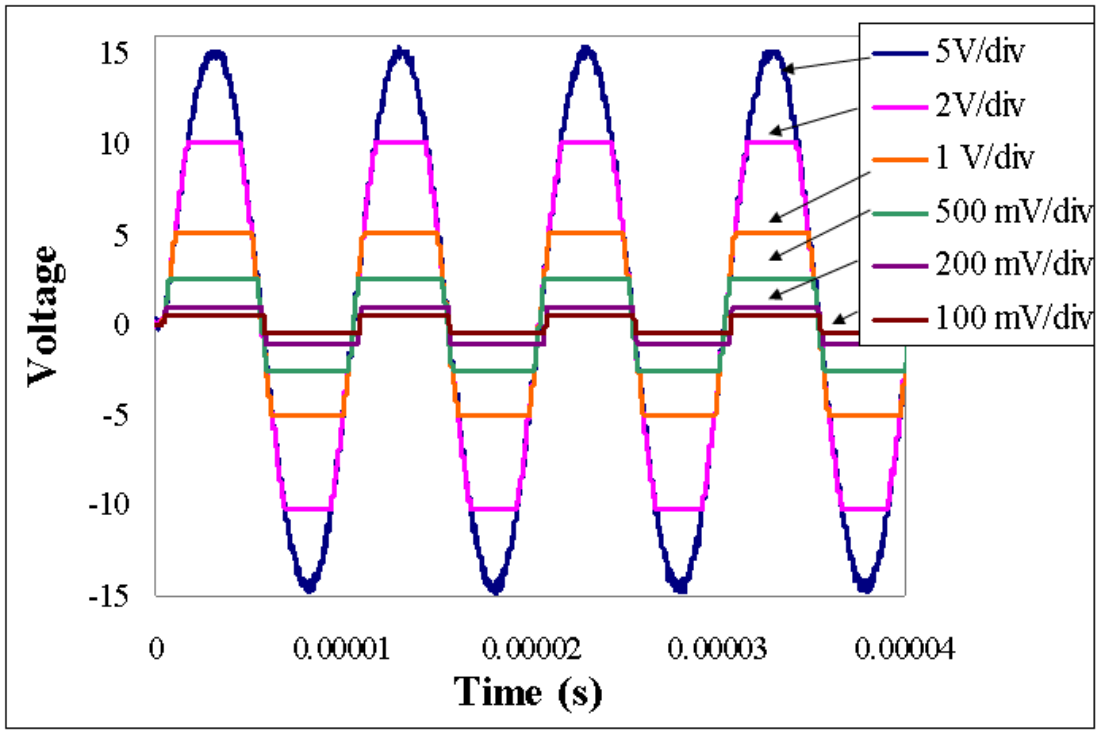

(a) Voltage waveform digitized at different gains.

Gain (V/div)	Max/Min (V)	Range (V)	Resolution (V)
5	±25.4	50.08	0.2
2	±10.6	20.32	0.08
1	±5.08	10.16	0.04
0.5	±2.54	5.08	0.02
0.2	±1.06	2.032	0.008
0.1	±0.508	1.016	0.004
0.05	±0.254	0.508	0.002
0.02	±0.106	0.2032	0.0008
0.01	±0.0508	0.1016	0.0004
0.005	±0.0254	0.0508	0.0002
0.002	±0.0106	0.02032	0.00008

(b) Summary of Voltage scales and resolution for each gain.

Figure 4.3.4.1: Digitization windows at different input gains. A 30 V peak-to-peak sinusoidal signal is digitized at variable gains by the Tektronix TDS1012B digital storage oscilloscope (DSO). Digitization windows and resolution are given in the table below for gains from 2 mV to 5 V per division.

Chapter 5 – Results

5.1 Apparatus Trouble Shooting and Characterization

5.1.1 Cell Capacitance

The macroscopic electric field inside the cell depends on the macroscopic capacitance of the cell, which depends on conductivity and dielectric constant of the cell contents. Chapter 2 discussed dielectrics of pure liquids and simple electrolytes. Since the local electric field felt by macroparticles in suspension is influenced by the surrounding electrolyte, it is important to have some understanding of how the macroscopically applied field E_0 (calculated from the applied voltage V_0 divided by distance d) relates to the internal field felt by solutions with different particle concentrations and conductivities. For this purpose, the time varying voltages across the cell and across an external load resistor in series with the cell were measured and used to solve the time-evolving differential equation relating to the equivalent circuit model of the system (shown in Figure 5.1.1.1). The differential equation relating to this circuit is

$$V_0 = \frac{dV_{R_1}(t)}{dt} R_0 C + \frac{R_0 + R_1}{R_1} V_{R_1}, \tag{5.1.1}$$

where R_1 is the resistance across the external load resistor, R_0 is the cell resistance, and C is the total cell capacitance arising from all possible electrochemical contributions. The applied voltage measured across the output of the amplifier is given by V_0. The solution to equation 5.1.1 was determined numerically with *Mathematica* (Wolfram Research, Version 4.). Table 5.1.1 summarizes the calculated resistance and capacitance for different

solutions from raw data, and example of which is shown in Figure 5.1.1.2. The electric field E is related to the applied voltage V_0 by

$$E = \frac{c}{c_0} E_0 = \frac{c}{c_0} \left(\frac{V_0}{d} \right), \tag{5.1.2}$$

where E_0 is the equivalent vacuum electric field, d is the distance between electrodes and $c_0 = (\epsilon_0 A)/d$ for the vacuum capacitance of a cell with the same area A. The approximate value of the electric field felt for each sample was calculated from an electrode area of A = 1 cm x 1 cm, a distance between the electrodes of 1 mm, and the vacuum permittivity $\epsilon_0 = 8.854X10^{-12}C^2/(N\ m^2)$ via Equation 5.1.2. The conclusion to be made is that the applied voltage (as measured across the cell) does not necessarily equate to the same electric field felt for different samples. Therefore, calculating Kerr constants from increasing field strength relies upon measurements of cell capacitance to determine true electric field values from applied voltage.

An additional concern is the time required for the cell to reach a steady state upon the application and termination of an external field. Figure 5.1.1.2 shows the voltage data for a 0.02% C.CNC solution and a conductivity control, which represent the lowest conductivity solution typically used throughout this research. We see that the voltage across the load resistor reaches steady state after 4 μs, with higher conductivities requiring less time, and a comparable settling time upon termination of the pulse as seen in Figure 5.1.1.3. Since pulsed fields were rarely applied for less than 100 μs, this was considered to have an insignificant overall effect upon the time dependent optical responses measured for the cell. It is however a matter to be aware of if less than 10 μs time scales are to be analyzed immediately after the application or termination of a square wave electric field (i.e. at the pulse edges.)

Since most of our experiments used sinusoidal pulses at frequencies between 50 kHz

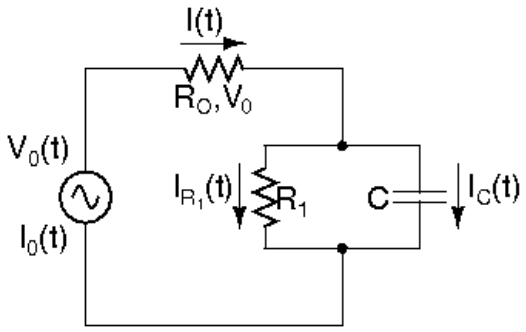

Figure 5.1.1.1: Equivalent circuit model used for capacitance measurement. R_1 and C are the resistance and capacitance of the cell and R_0 is the resistance of an external (1 MΩ) load resistor in series with the cell. V_0 is the applied voltage measured at the amplifier output terminals.

Table 5.1: Values of resistance and capacitance for different conductivities. Resistance and capacitance were calculated for an applied voltage V_0 for various samples. The internal electric field (last column) is calculated from the calculated capacitance of each sample and Equation 5.1.2. Sodium chloride control solutions were prepared at roughly equal conductivities for each C.CNC concentration to compare effects of macroion suspension versus simple electrolytes. No quantitative difference is seen macroscopically for comparable conductivities with and without C.CNC particles.

Sample	Conductivity μS	Capacitance (pF)	Resistance (MΩ)	V_0 (V)	Electric Field (V/cm)
Water	0	4.5	4.88	13	6648
0.02% C.CNC	15 μS	1.05	9.44	13	1551
NaCl	17 μS	1.08	9.52	13	1595
0.05% C.CNC	39 μS	0.65	11.07	13	960
NaCl	34 μS	0.65	11.07	13	960
0.5% C.CNC	144 μS	0.11	13.06	13	163
NaCl	136 μS	0.11	12.15	13	163

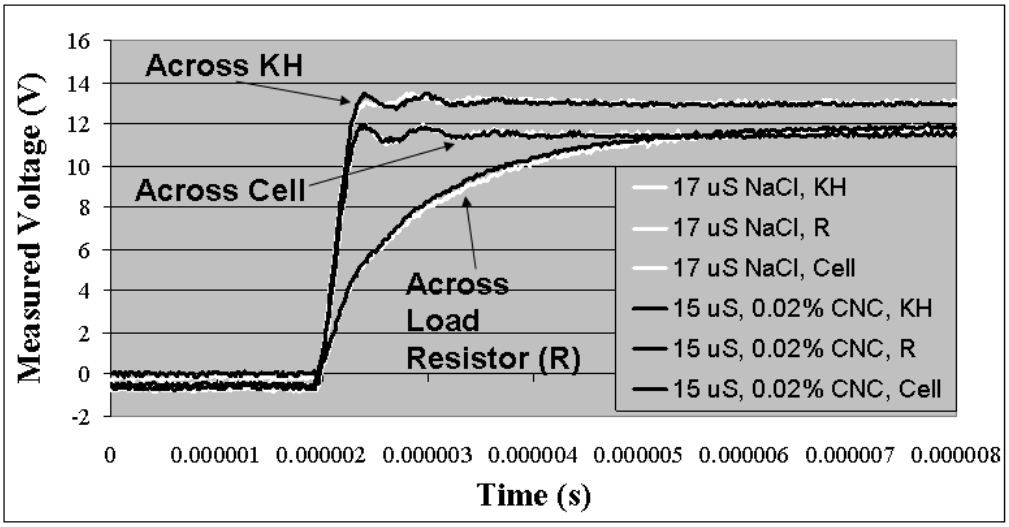

Figure 5.1.1.2: Data for cell capacitance calculated in Table 5.1.1. Voltages are measured across Krohn Hite amplifier (KH), an external load resistor (R) and the cell for the lowest conductivity C.CNC suspension tested (black lines) and a roughly equivalent sodium chloride control solution (white lines). The equivalent circuit for the experiment in shown in Figure 5.1.1.1.

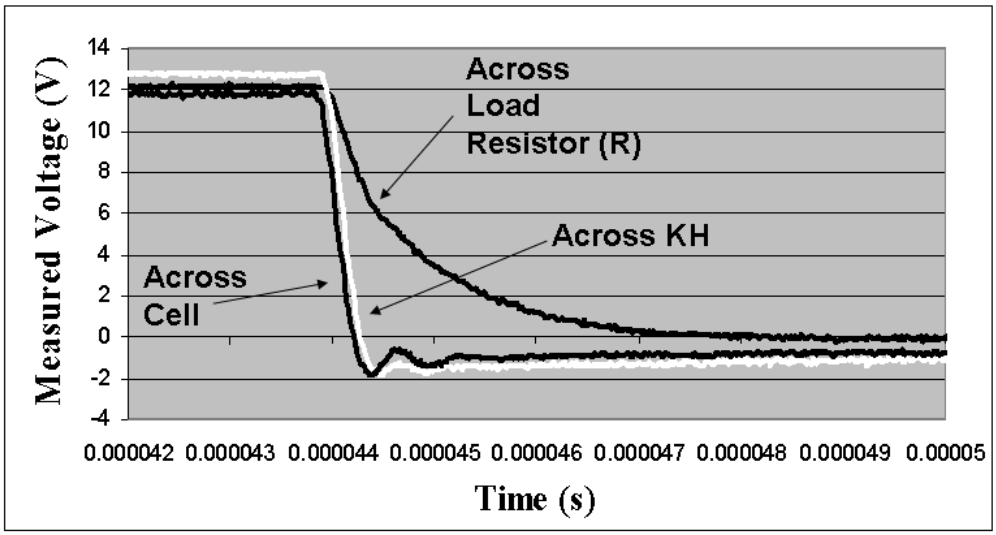

Figure 5.1.1.3: Falling edge data for cell capacitance calculations. Voltages are measured across Krohn Hite amplifier (KH), external load resistor (R) and the cell for the low conductivity C.CNC suspension shown in Figure 5.1.1.2. Decay times upon termination of an electric field are comparable to rise times upon field application as shown in Figure 5.1.1.2.

to 500 kHz, the phase delay was measured for two suspensions of C.CNC at representative extremes of experimental concentrations. Figure 5.1.1.4 shows the voltages measured across the amplifier and the external load resistor to the cell as a function of time. The low conductivity sample (15 μS) showed a 240 ns delay from the applied voltage, whereas the 144 μS suspension has a 64 ns delay.

5.1.2 Detector optimization

The detector used for this apparatus was developed in house by Photon Kinetics (Beaverton OR, USA) for use with optical fiber analysis, and was later donated to our lab. Since the initial application for which the detector was designed did not suit our particular measurement needs, modifications in the pre-amplification gain circuit had to be made. To

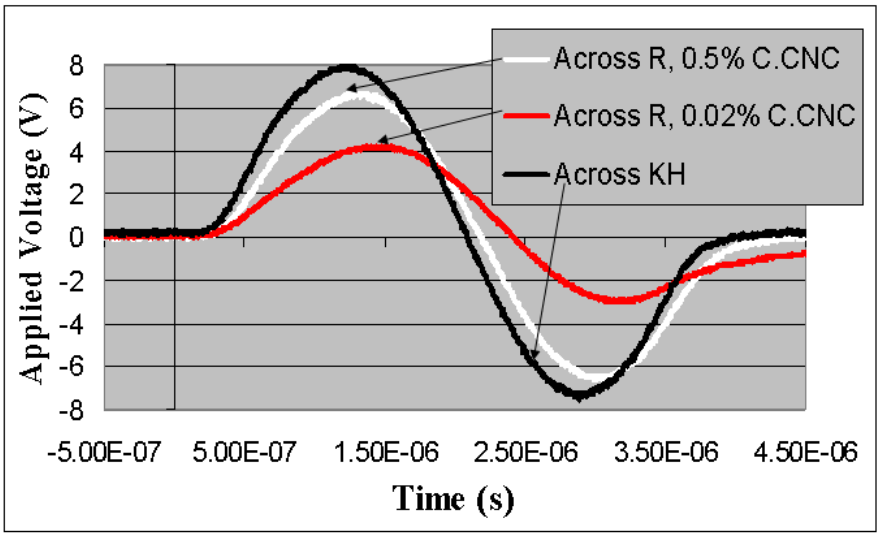

Figure 5.1.1.4: Phase delays for AC pulse across Kerr cell. Phase delays for C.CNCs at two different concentrations are shown alongside the applied voltage The lower C.CNC concentration (0.02% C.CNC, 15 μS conductivity) showed a 240 ns delay between applied voltage measured across the amplifier (KH) and the external load resistor (R) in Figure 5.1.1.1, whereas the 0.5% C.CNC (144 μS) showed a 64 ns delay.

ensure that the modified detector was operating as expected, a picosecond pulsed laser setup designed for high speed optical fiber measurements was used (specifically the 2500 Optical Fiber Analysis System (OFAS) from Photon Kinetics). The response of the commercial detector incorporated into the 2500 OFAS is shown in Figure 5.1.2.1 for comparison.

The initial gain of the donated detector was determined by the first operational amplifier (OPA127) feedback resistor (50 kΩ) and capacitor (5 pF), which gave a bandwidth of 4 MHz. This gain was not sufficient for our weak optical signals, however. An initial modification (adding 4.25 MΩ to the feedback resistor) was made, which resulted in significant optical gain. The bandwidth was significantly decreased, however, as seen by the slow decay to baseline (over 16 μS) in Figure 5.1.2.1. A compromise was made using a 5.6 pF capacitor in series with the 178 kΩ resistor in the feedback loop as shown

in Figure 4.3.2.2(b). The calculated bandwidth for this configuration was 1 MHz. This configuration, dubbed “Final Gain”, was used for all data presented in this dissertation.

The “TEB Detector, Final Gain” time response curve in Figure 5.1.2.1 shows a delay from the onset of the laser pulse voltage of around 600 ns, whereas the commercial detector has a delay of around 100 ns. Since the pulsed laser has a finite rise time upon the application of the voltage pulse shown in Figure 5.1.2.1, the true signal increase with time is represented more accurately by the 2500 OFAS detector response. The estimated delay in our detector based on this correlation was around 500 ns. The TEB detector additionally shows oscillatory behavior in the signal decay due to the delta pulse-like input signal and the slew rates and stabilization times inherent with the OPA127 devices. A more appropriate test of the detector behavior is shown in Figure 5.1.2.2 with the application of a sinusoidal pulse across a C.CNC sample. The sacrifice of bandwidth for increased signal is clear in Figure 5.1.2.2 (a) for the first modification, where the signal continues to rise for 6 μs after termination of the pulse. The final gain curve, although an order of magnitude lower in overall signal, shows a more immediate decay response at the pulse edge. The lower gain with improved bandwidth was deemed sufficient from the sampling rates and digital voltage resolution experimentally possible for this apparatus. Although data from the initial modification was rejected in our final analysis, both gain responses are shown here as a demonstration of the need for careful planning and characterization when designing electronic detection systems for laboratory signals.

5.2 Frequency Domain Experimental Results

In order to measure the electronic response of C.CNCs, as well as test the sensitivity and electronic limits of our apparatus, a frequency dependent study was carried out. The theory behind the frequency dependence was discussed in section 2.3.2. In short, a rela-

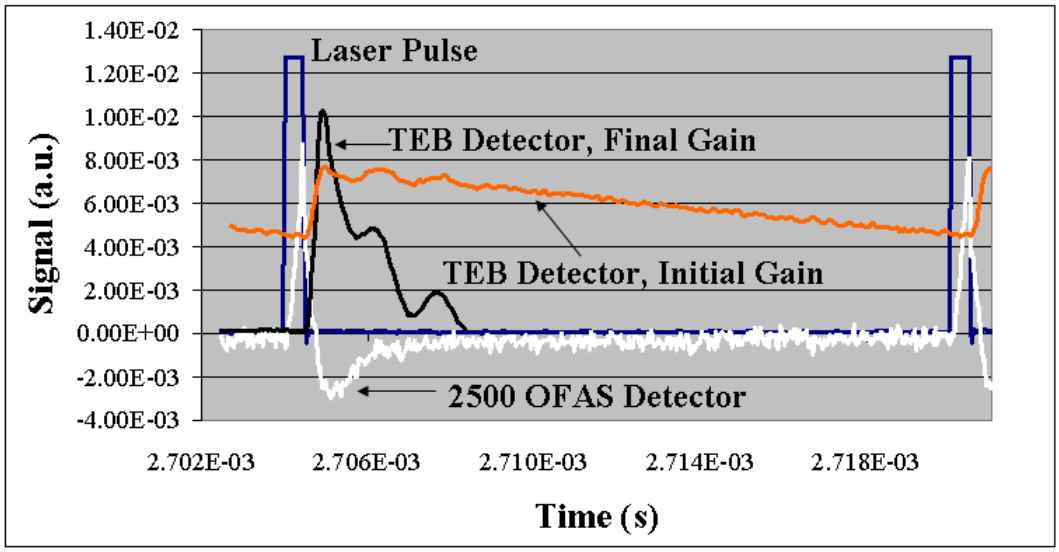

Figure 5.1.2.1: Response delay of detector for different circuit gains. A picosecond pulsed laser signal was used (the applied voltage of which is shown in the 'Laser Pulse' curve), and the commercial detector response for the 2500 Optical Fiber Analysis System (OFAS, from Photon Kinetics) is shown for comparison. The initial circuit gain corresponded to a 4.7 pF capacitor and 4.3 MΩ resistor in the first gain stage (Figure 4.3.2.2). The final gain (used for all data reported here) was 5.6 pF and 178 kΩ.

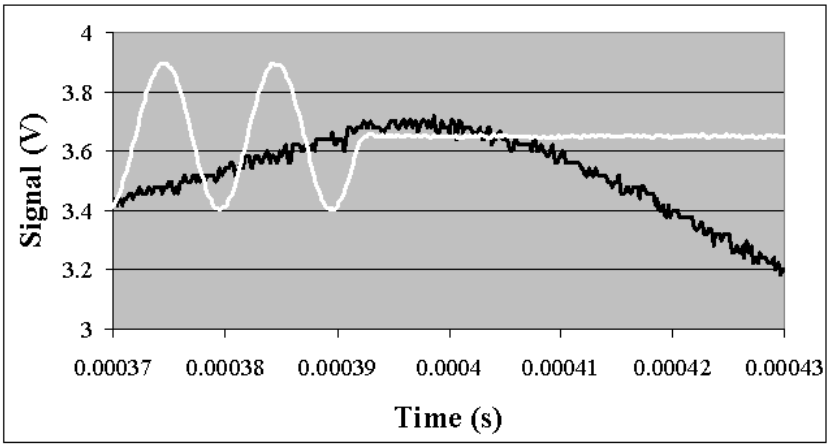

(a) Initial Gain

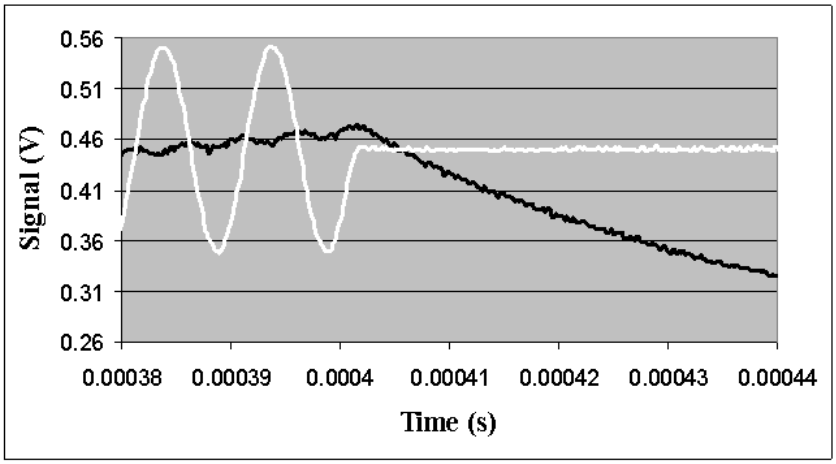

(b) Final Gain

Figure 5.1.2.2: Pulse edge for different detector amplifications. The black lines represent the optical response of the cell, and the white lines correspond to the excitation voltage across the cell (with scale adjusted to fit graph). (a) Shows a gain with a 4.7 pF capacitor and a 4.3MΩ resistor (50 kHz bandwidth), whereas (b) shows the response with the 5.6 pF, 178 kΩ gain (1 MHz bandwidth). A 10-fold decrease in overall signal is the price paid for the increase in response time.

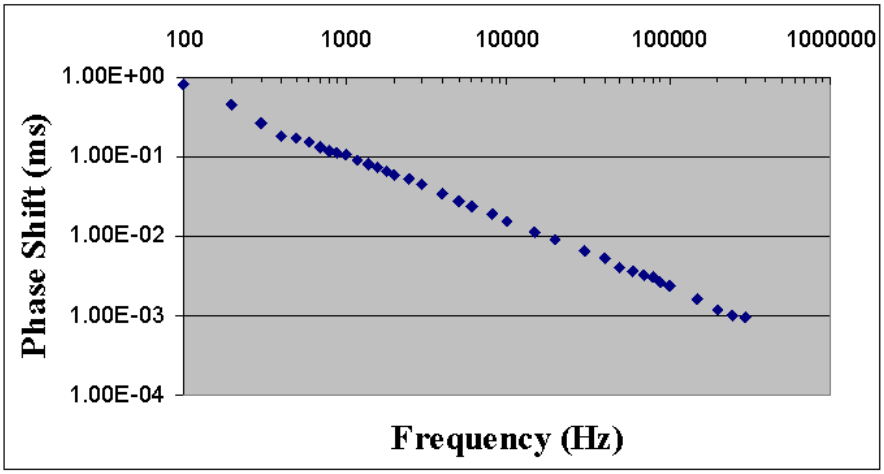

Figure 5.1.2.3: Phase delays measured as a function of frequency. Delays were measured for sinusoidally applied voltages between 100 Hz and 300 kHz. Sample is 0.05% C.CNC, pH 11.2, with an applied voltage of 300 V peak-to-peak for all frequencies. The optical phase delay at 300 kHz was measured to be 940 ns, compared to the measured voltage delay of 64 ns for comparable suspensions shown in Figure 5.1.1.4. The additional delay (excluding the 500 ns detector delay measured in Figure 5.1.2.1) is expected to arise from diffusional effects of the macroparticles.

tionship between the induced birefringence (Δn_i) and the average birefringence observed $\Delta n_{i,ave}$ is sought such that

$$\Delta n_i = \Delta n_{i,ave}\left[1 \pm \frac{cos(2\omega t - \phi_i)}{(1+4\omega^2\tau^2)^{1/2}}\right], \tag{5.2.1}$$

where ϕ_i is the phase angle between the birefringence and the applied field, τ is the characteristic relaxation time, and ω is the angular frequency of the field. The phase shift follows the relationship

$$tan\phi_i = 2\omega\tau. \tag{5.2.2}$$

In the limit of high frequencies, ϕ approaches 90 degrees. Therefore, the second term in equation 5.2.3 goes to zero and a steady state birefringence with magnitude $\Delta n_0 = A\,E_0^2/2$ is observed. The constant A is calculated from the measured Kerr constant K as $A = 2\pi nK\lambda_0$, for a wavelength λ_0 and a medium refractive index n [1]. The extrema of Δn, Δn_m is given by

$$\Delta n_m = \Delta n_{i,ave}\left[1 \pm \frac{1}{(1+4\omega^2\tau^2)^{1/2}}\right]. \tag{5.2.3}$$

The experimental difficulty in this method lies in measuring a valid Kerr constant for a given frequency. We found Kerr constant values to vary slightly at different applied field frequencies, and as such a universal K value could not be determined. This could be due to the frequency dependence of the cell capacitance, which will effect the internal electric field as discussed in section 5.1.1.

An alternative normalization method described by Thurston and Bowling [2] involves normalizing the birefringence to the low frequency limit. However, the low frequency limit could not be measured due to experimental limitations of the cell. The lowest frequency measured was 100 Hz, which corresponds to a 10 ms pulse upon one complete

cycle. Pulses longer than 10 ms resulted in significant drift in the steady state amplitudes, likely due to Joule heating and electrode polarization phenomena. Since at least one full sinusoidal cycle must be output by the function generator, 100 Hz is the approximate lower limit for this apparatus without further modification. As such, there is currently no ready means to normalize the results to the low or high frequency limits without modifications of the cell and detector. Results will therefore be presented as raw data rather than normalized birefringences.

An additional difficulty encountered in this experiment was the observation that frequencies above 75 kHz showed a multimodal response. This was later determined to arise from the detector resonating with the applied voltage over the cell, where signals became indistinguishable from detector harmonic noise above 70-80 kHz (Figure 5.2.0.4). As such, the AC component at limiting high frequencies can not be measured with our current detector. Our preliminary results will be shown here in the context of how to improve our apparatus for future experiments.

5.2.1 Tobacco Mosaic Virus

In order to compare our results with those of other TEB experimentalists, we obtained a sample of Tobacco Mosaic Virus (TMV), for which much TEB data has been published. In general, TMV is thought to be a monodisperse rod with a primarily induced dipole. There has been some conflicting results for TMV for different strains and sample preparations, some indicating a slight permanent dipole contribution, and many indicating deviations from monodispersity. We obtained two different samples from different labs, and the TEM images for each can be seen in Figures 5.3.3.1 and 5.3.3.5 later in this chapter. For both samples, smaller fragments were seen, negating the assumption of monodispersity. The diameters appear to be quite homogeneous within each sample,

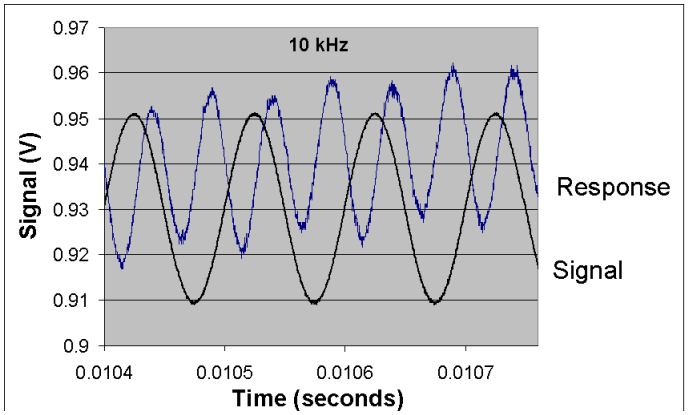

(a) At 10 kHz, the response starts to becomes modulated by the detector.

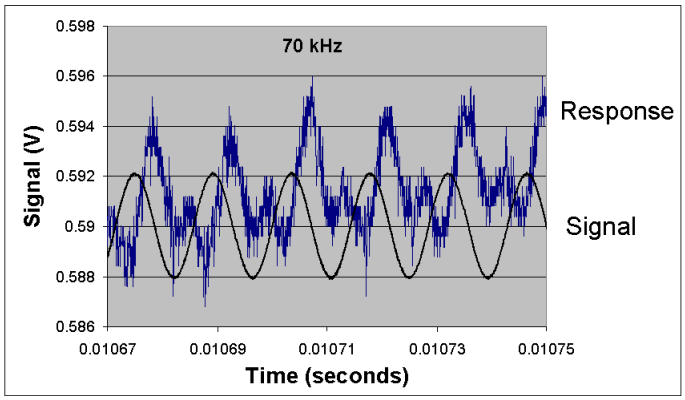

(b) At 70 kHz the detector ringing dominates. The sample double frequency response is still discernible as a small shoulder.

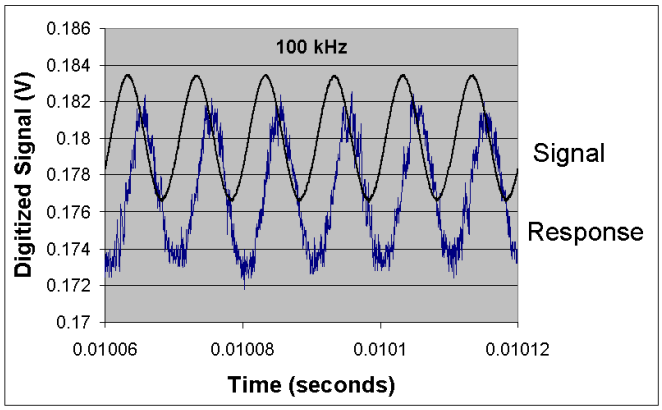

(c) By 100 kHz the signal is no longer discernible from detector ringing.

Figure 5.2.0.4: Detector response to an applied AC signal over the cell. Detector ringing (large peak) is compounded with experimental response (small peak) at frequencies above 50 kHz. At 100 kHz, the sample's response is indiscernible from the detector's.

however. The sample provided from Theo Dreher was used for the frequency experiment as follows.

5.2.1.1 Sample Preparation

The initial sample of TMV provided by Theo Dreher was at a TMV concentration of 26 mg/mL in a potassium phosphate buffer. The initial conductivity of the sample proved too high for successful TEB experiments, even after dilution to 0.05% solids in low ionic strength phosphate buffer. A 10 μL sample was therefore solvent exchanged into 1.5 x 10^{-4} M potassium phosphate (pH 7.0) via 10 x 500 μL volume dilutions using Centrifugal Filter Units (Amicon Ultra,Ultracel 50K Membrane, Millipore). The final product was diluted to 0.05% solids in 1.5 x 10^{-4} M potassium phosphate and used as such for TEB.

5.2.1.2 TMV Frequency Domain TEB

The TMV sample was placed in a 2 cm path length Kerr cell with planar stainless steel electrodes placed 1 mm apart. An alternating voltage of 270 V peak-to-peak was applied for all frequencies. Single pulses were applied for each frequency to avoid heating and polarization effects.

5.2.1.3 TMV Frequency Domain Observations

The raw data for the TMV frequency domain experiment is shown in Figure 5.2.1.1. The steady state birefringence for each frequency was calculated as the average of the alternating (peak-to-peak) signal just short of the pulse end. The steady state and alternating values are shown as a function of frequency in a log-log plot as per the method

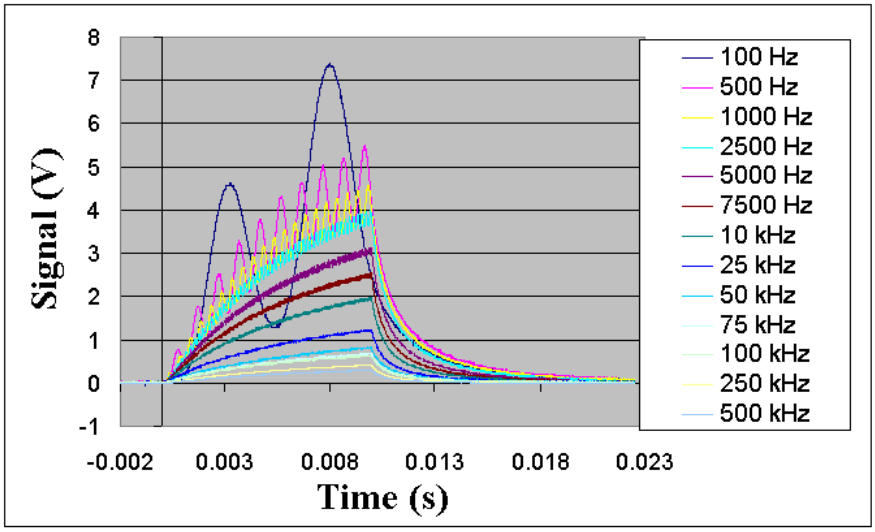

Figure 5.2.1.1: Raw data from frequency domain TEB of TMV. Pulsed electric fields of 10 ms duration, varying between 100 Hz (top-most curve) to 500 kHz (lowest curve), were applied at 270 V peak-to-peak field strengths. Steady state value of alignment decreased consecutively with increasing frequency. Tobacco Mosaic Virus (TMV) was provided by Dr. Theo Dreher (Department of Microbiology, Oregon State University).

of Thurston [2] in Figure 5.2.1.2. (See Figure 2.3.2.1 for comparison.) The minima and maxima of the alternating components are plotted according the method of O'Konski in Figure 5.2.1.3(a), with the results obtained for TMV by O'Konski shown in Figure 5.2.1.3(b).

The primary difference we saw in our experiment from similarly published results was the continued decrease in steady state birefringence with increasing frequency, even up to 500 MHz. This was contrary to the results of O'Konski, et al., who saw a levelling off of the steady state birefringence at around 10 kHz, as shown in Figure 5.2.1.3(b). It was thought perhaps that changes in cell capacitance with frequency (and thus the internal electric field) was to blame for this. The convergence of the alternating extrema occur at roughly the same frequency as reported by O'Konski, however.

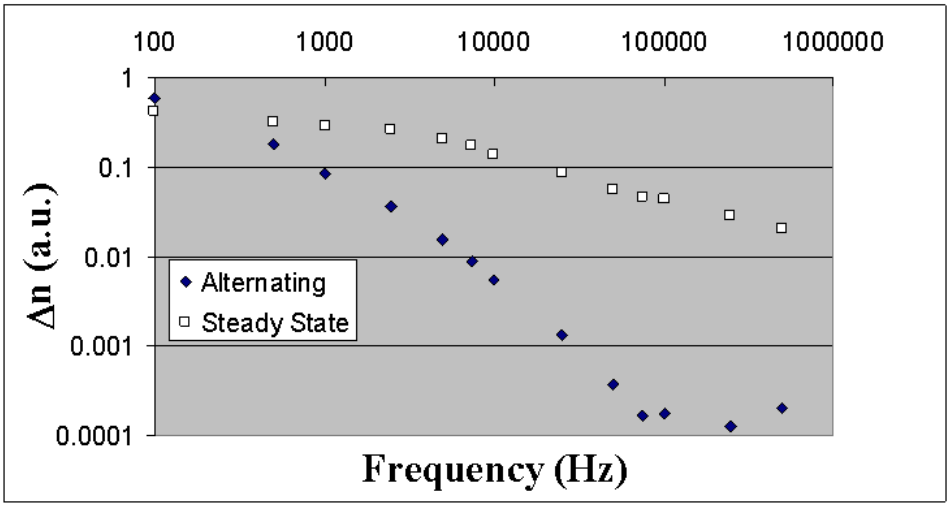

Figure 5.2.1.2: Steady state and alternating components for TMV. The frequency domain TEB steady state and alternating components are given versus frequency for TMV provided by provided by Dr. Theo Dreher.

5.2.2 Cellulose Nanocrystals

In order to determine whether slight shifts in protonation equilibrium contributed to electronic properties, a frequency domain experiment for cellulose nanocrystals was carried out at low and high pH. IR spectroscopy was used to confirm that the carboxilic acid surface groups of C.CNCs were predominantly in their acid and conjugate base forms at low and high pH, respectively.

5.2.2.1 Sample Preparation

Cellulose Nanocrystals were prepared from Avicel PH101 microcrystalline cellulose using TEMPO carboxylation as described in Section 4.1. After final dialysis, aliquots of the same preparation were adjusted to pH 4.8 and 11.2 with either HCl or NaOH, then dialized using a tangential flow, hollow fiber filtration module (Spectrum Labs MicroKros,

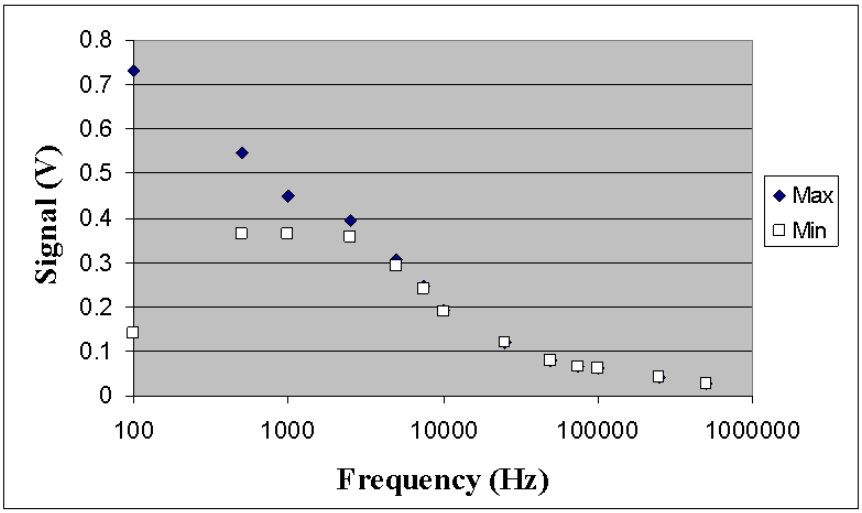

(a) Magnitude of alternating signal components for TMV.

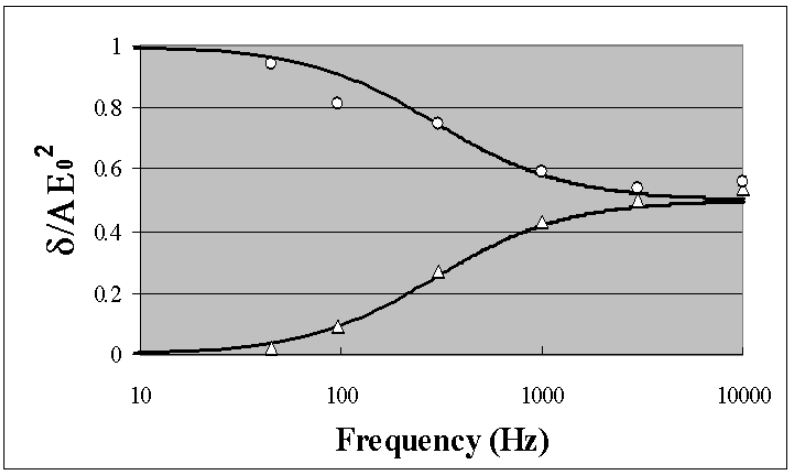

(b) Results for TMV from [1]

Figure 5.2.1.3: Maxima and minima of alternating component for TMV. Experimental values are shown as a function of frequency (a) and are compared to published results from [1] (b). White circles and triangles in (b) correspond to experimental maxima and minima, respectively, and solid lines represent calculated results. The vertical axis in (b) is normalized birefringence, $\Delta n/\Delta n_0 = \delta/AE_0^2$, whereas (a) reports non-normalized birefringence. The continued decrease for both components at frequencies above 5 kHz in (a) is not indicated by published results, and could represent competing mechanisms in our apparatus.

500 kDa pore size, 0.5 mm fiber ID) until permeate was less than 20 μS in conductivity. IR spectra were taken of each to validate that the samples were in acid or sodium salt form, respectively. Samples were adjusted to 0.05% solids and dynamic light scattering sizing analysis was done to determine the average hydrodynamic sizes of each.

5.2.2.2 AC Frequency Domain TEB

The samples were placed in an alternating electric field of 10 mS total duration, ranging in frequency between 100 Hz to 260 kHz. The peak-to-peak electric field amplitude was maintained at 300 V/mm throughout the frequency range. Detection and digitization of the signal was carried out as described in Chapter 4 using an 8-bit digital oscilloscope. For the signal generation, either a Wavetek 166 (analog) or a Tektronix AFG3021B (digital) function generator was used, with similar results from each.

5.2.2.3 C.CNC Frequency Dependence Results

The raw data for the frequency domain of C.CNC at pH 4.8 and 11.2 are shown in Figures 5.2.2.1 and 5.2.2.2. Figure 5.2.2.3 shows the phase shift as a function of frequency, from which the relaxation time τ was calculated in Figure 5.2.2.4. Frequencies above 80 kHz were not included in this calculation due to the uncertainties introduced by the detector. The resulting relaxation times for the low frequency range are 6.1 μs and 5.3 μs for pH 4.8 and 11.2, respectively, using the phase shift approach. The rotational diffusion coefficient D_R is related to τ by $\tau = 1/(6\ D_R)$, which gives values of 27,400 s^{-1} and 31,400 s^{-1}, respectively, for pH 4.8 and pH 11.2. These are not indicative of the steady state diffusion coefficient measured from the decay curves and are most likely dominated by smaller particles in the samples.

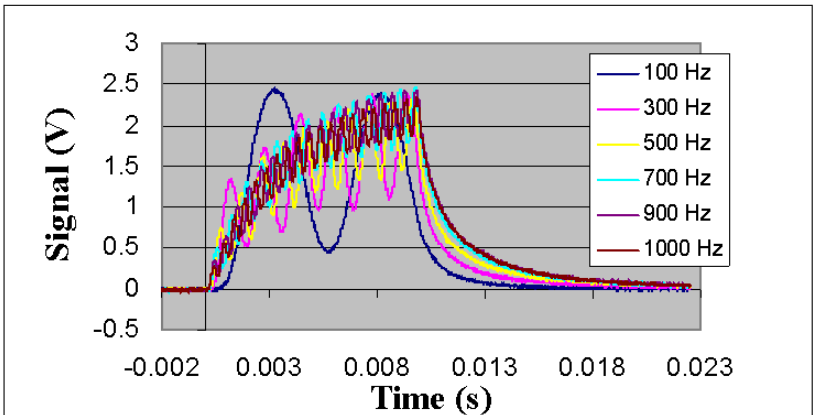

(a) Data for C.CNC at pH 4.8 for 100 to 1000 Hz

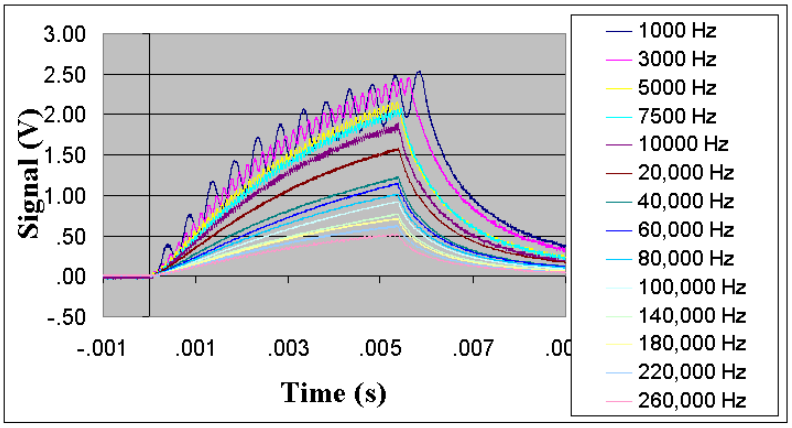

(b) Data for C.CNC at pH 4.8 for 1000 to 260000 Hz

Figure 5.2.2.1: Raw data for frequency domain C.CNC TEB at pH 4.8. Data is shown for frequencies between (a) 100 Hz and 1 kHz, and (b) 1 kHz (top curve) and 260 kHz (bottom curve). Above 1 kHz, steady state alignment degreased consecutively with increasing frequency.

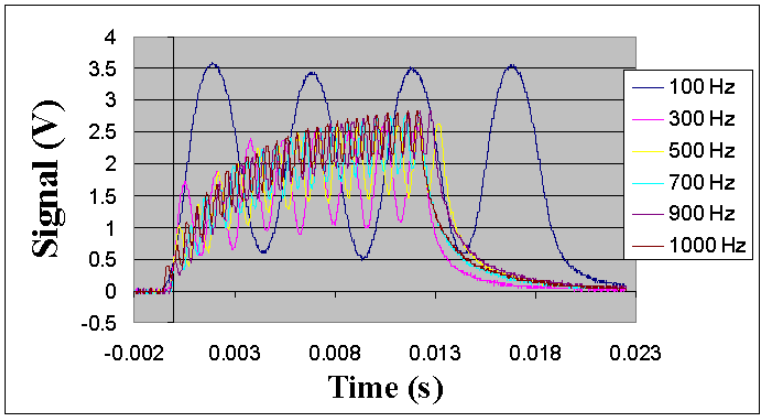

(a) Data for C.CNC at pH 11.2 for 100 to 1000 Hz

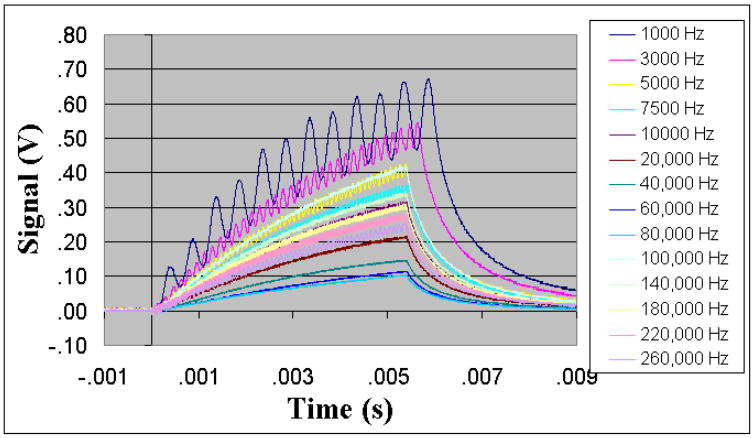

(b) Data for C.CNC at pH 11.2 for 1000 to 260000 Hz

Figure 5.2.2.2: Raw data for frequency domain C.CNC TEB at pH 11.2. Data is shown for frequencies between (a) 100 Hz and 1 kHz, and (b) 1 kHz (top curve) and 260 kHz (bottom curve). Again, frequencies above 1 kHz resulted in decrease of steady state alignment with increasing frequency.

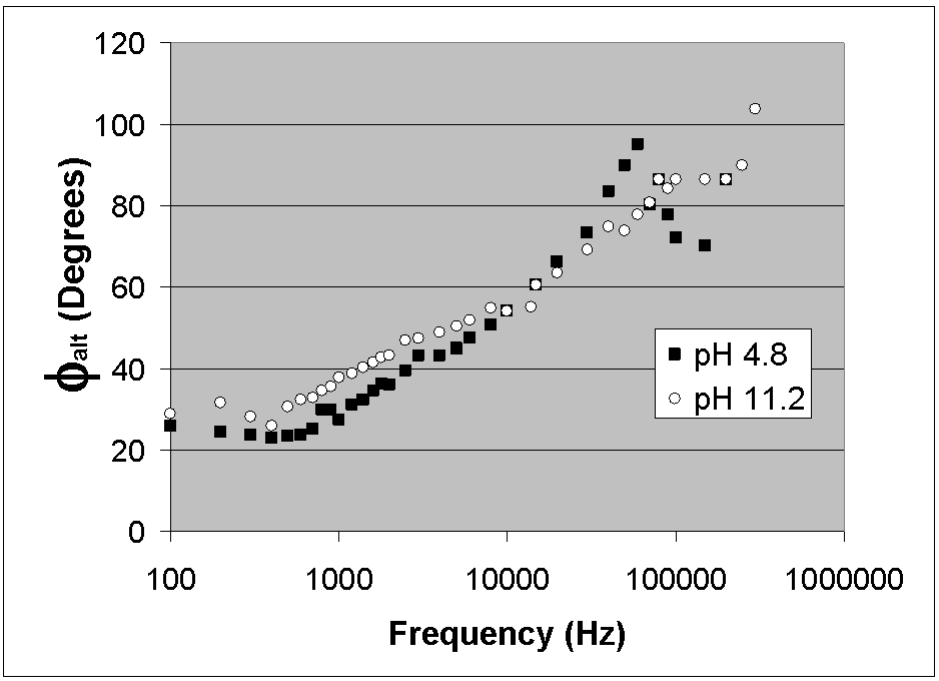

Figure 5.2.2.3: Phase angle as a function of frequency for C.CNCs. Phase shift for frequencies above 75 kHz were compounded with detector ringing and could not be measured accurately.

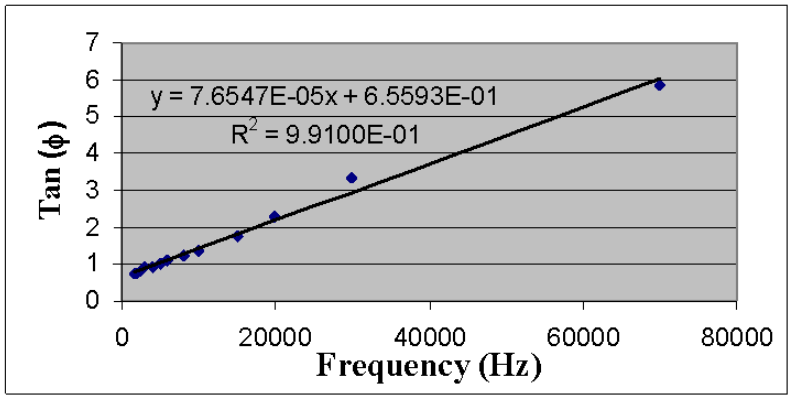

(a) Tanϕ versus frequency for C.CNC at pH 4.2

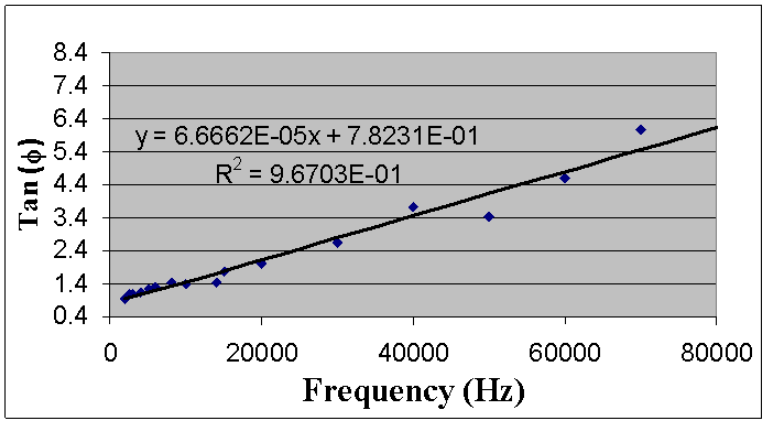

(b) Tanϕ versus frequency for C.CNC at pH 11.8

Figure 5.2.2.4: Relaxation time τ from frequency domain data for C.CNCs. τ is calculated for C.CNCs at different pH using the slope of the tangent of the phase shift ϕ versus frequency. The slope results in $4\pi\tau$ from equation 5.2.2, where τ is the characteristic relaxation time for the particle [1].

Figure 5.2.2.5(a) shows the steady state component of the birefringence for pH 4.8 and 11.2. There does not appear to be a significant difference between the samples, other than that of a total magnitude of intensity shift due to experimental drift or slight differences in concentration. Recall these are not normalized as in Figure 2.3.2.1 due to the experimental difficulty of measuring high and low frequency limits. The overall behavior up to 5 kHz could suggest a non-zero contribution of the permanent dipole to P in equation 2.3.8, as illustrated by Figure 2.3.2.1(a) for negative P values. The decrease above 5 kHz, however, is anomalous to any of the models suggested by [2] and Figure 2.3.2.1(a); we must conclude that a response not modelled by Thurston and Bowling is at work in this system. Figure 5.2.2.5(a) shows the alternating component of the birefringence to be compared to Figure 2.3.2.1(b), where again the overall behavior could suggest a non-zero P value indicative of a permanent dipole contribution.

In order to address anomalies from predicted models, it would behoove this research to first eliminate the possibility of electrode polarization effects and other electrochemical artefacts by coating the electrodes with an insulating material, or by using platinum electrodes as reported by [2] and [1]. As such, future frequency response studies will depend on a cell redesign with such issues in mind.

5.2.2.4 Mathematical Fitting Algorithms

The phase shifts charted in Figure 5.2.2.3 were measured using vertical (time) cursors on a digital oscilloscope, and as such a large degree of uncertainty is associated with them. The initial difficulty lies in selecting the appropriate maxima with electronically noisy data as seen in Figures 5.2.0.4 and 5.2.2.6. Additionally, the low resolution time increments reported by a digital scope tend to bias phase angles. A preferable approach would be to model the cosine behavior of the response using a mathematical algorithm,

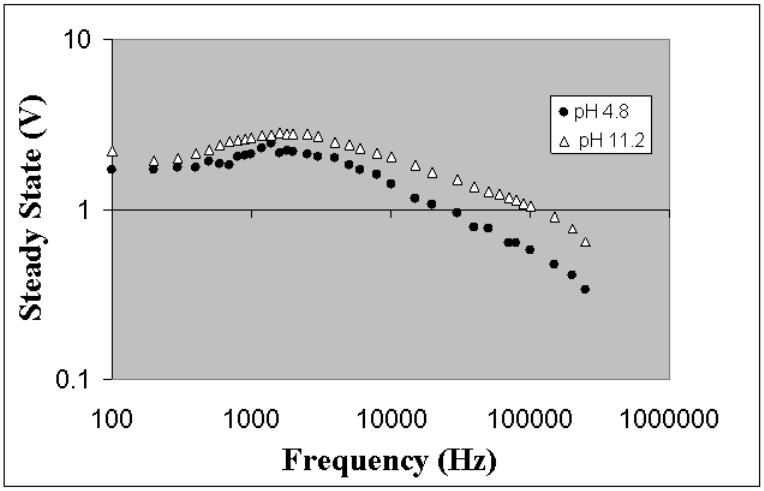

(a) Steady State

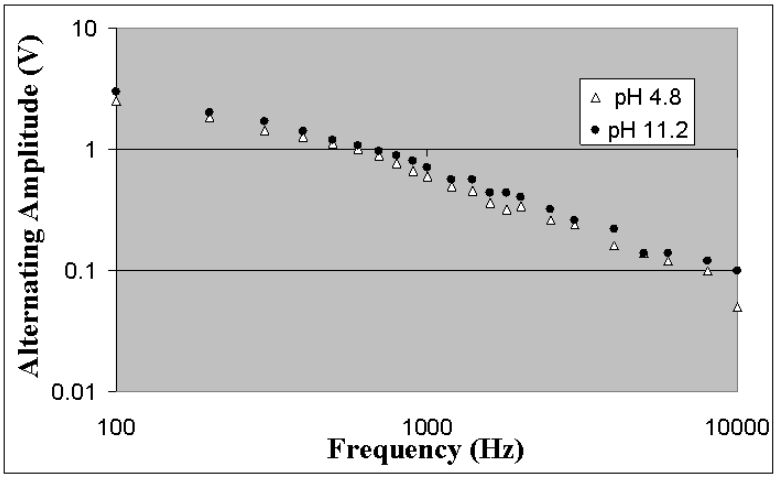

(b) Alternating

Figure 5.2.2.5: Steady state and alternating components for CNCs. Birefringence values for each component are given as a function of frequency for C.CNCs adjusted to pH 4.8 and 11.2.

then use the fitted equation to extract the three desired parameters, namely the magnitude of the alternating response (amplitude of the fit), the steady state response (given as a DC offset), and the relative phase of the response with respect to the excitation signal. A preliminary algorithm was written in *Mathematica* (Wolfram Research, Version 4.) to accomplish this; the fits to three different frequencies are shown in Figure 5.2.2.6. The advantages of this approach are clear. For the 5 kHz frequency the algorithm recognizes the double frequency response of the signal. At 50 kHz, the algorithm becomes biased to the first harmonic frequency detector response, ignoring the second harmonic peak as seen in Figure 5.2.2.6(c). With appropriate data, however, this difficulty will be avoided and the fitting approach can be used in preference to oscilloscope measurements (or estimations in many cases). Additionally, a mathematical fitting method could be incorporated into an automated sweep, allowing for *in situ* analyses. Work is in progress to develop such techniques from our current apparatus.

5.2.2.5 Summary and Future Work

The expected shift in phase angle with frequency was seen for both samples, as seen in Figure 5.2.2.3. The lower extrapolation to zero was compounded with the experimental limitations described above. The saturation at 90 degrees was evident at frequencies above 80 kHz, albeit using somewhat suspect deconvolutions of detector-biased data. Above 10 kHz, lack of resolution in the data and electronic noise made phase angle measurements somewhat uncertain, as seen for an experimental signals shown in Figure 5.2.0.4. While at first glance there appears to be a difference in the slopes for each pH, a full study cannot be concluded until a modified detector circuit can be constructed. Future work in this area involves the design and production of a printed circuit board with a ground plane for the amplification of the photodiode detector output. This will eliminate the

ground loop problems created by the through-hole breadboard circuit photographed in Figure 4.3.2.2(a). It will allow a greater range in frequency responses to be measured. In addition, more care will be taken in the next generation detector to minimise thermal noise such that clearer phase peaks can be measured. This, in combination with the mathematical fitting algorithm, will greatly reduce the experimental drift and uncertainty in the data shown so far.

This initial work, however, shows that the experiment is possible at the intensities and data resolution currently produced by this apparatus. The optics and electronics are sensitive enough to detect changes in modulation and phase at frequencies up to 300 kHz. Our hope is that future frequency response studies can be used as sensitive measurements for surface dielectric differences in our samples. With the recent acquisition of a 16-bit, 10 MSa/s analog-to-digital converter, resolution of phase shifts data will be greatly improved, facilitating this goal.

5.3 Sizing Data and Experimental Results

5.3.1 Sample Rates and Fitting Uncertainty

The majority of the data in this research was obtained using an 8-bit digital storage oscilloscope with a 2500 sample memory depth. Although an increase in sampling rate can be obtained by adjusting the time scale, the compromise is to sacrifice large portions of the trace in order to expand upon regions of interest. Since the diffusion coefficients were calculated using the initial slope of the field free decay region, the oscilloscope was adjusted such that the first 10 percent of the data contained the last of the rise region, and the remainder contained the initial decay (see Figure 5.3.1.2(b), for example). This allowed for edge finding algorithms to determine a consistent start of the decay in the event of a

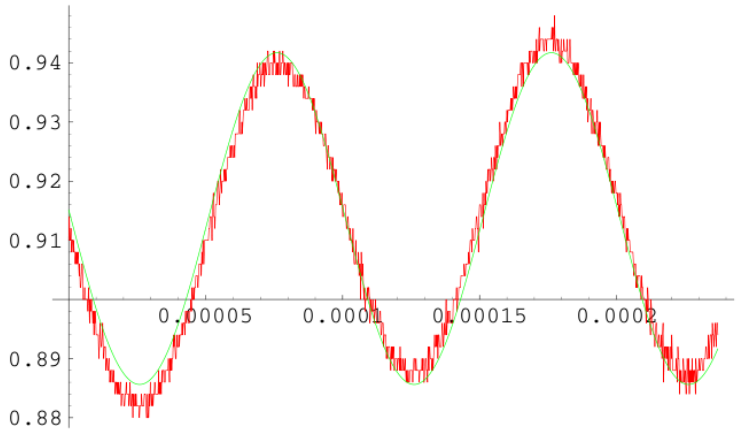

(a) 5 kHz

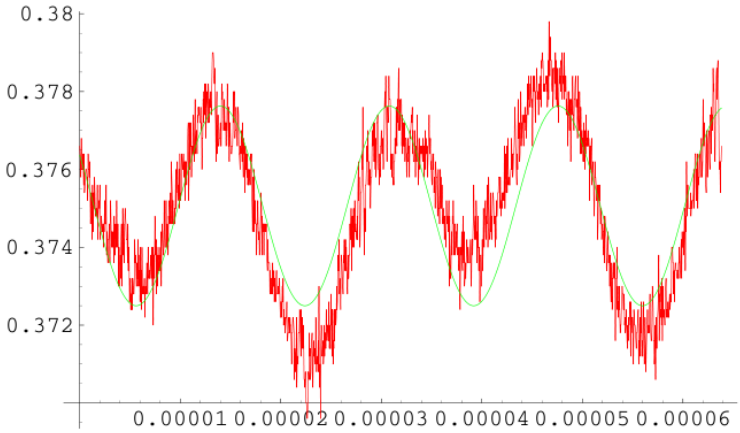

(b) 30 kHz

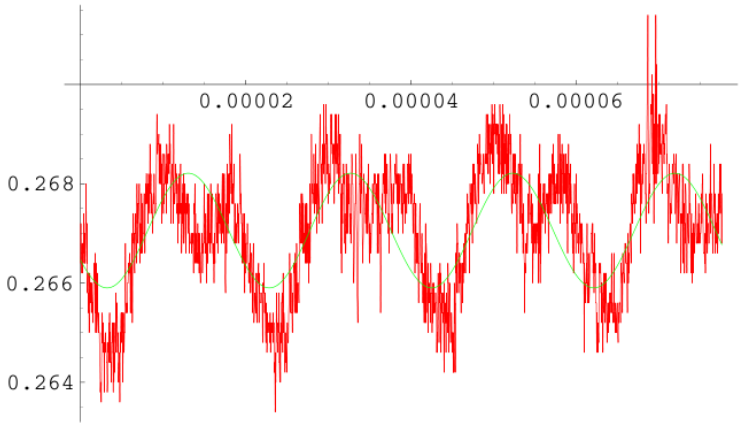

(c) 50 kHz

Figure 5.2.2.6: Mathematical fitting to experimental data. A sinusoidal fit (smooth green line) from *Mathematica* was applied to experimental data (jagged red line). By 50 kHz, the algorithm takes a weighted average of the detector ringing and the cell birefringence.

trigger delay or mistakes in oscilloscope settings on the part of the experimenter. Two sampling rates were found to be sufficient for adequate linear fits using this technique, specifically 100 μs per division (2.5 MHz sample rate) and 50 μs per division (5 MHz). Expanding around the pulse edge results in a loss of all baseline information however, and as such, normalization of the pulse cannot be accomplished. A full experiment would require a full pulse data capture, followed by a higher sample rate capture. Since experimental drift can be significant at long pulse lengths (see for example Figure 5.3.1.2a), the data in successive captures may not necessarily be representative of one another. Future work should involve a digitization method that can sample at sufficiently high sample rates to obtain trustworthy diffusion coefficients, while having enough memory depth to obtain full pulse information for the same pulse.

To demonstrate the uncertainty of the two pulse method, a TMV sample was pulsed twice and the signal digitized at two different frequencies, 2.5 MHz and 100 kHz. The diffusion coefficients were measured from each. Figure 5.3.1.1 shows representative AFM images for the TMV used, and Figure 5.3.1.2 shows the TEB data for two sample rates. Figure 5.3.1.3 shows the calculated diffusion coefficients for this data taken over the first 100 μs of the decay region for both sample rates. Although the diffusion coefficients appear to agree at first approximation, Figure 5.3.1.4 shows the raw data for the 1 ms truncation time pulse for the two rates. The linear fits for each illustrates the uncertainty in fitting under-sampled data, where the full pulse capture provides only 10 data points, as compared to the 250 points in the expanded pulse for the same time period.

5.3.2 Size Distributions of C.CNC

A cellulose nanocrystal suspension was concentrated to 5% solids and allowed to phase separate for two weeks, after which a distinct separation between anisotropic and isotropic

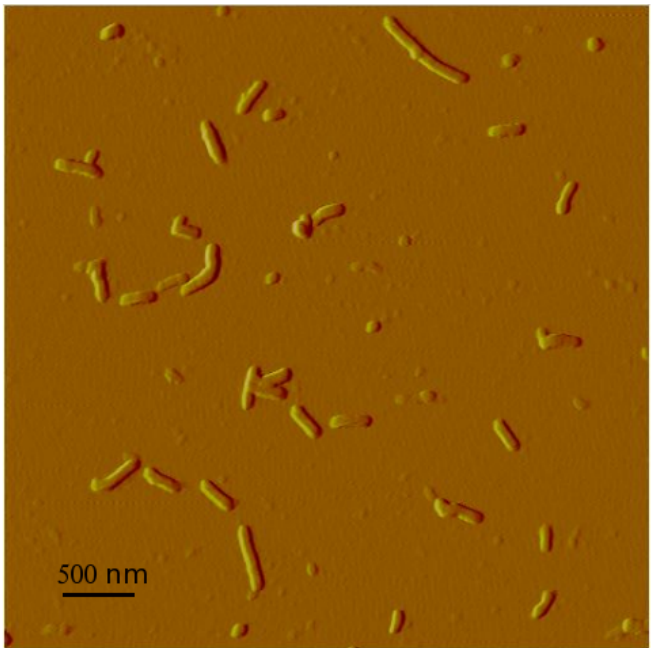

(a) 5 microns

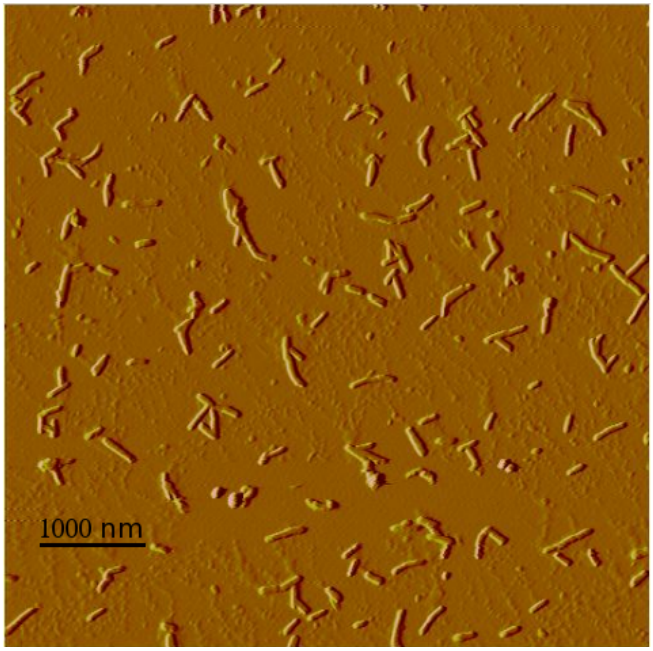

(b) 10 microns

Figure 5.3.1.1: AFM images of Tobacco Mosaic Virus (TMV). A roughly bimodal size distribution can be seen, including end-to-end dimers in linear and boomerang-shaped configurations. (Sample source is Qian Wang of the University of South Carolina.)

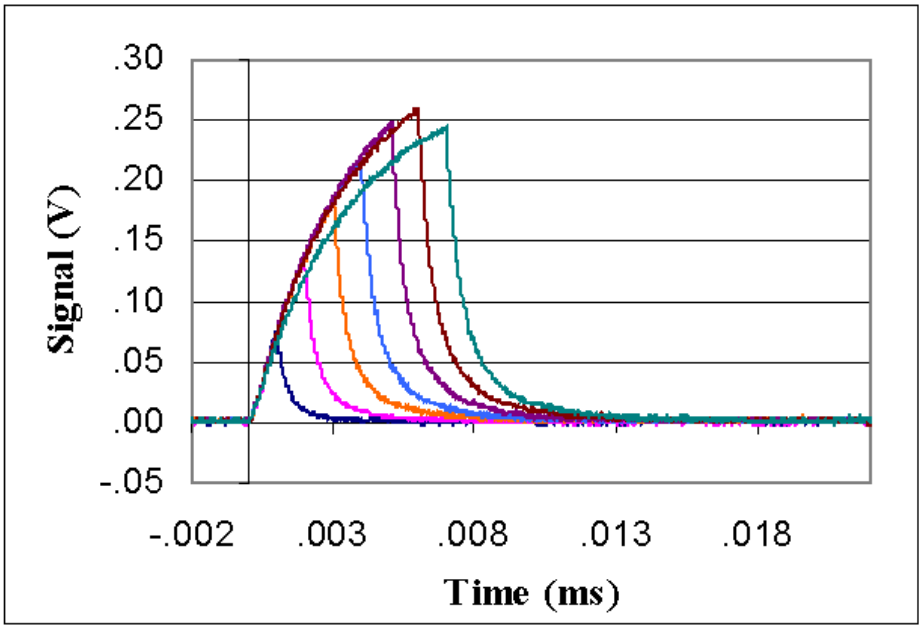

(a) Full Pulse (100 kSa/s)

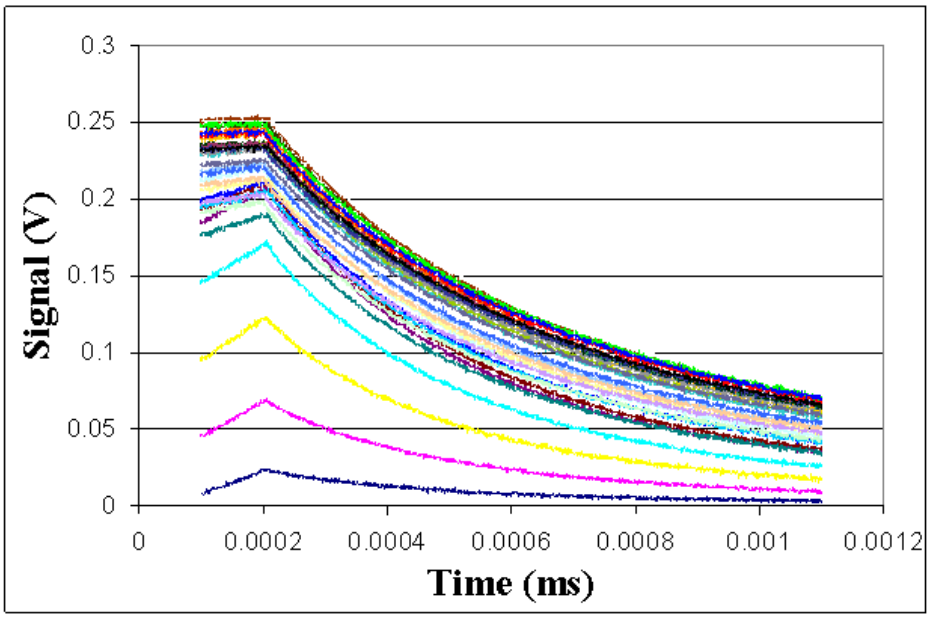

(b) Expanded Pulse (2.5 MSa/s)

Figure 5.3.1.2: Raw data for truncated pulse TEB at different sampling rates. In the expanded pulse plot the lowest curve corresponds to the shortest pulse, with curve peaks increasing with pulse length, and sequential pulses are offset in timescale for ease of comparison. (Sample is TMV provided by Qian Wang of the University of South Carolina.)

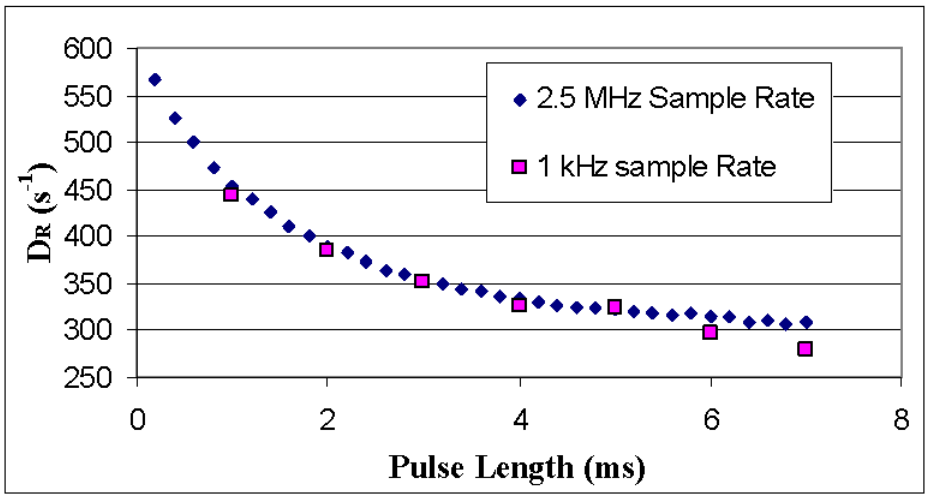

Figure 5.3.1.3: Diffusion coefficients calculated for two different sample rates. Coefficients were calculated over the same time range (100 μs) from the data shown in Figure 5.3.1.2. (Sample is TMV provided by Qian Wang.)

liquid crystal phases was observed (Figure 5.3.2.1). Phases were separated and diluted to 0.05% solids in dust-free deionized water for TEB measurements. The lower anisotropic phase was dubbed 'bottom' and the upper isotropic phase 'top'. An aliquot of the original suspension (unseparated) was likewise diluted to 0.05% solid and labelled 'total' to indicate to full size distribution of the unseparated batch.

5.3.2.1 TEM of Liquid Crystal Phase Separated C.CNC

Aliquots of 0.05% C.CNC) were placed onto Formvar Carbon TEM support grids (300 mesh, Electron Microscopy Sciences) and allowed to dry. Grids were then stained with 2% uranyl acetate (50/50 alcohol/water solutions). TEM images were taken by Teresa Sawyer at the Oregon State University Electron Microscopy Facility with a Philips CM12 Scanning Transmission Electron Microscope (STEM) running at 80 kV.

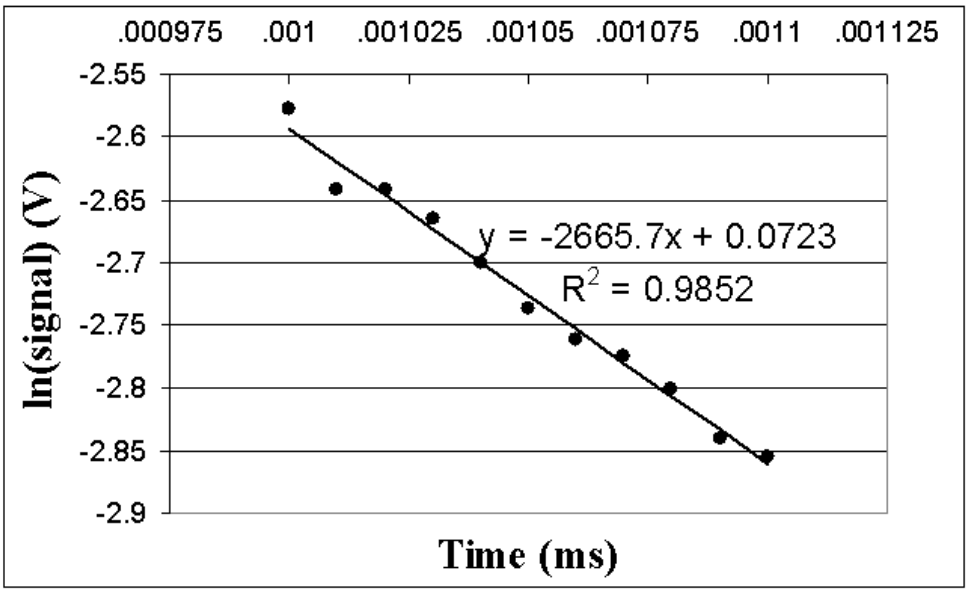

(a) 100kHz Sample Rate

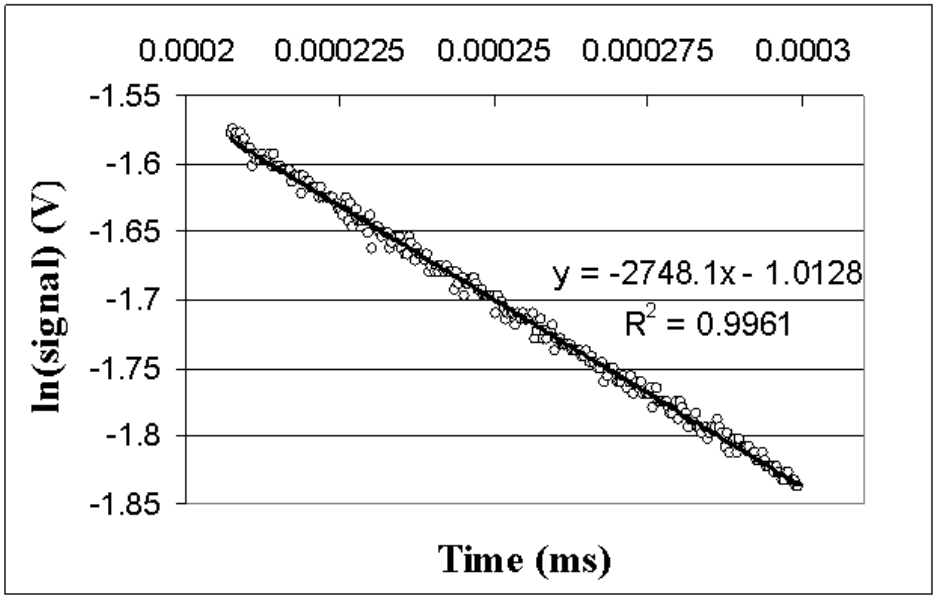

(b) 2.5 MHz Sample Rate

Figure 5.3.1.4: Linear fits of initial slope for two different sample rates. Data is from the 1 ms pulse truncation shown in Figure 5.3.1.3.

Figure 5.3.2.1: C.CNC liquid crystal phase separation for particle sizing.

5.3.2.2 TEB of Liquid Crystal Phase Separated C.CNC

Truncated pulse TEB measurements were carried out in a 2 cm path-length, quartz cuvette at 300 V/mm peak-to-peak field strength. Data digitization was carried out with the 8-bit Tektronix TDS 1012B oscilloscope at 50 μS per division time resolution (5 MHz sample rate) capturing only the initial falling trace at the edge of the pulse.

5.3.3 Size Distributions of TMV

Late in this research, a 16-bit, 10 MHz analog to digital converter was acquired, which allowed for entire pulse lengths to be captured at 10 MSa/second samples rates for two separate samples of Tobacco Mosaic Virus. The samples were provided by Dr. Theo Dreher (Department of Microbiology, Oregon State University) and Dr. Qian Wang (Department of Chemistry and Biochemistry, University of South Carolina). Representative TEM images of each are shown in Figures 5.3.3.1 and 5.3.3.5.

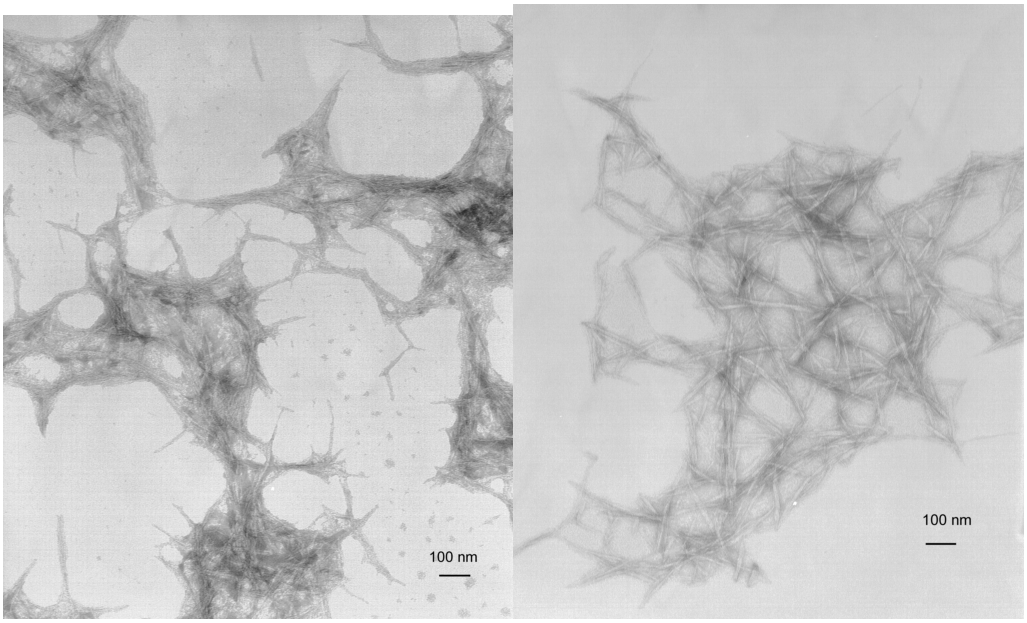

(a) Total (b) Top Phase

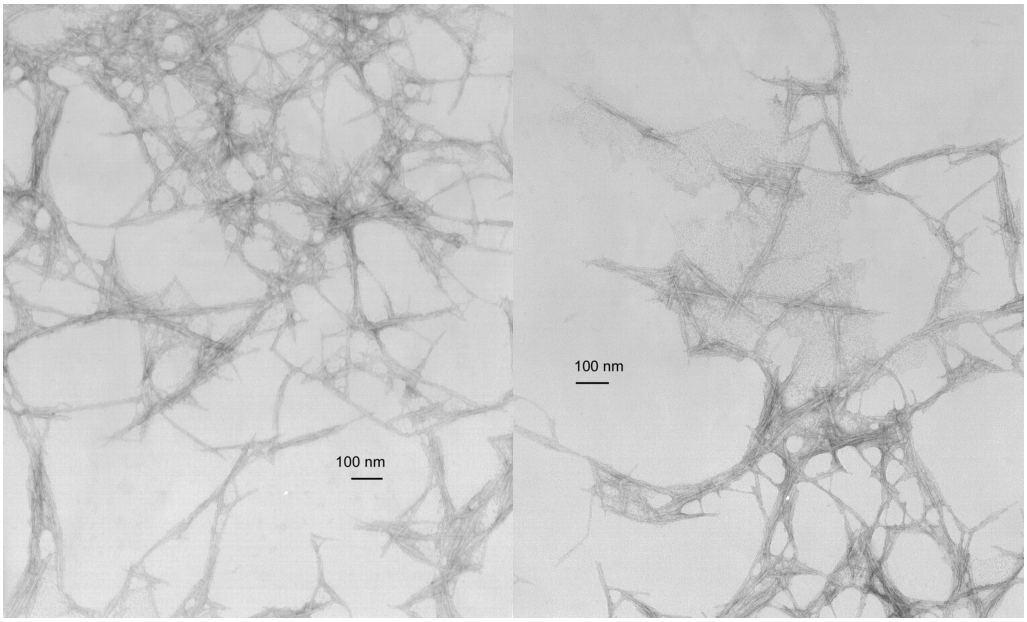

(c) Bottom Phase (d) Bottom Phase

Figure 5.3.2.2: TEM images of LC phase separated C.CNCs at 45kX magnification.

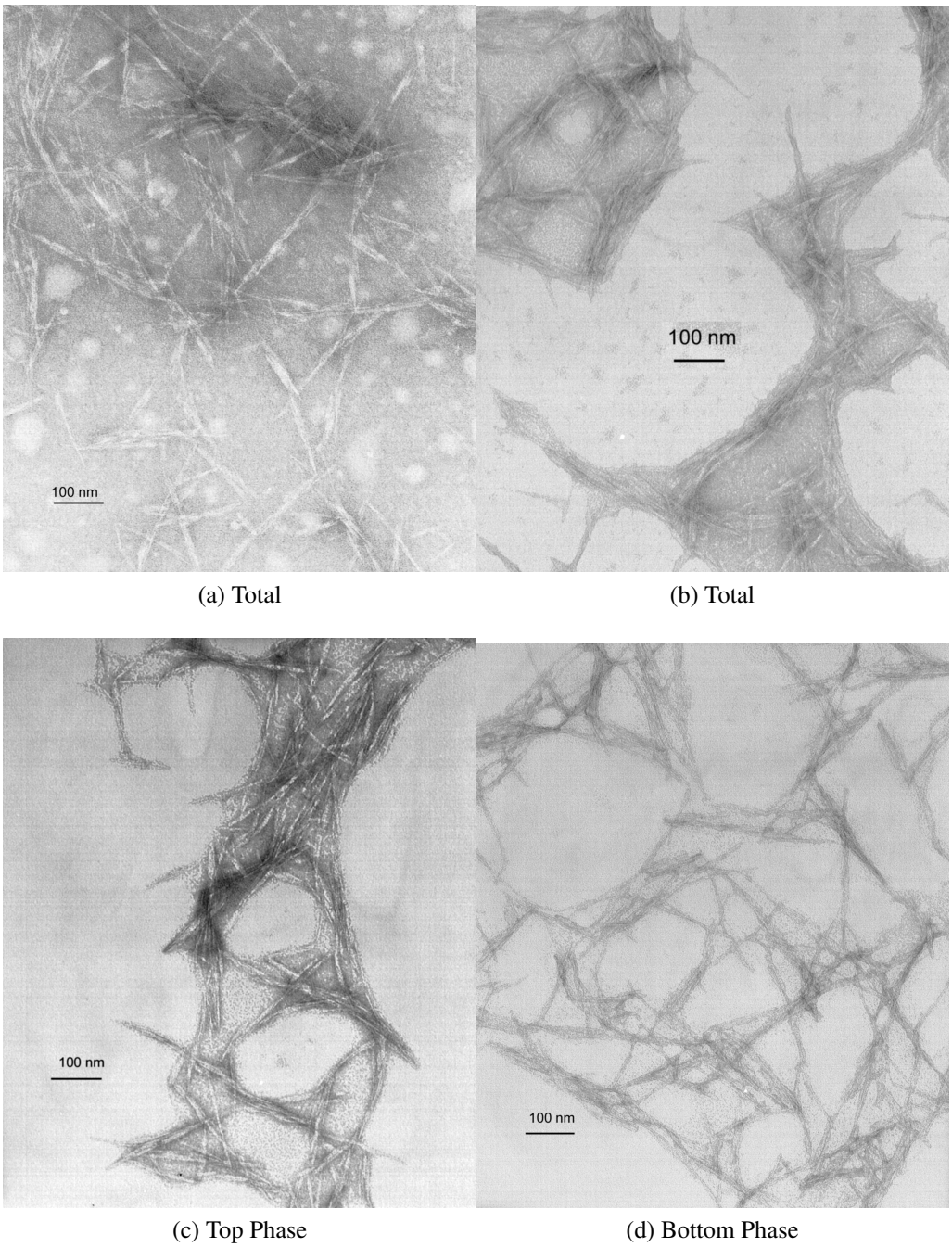

(a) Total (b) Total

(c) Top Phase (d) Bottom Phase

Figure 5.3.2.3: TEM images of LC phase separated C.CNCs at 75kX magnification.

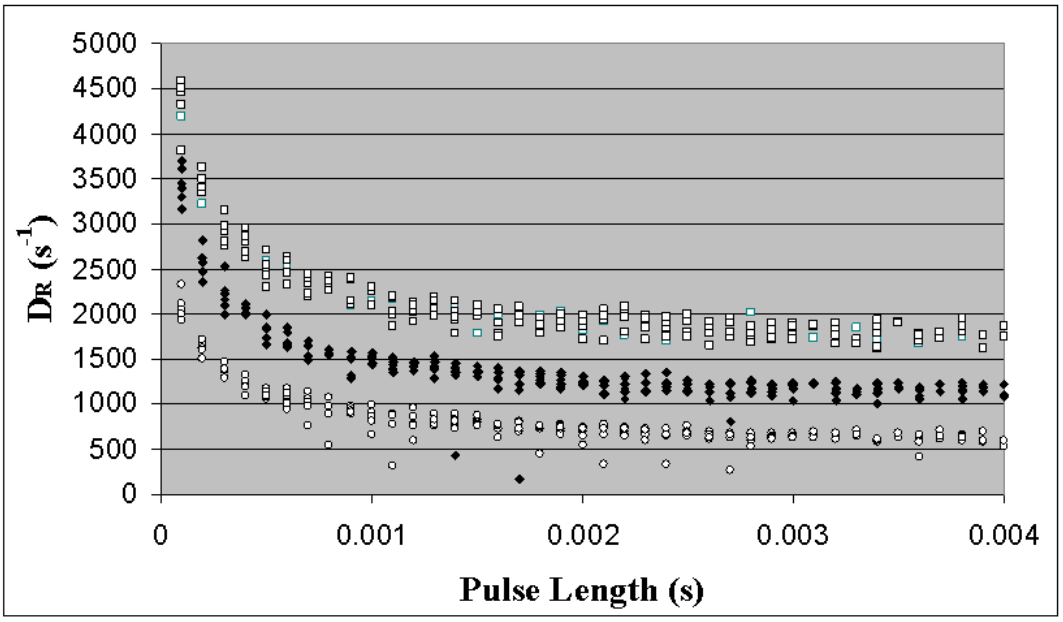

Figure 5.3.2.4: Diffusion coefficients of LC phase separated C.CNCs. Coefficients were calculated over six experiments using a mono-exponential decay model using *Mathematica*, and fitting was ceased when a set signal-to-noise criteria between the data and the model was reached. Outliers were typically shown to arise from fitting truncation due to intermittent noise from switching power supplies, microphonic pickup, and other laboratory contributions. White squares represent the top phase and white circles the bottom phase in Figure 5.3.2.1. Black diamonds indicate the suspension before LC phase separation.

5.3.3.1 TEM of Tobacco Mosaic Virus

Samples were cross linked in 0.5% aqueous gluteraldehyde for 30 minutes, then desalted using Centrifugal Filter Units (Amicon Ultra,Ultracel 50K Membrane, Millipore). Concentrated aliquots of the desalted TMV (1 μL) were placed onto Formvar Carbon TEM support grids (300 mesh, Electron Microscopy Sciences) for several minutes, then excess solutions were wicked off with lab tissue. Grids were then stained with 2% uranyl acetate (50/50 alcohol/water solutions). TEM images were taken by Teresa Sawyer at the Oregon State University Electron Microscopy Facility. The instrument was a Philips CM12 Scanning Transmission Electron Microscope (STEM) running at 80 kV.

5.3.3.2 TEB of Tobacco Mosaic Virus

Truncated pulse TEB measurements were carried out in a 2 cm path-length, quartz cuvette at 270 V/mm peak-to-peak field strength. Data digitization was carried out with a 16-bit, 10 MHz ADLINK ADI9816H analog-to-digital (ADC) converter at full sampling rate (10 MSa/s). Full rise and decay pulses were captured simultaneously with the ADC and the 8-bit Tektronix TDS1012B oscilloscope. Oscilloscope data is shown for illustration only. All diffusion coefficients were calculated from 16-bit data using *Mathematica* (Wolfram Research Version 4.). Mono-exponential decay fits were calculated directly from the initial decay.

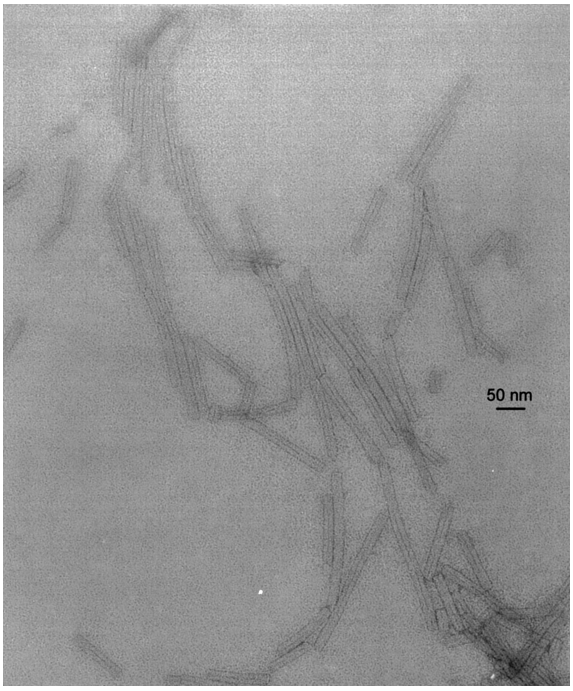

(a) Theo Dreher TMV, 885

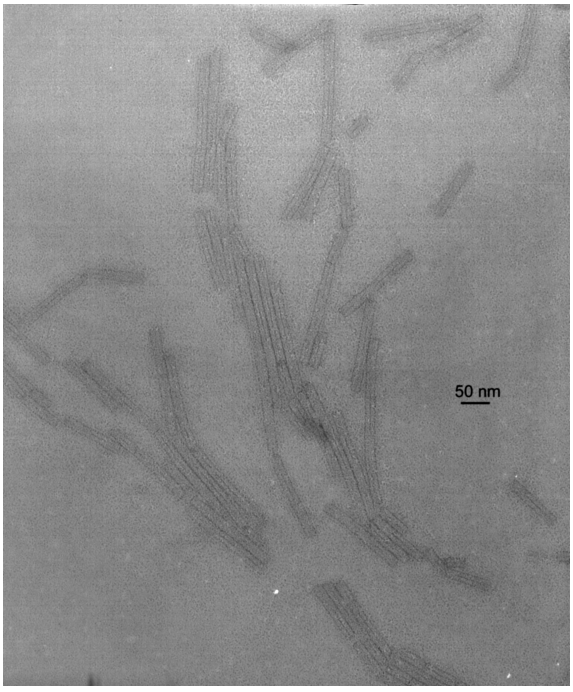

(b) Theo Dreher TMV, 886

Figure 5.3.3.1: TEM images of OSU Tobacco Mosaic Virus (TMV). TMV was provided by Theo Dreher, Department of Microbiology, Oregon State University. Grids were stained with 2% uranyl acetate and imaged at 80 kV.

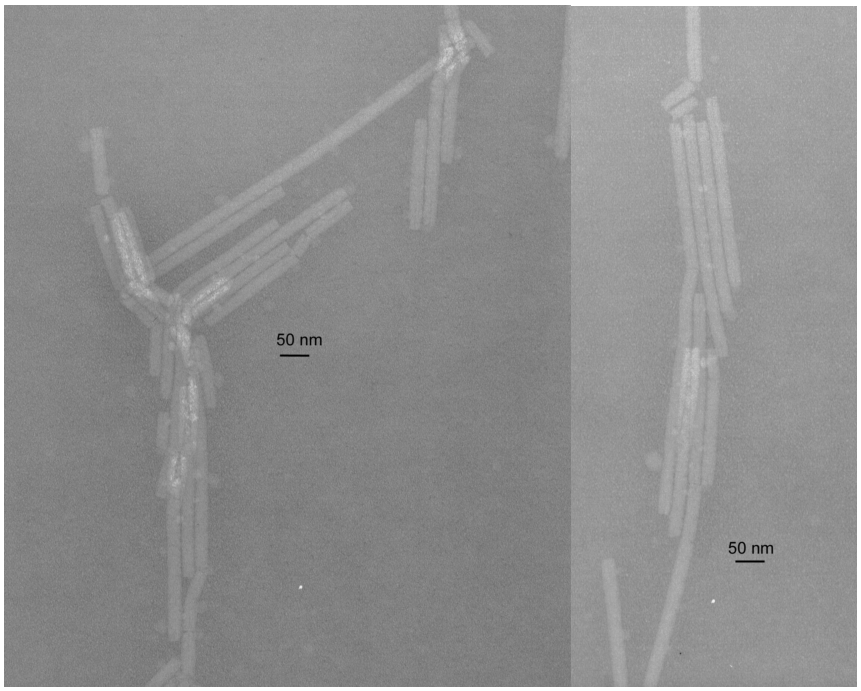

(a) Qian Wang TMV, 889 (b) Qian Wang TMV, 890

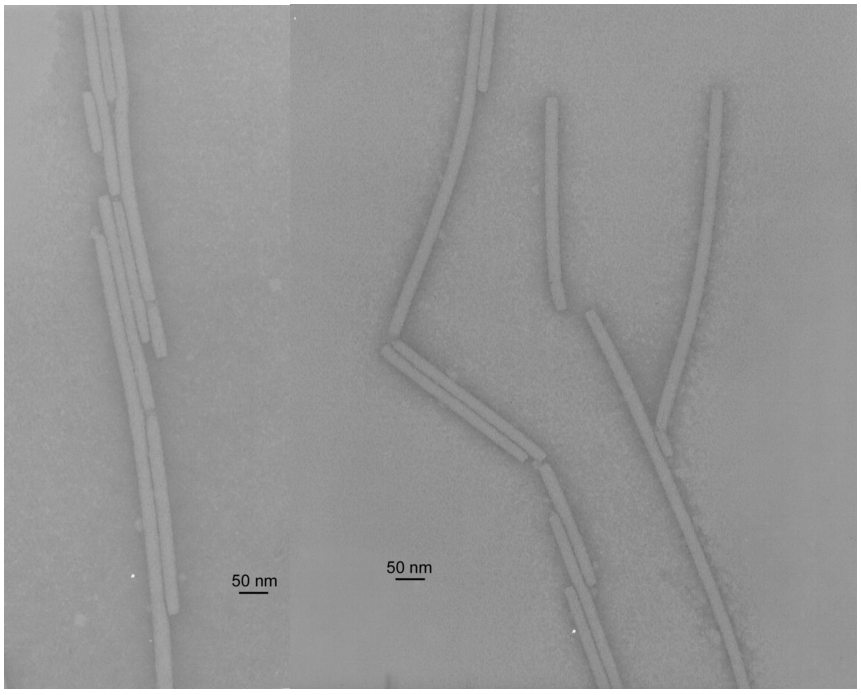

(c) Qian Wang TMV, 892 (d) Qian Wang TMV, 893

Figure 5.3.3.2: TEM images of USC Tobacco Mosaic Virus (TMV). TMV was provided by Qian Wang, Department of Chemistry and Biochemistry, University of South Carolina. Grids were stained with 2% uranyl acetate and imaged at 80 kV.

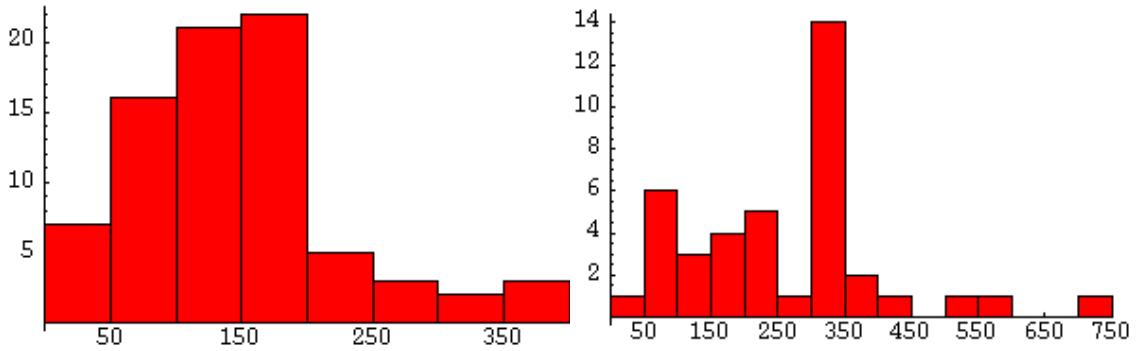

(a) Theo Dreher TMV size distribution

(b) Qian Wang TMV size distribution

Figure 5.3.3.3: Size distributions for OSU and USC TMV samples. Particles from TEM images (Figures 5.3.3.1 and 5.3.3.5) were compared against scale bars to get length distributions. TMVs from Theo Dreher were consistently 16 nm in width, whereas TMVs from Qian Wang appeared closer to 22 nm in diameter. Differences could be attributed to variation in image resolution and focusing, as the TEM was reported to have had focusing errors at the time of imaging.

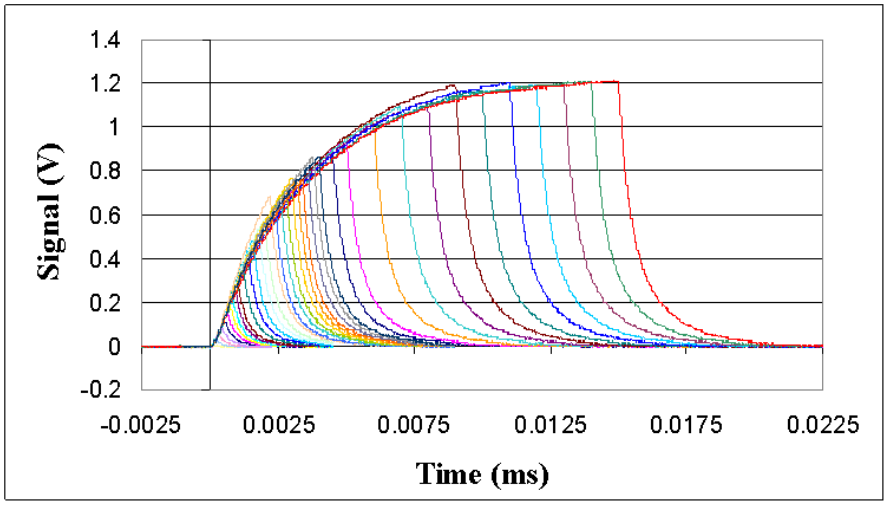

(a) Qian WangTMV

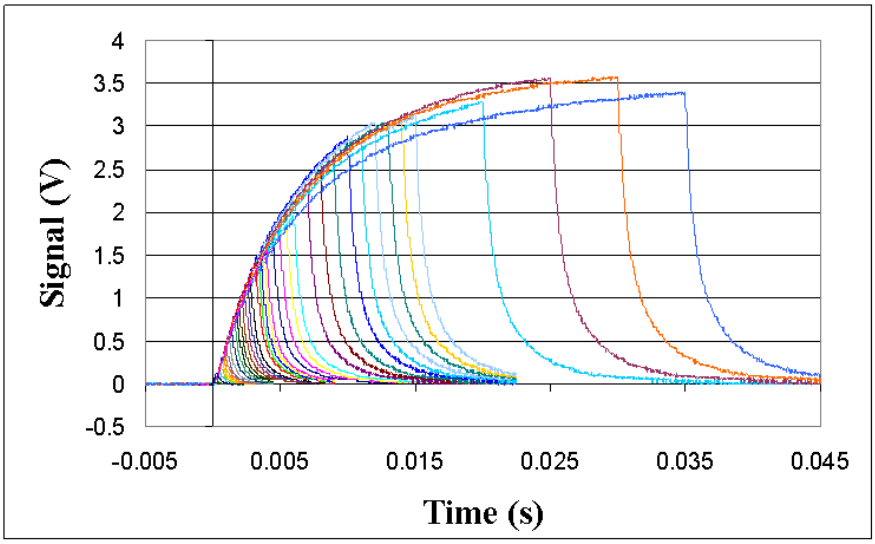

(b) Theo Dreher TMV

Figure 5.3.3.4: Raw data for truncated pulse TEB for different samples of TMV. Applied voltage was 270 V/mm through a 2 cm path-length quartz cell.

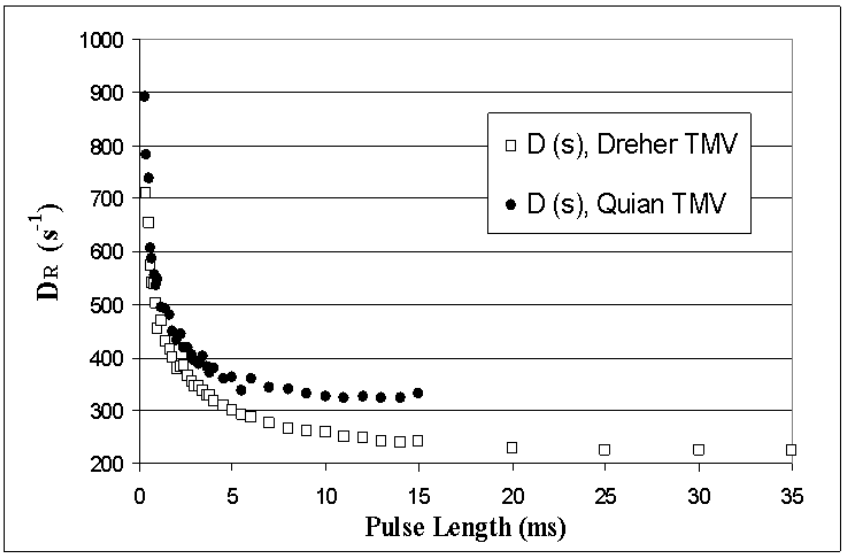

(a) Full Scale

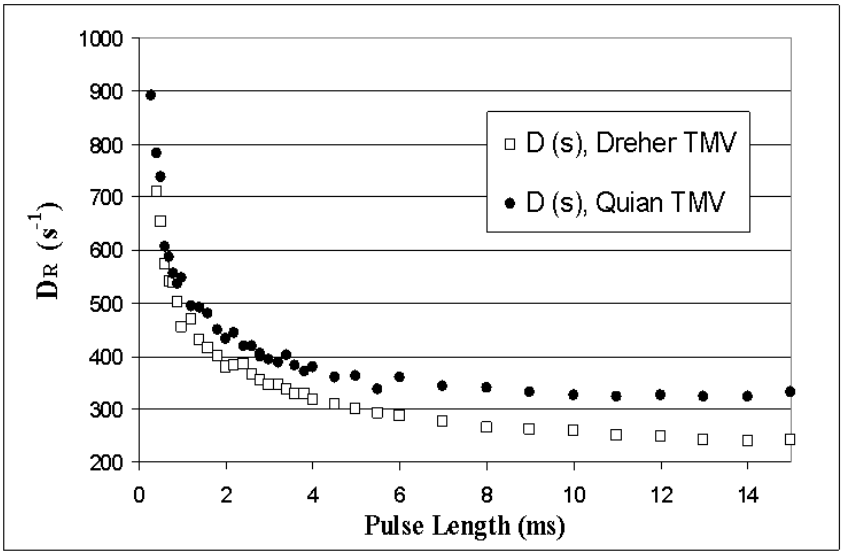

(b) Expanded Time Scale

Figure 5.3.3.5: Diffusion coefficients calculated for different samples of TMV. Truncated pulse experiments were performed for the two provided TMV samples and the diffusion coefficient extracted using *Mathematica*. The TMV from Qian Wang indicates a larger steady state diffusion coefficient at longer pulse lengths, as would be expected from the larger particles seen in TEM images (Figures 5.3.3.1and 5.3.3.5.)

Chapter 6 – Discussion

The outcome of this research was essentially an instrumental development project, where actual experimental data more often revealed instrumental errors to be addressed rather than reliable colloidal properties of our material of interest. Although the bulk of the labwork involved cellulose nanocrystal (CNC) production, these techniques generally involved published protocols rather than the development of novel CNC production methods. We did however run into discrepancies between the reported literature results and those obtained in our lab, which required slight modifications to published protocols. This chapter will start out by briefly discussing these modifications (Section 6.1), then move onto the more challenging development of the TEB apparatus.

6.1 Cellulose Nanocrystal Production

6.1.1 Avicel PH-101 HCl Hydrolysis

It has been well characterized that hydrolysis of native cellulose in strong hydrochloric or sulfuric acid results in a rapid decrease in degree of polymerization (DP) leading to a level-off DP (LODP) which remains constant over a long period of time [1–3]. The initial step in this process is the rapid protonation of the glycosidic oxygen, followed by the fission of the glycosidic bond and the formation of a carbonium ion. The rate determining step is the subsequent attack of water on this carbonium, followed by the regenerating the hydronium ion (Figure 1.2.2.1) [2]. When all the accessible glycosidic bonds have been hydrolyzed, the LODP is reached. This can be measured as a plateau in the increasing

fluidity of the reaction mixture. Beyond this point, the material continues to lose mass according to strictly first order kinetics. This has been attributed to reactions occurring at the (now accessible) ends of the freed crystallites [2].

The production of commercial microcrystalline Avicel PH-101 involves an HCl hydrolysis step which takes cotton linters down to their LODP. Previously published protocols have used this product directly for the TEMPO oxidation reaction and reported the production of nanocrystalline cellulose. The additional HCl hydrolysis in our protocol was found to increase yields of nanocrystals from 5-14% when TEMPO carboxylating directly from untreated Avicel PH-101 to 60-80% with HCl pre-treatment. It is unclear what effect the HCl hydrolysis has in this procedure, as no significant increase in nanocrystal concentration was observed directly from this step. It is thought that heating in HCl may provide better chemical access to oxidizers and catalysts in the subsequent acidification reaction by "activating" (swelling) cellulose as described by [4]. This could occur by reduction of crystallinity due to swelling of crystalline regions, although it has been reported that greater mercerization depth from this type of swelling is achieved in alkali or LiCl solutions rather than acidic solutions [5]. Swelling due to the introduction of water upon attack of the carbonium ion could also be attributed (Figure 1.2.2.1). This is consistent with results from modifying never-dried pulps as described by [6]. If this swelling allowed for greater penetration of the oxidation reactants into the bulk, the resulting carboxylate groups within cellulose aggregates could allow for greater dispersion into nanocrystals upon sonication. It has also been reported that polyuronic acid sodium salts should be soluble in the oxidation media at pH 10-11, and to that end oxidation of cellulose and chitin have been continued until clear solutions were obtained [7]. In our case, the larger scale of the reaction (80 g as opposed to 1 g cellulose) did not lead to clear solutions even after 48 hour TEMPO oxidation at pH $>$9.7. However, clear solutions of the oxidized and washed cellulose were readily obtained upon ultrasonication (Figure 4.1.1.3), with

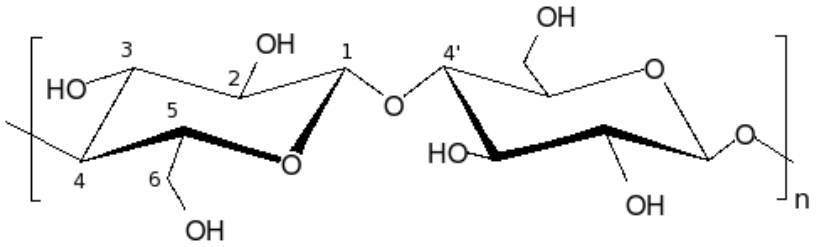

Figure 6.1.1.1: Alternative oxidation sites for cellulose. Hypochlorite in the absence of TEMPO free radical can attack at carbons 2, 3 and 6, and at the glycosidic bond between carbons 1 and 4'.

little agglomerates remaining upon microcscopic observation (Figure 4.1.1.4). It may be of some concern how much mechanical damage occurs to nanocyrstalline whiskers upon sonication. However, AFM imaging shows a high concentration of high aspect ratio, nanocrystalline cellulose in the resulting sonicated suspensions, as well as smaller particulates which could be precipitated salts or cellulose degradation products.

Although the Avicel-PH101 hydrolysis step is in addition to other published protocols for cellulose TEMPO-carboxylation, it was shown to greatly increase yields of nanocrystalline cellulose in our lab. The protocol outlined in this work will typically give upwards of 80% yields of nanocrystalline cellulose after 0.7 μm filtration when care is taken to prevent loss of solids during centrifugation, decanting, and dialysis steps. Since the goal of this work was to reproduce high yield CNC batches for subsequent applications, the additional HCl hydrolysis and sonication steps were deemed necessary. Size separation attempts were subsequently made to address the smaller particulates produced from the harsh acid hydrolysis and high energy sonication steps.

6.1.2 TEMPO Side Reaction Products and Reaction Feed Rates

In the absence of TEMPO, the hypochlorite oxidation of cellulose occurs non-specifically, including attacks at carbons 6, 2, and 3, as well as the glucosidic bond between carbons 1 and 4' (Figure 6.1.1.1). A detailed pH dependent study on the degradation and functional group formation of hypochlorite showed that aldehyde and ketone groups were predominantly formed at pH of 5 to 6, whereas carboxylic groups were predominantly formed at pH 9 to 10 [8]. Degradation to soluble oxidized by-products was determined to be minimal at pH 5-10, as determined by the 99% yields obtained after thorough washing in water. This was thought to be due to the pH 7-10 being too weakly alkaline to cause alkaline degradation, and pH 5-7 being too weakly acidic for acid hydrolysis [8]. As such, the ideal pH for carboxylic acid formation was generally thought to be between 9 and 10 in the absence of TEMPO-mediator.

More specific oxidants, such as periodate at the C2-C3 atoms, and N_2O_4 at carbon 6, may penetrate all phases of the fiber, causing changes in x-ray diffraction patterns. Non-specific oxidants do not penetrate the crystalline regions of the fiber [9]. In addition, non-specific oxidants can continue to attack primary oxidation products, resulting in a wide array of side products. In contrast, the presence of TEMPO-mediator turns the nonspecific hypochlorite oxidation into one preferential to primary alcohols over secondary, as first described by [10] for a variety of alcohols. The mechanism involves the production of a nitrosonium ion oxidant from the stable free-radical TEMPO precursor (Figure 6.1.2.1 (a and b)). Oxidation results in a hydroxylamine by-broduct, which must be regenerated to complete the catalytic cycle (Figure 6.1.2.1 c.)

The TEMPO reaction was introduced for the selective oxidation of primary alcohols in carbohydrate chemistry using OCl-/HOCl to regenerate the nitrosonium ion oxidant in [11–13]. Specifically, the C6 primary hydroxyl in cellulose and chitin is preferentially

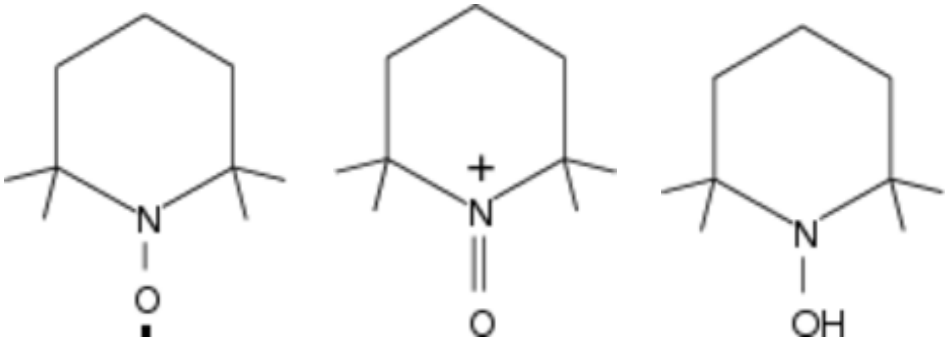

(a) TEMPO free radical (b) Nitrosonium Ion (c) Hydroxylamine

Figure 6.1.2.1: TEMPO intermediates for the cellulose oxidation reaction. The stable nitroxyl radical 2,2,6,6-tetramethyl-1-piperidinyloxy (TEMPO) (a) and the active oxidant generated from TEMPO, nitrosonium ion (b) are shown. The hydroxylamine by-product is produced from (c) upon oxidation of a primary hydroxyl.

carboxylated [14]. The rate of the TEMPO-mediated oxidation of α-D-glucopyranoside was found to significantly increase above pH 9.5 by de Nooy, e al. [8].

Although the addition of excess NaOCl will also maintain the pH at these alkaline conditions, this excess can cause cellulose degradation due to the competing oxidation (glycol cleavage) arising from sodium hypobromite [4]. The established protocol to avoid this reaction is to add small amounts of NaOCl at a time and wait for reaction to cease, or to use greater concentrations of TEMPO. To accomplish the former, it was decided to maintain pH with NaOH so that NaOCl could be added in controlled amounts.

In addition to the risk of degradation products from excess NaOCl, more recent studies have shown significant depolymerization of cellulose under alkaline conditions in the TEMPO reaction [15–17]. However, only recently has work been done to avoid this depolymerization by optimizing the carboxylic acid specificity under neutral conditions [18]. As such, TEMPO reactions for this work were done at pH 9-10 according to previously developed protocols. Subsequent work should, however try to adapt the neutral TEMPO reaction to avoid smaller contaminating particulates that arise from depolymerization.

6.2 Data Acquisition and Quantization Error

The majority of the data in this dissertation was obtained using a digital storage oscilloscope (DSO) as an analog-to-digital converter. Thus it becomes important to understand the basic operational capabilities and limitations of such an instrument.

6.2.1 ADC Conversion and Digital Storage Oscilloscope Operation

6.2.1.1 Scale and Resolution

An anolog-to-digital converter (ADC) is a device that converts a continuous anolog input value, such as a voltage, into a discrete digital number proportional to the magnitude of the input value. When an ADC converts a continuous input signal, the number of discrete values it can produce over the range of analog values is determined by the number of bits in the ADC. When stored in binary form, the number of values is proportional to the number of bits M by 2^M. An 8-bit ADC has 256 discrete values (2^8), for example. The resolution (R) of the ADC is determined by the full scale voltage range (E_{FRS}) by $R = \frac{E_{FSR}}{N}$, where $N = 2^M$ is the number of discrete intervals.

Quantization noise arises from the finite resolution of the ADC. When a linear ADC maps each continuous voltage input value to a corresponding discrete output value, a rounding or truncation occurs. The value the output is given is determined ultimately by the least significant bit (LSB), which comprises $\frac{1}{2^M}$ of the entire signal range. In an eight-bit ADC for example, the LSB is $1/256$th, or around 0.4%, of the total range. Therefore, as the full scale voltage range increases, the quantization noise increases linearly with it.

6.2.1.2 ADC Sample Rates and Synchronous Flash Conversion

The speed of an ADC defines the sample rate, or the number of values it can read and write over a unit time. To overcome the limitations of low sampling speed, various integrated circuit designs have been implemented. One such design, used commonly in laboratory and teaching quality DSOs, is the Synchronous Flash Conversion technology. This design uses an array of comparators, devices which sample two different voltages or currents and adjust their output to indicate which is higher. A single, high speed ADC can be replaced by a parallel array of $2^M - 1$ comparators, where M is the number of bits. The voltage to be sampled is fed into the non-inverting pin of each comparator, and a reference voltage (equal to the converter full scale voltage) into the inverting pin of each comparator in series with a high precision resistor (Figure 6.2.1.1). The circuit is designed such that, as the sampled voltage increases in value, the number of comparators outputting a HI value increases (in order from comparator 1 to comparator $2^M - 1$). The output of all comparators are input into a logic circuit which interprets the value as a binary number. This means that, for example, an 8-bit flash converter would require 255 different comparators. Ensuring that all 255 comparators are calibrated correctly imposes difficulties, as does the need for 2^M high precision resistors

A hybrid pipelined flash conversion technology is also used, where the conversion is split into stages. In this way, the number of comparators required is $(2^N - 1)/M$, where M is the number of stages. In order to get the full sampling rate of the ADC, the comparators are clocked in sequence, with each providing a different sample/value in the final waveform. In this way, only one digital device, the synchronizing clock, needs to be as fast as the compiled sample rate. This reduces the number of high speed comparators required, and thus the total cost of the device.

The synchronous flash conversion allows for much higher sampling frequencies than

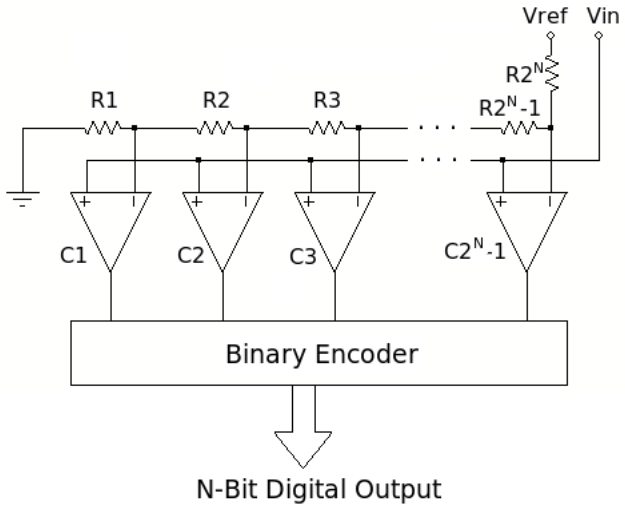

Figure 6.2.1.1: Circuit schematic for a Synchronous Flash Converter. Synchronous flash conversion for a N-bit ADC uses 2^N voltage comparators in the absence of interleaving. Hybrid pipelined conversion allows for comparitors to be clocked in sequence, reducing the number of comparitors required to $(2^N - 1)/M$, where M is the number of clocked stages.

many practical ADCs by dividing the continuous analog input into multiple comparators. The TDS1012B DSO for example has a sampling rate up to 1 GSa/s. However, the waveform is essentially interlaced with samples from multiple comparators, and as such it is prone to sampling errors when variability between input resistors and comparators arise. Regular calibration and maintenance is required to ensure that gain and DC offsets for all comparators are comparable.

6.2.1.3 Nyquist Frequency

The Nyquist sampling frequency theorem defines the minimum frequency of evenly spaced sampling required to uniquely represent a reproducible waveform as $2f_{max}$, where f_{max} is the fastest frequency component in the waveform. Figure 6.2.1.2 shows a waveform sampled at and below the Nyquist frequency. We can see that, although the waveform pe-

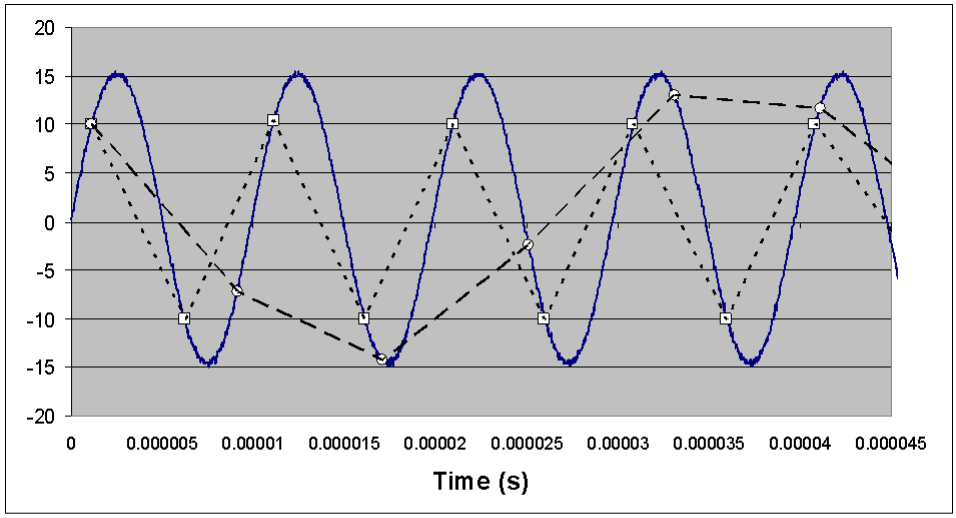

Figure 6.2.1.2: A 100 kHz signal sampled at and below the Nyquist frequency. The highest frequency component of the signal, f_{max}, is 100 kHz. It is sampled at 200 kHz ($2f_{max}$, i.e. the Nyquist frequency, shown as squares with short dashed line) and at 125 kHz (circles with long dashed line.) The periodicity of the signal is represented at the Nyquist frequency, but is misinterpreted at lower sampling frequency. Neither sampling accurately represents the shape of the waveform, however, which requires higher multiples of the Nyquist frequency depending on the periodicity of the waveform.

riodicity can be represented by $2f_{max}$, the actual shape of the waveform generally requires a much higher multiple of $10f_{max}$. A good approximation for a regular waveform would be f_{max}. For a waveform with no periodicity, the Nyquist frequency would in essence be infinite. While it is impractical to sample infinitely, the expected time responses in an experimental system should be understood from a priori data when designing the detection and digitization system so that the representative features are captured.

6.2.2 DSO Memory Depth and Sampling Rates

When a DSO trigger voltage threshold is reached, the trigger circuitry signals the ADC array to start inputting its output values to non-volatile memory. The device samples the

input voltage at regular time intervals, and stores each digitized output value until the memory is full. The number of samples the device can hold is referred to as the memory depth. The sampling rate (the number of samples per second) depends of the time base scale set for the instrument. In the case of the TDS1012B DSO, with a memory depth of 2500 for example, the time base of 5 ms/div x 10 div gives rise to a 50 kSa/s sample rate. The sample frequency becomes ultimately limited by the total length of the waveform. Capturing longer waveforms requires a sacrifice in the sampling frequency, and a loss in waveform information if the Nyquist frequency criteria is not met.

6.2.3 DSO Vertical Resolution

The quantization noise can be controlled by manipulating the input voltage range of the ADC, whereas the electronic and signal noise remain constant over all experimental input ranges. One would ideally like to ensure that the quantization error does not exceed the electronic noise, then maximize the signal-to-noise ratio within the optimal input voltage range. With bit noise increasing linearly with input voltage range (see table in Figure 4.3.4.1), the smallest input signal range that sufficiently dominates over signal noise must be used. This may require attenuation of the signal, either optically at the detector, or electronically with resistors ahead of the input. Optical attenuation can add strain birefringence due to imperfect optics, so a variable controlled resistor circuit may be preferable in this case. The application to data acquisition can be seen in the experimental data obtained by the 8-bit TDS1012B and TDS2024B oscilloscopes. For these devices, the input signal range can be varied from 2 mV to 5 V per division on the vertical scale, and the quantization noise changes for the same signal depending of the scale chosen. Figure 6.2.3.1 is an example of the same signal captured at different scales by the TDS1012B, illustrating the magnitude of quantization error that can be introduced by selecting an

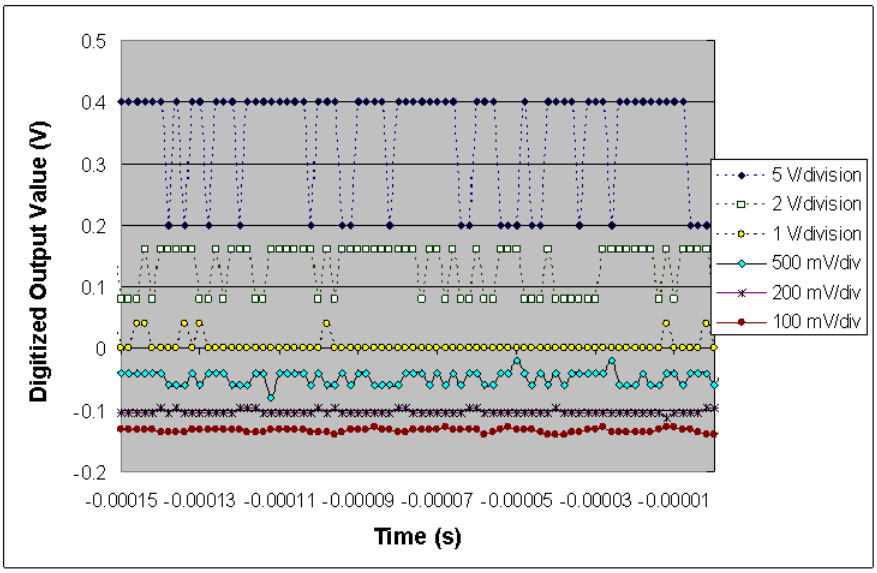

V/div	Resolution (V)
5	0.2
2	0.08
1	0.04
0.5	0.02
0.2	0.008
0.1	0.004

Figure 6.2.3.1: Baseline signal captured at different acquisition gains. The different voltage gains shows how the magnitude of quantization error increases with the full scale input voltage of the ADC. Individual traces have been deliberately offset from each other for clarity, with smallest gain (100 mV per division) at bottom of graph and successively increasing gains going from bottom to top.

inappropriate acquisition scale.

6.2.4 Instrumental and Electronic Noise

The entire experimental setup showed a consistent and reproducible electronic background signal at 50-60 kHz, 10-15 mV peak-to-peak as shown in Figure 6.2.4.1. This is overlaid by various faster signals at smaller amplitudes, possibly thermal noise in the detector compounded with quantization error. The lower frequency, higher amplitude signal has be shown to be unrelated to stray light, occurring with the detector blocked, and can be decreased in amplitude to 6 mV with Faraday shielding of the detector and preamp circuit. Although the exact source is unknown, this noise is generally negligible with respect to experimental data, and represents the maximum noise level that does not arise

from digitization effects.

When digitizing the baseline signal using the 8-bit TDS1012B oscilloscope, we can ascertain that the quantization error becomes comparable to the 50-60 kHz electronic noise at gains of 100 mV/div and higher. At 200 mV/div, the quantization error is equal to the amplitude of the electronic noise, causing a doubling in the background noise amplitude, as seen in Figure 6.2.4.2. At 500 mV/div gain and higher, the quantization error dominates over electronic noise, adding greater uncertainty with greater gain. The effect is somewhat diminished in rise and decay regions of experimental data as shown in Figure 6.2.4.3. However, gains above 1 V/div are still untenable for decay slope analysis as seen in Figure 6.2.4.3. The difficulty quickly arises in finding a suitable acquisition scale that both optimizes the signal-to-electronic-noise ratio while minimizing quantization error. For this system, no such window was found that was able to digitize the entire pulse from baseline to peak. As such, baseline information was discarded in favor of a higher resolution digitization of the falling edge of each truncated pulse.

For this work, the assumption is that the initial decay region upon pulse termination represents an average diffusion coefficient for that experimental condition. By minimizing the voltage gain setting on the oscilloscope and using optical attenuation for longer pulses, it was feasible to measure only the initial slope of the falling edge for each truncated pulse without significant contribution from quantization error. Two advantages to this approach exist, despite the dominance of quantization error over electronic noise in baseline signals at the same gain settings. The first advantage is the rapid change in voltage over time at the pulse edge, which provides better signal-to-noise ratios as described by Jennings [19, 20]. The second advantage is that the slope is taken as a semi-log plot of $ln(voltage)$ versus time. The slope is thus mathematically insensitive to attenuation effects. Slight differences were seen with baseline correction when such data was available, however, indicating a disadvantage in one aspect. It was therefore decided to align the analyzer as

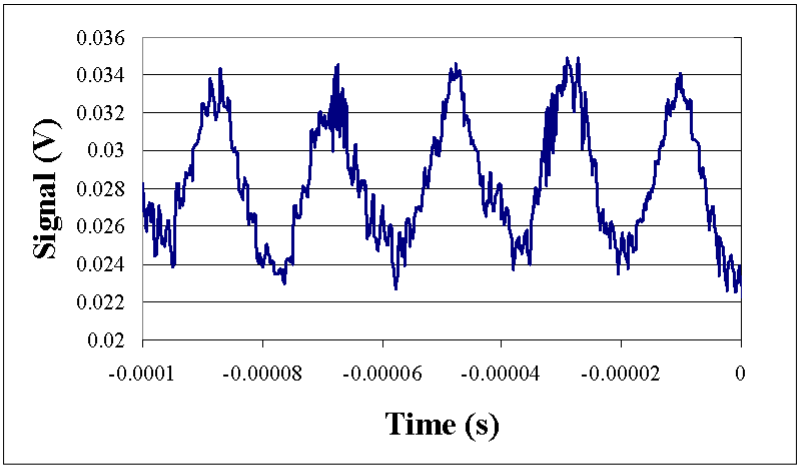

(a) Baseline Electronic Noise.

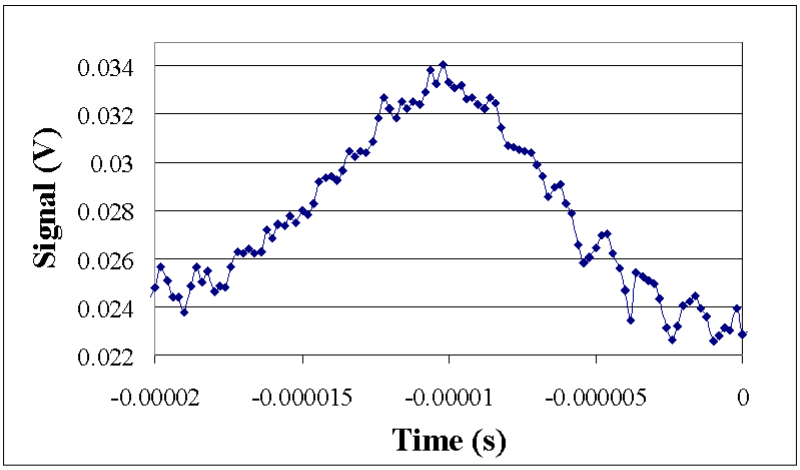

(b) Expansion of waveform showing quantization errors.

Figure 6.2.4.1: Systematic electronic noise. Baseline noise is digitized at 5 MSa/s time resolution and 2 mV/div voltage scale (0.08 mV resolution). Electronic noise is composed of 10-15 mV peak-to-peak, 50-60 kHz waveform, which is overlaid by faster waveforms of smaller RMS voltage, possible digitization errors from the synchronous flash conversion array.

closely as possible to crossed position with the polarizer, with the removal of the quarter wave plate for reasons discussed in Sections 4.2.2 and 4.2.6. This allowed us to minimize baseline contributions, and thus errors in the final analysis.

In addition to the increase in signal-to-noise ratio, a decrease in quantization error occurs upon taking the natural log of the voltage. While this allowed us to get more consistent diffusion coefficients for size analysis, it represents an artificial repression of random noise, which biases the linear inverse analysis in the final stage of processing. A better solution to this problem would be to increase the vertical resolution using a 12-bit or 16-bit ADC, and to take diffusion coefficients directly from an initial exponential decay region computed using mathematical algorithms. In this way larger voltage scales can be captured without significant quantization error. Moreover, baseline and rise curve information could be preserved with each pulse for other analytical applications without loss in fine signal resolution. Significant headway in this area has been made using an ADI9816H ADC (ADLINK Technologies) in tandem with *Mathematica*, as shown in Section 5.3.3.2.

6.2.5 ADC Conversion and Resolution Over Time

Using a digital storage oscilloscope as an ADC for data capture limits the experimenter in time resolution and scale. A continuous ADC board sending data to a computer can be used to save any file size not limited by the computer memory or processing rate. In contrast, a digital storage oscilloscope digitizes a single batch of data to a file that is obtained either by waveform interlacing and sample averaging, or single sequence acquisitions. In both cases, the data set digitized represents the waveform displayed on the screen of the oscilloscope and is limited in length by the memory depth of the oscilloscope, as discussed in the DSO operation section. In the same way the vertical resolution

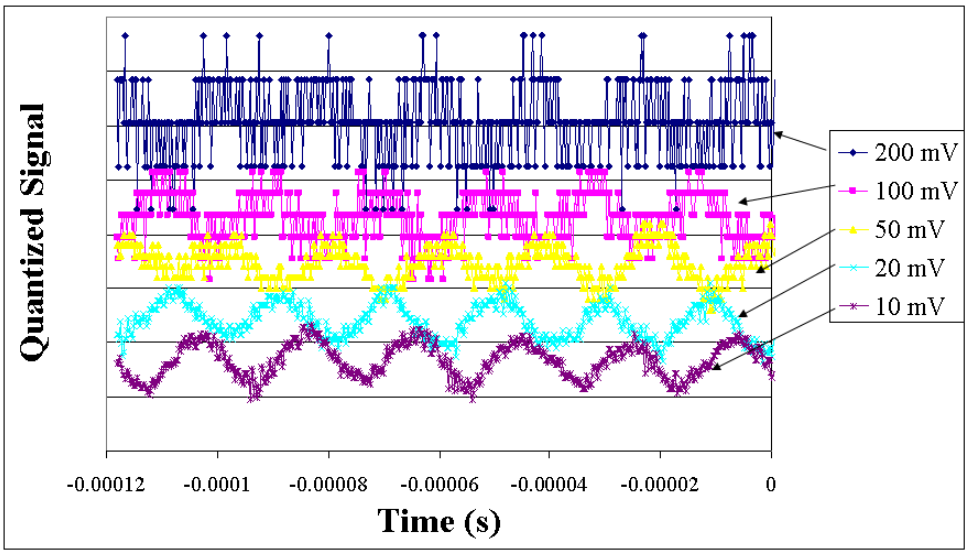

Figure 6.2.4.2: Electronic noise shown in Figure 6.2.4.1 digitized at different gains. The noise is digitized at vertical gains between 10 mV and 200 mV per division. At 100 mV/div gains and higher, quantization noise dominates over electronic noise.

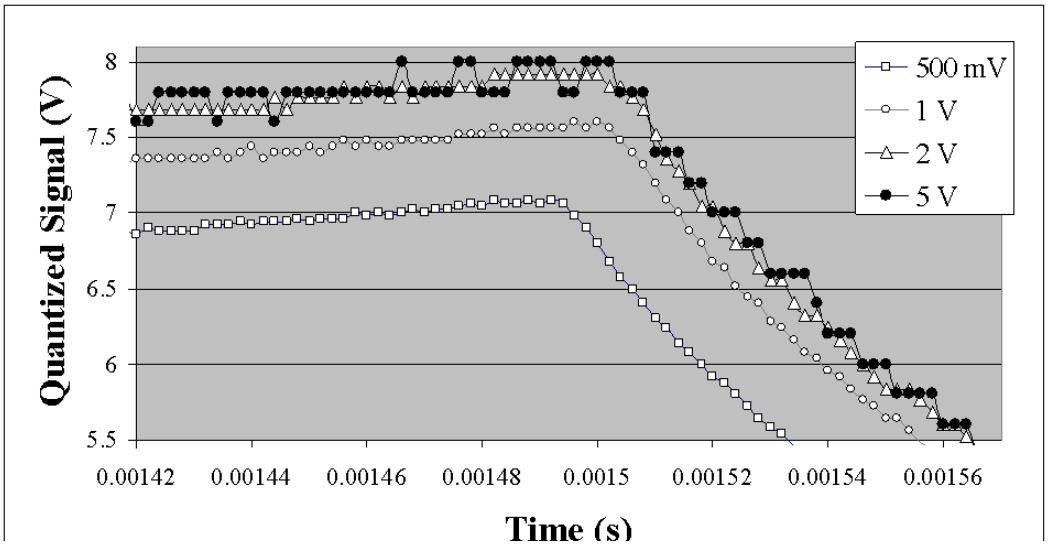

Figure 6.2.4.3: Quantization error over experimental signal. An example of quantization error compounded with the signal is expanded around edge of pulse, illustrating the magnitude of error in the initial slope introduced by quantization noise.

is determined by the total voltage scale chosen divided by the number of discrete digitized increments ($2^{bit\ number}$), the sampling rate is defined by the total time scale displayed by the screen divided by the memory depth. The resolution in time scale thus comes from the scale chosen by the experimenter.

As mentioned above for the this system, the TDS1012B series oscilloscope had a memory depth of 2500 points for all horizontal time scales, and variable time acquisition scales from 1GSa/s at 2.5 μs/div time scale (times 10 divisions to get a total capture period of 25 μs) to 5 Sa/s at 50 s/div (for a total waveform length of 500 s). The difficulty now arises in finding a time scale acquisition window that appropriately samples the high frequency features of the experimental signal, while still capturing enough of the signal to see the overall behaviour of the experiment. Figure 6.2.5.1 shows an example of experimental data samples at two different rates, illustrating how high frequency attributes can be lost in the process of under-sampling, also known as aliasing, when the Nyquist sampling frequency is not met. However, when the oversampled frequency merely reveals the level of quantization noise, as is clearly the case in Figure 6.2.5.1(b), no clear advantage is obtained. Increased resolution must come from both fronts, time sampling resolution and vertical bit-resolution.

As was the case for vertical resolution, a window was not found for this system that captured the full rise and decay regions of the typical truncated pulse while adequately sampling the initial decay region for analysis. The rise curve and the decay to baseline regions were therefore sacrificed in favor of expansion around the pulse edge. Figure 6.2.5.2 shows the same signal captured at 5 MSa/s and 250 kSa/s sampling rates. Although information can be obtained from each sampling, this method involves digitizing two separate pulses at two different times, where experimental drift from Joule heating and electrophoresis make the reproducibility of sequential pulses uncertain.

The long term solution for both voltage and time scale resolutions problems is to

develop a high frequency, 16-bit ADC board in tandem with a real-time operating system computer capable of capturing entire pulses at the optimal sampling rates. Here, additional computer automation can allow multiple pulses to be captured and averaged to account for experimental drift. Edge finding and exponential fitting algorithms could further be incorporated in real time to allow for *in situ* measurements of decay times. While robust mathematical models for estimating diffusion coefficient and size distributions from decay times may yet be lagging, there is no reason for electronics to be the major limiting factor in TEB analysis with current computing resources available.

6.2.6 16-Bit versus 8-bit data

Since the recent acquisition of a 10 MSa/s, 16-bit ADC (ADLINK ADI9816H), a number of comparative experiments were carried out against the Tektronix TDS1012B oscilloscope. The first captured the same signal at 10 MHz over the entire memory depth of the oscilloscope (2500 samples) at 50 mV per division vertical resolution TDS1012B. Figure 6.2.6.1 shows the digitization results for the two different vertical resolutions, showing the clear disadvantage of 8-bit data. Since most experiments require at least a 100 mV per division or greater resolution on the oscilloscope in order to capture the entire trace, the difficulties in data resolution become monumental under normal experimental conditions.

Apart from the obvious advantages of sampling rate and vertical resolution, the several order of magnitude increase in signal-to-noise ratio for the ADI9816H over the oscilloscope is apparent from the power spectral frequency plots (Figure 6.2.6.2.) In order to compare the experimental signal-to-quantization noise ratio (SNR_Q) of the TDS1012B scope to the reported SNR of the ADI9816H, a 1 MHz, 1.8 V peak-to-peak sinusoidal signal was input to the oscilloscope in order to match the conditions reported by the ADI9816H technical manual. The fast Fourier transform was measured for comparison.

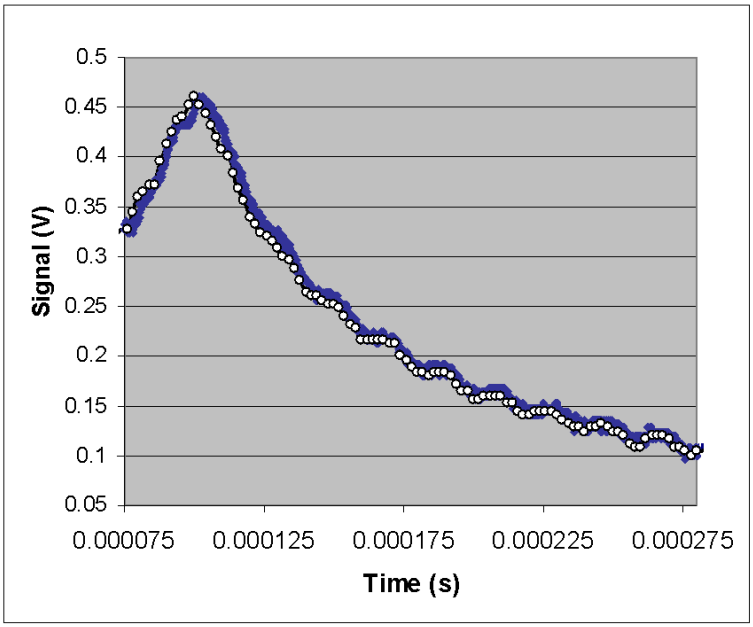

(a) Undersampling

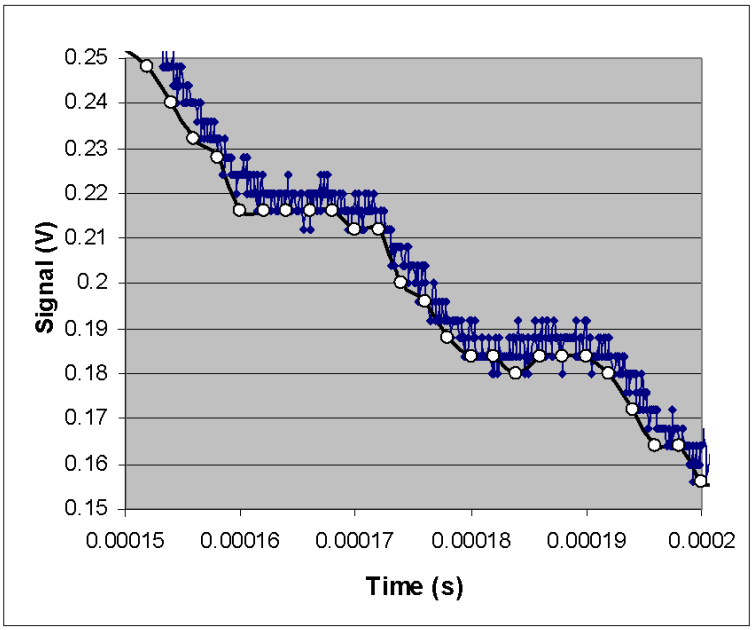

(b) Undersampling expanded

Figure 6.2.5.1: Undersampling bias on signal imposed with electronic noise. This example is digitized at 100 mV/div vertical scale, with a resolution of 4 mV. Lower frequency waveforms are represented by both sampling rates. Faster frequency components represented at 10 MSa/s (closed diamonds) are unrepresented at 500 kSa/s (open circles).

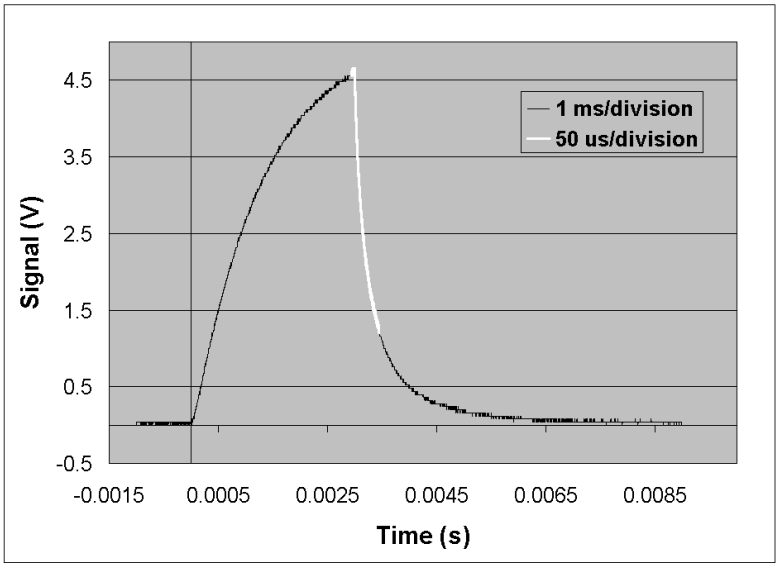

(a) Typical truncated pulse

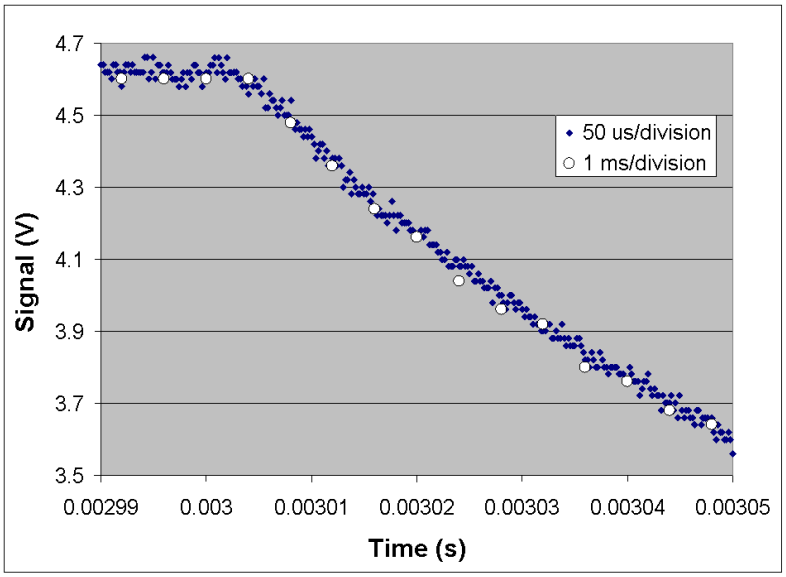

(b) Typical truncated pulse expanded

Figure 6.2.5.2: Typical truncated pulse for two different sampling rates. Entire memory depth waveforms are shown in (a) for sampling rates of 5 MSa/s (white line, digitized at 500 mV/div, 0.02 V resolution) and 250 kSa/s (black line, digitized at 1 V/div, 0.04 V resolution). Expansion around the pulse edge in (b) shows the effect of biasing from under-sampling at initial pulse edge.

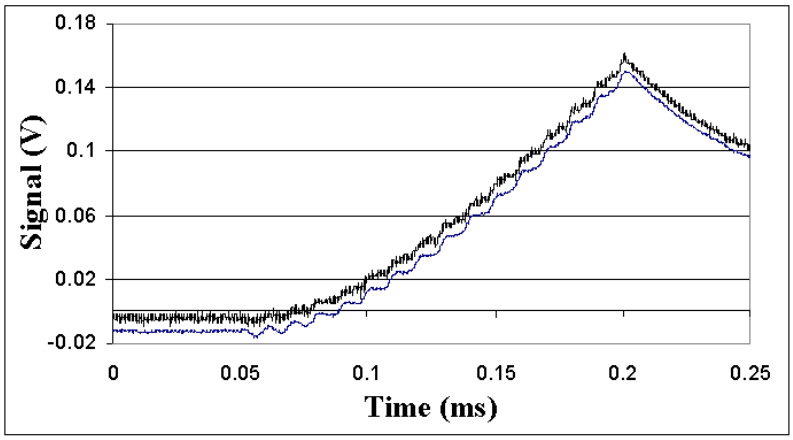

(a) Full Range

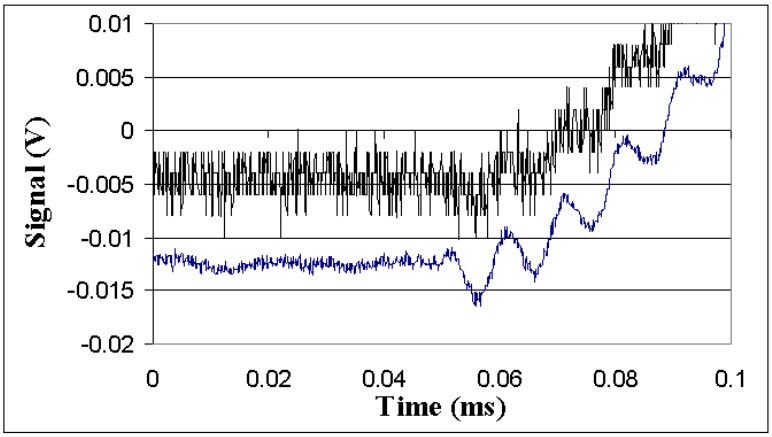

(b) Expanded around baseline

Figure 6.2.6.1: Digitization using 8-bit versus 16-bit ADCs. TEB traces are digitized by an ADLINK ADI9816H 16-bit ADC and a Tektronix TDS1012B 8 bit digital oscilloscope at 50 mV per division resolution

The definition of the SNR_Q for a given ADC is the ratio of the root mean square of the value of the input signal to the root mean square of the quantization noise of that ADC, and is given mathematically by

$$SNR_Q = 6.02N + 4.77 + 20log\ 10(L_F)\ [dB], \tag{6.2.1}$$

where N is the number of bits, and the loading factor L_F is equal to 0.707 for a sinusoidal input signal. Therefore, the maximum SNR_Q possible for a 16-bit ADC is 98.09 dB, whereas the maximum possible for an 8-bit ADC is 49.93 dB. These are confirmed in Figure 6.2.6.2 at the 1 MHz peak for each ADC. The ADI9816H actually has a greater than 98.09 dB SNR_Q, which could be explained as the effect of oversampling discussed in [21]. This difference may not seem significant until one recalls that dBs are measured on log scales, and this represents several orders of magnitude improvement in SNR_Q.

6.2.7 Data Acquisition Summary

TEB analysts have historically used oscilloscopes to capture traces, and with the advent of digitizing oscilloscopes, to obtain digital information for data processing and exponential fitting. The 8-bit oscilloscope represents a dated technology however. Despite the historical attachment many experimentalist still have for them, recent 16-bit, high speed ADCs are now relatively inexpensive and accessible for off-the-shelf applications. A revolution in data capture would benefit the TEB field. Fine detail in the frequency response is often lost in favor of gaining global information on the trace, which switching to an appropriate 16-bit ADC would prevent. In addition, the signal-to-noise ratio can often be improved by several orders of magnitude. All future work in our lab will use digital oscilloscopes for monitoring purposes only, and 16-bit data for all future data processing.

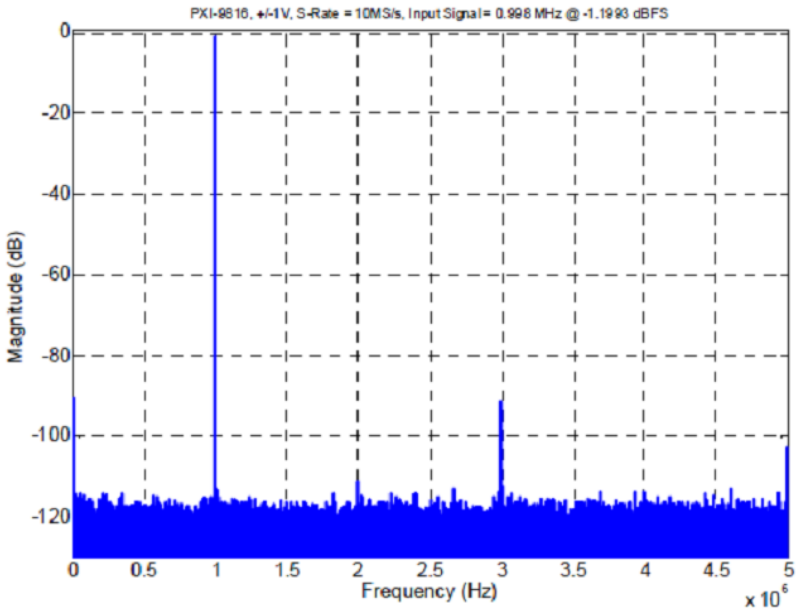

(a) ADLINK ADI9816H ADC

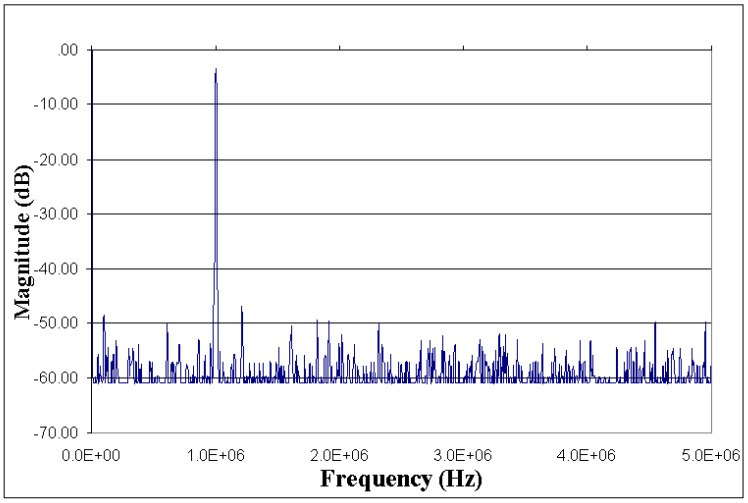

(b) Tektronix TDS1012B DSO

Figure 6.2.6.2: Power spectral density (PSD) plots of 16-bit versus 8-bit ADCs. An ADLINK ADI9816H 16-bit ADC PSD is compared to that of the TDS1012B 8-bit digital oscilloscope.

6.3 TEB for Macroparticle Characterization

6.3.1 Linear Inverse Calculations for Size Distribution Determination

For polydisperse systems, the challenge in applying inverse theory to the extraction of sizes via optical measurements of exponential decay is embedded in layers. Firstly, the exponential decay under any experimental condition represents multiple diffusion coefficients for each contributing species. Extracting each diffusion coefficient for each species is in itself an inverse problem, fraught with its own uncertainty. The data is also convoluted by optical and experimental drift. Complicating this, the models for diffusion coefficients as a function of particle dimensions are heavily debated. Solving this inverse problem requires a pulse of sufficient duration or amplitude such that all species in solution are represented, that is they have reached their steady state distribution. Steady state distribution does not, however, equate to the same degree of alignment for each species, since the degree of alignment will vary with the length of particle. The application of geometry sensitive models is therefore not necessarily straightforward.

Secondly, assuming that distinct diffusion coefficients can be measured for dominating species using controlled field conditions [19, 20, 22, 23], the determination of size distributions now becomes a second inverse problem requiring a quantized ensemble of estimated diffusion coefficients. Each of the estimated coefficients are associated with optical noise and drift, and are now additionally convoluted with no small degree of error and uncertainty given the measurement technique. The solution then requires an appropriate and accurate model to equate diffusion coefficient to particle dimensions. The matter is one of considerable debate in the field. The discussion below will attempt to describe the specific challenges encountered in this research.

6.3.1.1 Uncertainty in Determining Diffusion Coefficients

Although various methods have been suggested in the literature for estimating coefficients from multi-exponential decay curves, the method we relied upon most for this work was that proposed by O'konski [24] and later by Jennings [25]. Here, the initial linear decay from a semi-log plot of birefringence versus time was considered to be the average diffusion coefficient. Although there is no rigorous evidence that this is the case, the experimental ease of using this method makes it more appealing. We found however that the "initial linear" description in the literature came with significant ambiguity when it came time for experimental interpretation. Since the slope in the "initial linear" region decreases continuously with time, the curvature of which increases with polydispersity, increasing the amount of time over which the data was fit gave increasingly lower diffusion coefficients. This is shown in Figure 6.3.1.1. For the same series of pulses, diffusion coefficients were extracted for 6, 11, and 26 μs after the termination of pulse, with lower diffusion coefficients being obtained for longer sampling times. For the top and total phases, the diffusion coefficients clearly overlap for different fitting times.

In the absence of any theoretical rational for selecting one fitting time-range over another, we debated several methods. By selecting an arbitrary time scale for all samples, we could not be certain we were representing the same fraction for samples of different size distributions. That is, samples with a smaller overall size distribution may require a shorter decay region to represent the same fraction of particles that a sample with longer particles would require. Selecting a linear regression fit parameter did not prove to be a rigorous enough method for consistent results given the difficulties we had with undersampling and quantization noise arising from 8-bit data (Recall Section 6.2). What we found, however was that choosing the same time scale for all samples within any given experiment appeared to give consistent and reproducible results. We therefore present data

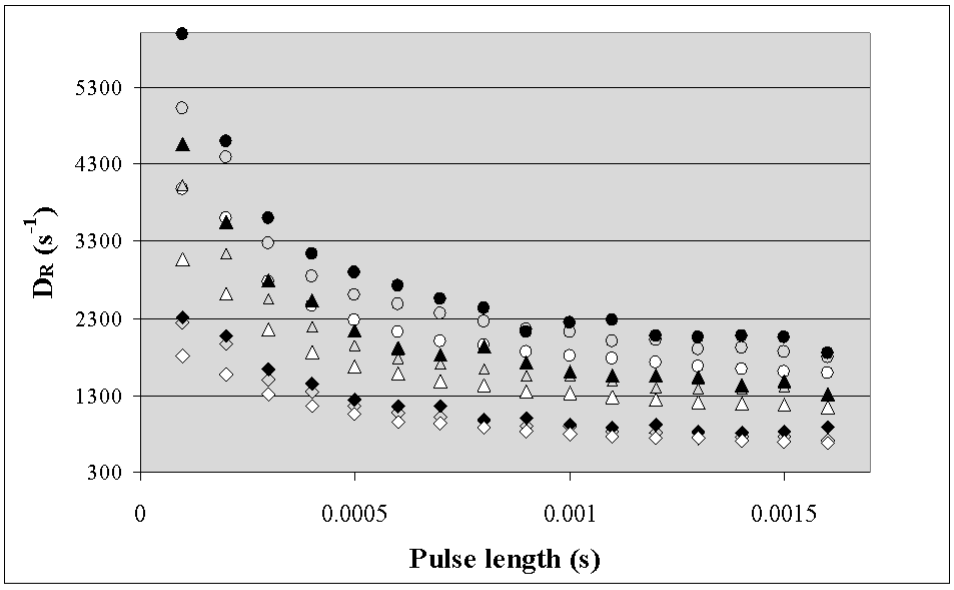

Figure 6.3.1.1: Diffusion coefficients calculated over three different decay times. Coefficients were determined from truncated pulse TEB for the top phase (circles) and the bottom phase (diamonds) in Figure 5.3.2.1, as well as for the total unseparated suspension (triangles). Coefficients were calculated using the semi-log plots of signal versus time, starting at the end of the excitation pulse and continuing for either 6 μs (black), 11 μs (gray), or 26 μs (white). The uncertainty in the 'initial linear' response method is apparent from the overlap in diffusion coefficients for top and total phases at long and short fitting times.

for sample diffusion coefficient distributions as relative to one another under identical processing conditions and make no claims as to the accuracy the the reported coefficients themselves.

6.3.1.2 Truncated Pulse: Difficulties with Jennings Method

In order for a linear inverse theory to be robustly applied to experimental data, several criteria need to be met. Firstly, a model that accurately describes the system must be applied. Secondly, the inverse method must suppress noise, or at least not amplify it. Thirdly, the noise should be 'small'. Fourthly, the data should be robust and trustwor-

thy (that is, have reasonable measurement uncertainties.) Fifthly, the solution must (a) converge when model data is applied, and (b) should still converge to model data when random noise is added. The sixth criteria is that he data should be oversampled in all parameter space.

The difficulty with the first point was addressed in section 3.1.2.5 in context of conflicting models for diffusional coefficients for cylindrical particles. The third and fourth points are issues in our data as seen from the experimental drift (take for example Figure 5.3.2.4), as well as the characterized noise associated with our digitization and detection methods. We hope in the future to control much of the drift using a thermally regulated cell and insulative coatings for electrodes. The quantization noise has largely been remedied with the 16-bit ADC; the planned improvements in the detector will reduce thermal noise and resonant effects, as well as improve the detector response time.

The second and fifth points come from the specific inverse method. Since real data will inevitably have noise, an exact fit to the model will not converge to a realistic solution unless a reasonable estimation of that noise is incorporated into the regression. Provencher develops a parameter called the regularizer to do this. In addition, they use a 'parsimony' analysis which attempts to use the most simple model that will yield novel information.

Although Jennings, et al. claim to use the 'Provencher parsimony' analysis in their statistical least squares procedure [19], they adopted several short-cuts which compromise the trustworthiness of their convergence. For one, they do not explicitly incorporate an experimental noise term, nor do they impose constraints such as all positive model parameters, as demonstrated by the negative values they obtained for overly restricted length ranges. Provencher states in [26] that for certain cases (when experimental error $\epsilon_k = 0$), there are exact analytic inversion formulas for s_λ. (Recall definitions from Equation 3.2.2 and Section 3.2.1.) He continues however, "any 'exact' inversion ignoring ϵ_k will select

from Ω one member which will depend on the ϵ_k. In view of the unboundedness of the errors$\cdots$ this member will be a poor estimate of true s_λ. Therefore exact inversion formulas or iterative algorithms converging on them cannot be directly applied to experimental data." Likewise, Jennings, et al. acknowledge that their "method had the disadvantage that it attempted to provide an exact fit to the data. It is not uncommon to fail to find an all-positive solution owing to experimental uncertainties in the transient decay data." [19] After significant work with the Jennings algorithm, our group came to realize the significance of this caveat. In order to obtain realistic convergences, some estimation of the uncertainty must be incorporated into (or estimated from) a least squares fitting algorithm just as would be required of a full linear inverse problem.

In order to test the Jennings method for cellulose nanocrystals, an algorithm was written by Dr. John Simonsen using the protocol outlined in [19]. To test the algorithm, model data was generated for bimodal size distributions of 50/50 size fraction, and trimodal size distributions for 22/56/22 and 33/33/33 size fractions. A constant diameter of 7 nm was assumed using the average diameter measured by AFM. The effects of changing the cycle criteria (lowest acceptable error for a cycle fit) and the order of the search (from low to high values versus from high to low values) were explored. Figure 6.3.1.2 shows the fit for the algorithm to model data for the bimodal distribution, with a chi-squared value of 93. Figure 6.3.1.3 shows an improvement in the chi-squared value with a more stringent cycle criteria imposed for trimodal data. The effects of search order are shown in Figure 6.3.1.4. From all three figures, it can be seen that the algorithm fails to converge satisfactorily for any of the distributions or processing methods, violating the fifth criteria listed at the beginning of this section. Despite this, the algorithm was applied to experimental data for LC phase separated C.CNCs to see if a statistical difference could be obtained.

An additional difficulty in Jennings method came from their oversimplification of the Perrin model for rigid rods. In their original paper, they assumed the diameter of their

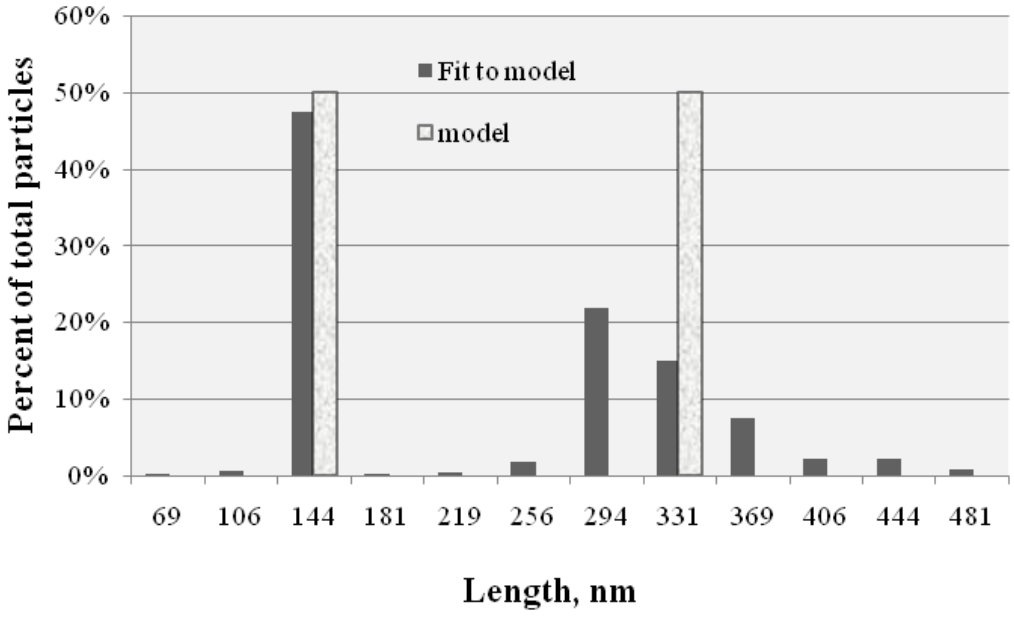

(a) Fit to model bimodal data

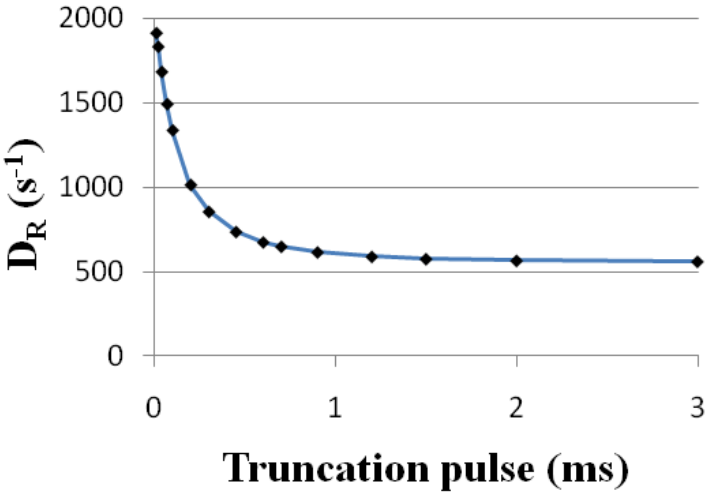

(b) Model diffusion coefficients for bimodal data

Figure 6.3.1.2: Model data for a bimodal distribution fit. The fit uses Jenning's least squares method [19]. Chi-squared value was 93.

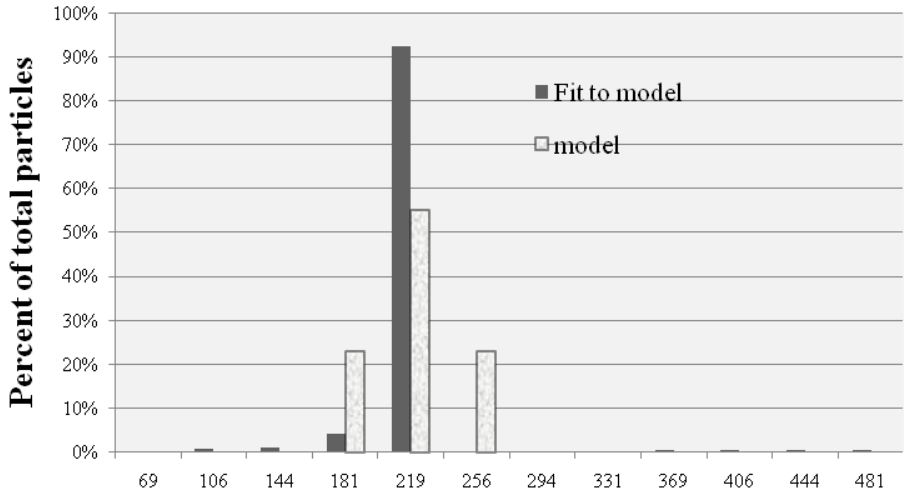

(a) Trimodel fit for a cycle criteria of 10^{-4}, chi-squared of 115.

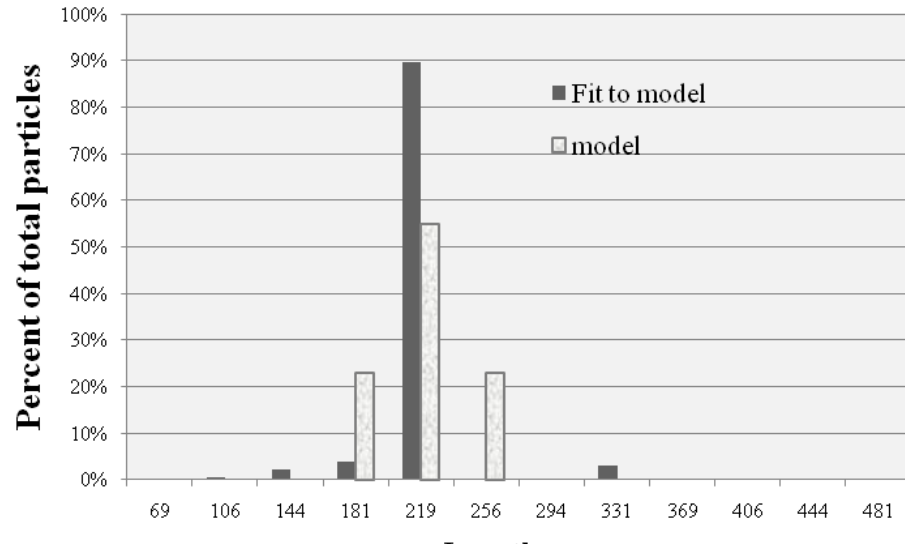

(b) Trimodel fit for a cycle criteria of 10^{-5}, chi-squared of 44.

Figure 6.3.1.3: Model data for a trimodal distribution fit using different cycle criteria. The cycle criteria sets the minimal acceptable error between the data and the converged solution throughout the iterative fitting process.

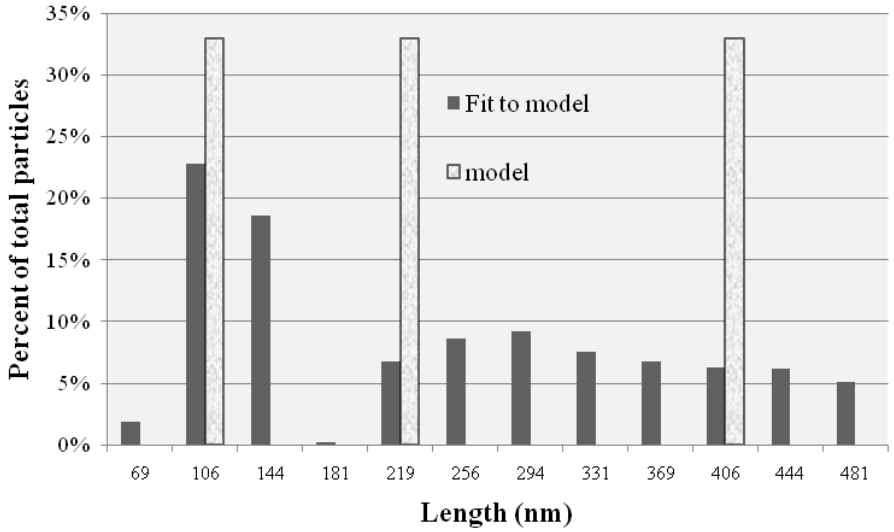

(a) Trimodel fit for a cycle criteria of 10^{-5}, searching from low to high. Chi-squared was 130.

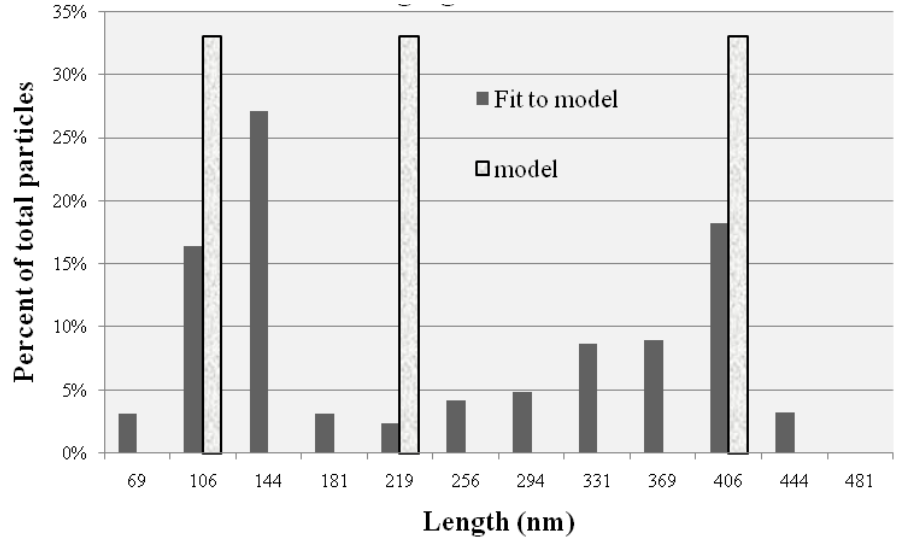

(b) Trimodel fit for a cycle criteria of 10^{-5}, searching from high to low. Chi-squared was 406.

Figure 6.3.1.4: Model data for a trimodal distribution fit. The fit uses a cycle criteria of 10^{-5}, and searches from low to high (a) or from high to low (b).

test particles was constant regardless of length. Since this in not supported in our AFM analysis of C.CNCs, we modified the method to include constant diameter, constant aspect ratio, and a gradiated aspect ratio with particle lengths. The converged results for each of these models is shown in Figures 6.3.1.5 and 6.3.1.6 for phase separated C.CNCs. Slight differences were seen between models for each phase, the statistical significance of which is still under discussion in our group. The fit regression between data and model is shown to the left of each generated histogram, indicating an improvement in fit with deviation from the constant diameter assumed by Jennings.

The final criteria, point six, is clearly not met by our TEB data as it is currently obtained. The parameter space for TEB includes variation in sample concentration, strength and frequency of applied field, and field duration. Without an automated measurement system, it is infeasible to get a full sampling of frequencies and field strengths. A one dimensional parameter was used for each inverse regression (in our case variation in field duration over constant field strength and frequency.) It may be intuitively thought that an increase in parameters degrees would narrow the convergence, i. e. a two dimensional inverse regression. However, the increased number of variables, and their associated uncertainty can lead to statistical over-fitting. As such, even more control over experimental noise is required. A two dimensional inverse regression would therefore require extensive modifications of the apparatus and the data capture methods currently in use. Additionally, a higher level of mathematical sophistication would be required for a two dimensional analysis. Future collaborations are currently being sought which will allow us to address these issues.

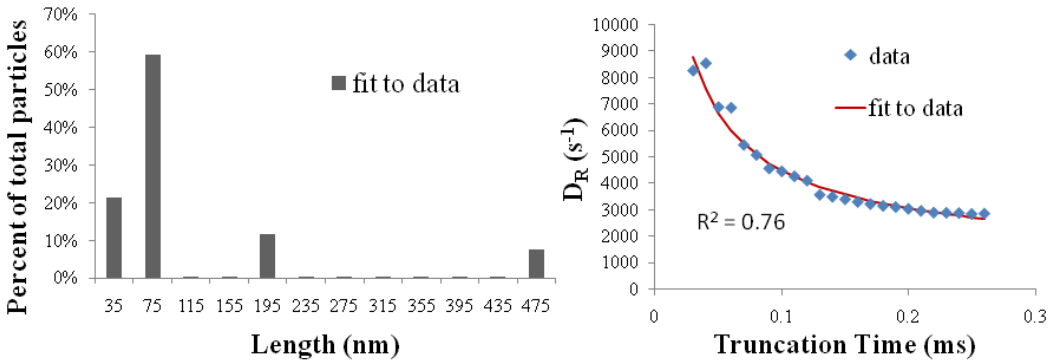

(a) Top phase, constant diameter (7 nm)

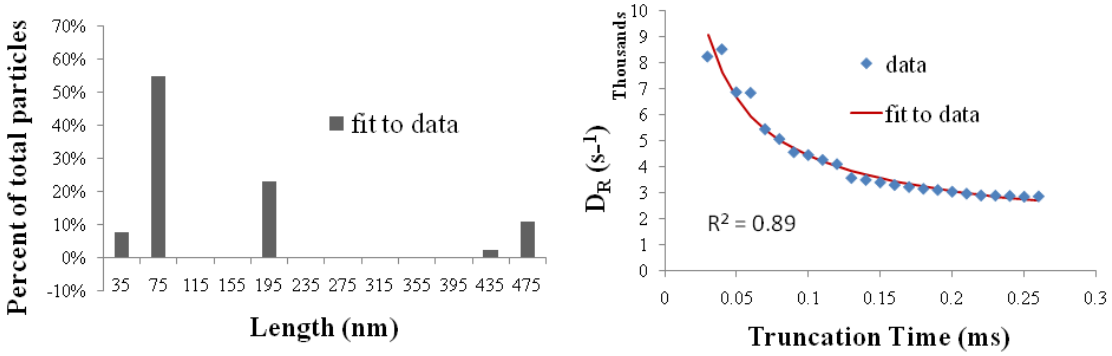

(b) Top phase, constant aspect ratio (20)

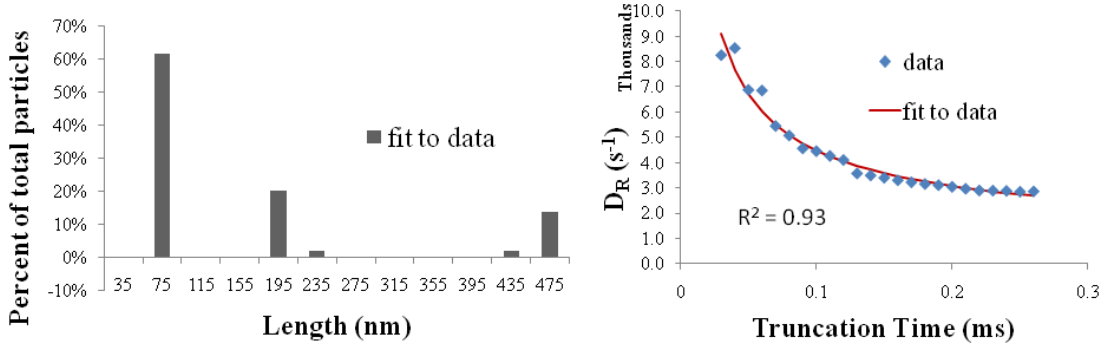

(c) Top phase, gradiated aspect ratio

Figure 6.3.1.5: Aspect ratio dependence of Jenning's method. A linear inverse fitting method [23] is applied for constant diameter, constant aspect ratio, and gradiated aspect ratio for the top phase of a C.CNC LC phase separation using TEB truncated pulse experiments. Size distributions are shown to the left, and the model fit to measured diffusion coefficients to the right.

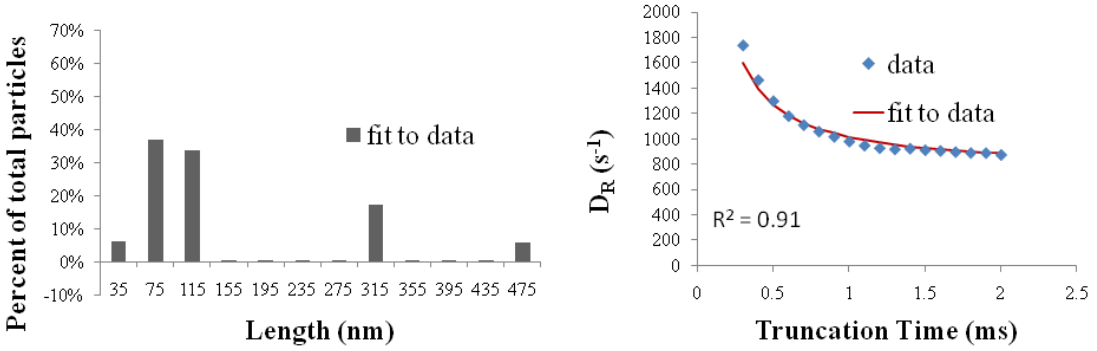

(a) Bottom phase, constant diameter (7 nm)

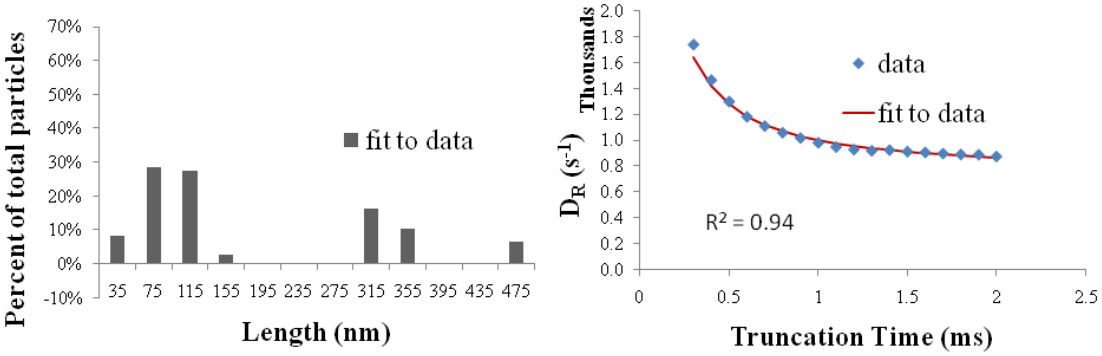

(b) Bottom phase, constant aspect ratio (20)

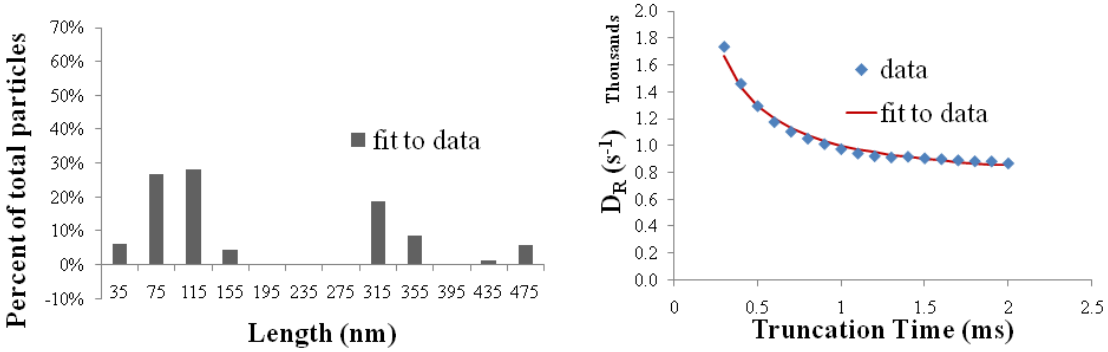

(c) Bottom phase, gradiated aspect ratio

Figure 6.3.1.6: Aspect ratio dependence of Jenning's method, bottom phase. The same linear inverse method is applied as in Figure 6.3.1.5 for the bottom phase of C.CNC phase separation. Size distributions are to the left, the model fit to measured diffusion coefficients to the right.

Chapter 7 – Conclusion

7.1 CNC Dispersions

A method for producing up to 80% yields of truly nanocrystal sized C.CNCs was developed from modifications of existing protocols, which we determined did not produce the reported percent yields after rigorous filtration and removal of all particles greater than nanosized crystallites. We demonstrated a size exclusion technique specific to C.CNCs using liquid crystal phase separation, and demonstrated a method for laboratory scale preparative separations. The difference in relative size distributions between phases was demonstrated using AFM and TEB. The necessity of surface charge was proven for the occurrence of C.CNC liquid crystal behavior and the inhibiting effect of shielding counterions was demonstrated.

7.2 TEB Apparatus and Protocols

We have developed a TEB apparatus with improved data resolution and signal-to-quantization noise ratios using a 16-bit ADC. The necessity for improved signal-to-electronic noise ratio for measured TEB signals was established from frequency domain experiments, and methods for improvement were outlined. This includes the development of a low noise detector optimized for the low input impedance ADC requirements for the optimization of overall system performance.

We also demonstrate that the linear approximation regimes for TEB optical systems using a quarter wave plate are in the most general case inadequate for accurate data inter-

pretation. Likewise, the use of a quarter wave plate in the absence of a means to precisely align it with six degrees of laboratory freedom yields highly questionable results, and is therefore not advisable for the electrochemist not trained in optics. Robust and precise mathematical models are given for the two optical configurations for TEB, with and without the quarter wave plate, as standards by which researchers can test the alignment and trustworthiness of their apparatus.

7.3 Size Distribution Calculations

The latter century is filled with research and mathematical attempts to relate measurable hydrodynamic properties of materials to their real physical properties via mathematical models of the system. These models are often intractably complicated due to the competing electrical and hydrodynamic mechanisms. In addition, polydispersity gives rise to continuous solutions requiring multi-exponential deconvolution which often end with unstable solution convergences due to experimental uncertainty. Although we have developed an apparatus to measure apparent rotational diffusion coefficients, the mathematical dilemma of determining absolute particle lengths remains for us as it does for similar techniques. We have educated ourselves to the difficulties and accepted protocols in the field, and hope to make further progress with improved data resolution and enriched research experiences. If the mathematical difficulties can be adequately addressed, TEB can provide a technique for measuring aspect ratios and size distributions of nanoparticles.

Bibliography for Chapter 1

[1] R. L. Whistler and J. M. BeMiller. *Carbohydrate Chemistry for Food Scientists*, volume 7, chapter Cellulosics, page 155. American Association of Cereal Chemists, 1997.

[2] M. Miriam de Souza Lima and Redouane Borsali. Rodlike cellulose microcrystals: Structure, properties, and applications. *Macromol. Rapid. Commun.*, 25:771–787, 2004.

[3] Antoinette C. O'Sullivan. Cellulose: The structure slowly unravels. *Cellulose*, 4:173–207, 1997.

[4] Kerian Fleming, Derek G. Gray, and Stephen Mathews. Cellulose crystallites. *Chem. Eur. J.*, 7(9):1831–1835, 2001.

[5] O. A. Battista. *Microcrystalline Polymer Science*. McGraw-Hill Book Company, 1975.

[6] B. G. Rånby. Fibrous macromolecular systems. Cellulose and muscle. The colloidal properties of cellulose micelles. *Discuss. Faraday Soc.*, 11:158–164, 1951.

[7] Stephanie Beck-Candanedo, Maren Roman, and Derek. G. Gray. Effect of reaction conditions on the properties and behaviour of wood cellulose nanocrystal suspensions. *Biomacromoelcules*, 6:1048–1054, 2005.

[8] Bengt G. Rånby. Aqueous colloidal solutions of cellulose micelles. *Acta Chem. Scand.*, 3:649–650, 1949.

[9] J. F. Revol, L. Godbout, and D. J. Gray. Solid self-assembled films of cellulose with chiral nematic order an optically variable properties. *J. Pulp Paper. Sci*, 24:146, 1998.

[10] The American Chemistry Council. Consideration for a definition for engineered nanomaterials. Technical report, The American Chemistry Council- Nanotechnology Panel, 2007.

[11] T. P. Nevell and S. Haig Zeronian, editors. *Cellulose Chemistry and its Applications*. Halsted Press: a Division of John Wiley and Sons, 1985.

[12] Peter Atkins and Julio de Paula. *Physical Chemistry*, pages 752–754. W. H. Freeman and Company, 2002.

[13] Kenneth S. Schmitz. *Macroions in Solution and Colloidal Suspension*. VHC Publishers, 1993.

[14] A. V. Delgado, F. González-Caballero, R. J. Hunter, L. K. Koopal, and J. Lyklema. Measurement and interpretation of electrokinetic phenomena (IUPAC technical report). *Pure Appl. Chem.*, 77(10):1753–1805, 2005.

[15] Allen J. Bard and Larry R. Faulkner. *Electrochemical Methods: Fundamentals and Applications*. John Wiley & Sons, 2001.

[16] Zeta-Meter Inc. Zeta-potential: A complete course in 5 minutes. Technical report, Zeta-Meter Inc., 765 Middlebrook Ave., PO Box 3008, Staunton VA, 24402.

[17] Brookhaven Instruments Corporation. *ZetaPlus Zeta Potential Analyzer Instruction Manual*, 2002.

[18] Brookhaven Instruments Corporation. BI-ZR3 Reference Material, 750 Blue Point Road, Holtsville NY, 11742, http://www.bic.com.

[19] Bengt G. Rånby and E. Ribi. Über den feinbau der zelulose. *Experimentia*, 6:12–14, 1950.

[20] S. M. Mukherjee and H. J. Woods. X-ray and electron microscope studies of the degradation of cellulose by sulphuric acid. *Biochim. Biophys. Acta*, 10:499–511, 1953.

[21] E. H. Immergut and B. G. Rånby. Heterogeneous acid hydrolysis of native cellulose fibers. *Ind. Eng. Chem.*, 48:1183, 1956.

[22] R. H. Marchessault, F. F. Morehead, and N. M. Walter. Liquid crystal systems from fibrillar polysaccharides. *Nature*, 184:632–633, 1959.

[23] J. F. Revol, H. Bradford, J. Glasson, R. H. Marchessault, and D. J. Gray. Helical self-ordering of cellulose microfibrils in aqueous suspension. *Intl. J. Biol. Macromol.*, 14:170–172, 1992.

[24] J. F. Revol and R. H. Marchessault. In vitro chiral nematic ordering of chitin crystallites. *Int. J. Biol. Macromol.*, 15:329–335, 1993.

[25] Jun Araki and Shigenori Kuga. Effect of trace electrolyte on liquid crystal type of cellulose microcrystals. *Langmuir*, 17:4493–4496, 2001.

[26] Xue Min Dong, Tsunehisa Kimura, Jean-Francois Revol, and Derek G. Gray. Effects of ionic strength on the isotropic-chiral nematic phase transition of suspensions of cellulose crystallites. *Langmuir*, 12:2076–2082, 1996.

[27] Xue Min Dong and Derek G. Gray. Effect of counterions on ordered phase formation in suspensions of charged rodlike cellulose crystallites. *Langmuir*, 13:2404–2409, 1997.

[28] Xue Min Dong, Jean-François Revol, and Derek Gray. Effect of microcrystallite perparation conditions on the formation of colloid crystals of cellulose. *Cellulose*, 5:19–32, 1998.

[29] W. J. Orts, L. Godbout, R. H. Marchessault, and J.-F. Revol. Enhanced ordering of liquid crystalline suspensions of cellulose microfibrils: A small angle neutron scattering study. *Macromolecules*, 31:5717–5725, 1998.

[30] L. Onsager. *Ann. N. Y. Acad. Sci.*, 51:627, 1949.

[31] A. Stroobants, H. N. W. Lekkererer, and T. Odjik. Effect of electrostatic interaction on the liquid crystal phase transition in solutions of rodlike polyelectrolytes. *Macromolecules*, 19:2232, 1986.

[32] Jun Araki, Masahisa Wada, Shigenori Kuga, and Takeshi Okano. Birefringent glassy phase of a cellulose microcrystal suspension. *Langmuir*, 16:2413–2415, 2000.

[33] Xue Min Dong and Derek Gray. Effect of counterions on ordered phase formation on suspensions of charged rodlike cellulose crystalites. *Langmuir*, 13:2404–2409, 1997.

[34] Weiliang Chen and Derek G. Gray. Interfacial tension between isotropic and anisotropic phases of a suspension of rodlike particles. *Langmuir*, 18:633–637, 2002.

[35] Taku Furuta, Eiji Yamahara, Toshiki Konishi, and Norio Ise. Ordering in aqueous cellulose hydrolysate dispersions: An ultra-small-angle-X-ray scattering study. *Macromolecules*, 29:8994–8995, 1996.

[36] Maren Roman and William T. Winter. Effect of sulfate groups from sulfuric acid hydrolysis on the thermal degragation behavior of bacterial cellulose. *Biomacromolecules*, 6(2):1048–1054, 2001.

[37] Pierre Mallet, C. A. Guérin, and Anne Sentenac. Maxwell-Garnett mixing rule in the presence of multiple scattering: Derivation and accuracy. *Phys. Rev. B*, 72:014205–1, 2005.

[38] Stoyl P. Stoylov and Maria V. Stoimenova, editors. *Molecular and Colloidal Electrooptics*, volume 134. CRC Press, Taylor & Francis Group, 2007.

[39] Anna Spanoudaki and Rolf Pelster. Effective dielectric properties of composite materials: The dependence in the particle size distribution. *Phys. Rev. B*, 64:064205–1, 2001.

[40] J. C. M. Garnett. *Philos. Trans. R. Soc. London*, 203:305, 1904.

[41] Ohad Levy. Maxwell Garnett theory for mixtures of anisotropic inclusions: Applications to conducting polymers. *Phys. Rev. B*, 56(13):8035–8046, 1997.

[42] H. Benoit. Contribution a l'Étude de l'effet kerr présenté par les solutions dilueés de macromolécules rigides. *Ann. Phys.*, 6:561, 1951.

[43] John Kerr. A new relation between electricity and light. *Phil. Mag.*, 50:337,446, 1875.

[44] John Kerr. *Phil. Mag.*, 8(85):229, 1879.

[45] John Kerr. *Phil. Mag.*, 13(53):284, 1882.

[46] John Kerr. *Phil. Mag.*, 37:380, 1894.

[47] John Kerr. *Phil. Mag.*, 38:144, 1894.

[48] P. Debye. *Handbuch der Radiologie*, 6:597, 1925.

[49] A. Peterlin and H. A. Stuart. Zur theorie der strömungsdoppelbrechung von kolloiden und groben molekülen in lösung. *Z. Physik*, 112:129–147, 1939.

[50] Chester T. O'Konski, Kishiro Yoshioka, William, and Orttung. Electric properties of macromolecules. IV. Determination of electric and optical parameters from saturation of electric birefringence in solutions. *J. Chem. Phys.*, 63(10):1558–1565, 1959.

[51] Jr. Ignacio Tinoco. The dynamic electrical birefringence of rigid macromolecules. *J. Am. Chem. Soc.*, 7(17), 1955.

[52] Chester T. O'Konski and Sonja Krause. Theory of the Kerr constant of rigid conducting dipolar macromolecules. *J. Phys. Chem*, 74:3243–3250, 1970.

[53] Chester T. O'Konski and A. J. Haltner. Electric properties of macromolecules. I. A study of electric polarization in polyelectrolyte solutions by means of electric birefringence. *J. Am. Chem. Soc.*, 79:5634, 1957.

[54] Chester T. O'Konski, editor. *Molecular Electro-optics Part 1: Theory and Methods*. Marcel Dekker, Inc., 1976.

[55] Chester T. O'Konski and Bruno H. Zimm. A new method for studying electrical orientation and relaxation effects in aqueous colloids: Preliminary results with tobacco mosaic virus. *Science*, 111(2875):113–116, 1950.

[56] K. W. Wagner. *Elektrotechn. Z.*, 36:111,121,135,163, 1915.

[57] H. Fricke. The Maxwell-Wagner dispersion in a suspension of ellipsoids. *J. Phys. Chem.*, 57:934, 1953.

Bibliography for Chapter 2

[1] John Kerr. A new relation between electricity and light. *Phil. Mag.*, 50:337,446, 1875.

[2] J. Larmor. *Phil. Trans.*, A190:232, 1897.

[3] P. Langevin. *Raduim*, 7:249, 1910.

[4] P. Langevin. *Compt. Rend.*, 151:475, 1910.

[5] A. Enderle. PhD thesis, Freidburg, 1912.

[6] W. Voigt. *Nadir. Kgl. Ges. Wiss. Göttingen*, pages 577–593. 1912.

[7] W. Voigt. *Chem. Abstr.*, 7:3914, 1913.

[8] R. Gans. *Ann. Physik.*, 63(4):97, 1921.

[9] P. Debye. *Polar Molecules*. Dover, 1929.

[10] P. Debye. *Handbuch der Radiologie*, 6:597, 1925.

[11] P. Debye and H. Sack. *Ann. d. Physik*, 6(69):179, 1934.

[12] A. Peterlin and H. A. Stuart. Zur theorie der strömungsdoppelbrechung von kolloiden und groben molekülen in lösung. *Z. Physik*, 112:129–147, 1939.

[13] H. Benoit. Contribution a l'Étude de l'effet kerr présenté par les solutions dilueés de macromolécules rigides. *Ann. Phys.*, 6:561, 1951.

[14] Chester T. O'Konski and Bruno H. Zimm. A new method for studying electrical orientation and relaxation effects in aqueous colloids: Preliminary results with tobacco mosaic virus. *Science*, 111(2875):113–116, 1950.

[15] Igor N. Serdyuk, Nathan R. Zaccai, and Joeseph Zaccai. *Methods in Molecular Biophysics*, chapter Part D. Hydrodynamics. Cambridge University Press, 2007.

[16] John David Jackson. *Classical Electrodynamics*. John Wiley and Sons, 1975.

[17] Grant R. Fowles. *Introduction to Modern Physics*. Holt, Rinehart and Winston, Inc., 1975.

[18] Wolfram Schnabel. *Polymers and Light. Fundamentals and Technical Applications*. Wiley-VCH, 2007.

[19] Evarist Riande and Enrique Saiz. *Dipole Moments and Birefringence of Polymers*. Prentice Hall, 1992.

[20] Ken A. Dill, Sarina Bromberg, and Dirk Stigter. *Molecular Driving Forces. Statistical Thermodynamics in Chemistry and Biology*. Garland Science, Member of Taylor and Francis Group, 2003.

[21] Kenneth S. Schmitz. *Macroions in Solution and Colloidal Suspension*. VHC Publishers, 1993.

[22] P. Debeye and H. Falkenhagen. Dispersion der leitfähigkeit starker elektrolyte. *Physik. Z.*, 29(121):401, 1928.

[23] Gerals S. Manning. Limiting laws and counterion condensation in polyelectrolyte solutions I. Colligative properties. *J. Chem. Phys.*, 51(3):924–933, 1969.

[24] Chester T. O'Konski. Electric properties of macromolecules. V. Theory of ionic polarization in polyelectrolytes. *J. Phys. Chem.*, 64:605–619, 1960.

[25] Kenneth S. Schmitz. *An Introduction to Dynamic Light Scattering by Macromolecules*. Academic Press, Inc, 1990.

[26] H. Plummer and B. R. Jennings. Light scattering by rodlike macromolecules oriented in alternating electric fields. *J. Chem. Phys.*, 50:1033–1034, 1969.

[27] I. Petkanchin, R. Br uckner, S. Sokerov, and Ts. Radeva. Comparison of electric light scattering and birefringence for polydisperse systems. *Colloid & Polymer Sci.*, 257:169–165, 1979.

[28] J. Schweitzer B. R. Jennings. Transient scattering changes induced by pulsed sinusoidal electric fields. *J. Phys. D: Appl. Phys.*, 5:297–309, 1972.

[29] Emma H. B. DeLacey and Lee R. White. Dielectric response and conductivity of dilute suspensions of colloidal particles. *J. Chem. Soc. Faraday Trans. 2*, 77:2007–2039, 1981.

[30] Chetser T. O'Konski. Effect of interfacial conductivity on dielectric properties. *J. Chem. Phys.*, 23(8):1559, 1955.

[31] G. B. Thurston and . I. Bowling D. The frequency dependence of the Kerr effect for suspensions of rigid particles. *J. Colloid. Interface. Sci*, 30(1):34–45, 1968.

[32] Chester T. O'Konski and A. J. Haltner. Electric properties of macromolecules. I. A study of electric polarization in polyelectrolyte solutions by means of electric birefringence. *J. Am. Chem. Soc.*, 79:5634, 1957.

[33] S. P. Stoylov. Colloid electro-optics. Electrically induced optical phenomena in disperse systems. *Adv. Colloid Interface Sci.*, 3:45–110, 1971.

[34] Chester T. O'Konski and Sonja Krause. Theory of the Kerr constant of rigid conducting dipolar macromolecules. *J. Phys. Chem*, 74:3243–3250, 1970.

[35] Chester T. O'Konski and Arthur J. Haltner. Characterization of the monomer and dimer of tobacco mosaic virus by transient electric birefringence. *J. Am. Chem. Soc.*, 78:3604–3610, 1956.

[36] Chester T. O'Konski, Kishiro Yoshioka, William, and Orttung. Electric properties of macromolecules. IV. Determination of electric and optical parameters from saturation of electric birefringence in solutions. *J. Chem. Phys.*, 63(10):1558–1565, 1959.

[37] Stoyl P. Stoylov and Maria V. Stoimenova, editors. *Molecular and Colloidal Electro-optics*, volume 134. CRC Press, Taylor & Francis Group, 2007.

Bibliography for Chapter 3

[1] Francis Perrin. Mouvement brownien d'un ellipsoid (I). Dispersion diélectrique pour des molécules ellispodales. *Le Journal de Physique et le Radium*, 1934.

[2] Francis Perrin. Mouvement brownien d'un ellipsoid (II). rotation libre et dépolarisation des flouresences. Translation et diffusion de molécules ellispodales. *Le Journal de Physique et le Radium*, 1936.

[3] A. Peterlin and H. A. Stuart. Zur theorie der strömungsdoppelbrechung von kolloiden und groben molekülen in lösung. *Z. Physik*, 112:129–147, 1939.

[4] H. Benoit. Contribution a l'Étude de l'effet kerr présenté par les solutions dilueés de macromolécules rigides. *Ann. Phys.*, 6:561, 1951.

[5] Chester T. O'Konski and Bruno H. Zimm. A new method for studying electrical orientation and relaxation effects in aqueous colloids: Preliminary results with tobacco mosaic virus. *Science*, 111(2875):113–116, 1950.

[6] Igor N. Serdyuk, Nathan R. Zaccai, and Joeseph Zaccai. *Methods in Molecular Biophysics*, chapter Part D. Hydrodynamics. Cambridge University Press, 2007.

[7] Kenneth S. Schmitz. *Macroions in Solution and Colloidal Suspension*. VHC Publishers, 1993.

[8] Jay Newman and Harry L. Swinney. Length and dipole moment of TMV by laser signal-averaging transient electric birefringence. *Biopolymers*, 15:301–315, 1976.

[9] J. M. Burgers. *Verk. Kon. Ned. Akad. Wet.*, 13:113, 1938.

[10] S. Broersma. Rotational diffusion constant of a cylindrical particle. *J. Chem. Phys.*, 32(6):1626–1631, 1960.

[11] Jacob Riseman and John G. Kirkwood. The intrinsic viscosity, translational and rotatory diffusion constants of rod-like macromolecules in solution. *J. Chem. Phys.*, 18(4):512–516, 1950.

[12] Broersma S. Viscous force and torque constants for a cylinder. *J. Chem. Phys.*, 74(12):6989–6990, 1981.

[13] Mana M. Tirado and Jose Garcia de la Torre. Rotational dynamics of rigid, symmetric top macromolecules. Application to circular cylinders. *J. Chem. Phys.*, 73(4):1986–1993, 1980.

[14] M. Mercedes Tirado, Carmen Lopez Martinez, and Jose Garcia de la Torre. Comparison of theories for the translational and rotational diffusion coefficients of rod-like macromolecules. Applications to short DNA fragments. *J. Chem. Phys.*, 81(4):2047–2052, 1984.

[15] Chester T. O'Konski and Arthur J. Haltner. Characterization of the monomer and dimer of tobacco mosaic virus by transient electric birefringence. *J. Am. Chem. Soc.*, 78:3604–3610, 1956.

[16] William Menke. *Geophysical data analysis: Discrete inverse theory*, volume 45 of *International Geophysics Series*. Academic Press, Inc., 1989.

[17] S. W. Provencer. CONTIN: A general purpose constrained regularization program for inverting noisy linear algebraic and integral equations. *Computer Physics Communications*, 27:229–210, 1982.

[18] S. W. Provencer. An eigenfunction expansion method for the analysis of exponential decay curves. *J. Chem. Phys*, 64(7):2772–2777, 1976.

[19] Stephen Provencher and Robert Vogel. Information loss with transform methods in system identification: A new set of transforms with high information content. *Mathematical Biosciences*, 50:251–262, 1980.

[20] S. W. Provencer. A constrained regularization method for inverting data represented by linear algebraic or integral equations. *Computer Physics Communications*, 27:213–227, 1982.

[21] R. M. J Watson and B. R. Jennings. Polydisperse size data from single electric birefringence transients. *Powder Technology*, 72:963–69, 1992.

[22] R. M. Pytkowicz and C. T. O'Konski. Characterization of *Helix Pomatia* hemocyanin by transient electric birefringence. *Biochim. Biophys. Acta*, 36:466, 1959.

[23] S. Krause and C. T. O'Konski. Electric properties of macromolecules. III. Kerr constants and rotational diffusion of bovine serum albumin in aqueous solutions. *J. Am. Chem. Soc.*, 81:5082, 1959.

[24] P. Ingram and H. G. Jerrard. Study by the Kerr effect of the action of enzymes on macromolecules. *Brit. J. Appl. Phys.*, 14:572, 1963.

[25] J. Schweitzer B. R. Jennings. Transient scattering changes induced by pulsed sinusoidal electric fields. *J. Phys. D: Appl. Phys.*, 5:297–309, 1972.

[26] M. Matsumoto, H. Watanabe, and K. Yoshioka. Electric and hydrodynamic properties of polypeptides in solution. II. Conformation of poly(L-glutamic acid) in various organic solvents. *Biopolymers*, 9:1307, 1970.

[27] C. Lanczos. *Applied Analysis*. Pitman, 1957.

[28] G. Boeckel, J. C. Genzling, G. Weill, and H. Benoit. *J. Chim. Phys.*, 59:999, 1962.

[29] C. T. O'Konski. *Encyclopedia of Polymer Science and Technology*, volume 9. Interscience, 1966.

[30] K. Yoshioka and H. Watanabe. *Physical Principles and Techniques of Protein Chemistry*.

[31] S. P. Stoylov and S. Sokerov. Transient electric light scattering II. Determination of distribution curves for solutions of polydisperse rods. *Journal of Colloid and Interface Science*, 27(3):542–544, 1968.

[32] J. Schweitzer and B. R. Jennings. Electro-optic decay analysis for polydisperse systems. II. Discrete averaging for rods. *Biopolymers*, 12:2439–2441, 1973.

[33] V. J. Morris, A. R. Foweraker, and B. R. Jennings. Particle size distributions from transient electric birefringence data: I. Polydisperse rods by two-parameter distribution functions. *Advances in Molecular Relaxation and Interaction Processes*, 12(1):65 – 83, 1978.

[34] Kevin Parslow and Barry R Jennings. Polydisperse particle size analysis by pulsed electric birefringence. *Philosophical Magazine Part B*, 49(5):457–469, 1984.

[35] M. Huntley-James and B. R. Jennings. Multimodal particle size measurement using truncated pulsed electro-optic birefringence. *Journal of Physics D: Applied Physics*, 23(7):922, 1990.

[36] J. K. Phalakornkuland A. P. Gast and R. Pecora. Rotational and translational dynamics of rodlike polymers: A combined transient electric birefringence and dynamic light scattering study. *Macromolecules*, 32(9):3122–3135, 1999.

[37] M. M. De Souza Lima, J. T. Wong, M. Paillet, R. Borsali, and R. Pecora. Translational and rotational dynamics of rodlike cellulose whiskers. *Langmuir*, 19:24–29, 2003.

[38] D. M. Oakley, B. R. Jennings, D. R. Waterman, and R C Fairey. An electro-optic birefringence fine-particle sizer. *Journal of Physics E: Scientific Instruments*, 15(10):1077, 1982.

[39] D. M. Oakley and B. R. Jennings. Clay particle sizing by electrically-induced birefringence. *Clay Minerals*, 17(3):313–325, 1982.

Bibliography for Chapter 4

[1] Denilson da Silva Perez, Suzelei Montanari, and Michel R. Vignon. TEMPO-mediated oxidation of cellulose III. *Biomacromoleculsuches*, 4:1417–1425, 2003.

[2] Henri Chanzy Youssef Habibi and Michel R. Vignon. TEMPO-mediated surface oxidation of cellulose whiskers. *Cellulose*, 13:697–687, 2006.

[3] J. F. Revol, H. Bradford, J. Glasson, R. H. Marchessault, and D. J. Gray. Helical self-ordering of cellulose microfibrils in aqueous suspension. *Intl. J. Biol. Macromol.*, 14:170–172, 1992.

[4] J. F. Revol, L. Godbout, and D. J. Gray. Solid self-assembled films of cellulose with chiral nematic order an optically variable properties. *J. Pulp Paper. Sci*, 24:146, 1998.

[5] E. V. Gert, V. I. Torgashov, O. V. Zubets, and F. N. Kaputskii. Preparation and properties of enterosorbants based on carboxylated microcrystaline cellulose. *Cellulose*, 12:515–526, 2005.

[6] Silvia Gomez-Bujedo, Etienne Fleury, and Michel R. Vignon. Preparation of cellouronic acids and partially acetylated cellouronic acids by TEMPO/NaClO oxidation of water-soluble cellulose acetate. *Biomacromolecules*, 5:565–571, 2004.

[7] Edward Collett. *Polarized Light: Fundamentals and Applications*. Marcel Dekker, Inc., 1993.

[8] Dennis Goldstein and Edward Collett. *Polarized Light, Revised and Expanded*. Marcel Dekker, Inc., 2003.

[9] Serge Huard. *Polarization of Light*. John Wiley and Sons, 1996.

[10] Christian Brosseau. *Fundamentals of Polarized Light. A Statistical Optics Approach*. John Wiley and Sons, 1998.

[11] David S. Kliger, James W. Lewis, and Cora Einterz Randall. *Polarized Light in Optics and Spectroscopy*. Academic Press, Inc., 1990.

[12] B. R. Jennings and D. R. Waterman. Precision in transient electric birefringence measurements for colloids. *Journal of Colloid and Interface Science*, 288:304–307, 2005.

[13] Chester T. O'Konski and Bruno H. Zimm. A new method for studying electrical orientation and relaxation effects in aqueous colloids: Preliminary results with tobacco mosaic virus. *Science*, 111(2875):113–116, 1950.

[14] Chester T. O'Konski and A. J. Haltner. Electric properties of macromolecules. I. A study of electric polarization in polyelectrolyte solutions by means of electric birefringence. *J. Am. Chem. Soc.*, 79:5634, 1957.

[15] Dietmar Porschke. Electric birefringence at small angles from crossed position: Enhanced sensitivity and special effects. *J. Phys. Chem. B*, 115:4177–4183, 2011.

Bibliography for Chapter 5

[1] Chester T. O'Konski and A. J. Haltner. Electric properties of macromolecules. I. A study of electric polarization in polyelectrolyte solutions by means of electric birefringence. *J. Am. Chem. Soc.*, 79:5634, 1957.

[2] G. B. Thurston and . I. Bowling D. The frequency dependence of the Kerr effect for suspensions of rigid particles. *J. Colloid. Interface. Sci*, 30(1):34–45, 1968.

Bibliography for Chapter 6

[1] Henri Chanzy Youssef Habibi and Michel R. Vignon. TEMPO-mediated surface oxidation of cellulose whiskers. *Cellulose*, 13:697–687, 2006.

[2] T. P. Nevell and S. Haig Zeronian, editors. *Cellulose Chemistry and its Applications*. Halsted Press: a Division of John Wiley and Sons, 1985.

[3] O. A. Battista. *Microcrystalline Polymer Science*. McGraw-Hill Book Company, 1975.

[4] C. Besemer A, A. E. J. de Nooy, and H. van Bekkum. Methods for the selective oxidation of cellulose: Preparation of 2,3-dicarboxycellulose and 6-carboxycelloluse. In *Cellulose Derivatives: Modification, Characterization and Nanostructures*, volume 688, pages 73–82, 1998.

[5] A. M. A. Nada, S. Abd El-Mongy, and E. S. Abd El-Sayed. Effect of different treatments on cellulose toward carboxylation and its application for metal ion absorbtion. *BioResources*, 4(1):80–93, 2009.

[6] Tsuguyuki Saito, Yoshiharu Nishiyama, Jean-Luc Putaux, and Akira Isogai. Homogeneous suspensions of individualized microfibrils from TEMPO-catalyzed oxidation of native cellulose. *Biomacromolecules*, 7(6):16871691, 2006.

[7] Akira Isogai and Yumiko Kato. Preparation of polyuronic acid from cellulose by TEMPO-mediated oxidation. *Cellulose*, 5:153–164, 1998.

[8] Arjan E. J. de Nooy, Arie C. Besemer, and Herman van Bekkum. Highly selective nitroxyl radical-mediated oxidation of primary alcohol groups in water-soluble glucans. *Carbohydrate Research*, 269:89–98, 1995.

[9] Menachem Lewin and Joseph A. Epstein. Functional groups and degradation of cotton oxidized by hypochlorite. *Journal of Polymer Science*, 58:1023–1037, 1962.

[10] M. F. Semmelhack, Chuen S. Chou, and David A. Cortes. Nitroxyl-mediated electrooxidation of alcohols to aldehydes and ketones. *J. Am. Chem. Soc.*, 105:4492–4494, 1983.

[11] R.V. Casciani, P.J.-M. Likibi, and G.L. German patent DE 4209869 A1 (1992). *Chem. Abstr.*, 119:9389, 1993.

[12] N. J. Davis and S. L. Flitsch. Selective oxidation of monosaccharide derivatives to uronic acids. *Tetrahedron Letters*, 34:1181–1184, 1993.

[13] A.E.J. de Nooy, A.C. Besemer, and H. van Bekkum. Highly selective TEMPO-mediated oxidation of primary alcohol groups in polysaccharides. *Recl. Trav. Chim. Pays-Bas*, 113:165–166, 1994.

[14] P. S. Chang and J. F. Robyt. Oxidation of primary alcohol groups of naturally occurring polysaccharides with 2,2,6,6-tetramethyl-1-pipelidine oxammonium ion. *Carbohydr. Chem*, 15:819–830, 1996.

[15] Tsuguyuki Saito and Akira Isogai. TEMPO-mediated oxidation of native cellulose. The effect of oxidation conditions on chemical and crystal structures of the water-insoluble fractions. *Biomacromolecules*, 5:1983–1989, 2004.

[16] A.C. Besemer A.E.J. de Nooy, H. van Bekkumand J. A. P. P. van Dijk, and J. A. M. Smit. TEMPO-mediated oxidation of pullulan and influence of ionic strength and linear charge density on the dimensions of the obtained polyelectrolyte chains. *Macromolecules*, 29:6541–6547, 1996.

[17] Izuma Shibata and Akira Isogai. Depolymerization of cellouronic acid during TEMPO-mediated oxidation. *Cellulose*, 10:151–158, 2003.

[18] Tsuguyuki Saito, Masayuki Hirota, Naoyuki Tamura, Satoshi Kimura, Hayaka Fukuzumi, Laurent Heux, and Akira Isogai. Individualization of nano-sized plant cellulose fibrils by direct surface carboxylation using TEMPO catalyst under neutral conditions. *Biomacromolecules*, 10:1992–1996, 2009.

[19] Kevin Parslow and Barry R Jennings. Polydisperse particle size analysis by pulsed electric birefringence. *Philosophical Magazine Part B*, 49(5):457–469, 1984.

[20] J. Schweitzer B. R. Jennings. Transient scattering changes induced by pulsed sinusoidal electric fields. *J. Phys. D: Appl. Phys.*, 5:297–309, 1972.

[21] Jayanth Murthy Madapura. Achieving higher ADC resolution using oversampling. Technical report, Microchip Tecnology Inc., 2008.

[22] J. Schweitzer and B. R. Jennings. Electro-optic decay analysis for polydisperse systems. II. Discrete averaging for rods. *Biopolymers*, 12:2439–2441, 1973.

[23] M. Huntley-James and B. R. Jennings. Multimodal particle size measurement using truncated pulsed electro-optic birefringence. *Journal of Physics D: Applied Physics*, 23(7):922, 1990.

[24] R. M. Pytkowicz and C. T. O'Konski. Characterization of *Helix Pomatia* hemocyanin by transient electric birefringence. *Biochim. Biophys. Acta*, 36:466, 1959.

[25] A. R. Foweraker and B. R. Jennings. Pulsed electric dichroism studies of the amylose tri-iodide complex. *Advances in Molecular Relaxation Processes*, 6:241–254, 1974.

[26] S. W. Provencer. CONTIN: A general purpose constrained regularization program for inverting noisy linear algebraic and integral equations. *Computer Physics Communications*, 27:229–210, 1982.

APPENDICES

Appendix A – Appendix I: List of Common Abbreviations

AC = Alternating Current

ADC = Analog-to-Digital Converter

AFM = Atomic Force Microscopy

CDIDM = (Surface) Charge Dependent Interfacial Dipole Moments

CNC = Cellulose Nanocrystal

C.CNC = Carboxylated Cellulose Nanocrystal

DC = Direct Current

DF-diH_2O = Dust Free deionized water

DLS = Dynamic Light Scattering

DP = Degree of Polymerization

DSO = Digital Storage Oscilloscope

EDL = Electric Double Layer

EMT = Effective Medium Theory

EO = Electro-Optic

FTIR = Fourier Transform Infrared Spectroscopy

IDM = Interfacial Dipole Moments

IS = Ionic Strength

LC = Liquid Crystal

LIT = Linear Inverse Theory

MG = Maxwell-Garnett

MSa/s = Mega Samples per second

MWIDM = Maxwell-Wagner Interfacial Dipole Moments

MWS = Maxwell-Wagner-Sillars (in terms Interfacial Dipole Moments, also called MW)

LODP = Level Off Degree of Polymerization

Sa/s = Samples per second (Referring to sample rate of an ADC)

SEM = Scanning Electron Microscopy

SNR = Signal-to-Noise Ratio (general for all laboratory noise contributions)

SNR_Q = Signal-to-Quantization Noise Ratio (specific to ADC bit resolution)

TEB = Transient Electric Birefringence

TEM = Tunnelling Electron Microscopy

TEMPO = 2,2,6,6-tetramethyl-1-piperidinyloxy (free radical)

TMV = Tobacco Mosaic Virus